Summer 2024

Measurement of the Photoproduction Cross-Section of $f_1(1285)$ in the Exclusive Reactions $\gamma p \to p' K^{\mp} K_S \pi^{\pm}$ at $7.5 < E\gamma < 11.5$ GeV With GlueX at Jefferson Lab

Tyler Viducic
Old Dominion University, tyler.viducic@gmail.com

MEASUREMENT OF THE PHOTOPRODUCTION CROSS-SECTION OF $f_1(1285)$ IN THE EXCLUSIVE REACTIONS $\gamma p \to p' K^{\mp} K_S \pi^{\pm}$ AT $7.5 < E_\gamma < 11.5$ GeV WITH GLUEX AT JEFFERSON LAB

by

Tyler Viducic
B.S. May 2016, The College of New Jersey
M.S. May 2018, Old Dominion University

A Dissertation Submitted to the Faculty of
Old Dominion University in Partial Fulfillment of the
Requirements for the Degree of

DOCTOR OF PHILOSOPHY

PHYSICS

OLD DOMINION UNIVERSITY
August 2024

Approved by:

Moskov Amaryan (Director)

Alexander Gurevich (Member)

Anatoly Radyushkin (Member)

Lawrence Weinstein (Member)

Richard Zimmerman (Member)

ABSTRACT

MEASUREMENT OF THE PHOTOPRODUCTION CROSS-SECTION OF $f_1(1285)$ IN THE EXCLUSIVE REACTIONS $\gamma p \to p' K^{\mp} K_S \pi^{\pm}$ AT $7.5 < E_\gamma < 11.5$ GeV WITH GLUEX AT JEFFERSON LAB

Tyler Viducic
Old Dominion University, 2024
Director: Dr. Moskov Amaryan

The $f_1(1285)$ meson is commonly understood to belong to the axial-vector nonet as the low-mass isoscalar partner to the $f_1(1420)$ but has been suggested as a candidate for a $KK^* + c.c$ molecule. A nearly mass-degenerate 0^{-+} state has been observed in πp scattering that calls into question the established branching ratios of the $f_1(1285)$ decays. Recently, the differential cross-section for the photoproduction of $f_1(1285)$ was measured by the CLAS experiment and the results disagreed with theoretical predictions. Additionally, the CLAS experiment did not observe a mass-degenerate 0^{-+} state. We present the results of the first photoproduction cross-section measurement $d\sigma/dt$ of $f_1(1285)$ at $7.5 < E_\gamma < 11.5$ GeV from the GlueX experiment at Thomas Jefferson National Accelerator Facility in the reactions $\gamma p \to p' K^- K_s \pi^+$ and $\gamma p \to p' K^+ K_s \pi^-$. We find that the production mechanism of $f_1(1285)$ is consistent with t-channel exchange. We also observe a difference in the differential cross-section of $f_1(1285)$ as a function of $-t$ as measured in the charge conjugated $K^{\mp} K_s \pi^{\pm}$ decay modes that we hypothesize to be due to baryonic N^* interference. The observed distributions of $M(KK)$ and $M(K\pi)$ are consistent with both a $q\bar{q}$ state and predictions for a $KK^* + c.c$ molecular state. Additionally, we find that the cross-section at low $M(KK\pi)$ is dominated by the 1^{++} state.

This work is dedicated to Gram and Dido. I wish you could have been here.

ACKNOWLEDGMENTS

The long journey towards earning my Ph.D. has been filled with many stumbles, trials, and failures. It is not hyperbole to say that I could not have done this alone.

To Jenna. Thank you for all the love and encouragement in the many years you have walked this road beside me. To Mom and Dad. I will never be able to express my gratitude for all the support you have given me as I pursued my doctoral dreams. To Connor and Logan. Thank you for anchoring me when the seas got rough.

To the rest of the Viducic/Beese/Scott clan. Your unwavering confidence in me over the last 8 year kept me going when things looked bleak. I love you all dearly. To the Boys. Thanks for all the laughs and good times. They kept me sane. To Brent, David, Jeremy, Josh, Josh, Lindsay, Mark, and Torri. Look guys, I finally made it. Thanks for being my friends in a state I was otherwise alone in.

To Bonnie Jablonski. Thank you for setting me on this road from AP physics to physics Ph.D.. To my TCNJ Physics professors. You were the proverbial giant upon whose shoulders I stood. To Wickramasinghe's Army. Thanks for helping me kill off the weak brain cells to ensure only the strong ones survived. To Gagik. Thank you for teaching me how to be a moderately better programmer and providing the levity in many early morning meetings. To Justin, Sean, Matt, Alex, Malte, Will, Amy, Edmundo, Boris, and everyone else at GlueX. Thank you for your endless patience guiding me along the path this research has taken. I owe you all a lot more than a few words on a page. To Dr. Gurevich, Dr. Radyushkin, and Dr. Zimmerman. Thank you for sitting on my committee, keeping me focused and diligent,

and providing feedback on this work. To Dr. Weinstein. I cannot thank you enough for all you've done for me. I am a better physicist and researcher because of your guidance. Finally, to Dr. Moskov Amaryan. You have taught me so much about physics, obscure soviet idioms, and myself that it is hard to put in words. Thank you for support and patience.

To everyone mentioned above - and many people unmentioned - you have my undying gratitude. Thank you for coming along with me on this journey. Thank you for making sure I kept taking the next step.

"The ancient code of the Knights Radiant says 'Journey Before Destination.' Some may call it a simple platitude, but it is far more. A journey will have pain and failure. It is not only the steps forward that we must accept. It is the stumbles. The trials. The knowledge that we will fail. That we will hurt those around us. But if we stop, if we accept the person we are when we fall, the journey ends. That failure becomes our destination. To love the journey is to accept no such end. I have found, through painful experience, that the most important step a person can take is always the next one."

- Brandon Sanderson, *Oathbringer*.

TABLE OF CONTENTS

Page

LIST OF TABLES x

LIST OF FIGURES xiii

Chapter

1. INTRODUCTION 1
   - 1.1 THE STANDARD MODEL 1
   - 1.2 QUARK MODEL 2
   - 1.3 AXIAL-VECTOR AND RADIALLY EXCITED PSEUDOSCALAR MESONS 6
   - 1.4 CURRENT EXPERIMENTAL AND THEORETICAL STATUS FOR $f_1(1285)$ AND $\eta(1295)$ 10

2. GLUEX EXPERIMENT 17
   - 2.1 THOMAS JEFFERSON NATIONAL ACCELERATOR FACILITY 17
   - 2.2 GLUEX 18
   - 2.3 HALL D PHOTON BEAM 19
   - 2.4 THE GLUEX SPECTROMETER 23
   - 2.5 TRACKING 33

3. EVENT SELECTION 36
   - 3.1 PRELIMINARY DATA SKIM 36
   - 3.2 PARTICLE IDENTIFICATION 37
   - 3.3 KINEMATIC FIT AND PHOTON TIMING 42
   - 3.4 EXCLUSIVITY 48
   - 3.5 LOW MOMENTUM PROTONS 49
   - 3.6 K_S SELECTION 51
   - 3.7 BARYON REJECTION 54
   - 3.8 $KK\pi$ MASS DISTRIBUTION 59
   - 3.9 K^* REJECTION 60

4. MONTE CARLO SIMULATION 65
   - 4.1 GENERATION OF MONTE CARLO DATA 65
   - 4.2 RECONSTRUCTED DATA 70

5. DATA ANALYSIS 76
   - 5.1 PHASE SPACE EFFICIENCY CORRECTIONS 76
   - 5.2 FITTING 80
   - 5.3 CROSS SECTION 87

Page

5.4 CROSS-SECTION ASYMMETRY 100
5.5 SYSTEMATIC UNCERTAINTY 115
5.6 HELICITY ANGLES 125
5.7 KK AND $K\pi$ MASS DISTRIBUTIONS 134

6. CONCLUSIONS 138
6.1 PARTICLE SPECIES IDENTIFICATION 138
6.2 CROSS-SECTION 139
6.3 SHAPE OF THE CROSS SECTION 142
6.4 MAGNITUDE OF THE CROSS SECTION 146
6.5 DIFFERENCE IN CROSS-SECTION BY DECAY MODE 148
6.6 $f_1(1285)$ AS A $KK^* + C.C.$ MOLECULE 151
6.7 FUTURE WORK 154

REFERENCES 155

APPENDICES
A. SYSTEMATICS 174
B. ANALYSIS PROCEDURE 203

VITA 218

LIST OF TABLES

Table Page

1. Meson Classification by J^{PC} 5

2. Branching fractions for the dominant $f_1(1285)$ decay modes 8

3. Relative fraction of the total GlueX-I luminosity for each of the 3 run periods 36

4. Timing cuts for each particle in the final state topology for this study 39

5. Tabulated selection criteria used to clean the GlueX dataset to measure the $f_1(1285)$ cross-section. 63

6. Voigt profile parameters from fits to the $M(K^-K_s\pi^+)$ and $M(K^+K_s\pi^-)$ distributions 86

7. Gaussian parameters from fit to integrated $M(KK\pi)$ distributions for both $\pi^+K^-K_s$ and $\pi^-K^+K_s$ decay modes 87

8. $-t$ bin centers and widths 88

9. Yield, uncertainty, and fit quality for $f_1(1285) \to K^-K_s\pi^+$ decay mode for each E_γ and $-t$ bin 91

10. Yield, uncertainty, and fit quality for $f_1(1285) \to K^+K_s\pi^-$ decay mode for each E_γ and $-t$ bin 92

11. $f_1(1285) \to K^\mp K_s\pi^\pm$ acceptance from signal Monte Carlo for the $\pi^+K^-K_s$ and $\pi^-K^+K_s$ decay modes for all bins of E_γ and $-t$ 97

12. Tagged GlueX-I luminosity for each E_γ bin the cross-section is measured in 99

13. Differential cross-section and statistical uncertainties for each bin of E_γ and $-t$ for $f_1(1285)$ from both of the $f_1(1285) \to K^\mp K_s\pi^\pm$ decay channels 102

14. Sequential cut efficiency in data and MC for $p'K^\mp K_s\pi^\pm$ 109

15. Fit variation descriptions 117

16. Statistical description of the fitting procedure component of the total systematic uncertainty 117

17. Cut variations used to calculate event selection systematic uncertainty 118

18. Cut systematic uncertainty for each bin of E_γ and $-t$ 122

Table Page

19. Source and values for various normalization uncertainties 124

20. Individual contributions and total relative uncertainty for the bin-by-bin cross-section measurement of $f_1(1285) \to KK\pi$ from the $f_1(1285) \to K^-K_s\pi^+$ decay channel 126

21. Individual contributions and total relative uncertainty for the bin-by-bin cross-section measurement of $f_1(1285) \to KK\pi$ from the $f_1(1285) \to K^+K_s\pi^-$ decay channel 127

22. Differential cross-section and uncertainties for each bin of E_γ and $-t$ for $f_1(1285)$ from the $f_1(1285) \to K^+K_s\pi^-$ decay channel 141

23. Differential cross-section and uncertainties for each bin of E_γ and $-t$ for $f_1(1285)$ from the $f_1(1285) \to K^-K_s\pi^+$ decay channel 142

24. Cross-section deviations for 1st-order polynomial model variation 175

25. Cross-section deviations for 3rd-order polynomial model variation 176

26. Cross-section deviations for removing Gaussian component model variation 177

27. Cross-section deviations for wider fit range on low mass side variation 178

28. Cross-section deviations for wider fit range on high mass side variation 179

29. Cross-section deviations for wider fit range variation 180

30. Cross-section deviations for narrower fit range on low mass side variation 181

31. Cross-section deviations for narrower fit range on high mass side variation 182

32. Cross-section deviations for narrower fit range variation 183

33. Cross-section deviations for narrower Voigtian variation 184

34. Cross-section deviations for wider Voigtian variation 185

35. Cross-section deviations for Gaussian mean lighter variation 186

36. Cross-section deviations for Gaussian mean heavier variation 187

37. Cross-section deviations for Gaussian width narrower variation 188

38. Cross-section deviations for Gaussian width wider variation 189

Table Page

39. Value and source for fit systematic for each E_γ and $-t$ bin for $f_1(1285) \to \pi^+K^-K_s$ decay mode 190

40. Value and source for fit systematic for each E_γ and $-t$ bin for $f_1(1285) \to \pi^-K^+K_s$ decay mode. 191

LIST OF FIGURES

Figure Page

1. Standard Model of particle physics....2

2. Vector meson nonet....3

3. Currently accepted nonets of the radially excited pseudoscalars and axial-vector mesons....7

4. The L3 f_1/η study results....11

5. Results from the E852 Collaboration PWA of $KK\pi$....12

6. Model predictions and CLAS results for $f_1(1285)$ cross-section at $E_\gamma \approx 3.1$ GeV....14

7. Feynman diagrams for potential $f_1(1285)$ photoproduction and He interpolated Regge model predictions....16

8. CEBAF and the experimental halls....18

9. Photon flux and beam polarization as a function of the photon beam energy E_γ....20

10. Photon energy tagging apparatus for GlueX....21

11. Schematic of the Hall D beam line and GlueX Spectrometer....23

12. Schematic for the pair spectrometer in GlueX....24

13. GlueX Start Counter and LH_2 target....26

14. Schematic for the straw positions of the CDC....27

15. Artist rendering of an FDC cell....28

16. Schematic view for various viewing orientations of the BCAL and the individual module....30

17. Picture of the FCAL....31

18. Picture of the TOF....32

19. Relative momentum resolution for protons and pions as a function of polar angle....35

20. β vs $\vec{p}$ distributions for negative tracks in the TOF....40

Figure Page

21. dE/dx vs $\vec{p}$ distributions for positively charged tracks in GlueX data and Monte Carlo simulation of $p'f_1(1285) \to p'K^-K_s\pi^+$ 41

22. Kinematic fit χ^2/ndf distributions for Monte Carlo and data 44

23. $\Delta t(RF) = t_{\text{RF}} - t_{\text{Event}}$ distributions with a central "in-time" peak and accidental beam bunch events extending outwards in time 46

24. A comparison in the cross-section of $\gamma p \to p'\eta' \to p'\pi^+\pi^-\eta_{\gamma\gamma}$ measured using the "Best χ^2" method and "RF Sideband Subtraction" method of handling mistagged out-of-time beam photon events 46

25. Distributions of $-\log(CL_{\text{KinFit}})$ for Monte Carlo and data 48

26. Distributions of $M_x^2(p'K^-K_s\pi^+)$ and $M_x^2(p'K^+K_s\pi^-)$ 50

27. Mandelstam-t distributions 51

28. Selection of K_s events with pathlength significance cut 53

29. $M(\pi^+\pi^-)$ with the model fit to the data 55

30. Invariant mass distributions of $M(p'\pi^+)$ and $M(p'\pi^-)$ 56

31. Distributions of $M(pK^-)$, $M(pK^-)$ and $M(pK_s)$ for the $pK^-K_s\pi^+$ and $pK^+K_s\pi^-$ final state topologies 58

32. $M(K^-K_s\pi^+)$ and $M(K^+K_s\pi^-)$ distributions after all event selection criteria has been applied except for the K^* rejections 60

33. Distributions of $M(K^-\pi^+)$, $M(K^+\pi^-)$, $M(K_s\pi^+)$, and $M(K_s\pi^-)$ 61

34. Dalitz plots of $K\pi$ for different regions of $M(KK\pi)$ 62

35. Distributions of $M(K^-K_s\pi^+)$ and $M(K^+K_s\pi^-)$ before and after applying the K^* rejection criteria 64

36. Thrown Monte Carlo distributions for $M(K^-K_s\pi^+)$ and $-t$ 70

37. Reconstructed distributions of Mandelstam-t and mass of the K_s via $M(\pi^+\pi^-)$
72

38. Detected proton p' momentum and θ for $p'K^-K_s\pi^+$ and $p'K^+K_s\pi^-$ in data and Monte Carlo 73

Figure Page

39. Detected pion momentum and θ for $p'K^-K_s\pi^+$ and $p'K^+K_s\pi^-$ in data and Monte Carlo 73

40. Detected kaon momentum and θ for $p'K^-K_s\pi^+$ and $p'K^+K_s\pi^-$ in data and Monte Carlo 74

41. Detection and analysis efficiency for $f_1(1285) \to K^{\mp}K_s\pi^{\pm}$ Monte Carlo as a function of $\vec{p}$ for the pion and kaon 75

42. Detection efficiency for bins of $-t$ as a function of $\vec{p}$ for the pion and kaon 75

43. K^* rejection efficiency vs $M(KK\pi)$ 78

44. Distributions of $M(K^-K_s\pi^+)$ and $M(K^+K_s\pi^-)$ before the K^* rejection, applying the rejection, and correcting for the phase space efficiency 79

45. Resolution extraction for $f_1(1285)$ from MC 82

46. $M(K^-K_s\pi^+)$ and $M(K^+K_s\pi^-)$ distributions with total model fit to the data 85

47. Fits to $M(KK\pi)$ distributions in selected bins of E_γ and $-t$ 90

48. Ratio of the standard deviation obtained from the bootstrapping procedure to the uncertainty given by MINUIT 94

49. Distributions of the Voigt profile amplitudes obtained via the bootstrapping procedure as a function of $-t$ for $K^-K_s\pi^+$ $K^+K_s\pi^-$ at $E_\gamma = 9$ GeV 95

50. $f_1(1285)$ photoproduction cross-section with statistical uncertainty only for different values of E_γ 101

51. The ratio of the acceptances for $f_1(1285) \to K^-K_s\pi^+$ to $f_1(1285) \to K^+K_s\pi^-$ from signal Monte Carlo for different bins of E_γ 104

52. Kaon kinematics comparison 105

53. Pion kinematics comparison 106

54. Count ratio of $K^-K_s\pi^+$ to $K^-K_s\pi^+$ vs $M(K^{\mp}K_s\pi^{\pm})$ 108

55. t-binned distributions of $M(p\prime K^{\mp})$ for the $K^-K_s\pi^+$ and $K^+K_s\pi^-$ final states in the mass region of $f_1(1285)$ 110

56. t-binned distributions of $M(p\prime K_s)$ for the $K^-K_s\pi^+$ and $K^+K_s\pi^-$ final states in the mass region of $f_1(1285)$ 111

Figure Page

57. t-binned distributions of $M(p'\pi^{\pm})$ for the $K^-K_s\pi^+$ and $K^+K_s\pi^-$ final states in the mass region of $f_1(1285)$ 113

58. t-binned distributions of $M(p\prime\pi^{\pm})$ for the $K^-K_s\pi^+$ and $K^+K_s\pi^-$ final states over the full $M(KK\pi)$ mass range 114

59. Barlow Test for each of the event selection criteria except the $\vec{p}(p)$ cut 120

60. Distributions of $M(K^{\mp}K_s)$ vs $M(K^{\mp}K_s\pi^{\pm})$ 131

61. Distributions of $M(K^-K_s\pi^+)$ and $M(K^+K_s\pi^-)$ before and after the cut on $M(K^{\mp}K_s)$ is made to select $a_0(980)$ 132

62. Phase space acceptance of $\gamma p \to K^+K_s\pi^-$ vs $\cos\theta_{\mathscr{H},a_0}$ and the acceptance corrected distribution of $\cos\theta_{\mathscr{H},a_0}$ for the $p'K^+K_s\pi^-$ final state 133

63. 0^{-+} and 1^{++} hypothesis fits to $\cos\theta_{\mathscr{H},a_0}$ for GlueX and CLAS 135

64. $M(KK)$ and $M(K\pi)$ distributions in mass region of $f_1(1285)$ 137

65. Photoproduction cross-section of $f_1(1285)$ with all uncertainties 140

66. Cross-sections of $f_1(1285)$ with fits for t-slope 144

67. b vs E_γ for ϕ (CLAS) and $f_1(1285)$ 145

68. Comparison between the cross-section of $f_1(1285)$ as measured in $f_1(1285) \to K^-K_s\pi^+$ and $f_1(1285) \to K^+K_s\pi^-$ and theoretical predictions for different values of E_γ 147

69. Differential cross-section $\frac{d\sigma}{dt}$ for $f_1(1285)$ from this work at GlueX and at CLAS for relevant values of $-t$ 148

70. Raw count distributions for $K^+K_s\pi^-$ and $K^-K_s\pi^+$ from CLAS and FNAL E690 150

71. $M(KK)$ distributions in data and theory for KK^* molecule hypothesis 152

72. $M(K\pi)$ distributions in data and theory for KK^* molecule hypothesis 153

73. CL_{KinFit} variations 192

74. Pathlength Significance variations 193

75. $M(\pi^+\pi^-)$ variations 194

76. $M(p\pi)$ variations 195

Figure Page

77. $M(pK^{\mp})$ variations 196

78. $M(pK_s)$ variations 197

79. $\vec{p}(p)$ variations 198

80. $M(K^{\mp}\pi^{\pm})$ variations 199

81. $M(K_s\pi^{\pm})$ variations 200

82. $M_x^2(p'K^{\mp}K_s\pi^{\pm})$ variations 201

83. Barlow test for the $\vec{p}(p)$ cut 202

84. Fits to t-binned distributions of $M(K^-K_s\pi^+)$ for photon beam energy $7.5 < E_\gamma < 8.5$ GeV 204

85. Fits to t-binned distributions of $M(K^-K_s\pi^+)$ for photon beam energy $8.5 < E_\gamma < 9.5$ GeV 205

86. Fits to t-binned distributions of $M(K^-K_s\pi^+)$ for photon beam energy $9.5 < E_\gamma < 10.5$ GeV 206

87. Fits to t-binned distributions of $M(K^-K_s\pi^+)$ for photon beam energy $10.5 < E_\gamma < 11.5$ GeV 207

92. Bootstrapped amplitude distribution for $K^-K_s\pi^+$ at $E_\gamma = 8$ GeV 208

88. Fits to t-binned distributions of $M(K^+K_s\pi^-)$ for photon beam energy $7.5 < E_\gamma < 8.5$ GeV 209

89. Fits to t-binned distributions of $M(K^+K_s\pi^-)$ for photon beam energy $8.5 < E_\gamma < 9.5$ GeV 210

90. Fits to t-binned distributions of $M(K^+K_s\pi^-)$ for photon beam energy $9.5 < E_\gamma < 10.5$ GeV 211

91. Fits to t-binned distributions of $M(K^+K_s\pi^-)$ for photon beam energy $10.5 < E_\gamma < 11.5$ GeV 212

93. Bootstrapped amplitude distribution for $K^-K_s\pi^+$ at $E_\gamma = 10$ GeV 213

94. Bootstrapped amplitude distribution for $K^-K_s\pi^+$ at $E_\gamma = 11$ GeV 214

95. Bootstrapped amplitude distribution for $K^+K_s\pi^-$ at $E_\gamma = 8$ GeV 215

Figure Page

96. Bootstrapped amplitude distribution for $K^+K_s\pi^-$ at $E_\gamma = 10$ GeV 216

97. Bootstrapped amplitude distribution for $K^+K_s\pi^-$ at $E_\gamma = 11$ GeV 217

CHAPTER 1

INTRODUCTION

1.1 THE STANDARD MODEL

The universe is comprised of fundamental particles called quarks and leptons. Leptons and quarks are fermions, which means they are described by Fermi-Dirac statistics. The fermions interact via 4 fundamental forces; gravity, the electromagnetic, strong, and weak force. The latter 3 of these forces are mediated by bosons, which are described by Bose-Einstein statistics. The Standard Model of particle physics is the theory that describes these particles and their interactions with one another. Figure 1 shows the Standard Model particles and the ways in which they interact. There are 6 types, or "flavors", of quarks and leptons and 4 types of bosons. The quark flavors are up (u), down (d), charm (c), strange (s), top (t), and bottom (b). The lepton flavors are the electron (e), muon (μ), and tau (τ) and each has a corresponding neutrino (ν_e, ν_μ, ν_τ). Each fermion has a corresponding anti-particle $\bar{q}$ which has the same mass but opposite electrical charge. The bosons consist of the photon (γ), W and Z bosons, gluons (g), and the Higgs boson (H). The photon, W/Z, and gluons are "gauge" or "vector" bosons and they mediate the electromagnetic, weak, and strong forces respectively. The Higgs boson is a "scalar" boson and is an excitation of the Higgs field, which other particles interact with or "couple to". This coupling generates the particle's mass.

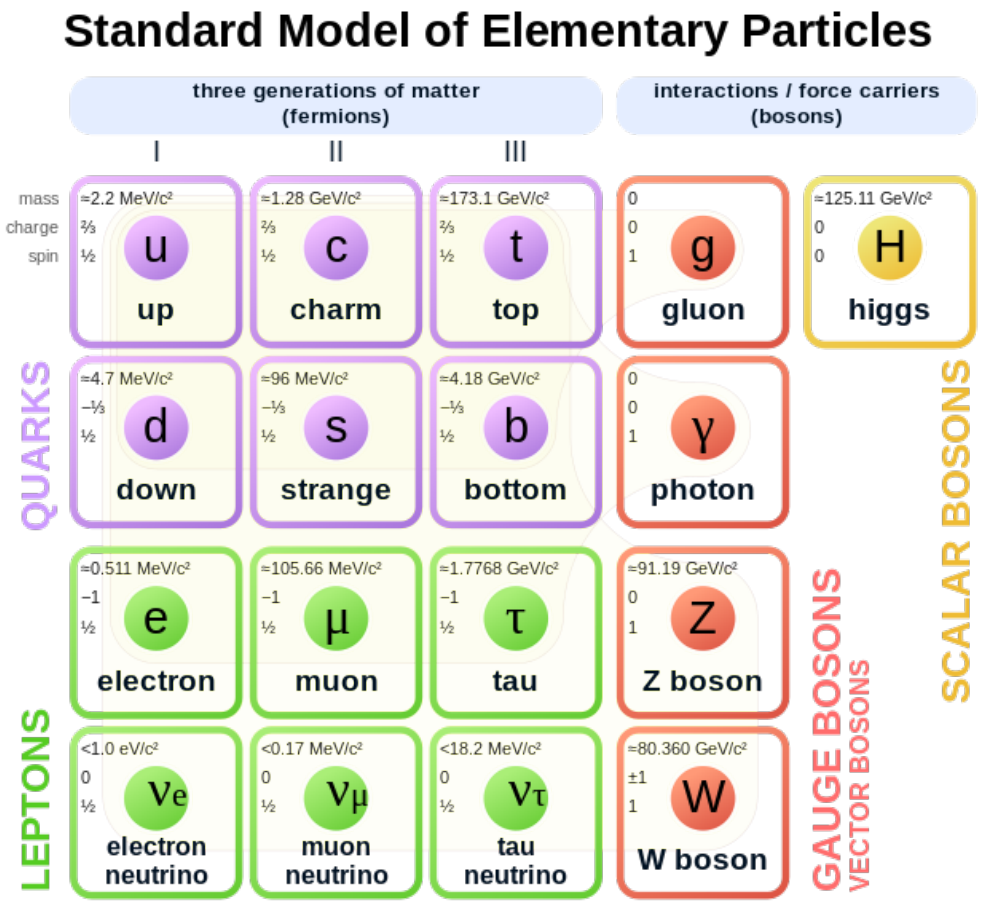

Figure 1. The Standard Model of particle physics. Figure from [1].

1.2 QUARK MODEL

Quarks and gluons have a unique intrinsic property called color charge. Particles with color charge do not exist on their own in nature and are "confined" to colorless combinations at low energies. These confined states are composite particles called hadrons. There are two types of well established hadrons: baryons and mesons. Quarks, gluons, and their interactions are modeled by a quantum field theory with SU(3) symmetry called

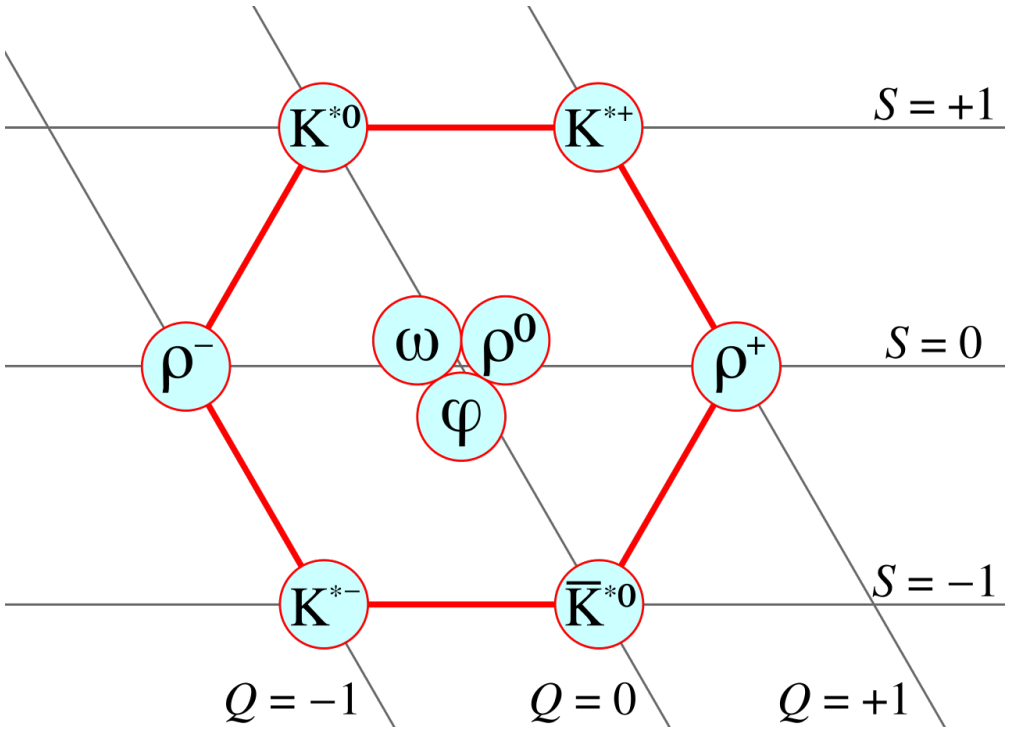

Figure 2. Vector meson nonet. Lines are drawn to show grouping by charge Q and strangeness S $(N_s - N_{\bar{s}})$. Figure from [5].

Quantum Chromodynamics (QCD). The hadronic bound states governed by QCD can be described by the quark model. The quark model was developed by Gell-Man [2], Zweig [3], and Ne'eman [4] to classify hadrons according to their constituent quarks. In the quark model, we can think of baryons, like protons and neutrons, as a combination of 3 quarks or antiquarks held together by gluons (qqq or $\bar{q}\bar{q}\bar{q}$) and mesons, like the pion (π), as quark-antiquark pairs held together by a gluon ($q\bar{q}$).

The 3 flavors of quarks (u, d, s) and antiquarks ($\bar{u}$, $\bar{d}$, $\bar{s}$) can be grouped into 9 quark/antiquark combinations called a nonet. Figure 2 shows the vector meson nonet. These nonets are identified by the quantum numbers of the mesons that comprise them. The quantum

numbers of a particle are expressed as,

$$J^{PC}. \tag{1}$$

J is the total angular momentum of the particle,

$$|L-S| \leq J \leq L+S, \tag{2}$$

where L and S are the orbital and spin angular momentum respectively. Quarks are fermions and as such have spin $= 1/2$. This means that the spin S of a meson is either 0 or 1. P is the parity of the particle given by,

$$P = (-1)^{L+1}, \tag{3}$$

and C is the charge parity given by,

$$C = (-1)^{L+S}. \tag{4}$$

The different J^{PC} nonets are given in Table 1.

There are two more quantum numbers that are used in the classification of mesons, I^G. I is a particles isospin. Isospin is a concept developed by Heisenberg [6] to describe the proton and neutron as two states of a nucleon. Isospin is mathematically analogous to the concept of spin but has nothing to do with angular momentum. The proton was assigned isospin of $I = 1/2$ and the neutron $I = -1/2$. It was since expanded upon to describe the u

Table 1. Meson Classification by J^{PC}. Allowed quantum numbers for meson and the corresponding classification.

L	S	J	P	C	J^{PC}	**Classification**
0	0	0	-	+	0^{-+}	Pseudoscalar
0	1	1	-	-	1^{--}	Vector
1	0	1	+	-	1^{+-}	Pseudovector
1	1	0	+	+	0^{++}	Scalar
1	1	1	+	+	1^{++}	Axial-Vector
1	1	2	+	+	2^{++}	Tensor

and d quark content of a hadron. The I_3 component of isospin is defined as,

$$I_3 = 1/2(n_u - n_d), \tag{5}$$

where n is the number of u and d quarks respectively. G is the G-parity, introduced to generalize the charge parity to the different quark groups. G is given by,

$$G = (-1)^{I+L+S}. \tag{6}$$

We can then classify hadrons via the quantum numbers,

$$I^G(J^{PC}). \tag{7}$$

Experimentally, more potential meson states have been observed than the quark model predicts. These excess states could be states outside of the quark model that are allowed by QCD, like bound states of all valence gluons called glueballs, bound states of valence quarks and gluons called hybrids, and bound states of more than 3 quarks called

tetraquarks/pentaquarks $(qq\bar{q}\bar{q})/(qqqq\bar{q})$. A full review of the current meson landscape is provided in the most recent PDG review [7].

1.3 AXIAL-VECTOR AND RADIALLY EXCITED PSEUDOSCALAR MESONS

This work seeks to study the $f_1(1285)$ meson through decays of $f_1(1285) \to K^{\mp}K_s\pi^{+}$. The $f_1(1285)$ is one of several potential resonant states that exist in the $M = 1.2 - 1.5$ GeV mass region for axial-vector $J^{PC} = 1^{++}$ and pseudoscalar mesons $J^{PC} = 0^{-+}$. We discuss the $f_1(1285)$ and other relevant resonances below. These other particles are all in the proximity of the $f_1(1285)$ and could potentially make the study of the $f_1(1285)$ more complicated. Additionally, there is some uncertainty about the axial-vector and radially excited pseudoscalar nonets. There are too many observed states relative to the quark model predictions. Identifying which of the observed 1^{++} and 0^{-+} states are nonet members and if there are potentially supernumerary or exotic states in this region is important for verification of the standard model. A full review of the light meson spectrum, including a more detailed discussion of the axial-vectors and pseudoscalars, is provided by the PDG [8]. The currently accepted axial-vector and radially excited pseudoscalar nonets are shown in Figure 3.

1.3.1 $f_1(1285)$

The $f_1(1285)$ meson is an axial-vector meson with quantum numbers $I^G(J^{PC}) = 0^+(1^{++})$. It is flavorless, which means it has no strangeness $(N_s - N_{\bar{s}})$, charm $(N_c - N_{\bar{c}})$, topness $(N_t - N_{\bar{t}})$, or bottomness $(N_b - N_{\bar{b}})$. The nominal mass and width of $f_1(1285)$ are 1281.9 and 22.7 MeV respectively [10]. $f_1(1285)$ was discovered independently in 1965 at both

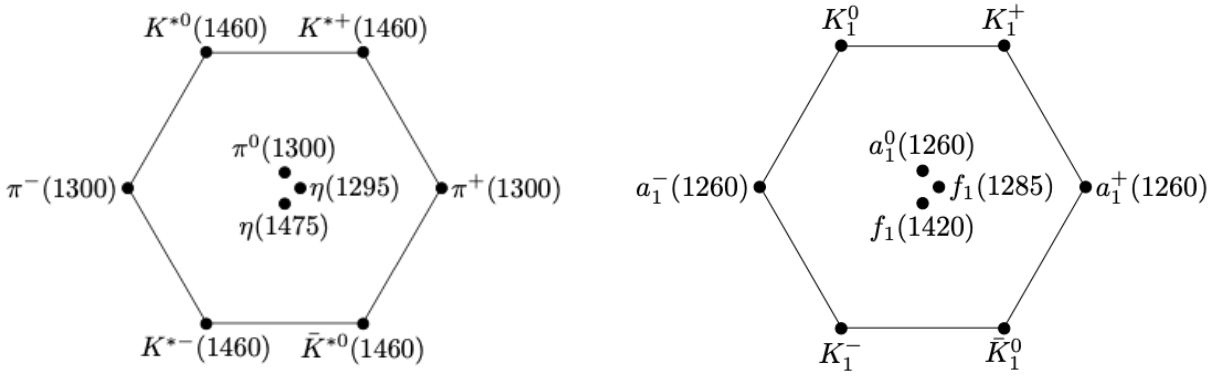

Figure 3. Currently accepted nonets of the radially excited pseudoscalars (A) and axial-vector mesons (B). Figures from [9].

Brookhaven National Lab (BNL) [11] and European Organization for Nuclear Research (CERN) [12] in $KK\pi$ decays and hypothesized to be a $0^+(1^+)$ resonance. The 1^+ designation was subsequently confirmed in 1980 [13]. It fits in well with quark model predictions for the axial-vector nonet as the isoscalar partner of the $f_1(1420)$, given by,

$$\begin{pmatrix} f_1(1285) \\ f_1(1420) \end{pmatrix} = \begin{pmatrix} \cos\theta_{1^{++}} & -\sin\theta_{1^{++}} \\ \sin\theta_{1^{++}} & \cos\theta_{1^{++}} \end{pmatrix} \begin{pmatrix} f_1 \\ f_8 \end{pmatrix}, \tag{8}$$

where $\theta_{1^{++}}$ is the mixing angle and f_1 and f_8 are given by,

$$f_1 = \frac{1}{\sqrt{3}}\left(u\bar{u} + d\bar{d} + s\bar{s}\right), \tag{9}$$

and,

$$f_8 = \frac{1}{\sqrt{6}}\left(u\bar{u} + d\bar{d} - 2s\bar{s}\right). \tag{10}$$

Table 2. Branching fractions for the dominant $f_1(1285)$ decay modes as given in [10].

Decay Mode	Branching Fraction (%)
4π	32.7 ± 1.9
$\eta\pi\pi$	52.2 ± 2
$KK\pi$	9.0 ± 0.4
$\rho\gamma$	6.1 ± 1.0

The mixing angle was calculated to be $\theta_{1^{++}} = 23^\circ$ [14] and experimentally measured by the LHCb collaboration to be $\theta_{1^{++}} = 23^\circ$ [15]. The $f_1(1285)$ has been hypothesized to be a dynamically generated $K^*\bar{K} + c.c$ molecular state [16], [17], though the results of [15] find the $f_1(1285)$ to be consistent with an $n\bar{n}$ state. The dominant decay modes of $f_1(1285)$ are given in Table 2 [10].

1.3.2 $f_1(1420)$ and $f_1(1510)$

The $f_1(1420)$ was first observed in 1980 in K^*K decays [18] and is assumed to be the isoscalar partner to the $f_1(1285)$ [19]. It has a nominal mass and width of 1426.3 and 54.5 MeV [20]. It also has been suggested as a potential K^*K molecule [21]. The $f_1(1420)$ has predominantly been seen in $KK\pi$ decays where $K^* \to K\pi$, but potentially has also been seen in the $\eta\pi\pi$ final state. Other decay modes have not been well established [20].

There is some speculation that the $f_1(1420)$ is not the $s\bar{s}$ partner to the $f_1(1285)$ because it hasn't been well established in K^-p scattering. Instead, the isoscalar partner to the $f_1(1285)$ would then be the $f_1(1510)$. The existence of $f_1(1510)$ is not well established but has been observed in several experiments [22]. Non-observations of the state are more common than observations, however, so the general convention is to assume that the $f_1(1285)$ and $f_1(1420)$ belong to the axial-vector 1^{++} nonet. If both the $f_1(1420)$ and

$f_1(1510)$ exist, then one is likely to be the axial-vector meson predicted by the quark model and the other a supernumerary or exotic state.

1.3.3 Radially Excited Pseudoscalars

The first radial excitation - excitation in the radial component of the wave function which preserves the quantum numbers - of the pseudoscalar nonet for η and η' are predicted to lie between 1200-1500 MeV [23]. There are three potential candidates for these radial excitations. They are $\eta(1295)$, $\eta(1420)$, and $\eta(1475)$. The $\eta(1295)$ is commonly accepted as the lowest-mass radially excited psuedoscalar. It has been observed in $\pi^- p$ scattering in the $KK\pi$ [24] and $\eta\pi\pi$ final state [25]. The $\eta(1420)$ and $\eta(1475)$ were originally thought be to be a single state $\eta(1440)$ but subsequent studies measured two states simultaneously in $\pi^- p$ scattering, $p\bar{p}$ annihilation, and J/ψ radiative decay [26]–[32]. The $\eta(1405)$ has been observed in $KK\pi$ and $\eta\pi\pi$ decays via K^*K and $a_0\pi$ and the $\eta(1475)$ has been observed in $KK\pi$ decays via K^*K. Various studies have observed some or none of the excited pseudoscalar candidates [33], [34].

As there are 3 candidate resonances for the 2 constituents of the radially excited pseudoscalar nonet, there are several interpretations of these states. First, the $\eta(1295)$ and $\eta(1475)$ are members of the nonet and $\eta(1405)$ is a glueball, as predicted by the flux tube model [35]. Lattice QCD predicts that the lightest glueball will have a mass $M > 2.0$ GeV [36], so there is disagreement about this interpretation. Second, that $\eta(1295)$ and one of $\eta(1405)$ or $\eta(1475)$ are the isoscalar nonet partners where either one or the other state exists [37]. Finally, that $\eta(1295)$ does not exist and $\eta(1440)$ is the first radial excitation [38], [39]. In this scenario, observations of $\eta(1295)$ are due to bleed-through from the

$f_1(1285)$ and observations of $\eta(1405)$ and $\eta(1475)$ are due to the splitting of $\eta(1440)$ due to a node in the wave function.

1.4 CURRENT EXPERIMENTAL AND THEORETICAL STATUS FOR $f_1(1285)$ AND $\eta(1295)$

The $f_1(1285)$ meson was cleanly measured in pp central production by WA102 at CERN and E690 at Fermilab [40]–[44]. In particular, the WA102 experiment was able to measure the branching fraction for all 4 of the major decay final states: 4π, $KK\pi$, $\eta\pi\pi$, and $\rho\gamma$. None of these studies saw evidence for a 0^{-+} state at $M = 1.28$ GeV, though 0^{-+} states are suppressed in central production. WA102 concluded that the central production of $f_1(1285)$ was consistent with double pomeron exchange [40]. The L3 collaboration at CERN measured $f_1(1285)$ in virtual $\gamma\gamma$ fusion [33]. Figure 4 shows the L3 results, where an 1^{++} signal corresponding to the $f_1(1285)$ in $KK\pi$ is seen at high P_T^2. No peak is seen in either $M(KK\pi)$ or $M(\eta\pi\pi)$ at low P_T^2, where spin-0 production should dominate. The lack of a clear 0^{-+} peak led to the establishment of upper limits on the $\gamma\gamma$ width for the radially excited psuedoscalar candidates. They also determined the $f_1(1285)$ branching fraction $\Gamma(a_0(980)\pi)/\Gamma(\eta\pi\pi)$ to be 100% and thus proposed branching fractions of $a_0(980)$. However, the L3 $\Gamma(a_0(980)\pi)/\Gamma(\eta\pi\pi)$ measurements are in disagreement with more recent results [45]. The DELPHI Collaboration performed a partial wave analysis (PWA) on the $KK\pi$ final state and both 1^{++} and 0^{-+} waves could be used to describe the low $M(KK\pi)$ region [46]. Further analysis of the quark content determined that the resonance was more likely to be $f_1(1285)$. Most recently, the $f_1(1285)$ was measured in photoproduction by the CLAS experiment [9], [45], [47]. These studies concluded that the resonance observed at

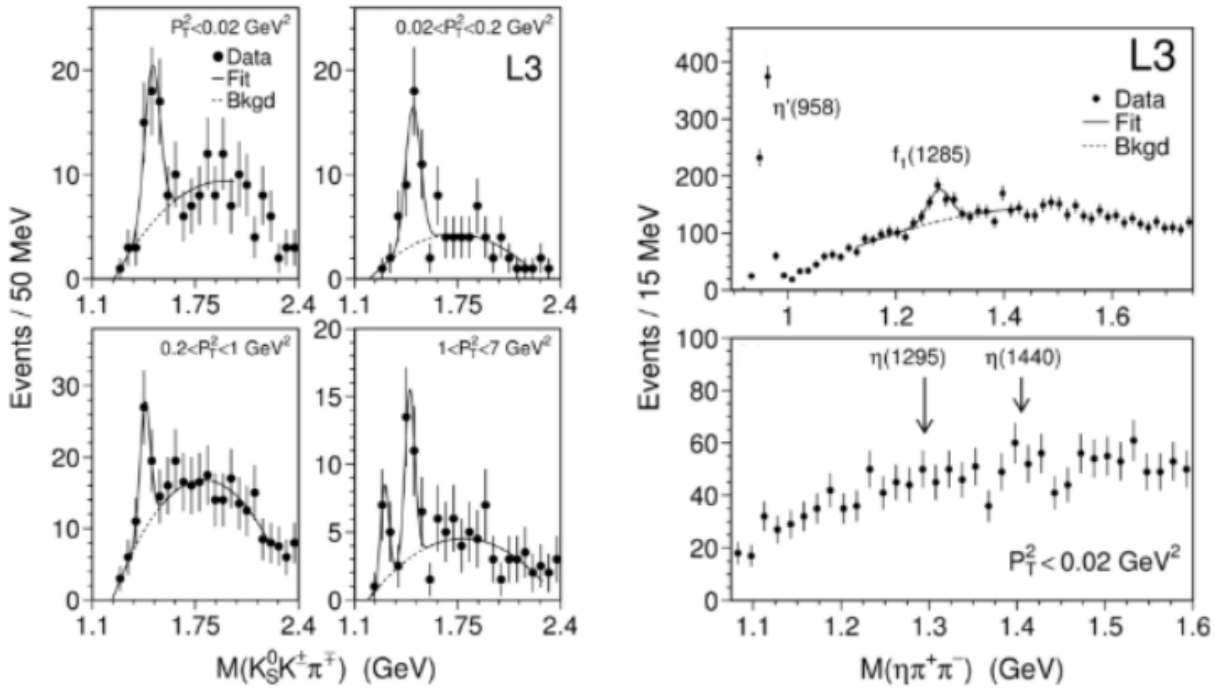

Figure 4. The L3 f_1/η study results. Distributions of $M(KK\pi)$ (A) and $M(\eta\pi\pi)$ (B) for different values of P_T^2 are shown. In the low P_T^2 region, where production is driven by quasi-real photons, the spin-0 state should be enhanced but no peaks are seen. Figures from [33].

$M = 1.28$ GeV was dominated by the $f_1(1285)$, but neither performed a PWA.

The recent non-$p\pi$ scattering experiments have failed to identify the existence of a 0^{-+} state in the region of $M = 1290$ MeV. Two $p\pi$ experiments from the E852 collaboration that have observed the $\eta(1295)$ measure mass and widths of the $f_1(1285)$ that are inconsistent with the currently accepted nominal values [10], [24], [25]. This could suggest a potential issue with the PWA procedure. [24] performed a cross-check to ensure that the $f_1(1285)$ was not leakage from the $\eta(1295)$ and found that it was not. They did not investigate if the reverse was true. The results from [25] are shown in Figure 5.

The cross-section for photoproduction of $f_1(1285)$, shown in Figure 6 was measured

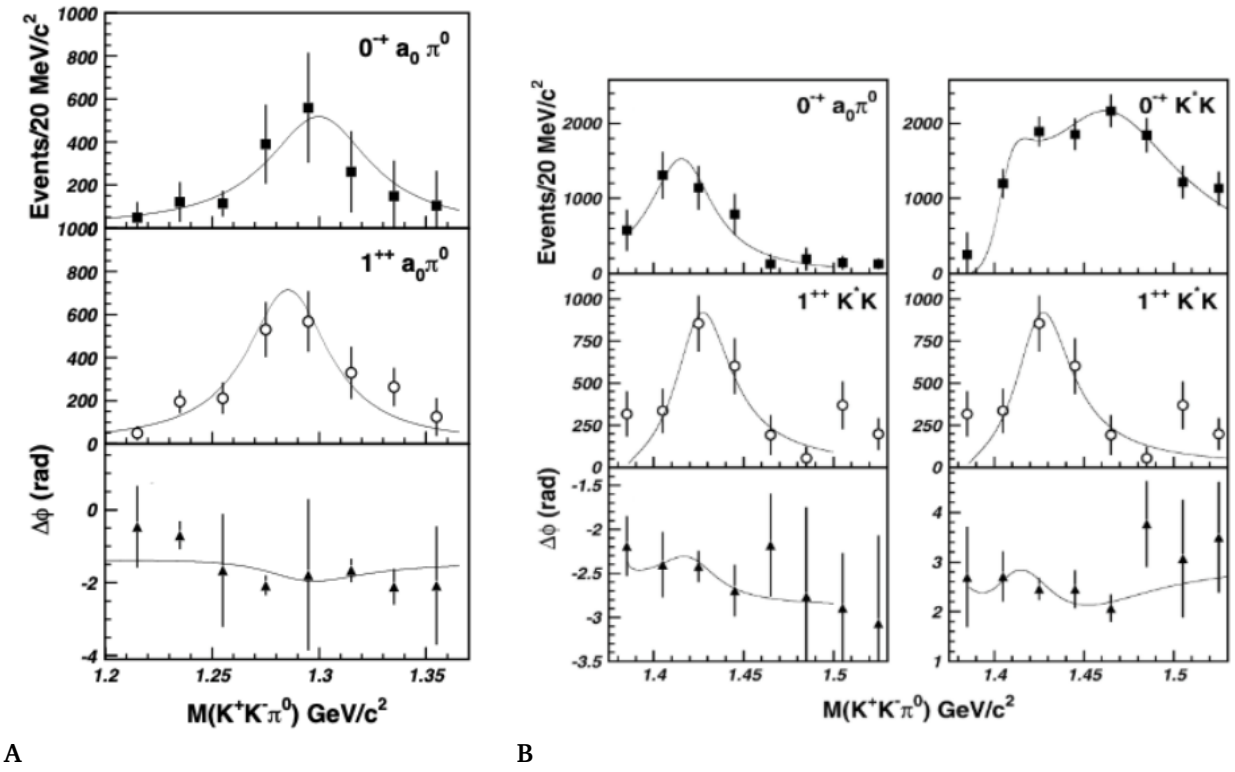

Figure 5. Results from the E852 Collaboration PWA of $KK\pi$. The low (A) and high (B) mass regions both show 0^{-+} and 1^{++} signals for mass dependent (lines) and independent (points) fits. Figures from [25].

at CLAS [45], [47]. For values of low E_γ, a flatter differential cross-section was observed relative to theoretical predictions, suggesting an s-channel N^* decay production mechanism. s-channel production occurs when the incoming beam photon excites the proton to a higher mass state like a Δ or N^* baryon which then decays to the $f_1(1285)$ and a proton. Theoretical models had predicted that t-channel Regge exchange was the dominant production mechanism for $f_1(1285)$ [48]–[50]. t-channel production is modeled as an interaction of a light meson like the ρ or ω between the proton and photon to produce the $f_1(1285)$. These processes are shown in Figure 7A. The Regge model is an approach to calculating scattering amplitudes via t-channel exchange of Regge trajectories. Scattering amplitudes, like cross-sections, represent the probability of a physics process occurring and are expressed as a function of these Regge trajectories, which represent different types of exchange particles. The amplitudes are given by,

$$A \propto s^{2(\alpha(t)-1)}, \tag{11}$$

where s and t are Mandelstam variables and $\alpha(t)$ are the Regge trajectories given by,

$$\alpha(t) = a + bt. \tag{12}$$

Mandelstam-s is the square of the center-of-mass energy for the initial state particles,

$$s = (p_1 + p_2)^2, \tag{13}$$

and Mandelstam-t is the momentum transfer,

$$t = (p_1 - p_3)^2, \tag{14}$$

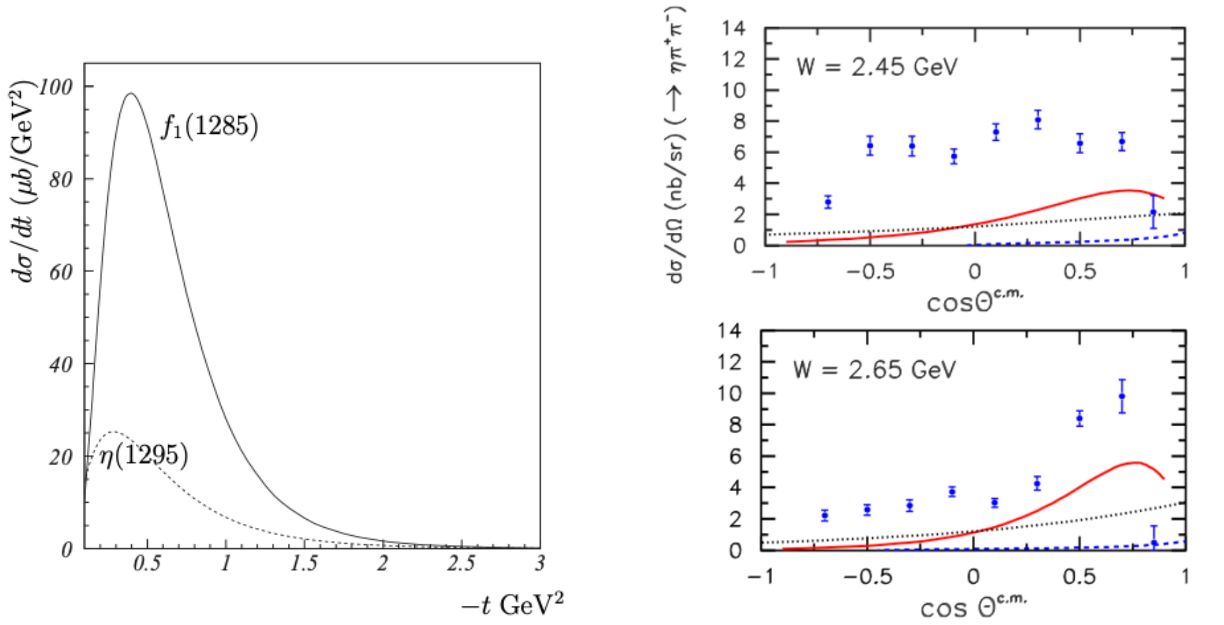

A **B**

Figure 6. Model predictions and CLAS results for $f_1(1285)$ cross-section at $E_\gamma \approx 3.1$ GeV. Regge model predictions for photoproduction of $f_1(1285)$ and $\eta(1295)$ (A) are compared to the results from CLAS (B) for the $f_1(1285)$ cross-section (blue points). The predictions from Kochelev (red line), Domokos (dashed blue), and Huang (dotted black) are shown. Figures from [45], [48]–[50].

In response to these results, two new theoretical models for $f_1(1285)$ photoproduction were produced by He [51] and by Wang [52] that sought to describe the CLAS data. The He model fit to the CLAS result is shown in Figure 7B. The He does not use any nucleon s-channel contributions to describe the data but the Wang model includes an s-channel

contributions from $N(2300)$. Both models claim good agreement with the CLAS result but a review of both models [53] published too recently to be considered for this study found that the s-channel contribution in [52] was necessary to describe the data.

The study of $f_1(1285)$ photoproduction is important to understand how the meson is produced. Additionally, a better understanding of the $f_1(1285)$ can constrain the axial-vector and radially excited pseudoscalar nonets to further validate quark model and standard model predictions. Analysis of the $f_1(1285)$ is complicated by a potentially mass degenerate 0^{-+} state along with additional 1^{++} and 0^{-+} states in the $M < 1.5$ GeV mass region. In this thesis, we present the results of the measurement of the photoproduction differential cross-section of $f_1(1285)$ at beam photon energies $7.5 < E_\gamma < 11.5$ GeV in the reactions $\gamma p \to p' K^- K_s \pi^+$ and $\gamma p \to p' K^+ K_s \pi^-$. With all experimental evidences in hand below we assume that the photoproduction cross-section at $M(KK\pi) \simeq 1.28$ is dominated by the $f_1(1285)$ axial-vector meson. The results are compared to the He model [51], which has been extrapolated to higher energies [54]. We also investigate the helicity angle distribution of the $f_1(1285)$ decay products as a completeness test of the 1^{++} identity and present the $M(KK)$ and $M(K\pi)$ distributions which may be relevant to recent work on the nature of $f_1(1285)$ as a dynamically generated vs. a traditional $q\bar{q}$ state. The results of this work expand the available world data of the $f_1(1285)$ pursuant to a deeper understanding of the $f_1(1285)$ and other axial-vector mesons.

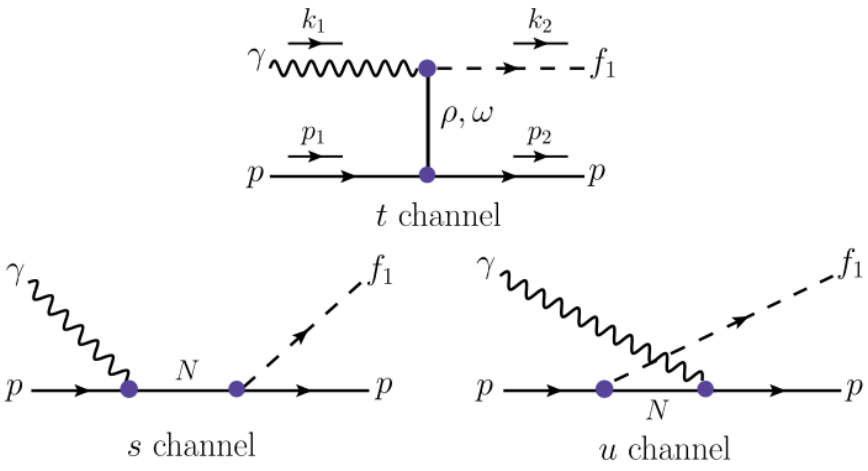

A

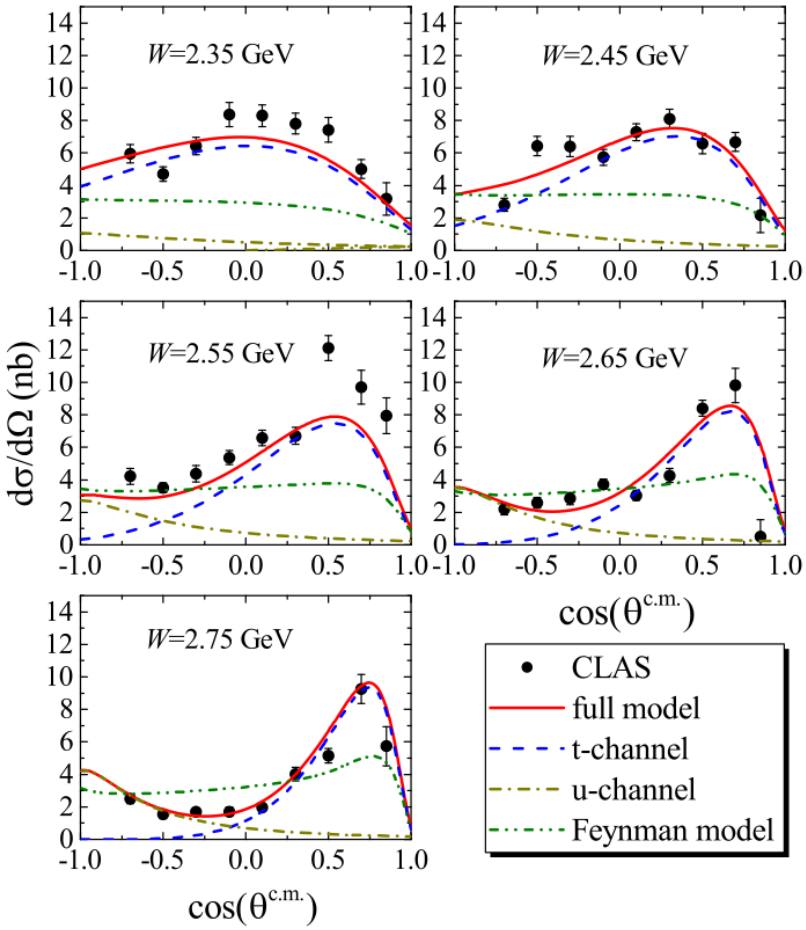

B

Figure 7. Feynman diagrams for potential $f_1(1285)$ photoproduction (A) and He interpolated Regge model predictions (B). The He model is fit to the CLAS data and does not include s-channel contributions. Figures from [51].

CHAPTER 2

GLUEX EXPERIMENT

2.1 THOMAS JEFFERSON NATIONAL ACCELERATOR FACILITY

The GlueX experiment is one of the many experiments ran at Thomas Jefferson National Accelerator Facility (Jefferson Lab or JLab) with the use of the Continuous Electron Beam Accelerator Facility (CEBAF). Located in Newport News, Virginia, Jefferson Lab was approved for construction in 1984 and first delivered beam to an experimental hall on July 1, 1994. [55]. Since then, 96 experiments have been run "behind the gate" during the 12 GeV beam era, which began on December 14, 2015, after the $335M upgrade to CEBAF to double the energy of the deliverable electron beam [56].

2.1.1 Continuous Electron Beam Accelerator Facility

Nearly all of the experiments run at Jefferson Lab make use of Continuous Electron Beam Accelerator Facility (CEBAF), the system and facility which produces, accelerates, and delivers a continuous electron beam to the experimental halls. CEBAF resembles a running track and is comprised of an electron injector, two parallel linear accelerators (LINACs), and two arcs divided into 5 segments that allow the electrons to pass through the LINACs multiple times [57]. After electrons are added to the machine, the particles are accelerated through the LINACs through the use of 50 cryomodules - 25 per LINAC - which contain Superconducting Radio Frequency (SRF) cavities. For every pass through

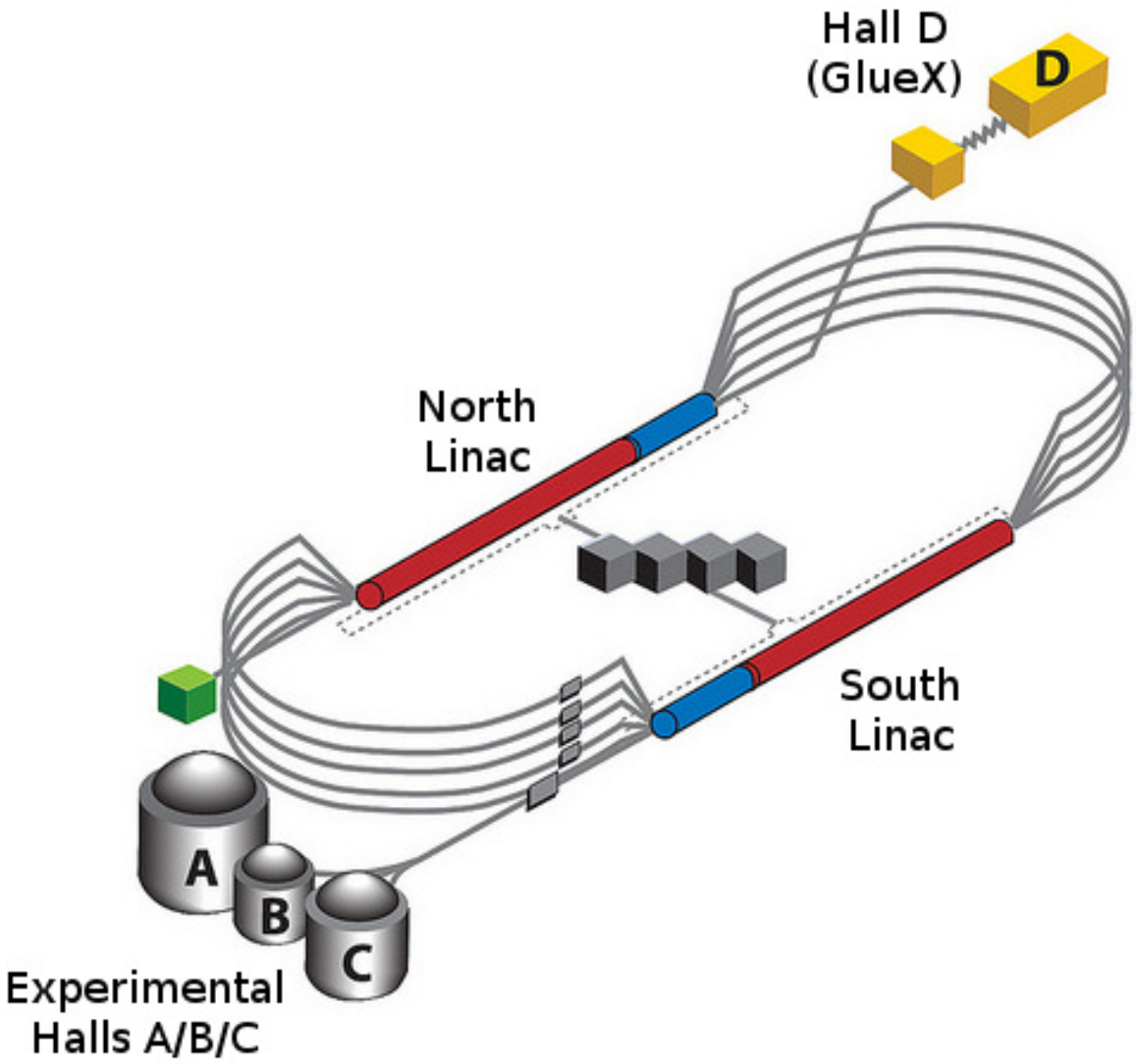

Figure 8. CEBAF and the experimental halls. GlueX is housed in Hall D. Figure from [58].

the LINACs, the electrons increase their energy by 2.2 GeV. Hall D receives electrons that have undergone 5.5 passes through the LINAC, corresponding to a max electrons energy of 12.1 GeV. A schematic of CEBAF and the experimental halls is shown in Figure 8.

2.2 GLUEX

GlueX, which is housed in the most recently built experimental hall at JLab, Hall D,

seeks to study the existence of so-called "exotic" mesons. In its mission to do so, an extremely robust physics dataset has been produced, allowing for the investigation of many hadronic states [59]. The GlueX experimental apparatus is summarized in the following sections. A more in-depth overview of the GlueX experiment can be found in Ref.[60].

2.3 HALL D PHOTON BEAM

Unlike the other experimental halls at JLab, GlueX does not directly use an electron beam for its experimental program. GlueX makes use of a photon beam, which is produced from the electron beam by way of coherent bremsstrahlung [61], [62]. Bremsstrahlung is German for "braking radiation", and it is the process by which radiation is produced when electrons are accelerated. The Hall D complex includes a tagger hall, which is where the photon beam is produced. Located in the tagger hall is a diamond radiator $20-60\mu m$ thick. An incident electron beam on this radiator will produce a linearly polarized photon beam via coherent bremsstrahlung. The properties of the radiator, like the orientation and thickness, control the properties of the polarization, like the coherent peak energy and the degree of polarization. The GlueX collaboration has chosen a 9 GeV coherent energy peak which corresponds to a 40% peak polarization for a 12 GeV electron beam. The photon flux and polarization vs beam energy is shown in Figure 9. The electron beam is tuned in such a manner as to create a half-millimeter virtual focal point at the Hall D collimator, located 75m upstream, which consequently also focuses the photon beam onto the collimator position, though at cm scale size. Electrons that have interacted with the diamond radiator and produced a photon are deflected into the tagging spectrometer, called the tagger, via the tagger magnet. Non-interacting electrons, which still carry their

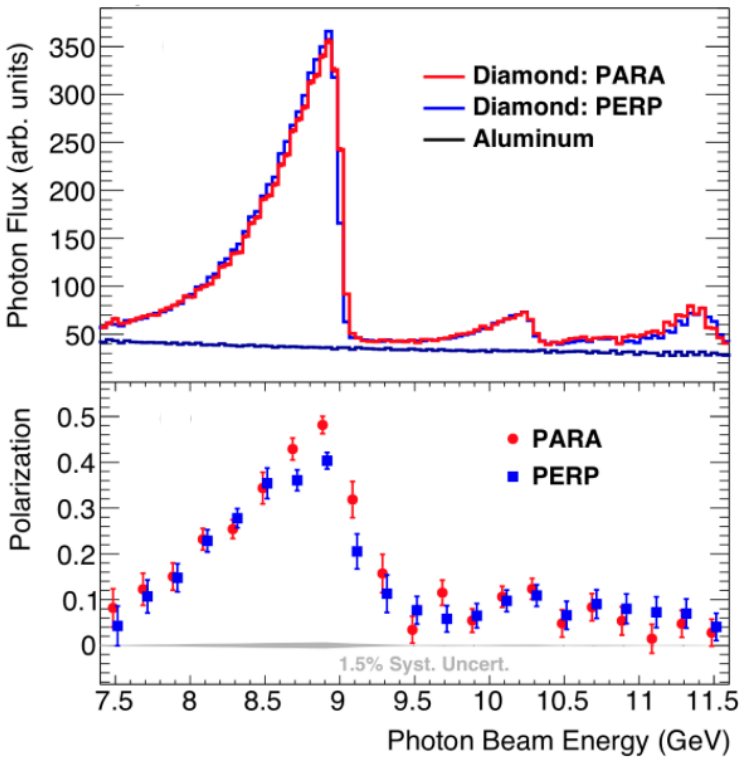

Figure 9. Photon flux (top) and beam polarization (bottom) as a function of the photon beam energy E_γ. A majority of the beam photons are between $8.2-9.0$ GeV. Figures from [60].

full energy, are bent at 13.4° into the tagger dump [60].

2.3.1 TAGH and TAGM

To calculate the photon beam energy, we use a tagger hodoscopes (TAGH), called the broadband tagging hodoscope, and tagger microscope (TAGM) to measure the energies of the post-bremsstrahlung electrons [60]. Both of these detectors measure the energy of the deflected electron, from which the paired photon's energy can be calculated with,

$$E_\gamma = E_0 - E_e. \tag{15}$$

The TAGH, just behind the focal point of the tagger magnet, measures electrons with energies between 25-97% of the incident electron beam. The TAGM is movable such that it can be positioned to measure electrons corresponding to the coherent peak. Nominally this means the TAGM is positioned to measure electrons with energy corresponding to photon energy between 8.2-9.0 GeV. A schematic of the photon tagging system is shown in Figure 10.

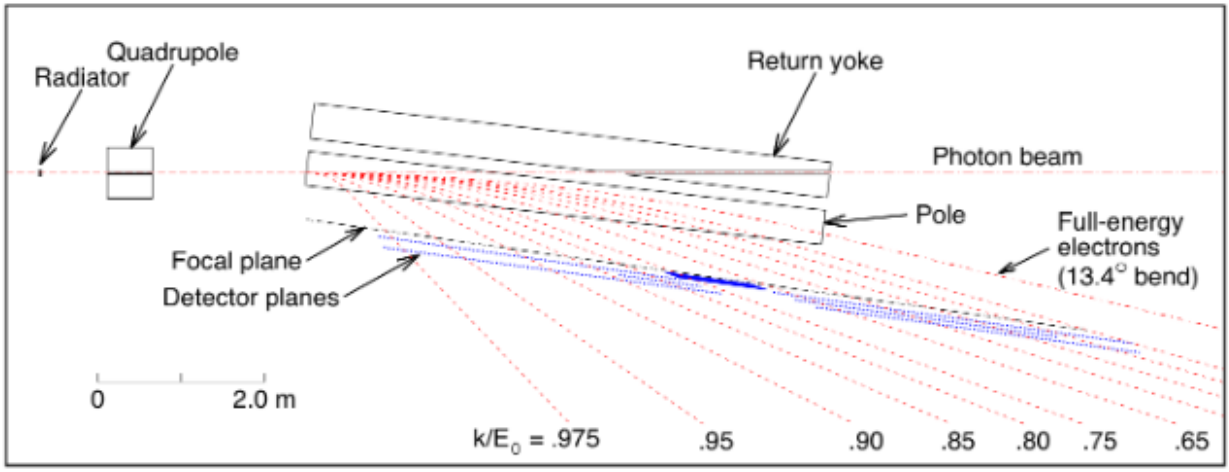

Figure 10. Photon energy tagging apparatus for GlueX. The red dotted lines indicate electron scattering trajectories corresponding to various values of "lost" energy to the beam photon. The blue dotted lines show the position of the TAGH and the shaded blue region shows the position of the TAGM. Figure from [60].

2.3.2 TPOL

To measure the polarization of the beam, GlueX uses a Triplet Polarimeter [63]. Via the process of triplet photoproduction, we can calculate the degree of polarization of the photon beam. Triplet photoproduction is the process by which a photon interacts with an

electron in an atom and produces a high energy e^+e^- pair. The struck electron is ejected from the atom. For a polarized photon beam, the cross-section σ_t for triplet photoproduction is given by,

$$\sigma_t = \sigma_0[1 - P\Sigma(2\phi)], \tag{16}$$

where σ_0 is the unpolarized triplet photoproduction cross-section, P is the photon beam polarization, Σ is the beam asymmetry for the given physics process, and ϕ is the azimuthal angle relative to the relative to the plane of polarization for the incident photon beam for the recoil electron. At GlueX, the polarization is determined by measuring and fitting the azimuthal distribution of the recoil electron to the function,

$$\sigma_t = A[1 - B\cos(2\phi)], \tag{17}$$

where A and B are fit parameters, with,

$$B = P\Sigma, \tag{18}$$

such that the polarization [60],

$$P = B/\Sigma. \tag{19}$$

The asymmetry, Σ, is dependent on the energy of the beam photon and the thickness and geometry of the triplet production target and setup. For the GlueX setup, $E_\gamma = 9$ and the $75\mu m$ Be converter, $\Sigma = 0.1990 \pm 0.0008$.

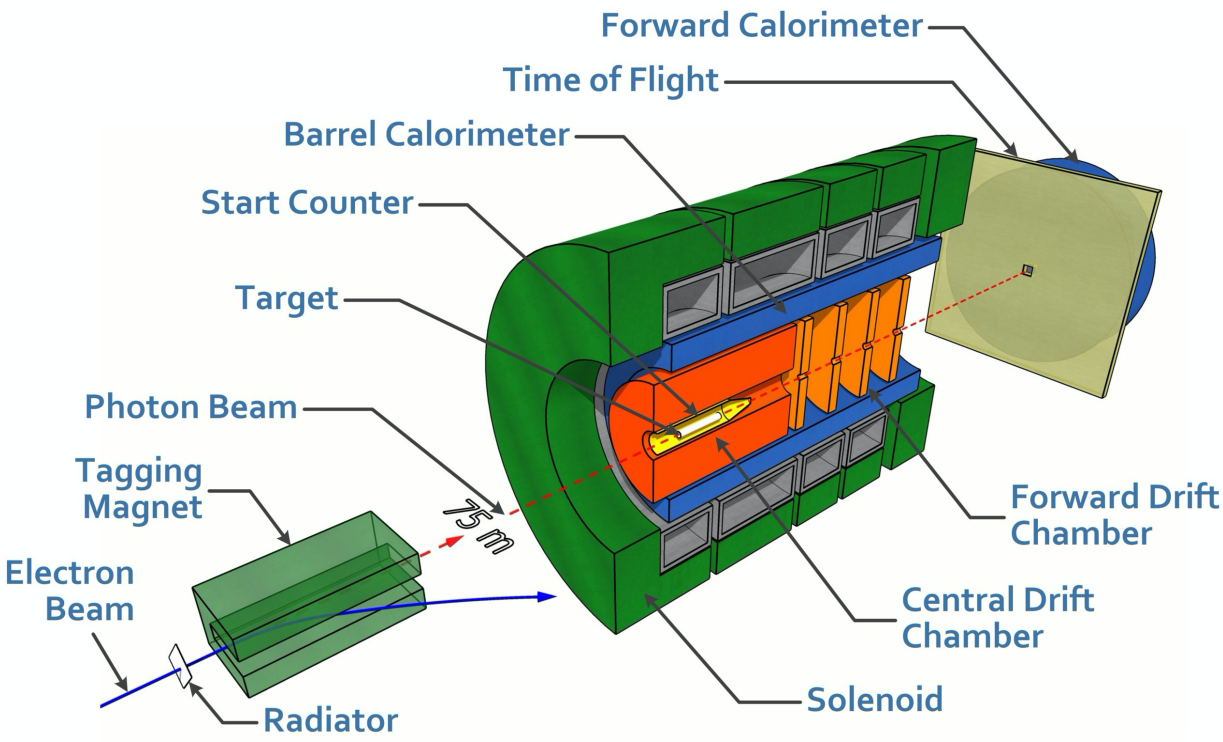

Figure 11. Schematic of the Hall D beam line and GlueX Spectrometer. Figure from [60].

2.4 THE GLUEX SPECTROMETER

The GlueX Spectrometer is located in Hall D proper, downstream from the tagger hall. The detector is comprised of many different components. Those components will be discussed in further depth in this section. A schematic of the GlueX Spectrometer is shown in Figure 11.

2.4.1 Pair Spectrometer

The Pair Spectrometer is located at the entrance to Hall D and is comprised of a high resolution hodoscope (PS) and a coarse hodoscope (PSC) [64]. It is primarily used in

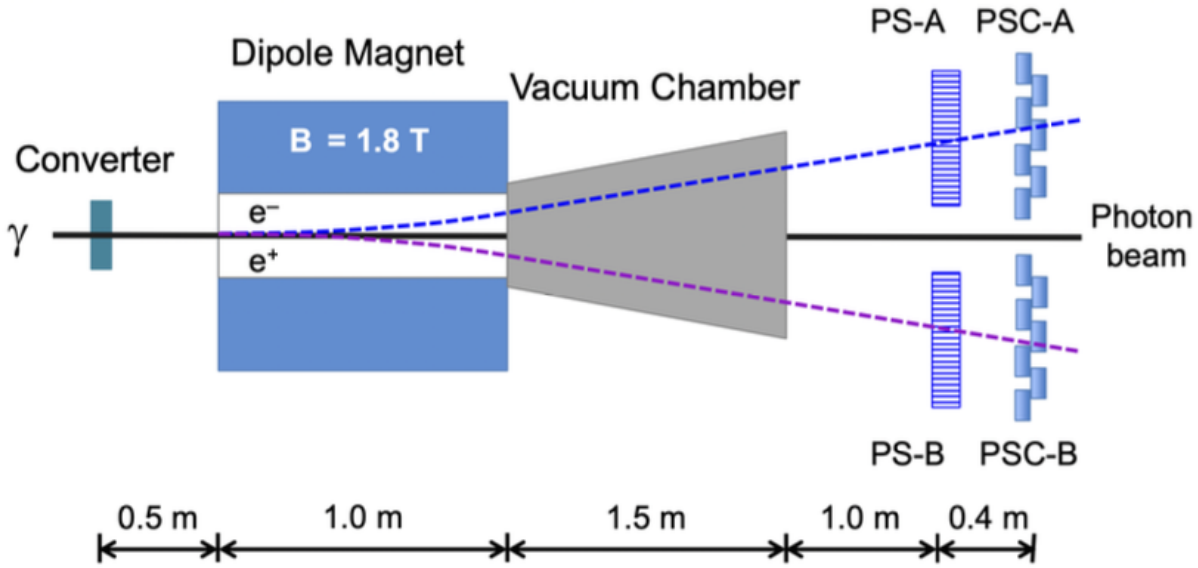

Figure 12. Schematic for the pair spectrometer in GlueX. Figure from [64].

the measurement of the photon beam polarization and energy, but also is used to measure the photon beam flux. The PS works in conjunction with the TPOL to measure the photon beam energy. The TPOL measures the energy of the recoil atomic nucleus while the PS measures the produced e^+e^- pair. The PS can measure electrons with momentum $3.0 < E_e < 6.2$ GeV/c, corresponding to photons in the energy range of 6.0 to 12.4 GeV. Additionally, detection of an e^+e^- pair in the PS is the "trigger" for the TPOL upon detection of a recoil electron. The flux of the photon beam can be calculated by calculating the fraction of photons interacting with atomic electrons in the Be target and hitting the PS. A schematic of the PS is shown in Figure 12.

2.4.2 Solenoid Magnet

Built at SLAC in the 1970s and refurbished at JLab, the GlueX superconducting solenoid

magnet is the core component of the GlueX spectrometer, housing various drift chambers and calorimeters [60]. The magnet is comprised of four superconducting coils and cryostats and operates at a nominal current of 1350A, producing a 2T field along the beam line, where the magnet's axis lies. Because the momentum resolution of the GlueX detector is worse than 1%, fraction-percent accuracy is sufficient for field determination of the solenoid. The field was calculated with a 2-dimensional field calculator and compared to measured values of the field at various radial distances and azimuthal angles. At $R = 0$, the deviation from the calculation did not exceed 0.2%, and the largest deviation was 1.5% on the downstream edge at the largest measured radius, which has no noticeable impact on momentum resolution. The mapped field is used to reconstruct particle tracks in the detector.

2.4.3 Target

The GlueX experiment uses a hydrogen target for it's physics program. The helium itself is contained in a vacuum chamber and cooled to approximately 18K /18 psi. The vacuum chamber is 30cm long and has a radius of about 0.8cm

2.4.4 Start Counter

The GlueX Start Counter (SC) is used to measure the start time of a scattering event off of the target [65]. The SC provides up to 90% of solid angle coverage for particles scattering off the center of the target. The SC is made of 30 scintillator paddles in the shape of a cylinder of radius 78mm with a downstream conical "nose" section that slopes down to a radius of 20mm. Each paddle has a decay time of 2.1 ns and a bulk attenuation length

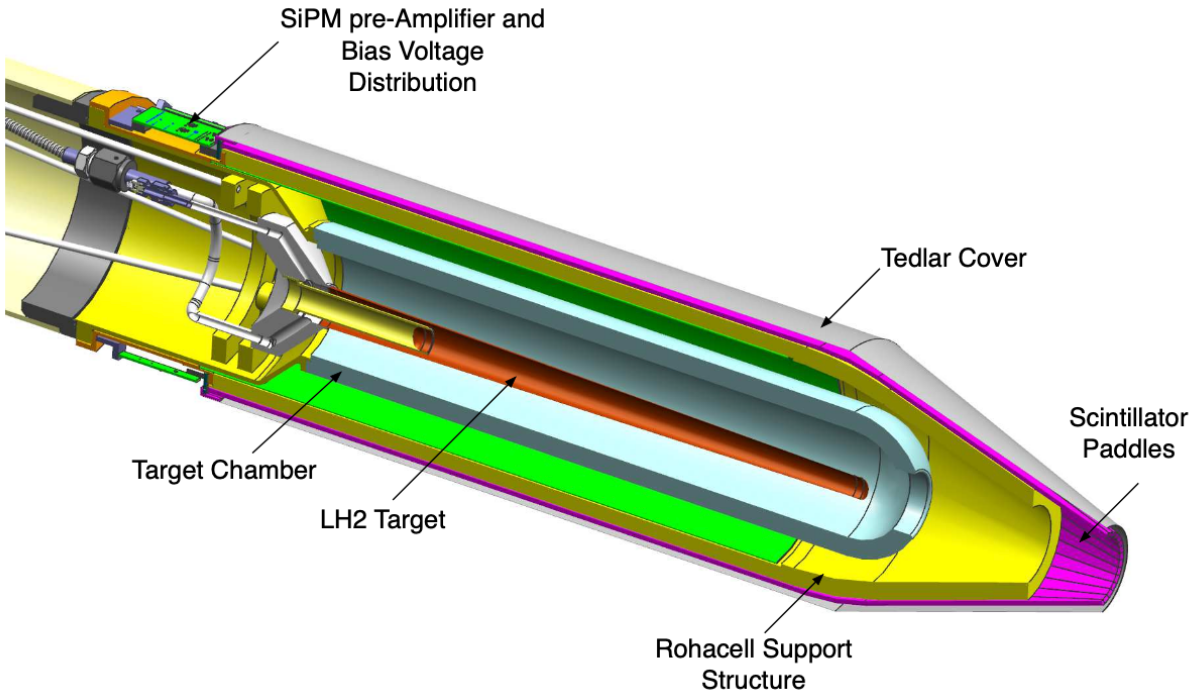

Figure 13. GlueX Start Counter (SC) and LH_2 target. Figure from [65].

of 380 cm. Because the resolution of the SC must be sufficient to identify the electron beam bunch corresponding to the scattering event, the SC was designed to operate for tagged photon beams with intensities up to 10^8 photons/s. The timing signal of the SC is mostly independent of particle type and trajectory, and as such can function as a first level trigger if needed. For the same magnetic insensitive requirements as the BCAL, SiPMs at the upstream end of each paddle are used to detect the light. A schematic for the target and SC is shown in Figure 13.

2.4.5 Central Drift Chamber

The Central Drift Chamber (CDC) is located inside the solenoid magnet, surrounding the target and start counter. The CDC is used to track charged particles after scattering

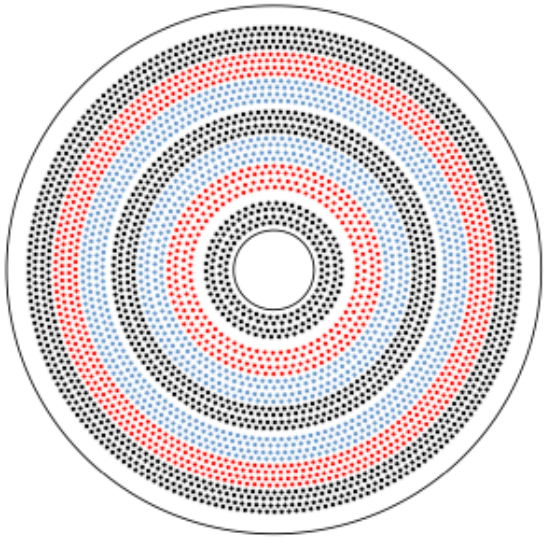

Figure 14. Schematic for the straw positions of the CDC. Black dots represent the position of axial wires, red dots represent the position of $+6^\circ$ stereo wires, and blue dots represent the position of -6° stereo wires. Figure from [66].

off of the Hydrogen target at polar angles between 6° and 168° [66]. The detector itself is made of 3522 $20\mu m$ Gold-plated Tungsten anode wires inside layers of Mylar straw tubes. The tubes each have a diameter of 1.6cm and are arrayed in a 1.5m long cylindrical volume with an inner and outer radius of 10cm and 56cm respectively as measured from the beam line. 12 of the 28 layers are axial, and 16 are arranged at stereo angles of $\pm 6^\circ$ for 2-D spatial tracking. The cross-sectional straw positions are shown in Figure 14. A mixture of 50% Argon and 50% Carbon Dioxide gas along with an admixture of 1% isopropanol is run through the tubes. The gas mixture was chosen for its drift time characteristics. The isopropanol is used to prevent age-related performance loss. The process for track reconstruction and momentum determination in the CDC and FDC (§2.4.6) is outlined in §2.5.

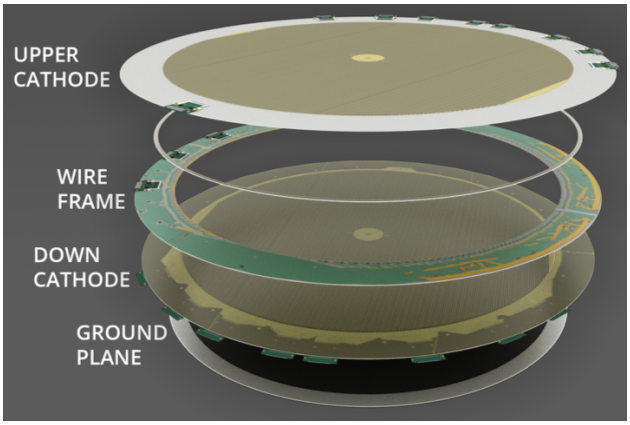

Figure 15. Artist rendering of an FDC cell. Figure from [60].

2.4.6 Forward Drift Chamber

The Forward Drift Chamber (FDC) is located downstream of the CDC and target and is used for tracking scattered particles in the forward direction [60]. The FDC is comprised of 24 1m diameter disc-shaped planar drift chambers separated into 4 groups at the bore of the solenoid magnet. Particles scattering at polar angles between 1° and 10° can be detected with all of the chambers, with partial coverage extending to 20°. Each chamber consists of a wire plane of sense and field wires spaced 5mm apart. The sense wires are 20μm in diameter and the field wires are 80μm in diameter. The wires are held at a high voltage of 2.2kV and -0.5kV for the sense and field wires respectively. A schematic of an FDC cell is shown in Figure 15. Each package of 6 chambers is separated by thin aluminum Mylar. Each of the chambers in the package is rotated 60° relative to the previous chamber for 2D spatial tracking. In order to reduce effects of the magnetic field on tracking, a "slow' gas mixture is used for the FDC, comprised of 40% Ar and 60% carbon dioxide. The total length of the detector, the distance between the first and last package, is 1.69m.

2.4.7 Barrel Calorimeter

The Barrel Calorimeter (BCAL) is an electromagnetic sampling calorimeter that used to detect photons with a minimum energy of 0.05 GeV up to several GeV over a polar angle range of $11^\circ - 126^\circ$ [67]. Because it is shaped like an open cylinder, the BCAL provides a full 360° coverage in the azimuthal plane. The target is located near the upstream end of the calorimeter. The BCAL is comprised of 48 optically isolated modules, where each module had 158 layers of the 0.5mm lead sheets and 15,000 1.0mm fibers which run parallel to beam line, which is also the axis of the detector. The modules are trapezoidal and form a 3.9m long cylinder with an inner radius of 65cm and an outer radius of 90cm. Light generated by the fibers is collected by light guides which transport the light to silicon photomultipliers (SiPMs). The SiPMs were specifically chosen due to their insensitivity to magnetic fields. Various schematics of the BCAL geometry and modules are shown in Figure 16.

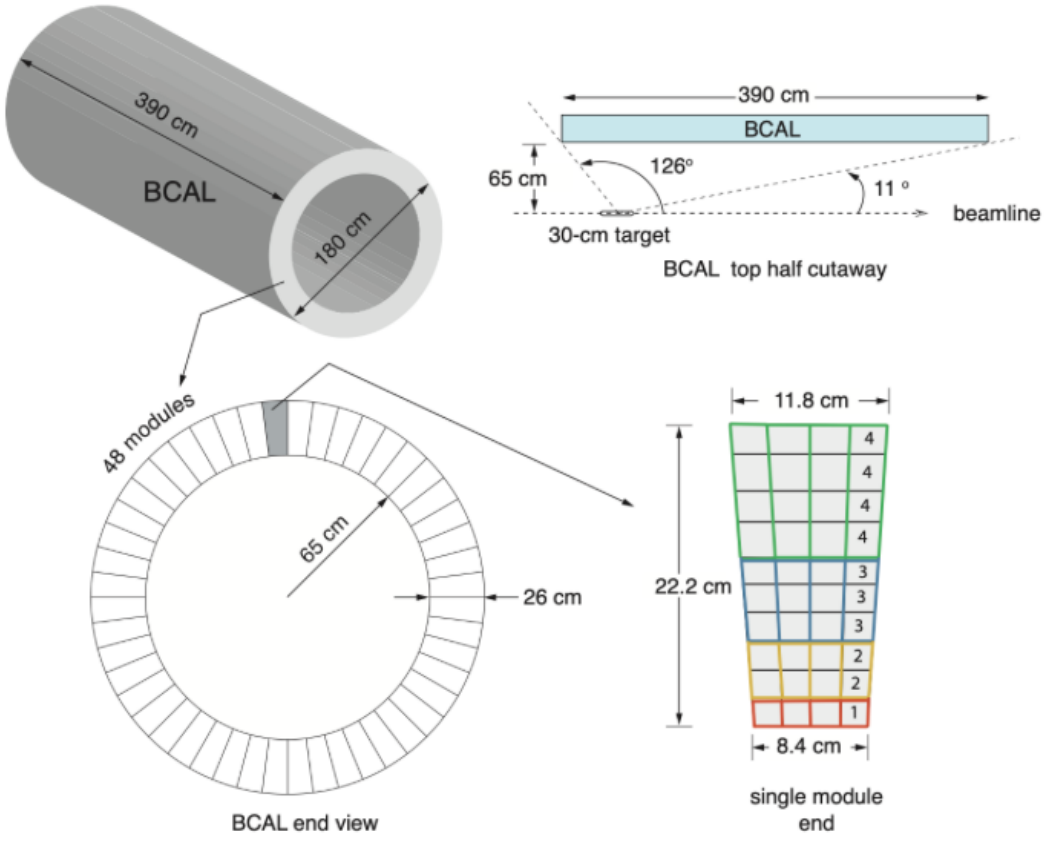

Figure 16. Schematic view for various viewing orientations of the BCAL and the individual module. Figure from [67].

2.4.8 Forward Calorimeter

The second calorimeter used by GlueX is located 5.6m downstream of the target. The Forward Calorimeter (FCAL) consists of 2800 4x4x45cm lead glass blocks arrayed in a circle with a diameter of 2.4m and can detect photons with energies ranging from 0.1 GeV to several GeV over a polar angle range of $1^\circ - 11^\circ$ [60]. The lead blocks and most of the photomultiplier tubes (PMTs) were repurposed from the E852 experiment at Brookhaven National Laboratory and the RadPhi Experiment at JLab. Prior to being used in the GlueX

Figure 17. Picture of the FCAL. Figure from [68].

FCAL, glass on the blocks is annealed via heating treatment. An image of the FCAL in Hall D is shown in Figure 17.

2.4.9 Time of Flight Counters

The Time of Flight Counter (TOF) is used to measure fast time signals from scattered charged particles such that we can identify the species of the detected particle (PID) [60]. The TOF is a "wall" of comprised of two planes scintillator paddles stacked in both the horizontal and vertical directions located 5.5m downstream of the target. A majority of the paddles measure 2.54x6x252cm,4 shorter paddles measure 2.54x6x120cm and 2 measure 2.54x3x252cm. The four paddles of length 120cm are used to make a "hole" in the detector to allow unscattered beam photons to continue along the beam line. The two "thin" paddles

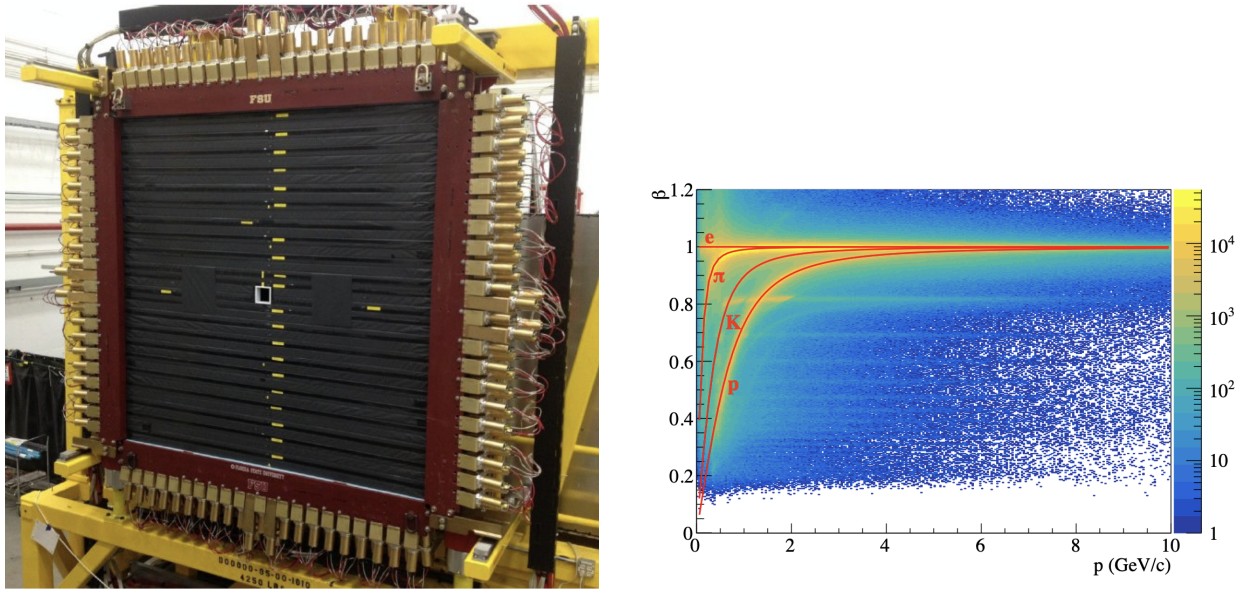

A **B**

Figure 18. Picture of the TOF (A). Theoretical β vs $\vec{p}$ curves for various particle species calculated for the TOF in GlueX (B). Figures from [69].

are the first two full-length paddles closest to the beam hole on either side and are used to keep detector counts below 2MHz. To move the light from the scintillator to the PMT, light guides made of UV transmitting plastic are used. Every paddle is wrapped in a layer of highly reflective material and a layer of black film to ensure light "tightness". The full length paddles have a PMT to readout the detector on either end, whereas the shorted paddles have just a single readout PMT. A picture of the TOF and the theoretical particle species curves in the detector are shown in Figure 18.

2.4.10 Trigger

The GlueX trigger is used to select as many high-energy hadronic interaction events as possible while reducing electromagnetic and low-energy hadronic interaction background events to an acceptable level [60]. While many detectors - like the PS, taggers, SC, and

TOF - can be used as supplementary triggers, the primary GlueX trigger is based on the PS Trigger measuring beam photon flux and on energy deposited into the FCAL and BCAL. The physics trigger is satisfied when either,

$$2E_{FCAL} + E_{BCAL} > 1 \text{ GeV and } E_{FCAL} > 0 \text{ GeV}, \tag{20}$$

or,

$$E_{BCAL} > 1.2 \text{ GeV}. \tag{21}$$

The trigger conditions were chosen to accept 100% of events with 2 or more hadrons with minimally ionizing signals left in the calorimeter. A majority of the scattering events of interest have forward-moving particles, which will satisfy the first trigger requirement. The second trigger requirement is to measure physics with scattered with large p_T. The PS trigger rate for the GlueX-I Spring 2018 run period was $\approx$ 3kHz, corresponding to a coherent peak photon flux of about 2.5×10^7 photons/s. The total trigger rate was $\approx$ 40kHz. When operating at maximum livetime, GlueX collects about 600 MBs of data per second.

2.5 TRACKING

The flight path, or "tracks", for charged particles can be measured in the CDC and FDC. Drift chambers are filled with wires held at some constant potential and a gas. When charged particles fly through a drift chamber, they interact with the gas and produce ions. These ions then "drift" towards the wires. As they do, they also interact with the gas and produce more ions, which also drift towards the wires. This creates a shower of ions. As

they reach the wires, a "pulse", or "hit", is read out. The drift time t_d of the hit is,

$$t_d = t_p - t_0, \tag{22}$$

where t_p is the pulse time and t_0 is event vertex time as reconstructed by any of the fast timing detectors. The drift velocity v_d of the ions is a known property of the gas. Therefore the position r_i of the particle relative to a wire is,

$$r_i = v_d t_{i,d}, \tag{23}$$

where $t_{i,d}$ are the drift times of the particle traveling across the drift chamber.

Charged particle tracks are reconstructed in three stages [60]. First, hits in adjacent CDC straws and or FDC chambers are put together to form potential track segments. These track segments are combined to form track hypotheses. Then, a Kalhman Filter is used to estimate the properties of the track at point closest to the beamline, starting from hits furthest away and working inwards [70]. The drift time information is not used at this stage. All tracks with $p > 0.8$ GeV are assumed to be pions and tracks with $p < 0.8$ GeV are assumed to be protons. After the initial track properties are estimated, each track is matched to one of the fast timing detectors (TOF, BCAL, FCAL) to determine the track's vertex time t_0. Then, each track is re-fitted for each of the potential charged particle hypotheses (e, π, K, p).

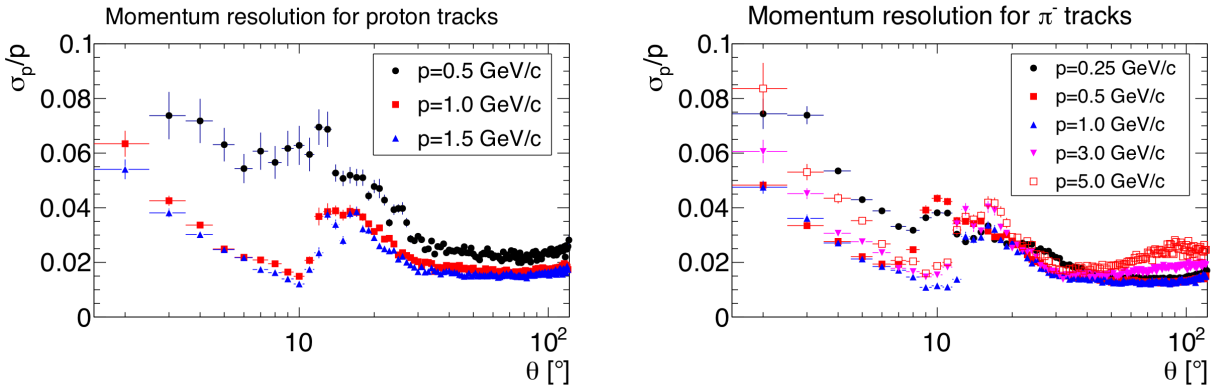

A **B**

Figure 19. Relative momentum resolution $\frac{\sigma_p}{p}$ for protons (A) and pions (B) as a function of polar angle θ. Figures from [60].

The track's momentum p is given by,

$$|\vec{p}| = q\vec{r} \times \vec{B}, \tag{24}$$

where q is the particle charge, r is the radius of curvature of the track, B is the magnetic field. and θ is the track's measured azimuthal angle. The charge q is determined via the direction the particle travels in the magnetic field. The momentum resolution for pions and protons is shown in Figure 19. There is significant uncertainty on very small angle detected particles and for protons with $\vec{p} < 0.5$ GeV/c

CHAPTER 3

EVENT SELECTION

In this analysis, we studied two charge-conjugated channels of $\gamma p \to p' K^{\pm} K_s \pi^{\mp}$ in the exclusive final states $p' K^- \pi^+ \pi^+ \pi^-$ and $p' K^- \pi^- \pi^- \pi^+$ where a $\pi^+\pi^-$ pair is assumed to be decay products of K_s. The GlueX-I dataset was taken over 3 run periods in the Spring of 2017, the Fall of 2018, and the Spring of 2018. The entirety of the 3 run periods combines for an integrated luminosity of 499.6pb^{-1}. The fractional luminosity is given in Table 3 [71]. The analysis code was primarily written in Python using `pyROOT` and can be found in the GitHub repository at [72].

3.1 PRELIMINARY DATA SKIM

An initial skim of our final state is done using the GlueX `ReactionFilter` software [73]. This software is used to skim across all of the GlueX-I data to identify candidate events for a given final state topology. An event will pass the `ReactionFilter` and be added to the data skim if it satisfies several conditions. Our analysis requires that an event must contain 3 positively charged tracks and 2 negatively charged tracks corresponding to the proton,

Table 3. Relative fraction of the total GlueX-I luminosity for each of the 3 run periods [71].

Run Period	Fraction of GlueX-I
Spring 2017	0.174
Spring 2018	0.504
Fall 2018	0.321

final state kaon, final state pion, and the decay products of the neutral kaon. The event RF Time must correspond to a beam photon within 4 timing bunches of the central timing peak. The kinematic fit must converge, i.e the value of the confidence level cannot be null. The kinematic fit and confidence level are discussed further in §3.3. To select potential K_s decays, the invariant mass of at least 1 combination of the positive and negative tracks must be within a loose range around the nominal value of the K_s mass. Two of the positive tracks and one of the negative tracks must share a vertex and the remaining positive and negative track corresponding to the K_s candidate must also share a vertex. The vertex is defined by the kinematic fit. All of the particles must satisfy at least one of the particle identification (PID) criteria defined by various detector responses and properties in §3.2. The missing mass squared of the event (Eqn. 36) must be less than ± 0.1 GeV. The missing mass squared of the event is discussed further in §3.4.

3.2 PARTICLE IDENTIFICATION

PID is done by combining information from various detector subsystems and fundamental properties of physics to identify which particle is being measured. No neutral particles are in our final state topology, so neutral particle PID at the detector level will not be discussed. A charged particle hypothesis is only considered if it has a hit in one of the BCAL, FCAL, or TOF. More information about PID can be found in [74].

3.2.1 Timing Cuts

Timing cuts are applied only for the detector with the best timing information. The ordering of detectors by quality of timing information is: BCAL, TOF, FCAL, SC. The BCAL

is ordered ahead of the TOF for convenience as there is almost zero overlap between hits in the BCAL and TOF. Some events will not have a hit in any of these detectors and will therefore not have any timing cuts applied. These cuts are applied first with the measured quantities for preliminary hypothesis selection and then again after the kinematic fit (§3.3) using the "true" momentum and vertex quantities. The cuts are applied to the difference between the RF time and the reconstructed start time from the detector timing readout propagated back to the event vertex $\Delta t(RF)$. For particles coming from a detached vertex, the timing is first propagated back to the secondary vertex and then to the event vertex. For an incorrect particle hypothesis, the back-propagation will lead to larger $\Delta t(RF)$ because the assumed relationship between velocity and momentum will be wrong. Since measure the momentum of charged tracks with the CDC/FDC, for a given PID hypothesis for a particle with mass m we can relate the momentum to the particles velocity via,

$$m = |p|\sqrt{1-\beta^2}/\beta, \tag{25}$$

where the relativistic velocity β is given by,

$$\beta = r_t/(t_t c), \tag{26}$$

and r and t are the distance and time, respectively, from the particle vertex to the detector with the best measured timing information [75]. The timing cuts for a given particle species are given in Table 4. For kaon hypotheses, an additional constraint is applied to reduce large background from pions and protons. The kaon hypothesis must have a hit

Table 4. Timing cuts for each particle in the final state topology for this study. The cuts are placed on the difference between the back-propagated start time from the detector and the RF start time, $\Delta t(RF)$, and are given in nanoseconds (ns)[74].

Particle	BCAL	TOF	FCAL	SC
π^+	± 1.00	± 0.50	± 2.00	± 2.50
π^-	± 1.00	± 0.50	± 2.00	± 2.50
K^+	± 0.75	± 0.30	± 2.50	± 2.50
K^-	± 0.75	± 0.30	± 2.50	± 2.50
p	± 1.00	± 0.60	± 2.00	± 2.50

in at least one of the timing detectors or have a sufficient number of hits in the CDC to calculate the energy loss as a function of position (dE/dx) (§3.2.2).

The β vs $\vec{p}$ plots for negatively charged tracks in the GlueX data and $f_1(1285)p' \to p'K^{\mp}K_s\pi^{\pm}$ Monte Carlo samples are shown in Figure 20. Kaon/pion separation is possible up to ~ 2 GeV. Beyond that, we must rely on the kinematic fit for pion/kaon separation.

3.2.2 Track Energy Loss

Particles traveling through the GlueX Central Drift Chamber (CDC) will deposit energy into the detector as a function of the distance traveled dE/dx. For each particle species, the dE/dx "curve" as a function of the measured momentum is extracted by fitting an exponential function to the dE/dx vs $\vec{p}$ distribution for a given species. We can apply a cut for a given particle hypothesis based on this function. If the dE/dx for a given hypothesis does not fall below the upper bound of the hypothesis species dE/dx curve, that event is cut. For kaons and pions, the hypothesis must satisfy,

$$dE/dx < e^{-7p+3} + 6.2, \tag{27}$$

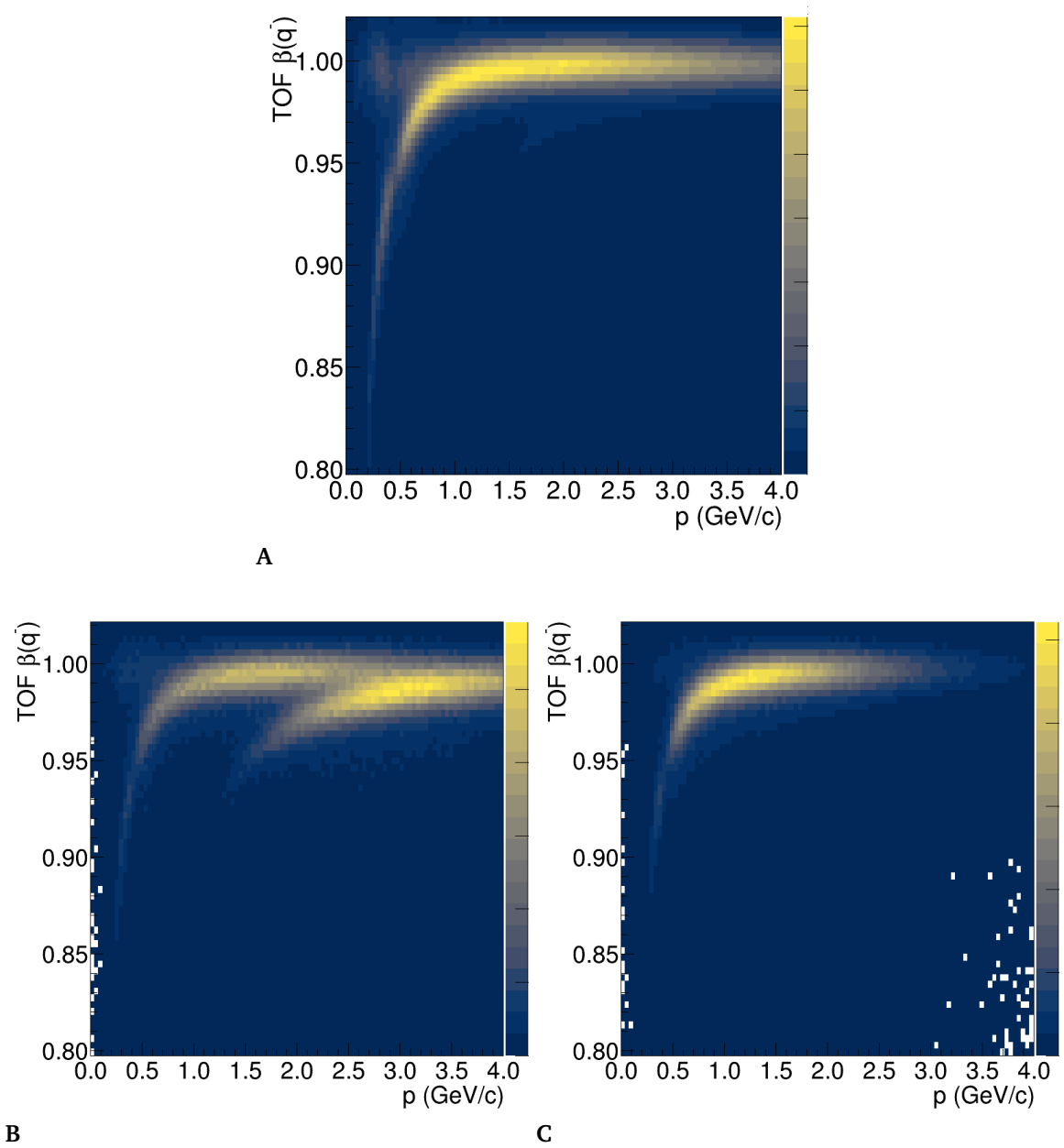

Figure 20. β vs $\vec{p}$ distributions for negative tracks in the TOF. The data (A) and Monte Carlo sample of $f_1(1285)p' \to p'K^-K_s\pi^+$ (B) have bands corresponding to the π^- from K_s decay and the K^-. The $f_1(1285)p' \to p'K^+K_s\pi^-$ Monte Carlo sample (C) does not have a K^- in the final state, so only the π^- track curve is observed.

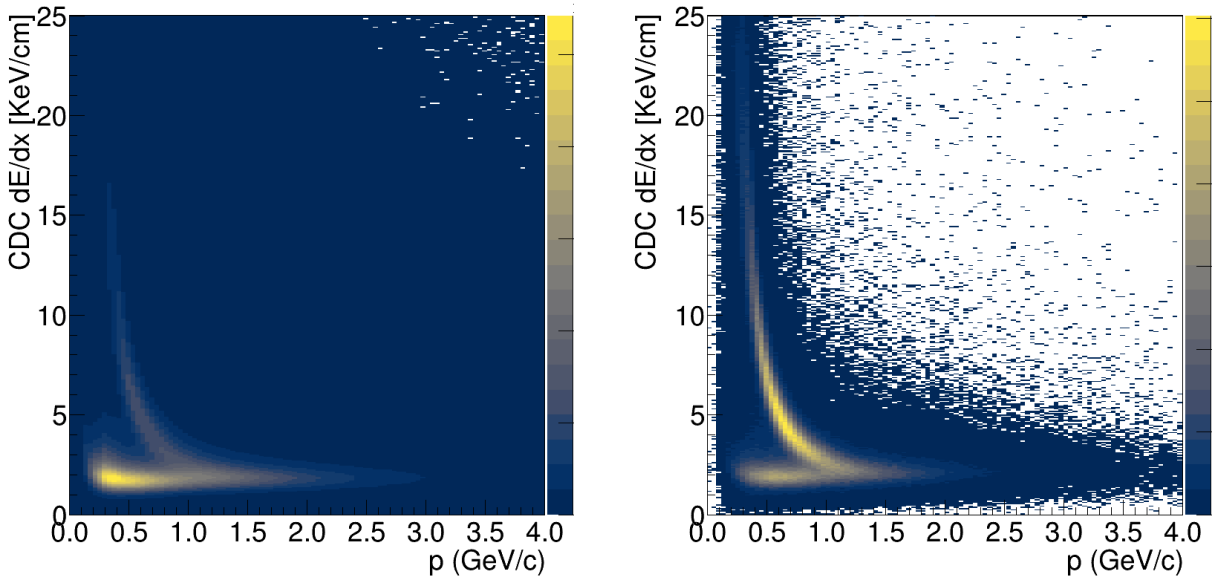

A B

Figure 21. dE/dx vs $\vec{p}$ distributions for positively charged tracks in GlueX data (A) and Monte Carlo simulation of $p' f_1(1285) \to p' K^- K_s \pi^+$ (B). The curved band represents proton tracks and the horizontal line represents pion, kaon, and electron tracks.

where p is the momentum of the particle. Proton hypotheses must satisfy,

$$dE/dx < e^{-4p+2.25} + 1.0. \tag{28}$$

Figure 21 shows the dE/dx vs $\vec{p}$ curves for GlueX data and Monte Carlo. Our Monte Carlo sample has a more prominent proton band, as a majority of our protons are low momentum by virtue of the generated t-slope of the Monte Carlo. The Monte Carlo sample is discussed further in Chapter 4

3.2.3 Invariant Mass and Missing Energy

Exclusive reactions are reactions in which there are no "missing" particles i.e each final

state particle is detected. For exclusive reactions, a cut is placed on the missing energy of the system such that,

$$|E_\gamma + E_p - \sum_i E_i| < 3 \text{ GeV}, \tag{29}$$

where i is the number of particles in the final state and E_i is the energy of the ith particle hypothesis in the event.

For "long-lived" intermediate particles, a cut is placed on the invariant mass of the decay particle hypotheses. The invariant mass of any system of particles is defined to be,

$$M^2 = p^\mu p_\mu, \tag{30}$$

where p is the 4-momentum $p^\mu = (E, p_x, p_y, p_z)$. For a K_s hypothesis we require,

$$0.3 < M(X^+X^-) < 0.7 \text{ GeV}, \tag{31}$$

where M is the invariant mass of the decay particle hypotheses X^+, X^-. for the K_s this will be the invariant mass of the $\pi^+\pi^-$ from a shared vertex.

Beyond these loose selection criteria, PID is predominantly done via selections on the Kinematic Fit and kinematic cuts.

3.3 KINEMATIC FIT AND PHOTON TIMING

After reducing the total GlueX-I dataset to events that may satisfy our final state hypothesis, we take advantage of the GlueX Kinematic fitter to further shrink our dataset to a reasonable size for targeted data analysis. The kinematic fitter serves two primary

purposes in our analysis:

- Account for measurement uncertainty by adjusting measured momenta and vertex positions to "true" values.
- Quantify the likelihood of a given event satisfying the final state topology hypothesis.

The kinematic fitter works by shifting the values of the momenta and vertices based on prescribed constraints to minimize some defined χ^2 of the fit using a method called the least squares fit with constraints. The expression that we seek to minimize is given by,

$$\chi^2 = (\mathbf{y} - \boldsymbol{\eta})^T \mathbf{V}_y^{-1} (\mathbf{y} - \boldsymbol{\eta}) + 2\boldsymbol{\lambda}^T \mathbf{f}, \tag{32}$$

where $\mathbf{y}$ is the measured quantity in our detector, like $\vec{p}$, θ, and ϕ, $\boldsymbol{\eta}$ is the "true" value of the quantity, $\mathbf{V_y}$ is the covariance matrix for the measured quantity, $\boldsymbol{\lambda}$ is the set of Lagrangian multipliers that minimize χ^2, and $\mathbf{f}$ are the physics constraints,like conservation of momentum and energy.

The constraints in this analysis are four-momentum conservation and shared vertices. The four-momentum constraint is $p_i^\mu = p_f^\mu$, requiring the initial state four-momentum $(\gamma + p)$ must be equal to the four-momentum of the final state $(p' + K^\mp + \pi^\pm + \pi^+ + \pi^-)$. The vertex constraint requires that the detected proton, charged kaon, and a charged pion share a vertex while the remaining pion pair also share a vertex. Details of the implementation of the constraints, and how the fitting algorithm works, can be found in[76], [77]. We do not use the K_s invariant mass constraint for the decay of $K_s \to \pi^+\pi^-$, as that will lead to some non-negligible background contribution that we will attempt to subtract out.

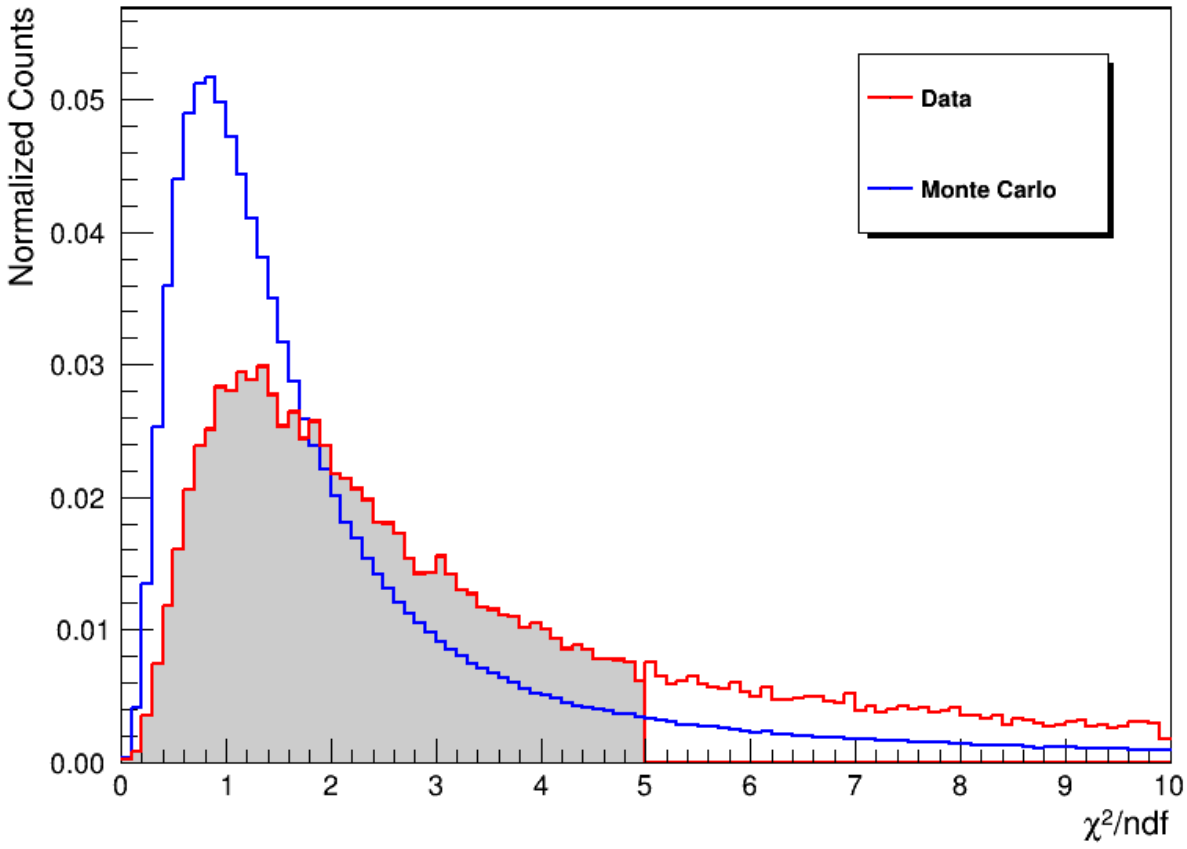

Figure 22. Kinematic fit χ^2/ndf distributions for Monte Carlo (blue) and data (red). The shaded region shows the selected data events. All selection criteria is applied to both plots except for the χ^2/ndf and CL_{KinFit} cuts.

To ensure a level of confidence that our selected events satisfy our final state hypothesis of $\gamma p \to p' K^{\mp} K_s \pi^{\pm}$, we place a preliminary loose cut on the kinematic fit $\chi^2/ndf < 5$. This is determined via our Monte Carlo $f_1(1285)$ sample (Chapter 4). We find that nearly all of the signal Monte Carlo events populate the region below $\chi^2/ndf = 5$. We can confidently assume most of the events with higher χ^2/ndf values are not $f_1(1285) \to K^{\mp} K_s \pi^{\pm}$ events. The χ^2 distributions of the data and Monte Carlo are shown in Figure 22.

For each event, there can be multiple combinations of the final state particle hypotheses

that satisfy the outlined conditions. To significantly reduce the impact of beam accidentals and combinatorics, we "flatten" our data by selecting only the "best" in-time combination per event, defined to be the combo with the smallest χ^2/ndf. If an event does not have an "in-time" beam photon, that event is discarded. In-time refers to events with a time difference between the event vertex and RF time that lies within the central peak around 0. The event vertex time is determined from the times of the final state particles in the detector propagated back to the vertex. Our initial data skim contains all events within ± 4 timing peaks, but we consider only combos within the central timing peak. The peaks around the central timing peak provide information about the expected number of mistagged events that mimic in-time combos. Figure 23 demonstrates a reduction in the statistical background arising from mistagged timing events by applying a χ^2/ndf cut. The assumption follows that choosing only the best in-time combo per event reduces the statistical significance of mistagged events to a negligible amount, as mistagged events are unlikely to satisfy that requirement. Internal studies at GlueX have shown that the "best χ^2" method of event selection yields consistent cross-section values compared with the accidental RF sideband statistical subtraction method, which involves using events from any of the timing peaks to assign each combo a weight corresponding to how far away from the central peak the event occurs [78]. A comparison of the two methods for the cross-section of $\gamma p \to p'\eta' \to p'\pi^+\pi^-\eta_{\gamma\gamma}$ is shown in Figure 24.

An additional cut is placed on the kinematic fit confidence level later in the event selection process, after using the $\chi^2/ndf < 5$ criteria to reduce and flatten to 1 combo per

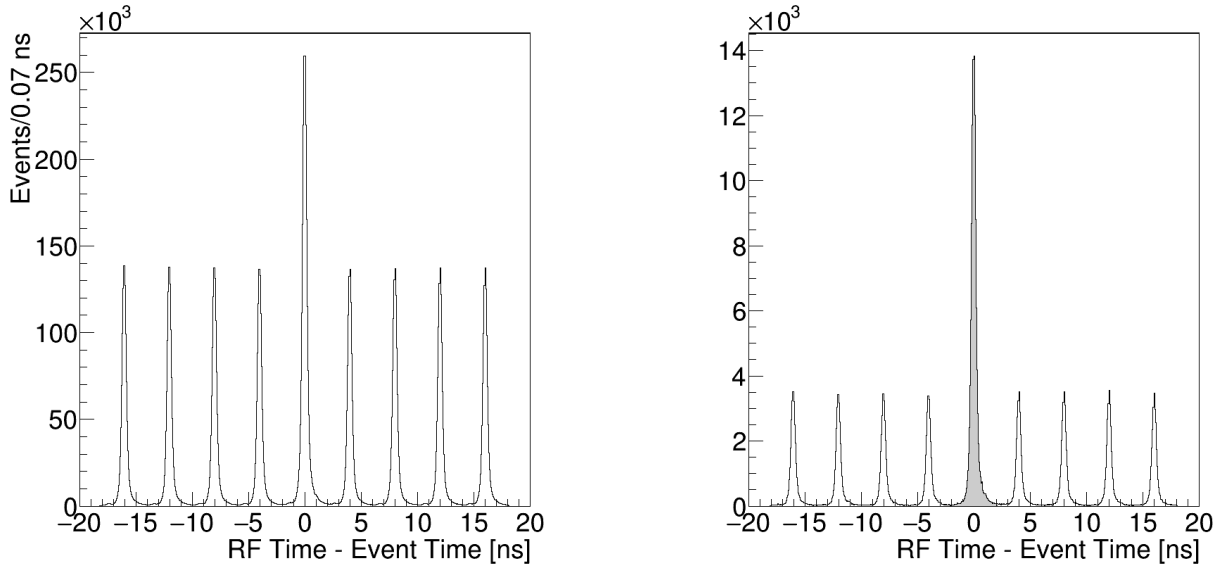

A B

Figure 23. $\Delta t(RF) = t_{\text{RF}} - t_{\text{Event}}$ distributions with a central "in-time" peak and accidental beam bunch events extending outwards in time. (A) does not have a requirement on χ^2/ndf and (B) requires $\chi^2/ndf < 5$. Placing a requirement on $\chi^2/ndf < 5$ for the kinematic fit reduces mistagged timing events by a substantial degree. The grey shaded region in (B) shows the in-time event peak.

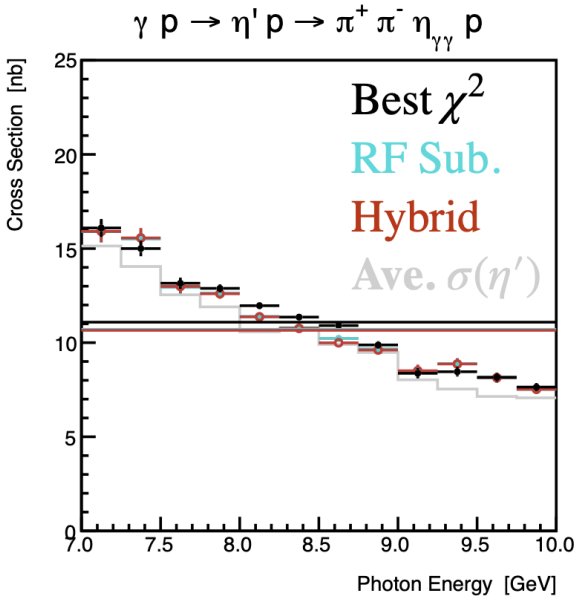

Figure 24. A comparison in the cross-section of $\gamma p \to p'\eta' \to p'\pi^+\pi^-\eta_{\gamma\gamma}$ measured using the "Best χ^2" method (black points) and "RF Sideband Subtraction" method (blue points) of handling mistagged out-of-time beam photon events. The two methods produce comparable results. Figure from [78].

event. The confidence level [79] for the kinematic fit is given by,

$$CL_{\text{KinFit}} = 1 - P(\frac{ndf}{2}, \frac{\chi^2}{2}), \tag{33}$$

where P is the regularized gamma function [80] given by,

$$P(n, \chi^2) = \int_{\chi^2}^{+\infty} \frac{1}{\Gamma(n/2)2^{n/2}} \chi^{2\prime(n/2)-1} e^{-\chi^{2\prime}/2} d\chi^{2\prime}, \tag{34}$$

with $n = ndf$ and the Γ function [81] is given by,

$$\Gamma(n) = \int_0^{\infty} t^{n-1} e^{-t} dt. \tag{35}$$

The confidence level of the kinematic fit tells us the probability of a larger χ^2 value being produced for a correct modeled event by chance. A confidence level close to 1 is the ideal value. We determine our cut value by comparing the signal Monte Carlo CL_{KinFit} distribution against the data distribution with all selection criteria applied and make a judgement call that selects good events that preserve enough real data events to perform our analysis. These distributions are shown in Figure 25.

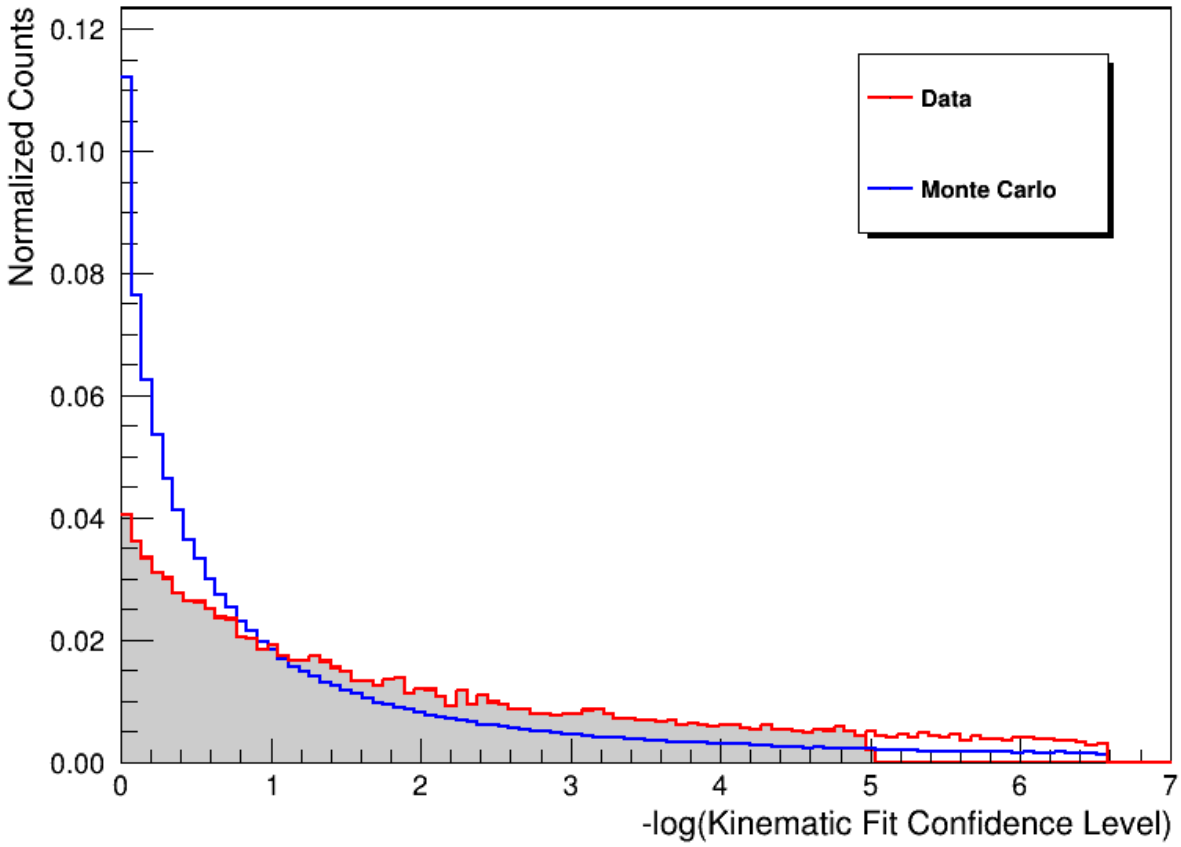

Figure 25. Distributions of $-\log(CL_{\text{KinFit}})$ for Monte Carlo (blue) and data (red). The shaded region shows the selected data events corresponding to $CL_{\text{KinFit}} > 10^{-}5$. All selection criteria except the CL_{KinFit} cut is applied to both distributions.

3.4 EXCLUSIVITY

To ensure exclusivity, we require that the missing mass squared be very close to zero such that no undetected massive particles were a part of the event combo. The missing mass squared for our final state is defined to be,

$$M_x^2(pKK\pi) = p^\mu p^\nu(\gamma + p - p' - K^\mp - \pi^\mp - \pi^+ - \pi^-). \tag{36}$$

We require that,

$$|M_x^2(pKK\pi)| < 0.01 \text{ GeV}^2. \tag{37}$$

The distributions of $M_x^2(pKK\pi)$ before and after the event selection criteria is applied for both charge conjugated modes are shown in Figure 26. This cut is a more-strict veto compared to the cut on the kinematic fit χ^2/ndf. By choosing the best kinematic fit χ^2/ndf combo per event, we reduce the number of events with a non-negligible missing mass. This cut ensures further exclusivity.

3.5 LOW MOMENTUM PROTONS

The GlueX detector has a poor reconstruction efficiency for events with low proton momenta. This region represents an "edge case", so we cannot be confident that our Monte Carlo simulation is correctly modeling the detection efficiency of these protons. In the interest of staying within the well-modeled bounds of our detector, a cut is placed on the momentum of the detected scattered proton,

$$\vec{p}(p') > 0.4 \text{ GeV}. \tag{38}$$

This also represents a cut on the region of Mandelstam-t that our differential cross section will be measured over, as we define,

$$-t = \left(p - p'\right)^2, \tag{39}$$

where p is four-momentum of our target proton and p' is the four-momentum of our

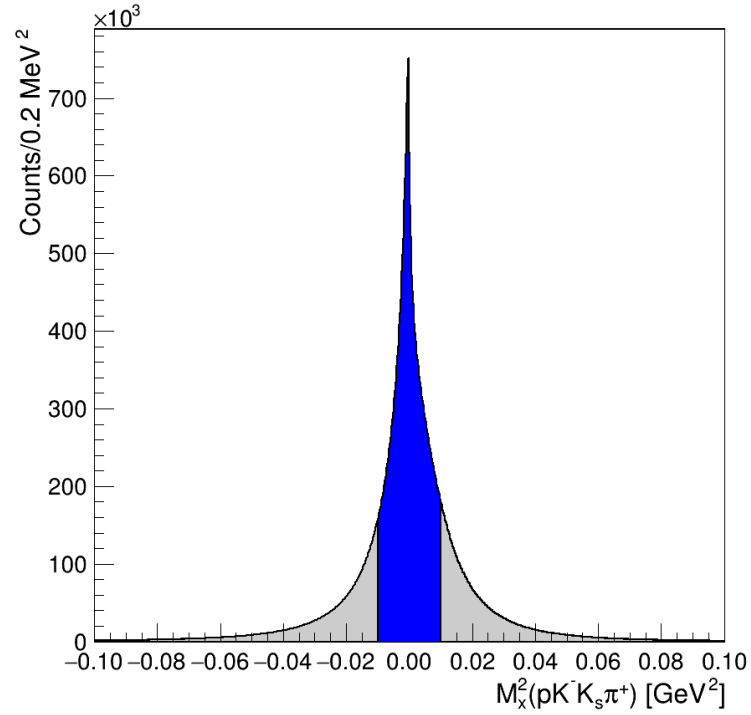

A

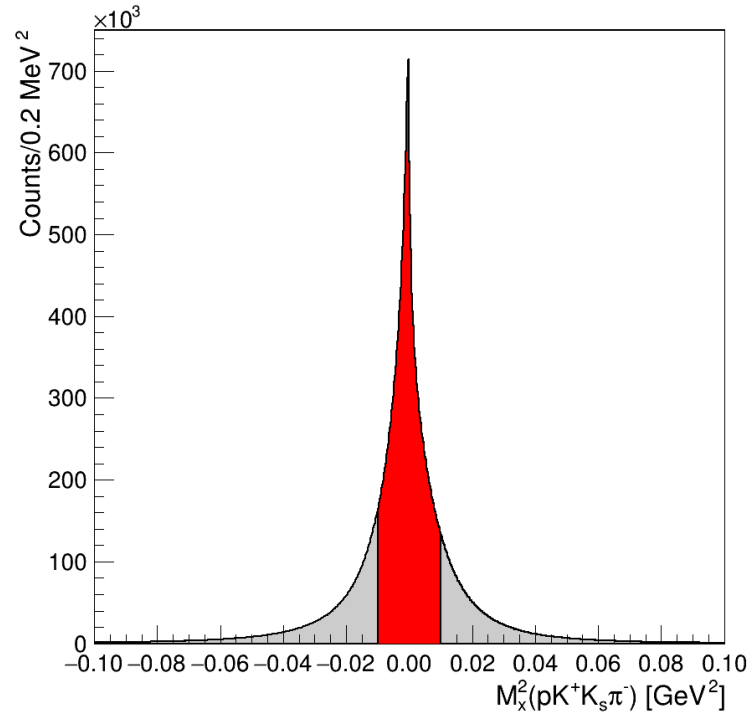

B

Figure 26. Distributions of $M_x^2(p'K^-K_s\pi^+)$ (A) and $M_x^2(p'K^+K_s\pi^-)$ (B). The the blue/red filled regions indicate the events that satisfy Eqn. 37.

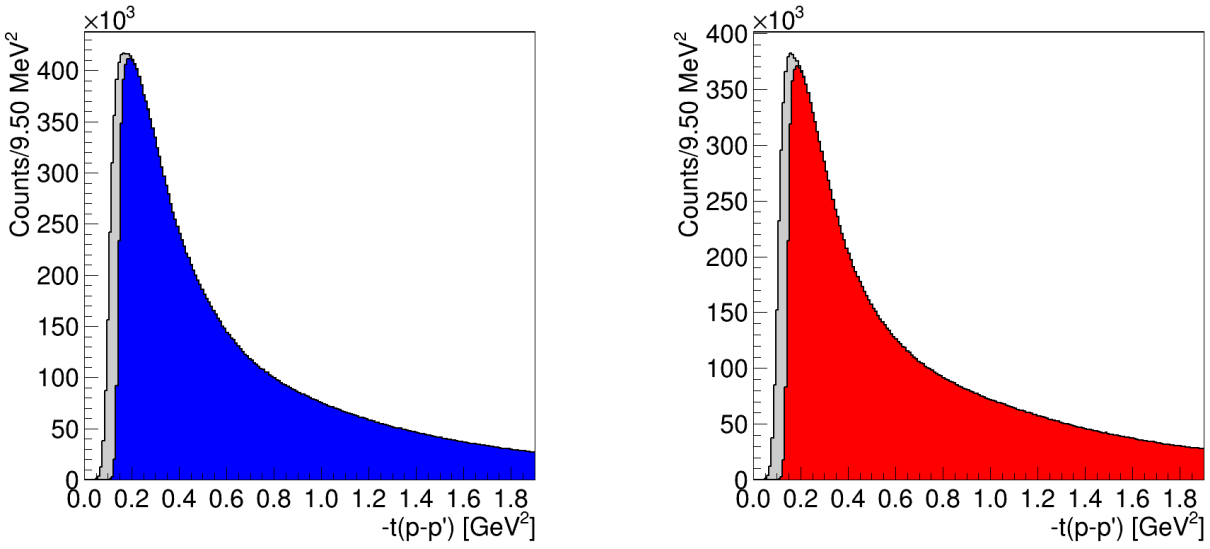

A **B**

Figure 27. Mandelstam-t distributions before and after $\vec{p}(p)$ cut. Final states $p'K^-K_s\pi^+$ (A) and $p'K^+K_s\pi^-$ (B) before (gray) and after (blue/red) we place a cut on the proton momentum $\vec{p}(p) > 400$ MeV.

detected scattered proton. The effect of this cut on the Mandelstam-t distributions is shown in Figure 27.

3.6 K_S SELECTION

The short-lived neutral kaon, K_s decays most often to two pions $K_s \to \pi^+\pi^-$. This decay occurs rapidly after the particle is produced, such that the kaon itself is not detected in the experiment but rather it's decay products are. Our final state requires two oppositely charged pions be detected in the mass range of the K_s, between 0.3 GeV and 0.7 GeV.

3.6.1 Pathlength Significance

The pathlength significance is defined to be the vertex separation from the kinematic

fit results divided by the uncertainly of the vertex separation,

$$\text{Pathlength Significance} = \frac{r}{\sigma_r}, \tag{40}$$

where r is the distance between the primary event vertex and the secondary vertex of the K_s hypothesis as determined by the kinematic fit. Even for small vertex separations, a small uncertainty will lead to larger pathlength significance values. As the value of pathlength significance increases, there are fewer non-resonant background events. We select events that satisfy,

$$\text{Pathlength Significance} > 5. \tag{41}$$

Figure 28 shows the $M(\pi^+\pi^-)$ distributions of both final states before and after the pathlength cut is applied. A Gaussian-like feature is observed around the mass of the K_s consistent with the value provided in the PDG [82], but there is significant background. The pathlength cut significantly reduces the background. The width of this distribution is due to the detector resolution.

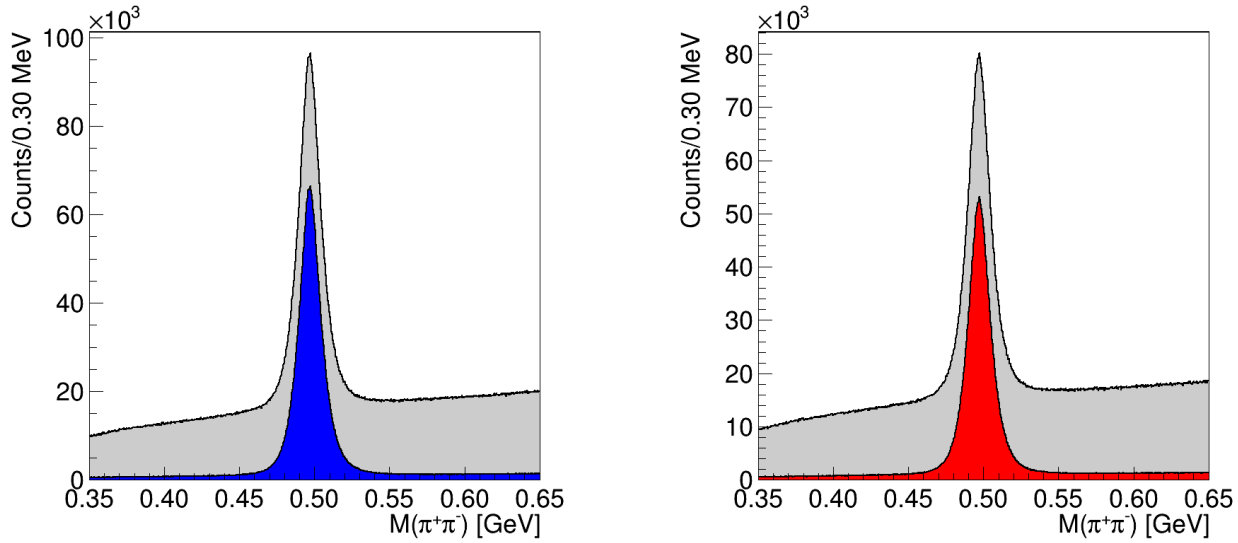

Figure 28. Selection of K_s events with pathlength significance cut. Invariant mass distributions of the dipion system $M(\pi^+\pi^-)$ for final states $p'K^-K_s\pi^+$ (A) and $p'K^+K_s\pi^-$ (B) before (gray) and after (blue/red) after applying a cut on the pathlength significance according to Eqn. 41.

3.6.2 K_s Mass Cut

After applying the pathlength significance cut to select only $\pi^+\pi^-$ pairs with a good likelihood of originating from a secondary vertex, we then remove events far outside of the region of the K_s mass. To do this, the $M(\pi^+\pi^-)$ distribution is fit with a function of the form,

$$F(M;\sigma) = G_1(M;\sigma_1) + G_2(M;\sigma_2) + B(M), \tag{42}$$

where M is $M(\pi^+\pi^-)$, $G_1(M;\sigma)$ and $G_2(M;\sigma)$ are Gaussian distributions given by,

$$G(M;\sigma) = \frac{1}{\sqrt{2\pi\sigma^2}} e^{-M^2/2\sigma^2}, \tag{43}$$

σ is the width of the distribution, and $B_1(M)$ is a first-order polynomial of the form

$$B(M) = c_1 M + C. \tag{44}$$

The mean and width of this distribution is determined by weighting the mean and width of each Gaussian by the relative size of each distribution with [83],

$$\sigma_{K_s} = g_1\sigma_1 + (1-g_1)\sigma_2, \tag{45}$$

where g_1 is the fraction of events in $G_1(M;\sigma_1)$. The fit to the data is shown in Figure 29. The mean and width are taken to be the mass $M(K_s)$ and detector resolution σ_{K_s}, respectively, of the K_s. For normal distributions, 95% of events will fall within $\pm 2\sigma_{K_s}$ of the mean of a given distribution[84]. Therefore, we keep events that satisfy,

$$|M(\pi^+\pi^-) - M(K_s)| < 2\sigma_{K_s}. \tag{46}$$

We have sufficiently removed non-resonant $\pi^+\pi^-$ events from our sample so we will designate the secondary vertex dipion system as K-short (K_s) for the rest of the analysis. We have now identified events that satisfy the exclusive final state hypothesis of $K^{\mp}K_s\pi^{\pm}$.

3.7 BARYON REJECTION

There are several reactions with baryonic $\Delta/N^* \to p\pi$ and $\Lambda \to K\pi$ decays that have a $pKK\pi$ final state. To isolate the $f_1(1285) \to K^{\mp}K_s\pi^{\pm}$ decay channel, we attempt to remove these baryonic events via kinematic cuts.

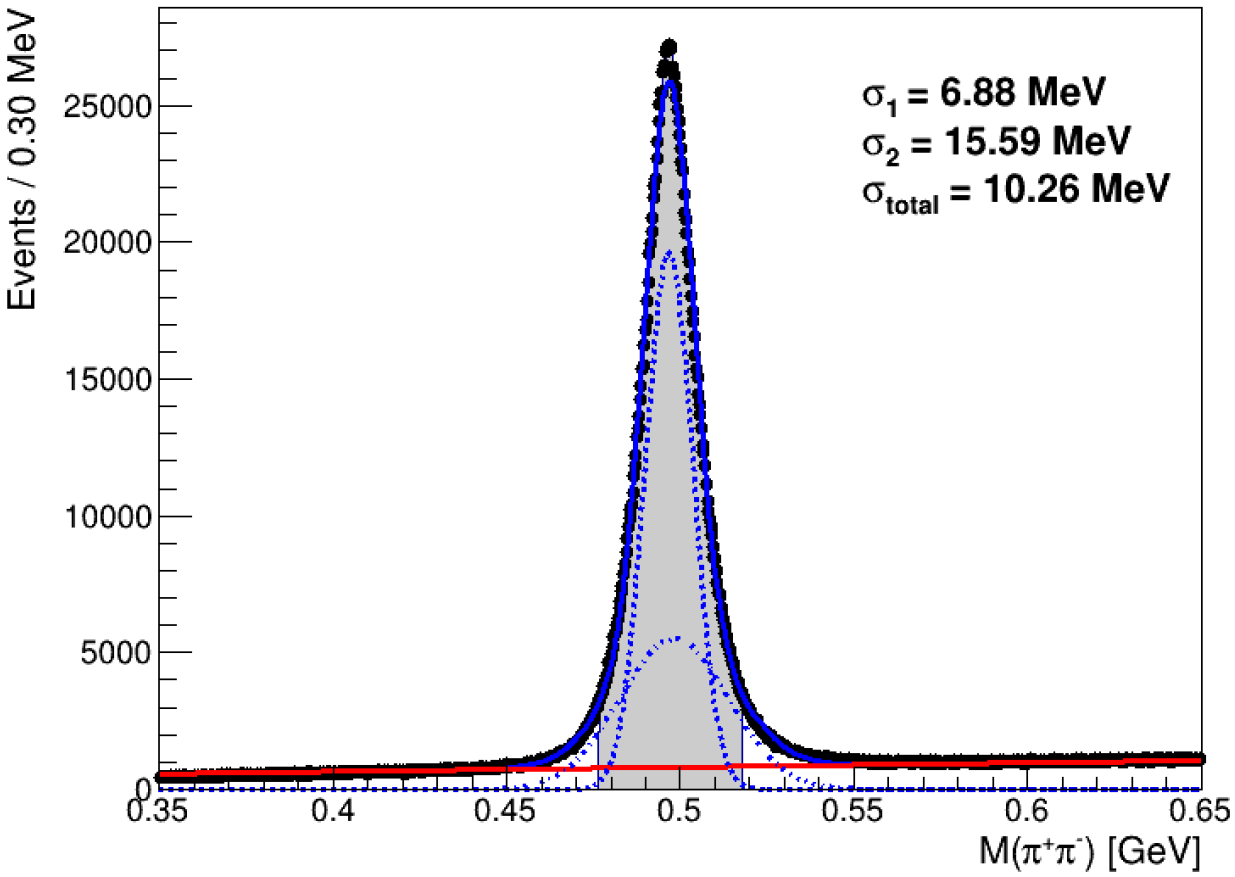

Figure 29. $M(\pi^+\pi^-)$ with the model in Eqn. 42 fit to the data. The full model (solid blue line) is shown along with the constituent Gaussian functions (dashed/dotted blue lines) and background linear function (solid red line). The widths σ of the constituent and composite Gaussian are shown on the figure. Events that satisfy the cut criteria given by Eqn. 46 are marked in the gray shaded region.

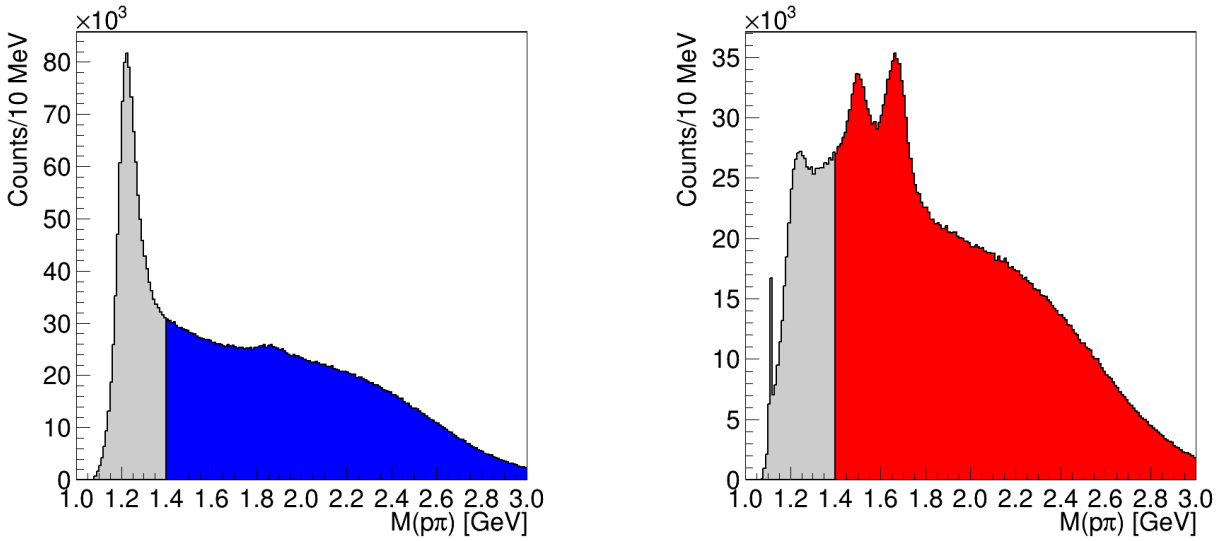

Figure 30. Invariant mass distributions of $M(p'\pi^+)$ (A) and $M(p'\pi^-)$ (B). The colored blue/red region shows the events that survive after a cut is applied according to Eqn. 47. An excess of N^* events can be seen in the $M(p\pi^-)$ distribution.

3.7.1 Δ/N^* Rejection

The final state topology of our reaction allows for Δ and N^* baryons to be included in our data in the decay of $\gamma p \to \Delta^{++/0} K^{\mp} K_s$ and $\gamma p \to N^* K^{\mp} K_s$ where $\Delta^{++/0} \to p'\pi^{\pm}$ and $N^* \to p'\pi^-$. In the $M(p\pi\pm)$ distributions shown in Figure 30, there are peaks corresponding to the Δ baryon, which has a mass of 1.238 GeV [85]. To exclude these events, we select events that satisfy,

$$M(p'\pi^{\pm}) > 1.4 \text{ GeV}. \tag{47}$$

This cut removes Δ contamination from both final states. However, there are other peaks corresponding to N^* decays. There are many N^* resonances [86] that lie in the region of $1.4 < M(p\pi^-) < 3.0$ GeV and the most narrow of them has a decay width of 70

MeV. This means that there is no simple way of removing these events via kinematic cut while allowing for a sufficiently large population of $f_1(1285)$ signal events to survive such that yields in bins of Mandelstam-t can be extracted.

3.7.2 Λ and Σ Rejection

There may also be Λ and Σ baryons in the $p'K^{\pm}K_S\pi^{\mp}$ data sets via the reaction $\gamma p \to \Lambda K\pi$ and $\gamma p \to \Sigma K\pi$ where $\Lambda \to p'K^{\pm}$ and $\Sigma \to p'K_s$. We consider the $p'K^{\mp}$ and $p'K_s$ combinations to evaluate Λ/Σ contributions.

The distribution for $M(p'K^-)$ is given in Figure 31A. We observe two peaks in the lower mass side of the distribution, which likely indicate the presence of $\Lambda(1520)$ and $\Lambda(1820)$. Both $\Lambda(1520)$ and $\Lambda(1820)$ have a primary decay mode of $N\bar{K}$ [87], [88]. To remove these unwanted resonances, we select only events that satisfy,

$$M(p'K^-) > 2.0 \text{ GeV}. \tag{48}$$

The charge conjugated distribution for $M(p'K^+)$ is shown in Figure 31B. We observe no obvious enhancements that would indicate the presence of any baryon resonance but the same cut is applied to $M(p'K^+)$ for completeness and to exclude any non-obvious resonances lurking under the large phase space background. In Figures 55 and 56, it can be seen that choosing symmetric cuts has a minimal impact on the final measurement of the $f_1(1285)$ cross-section.

The $p'K_s$ combination appears in both final states. In the topology of $p'K^+K_s\pi^-$, as seen in Figure 31D there is an enhancement in the region of $M(p'K_s) = 1.75$ GeV that could

be the $\Sigma(1775)$ baryon. Just like in the case of the Λ rejection, only events which satisfy $M(pK_s) > 2.0$ GeV in either final state are kept.

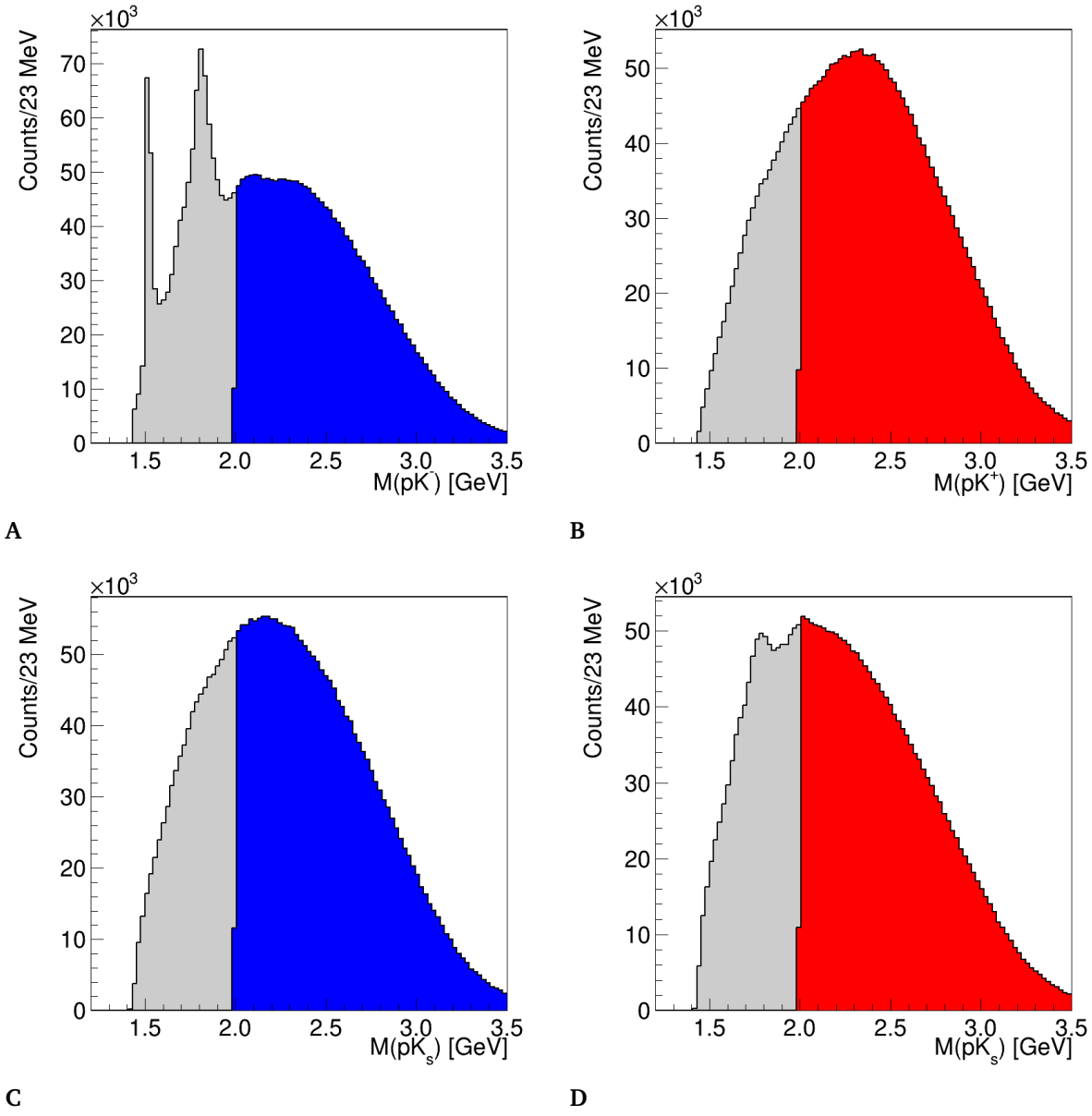

Figure 31. Distributions of $M(pK^-)$ (A), $M(pK^-)$ (B) and $M(pK_s)$ for the $pK^-K_s\pi^+$ (C) and $pK^+K_s\pi^-$ (D) final state topologies. Features are seen in the $M(p'K^-)$ and $M(p'K_s)$ ($p'K^-K_s\pi^+$) distributions. A symmetrical cut is applied for completeness.

3.8 $KK\pi$ MASS DISTRIBUTION

The $KK\pi$ mass distributions with all of the outlined selection criteria applied are shown in Figure 32. There is a clear enhancement around $M(KK\pi) = 1.28$ GeV and potentially another enhancement around $M(KK\pi) = 1.4$ GeV. Both enhancements sit atop a large phase space background. The enhancement around $M(KK\pi) = 1.4$ GeV may be some combination of $f_1(1420)$ [20], $\eta(1405)$ [89], and $\eta(1475)$ [90], which have all observed in $KK\pi$ decays. As discussed in §1.3.2 and §1.3.3 there is lots of uncertainty about these states. This uncertainty makes prospect of using Monte Carlo methods to model the region a daunting one. Without a way to accurately model the potential superposition of these particles, we seek a way to dramatically reduce the contamination from these enhancements in the $M(KK\pi)$ distribution.

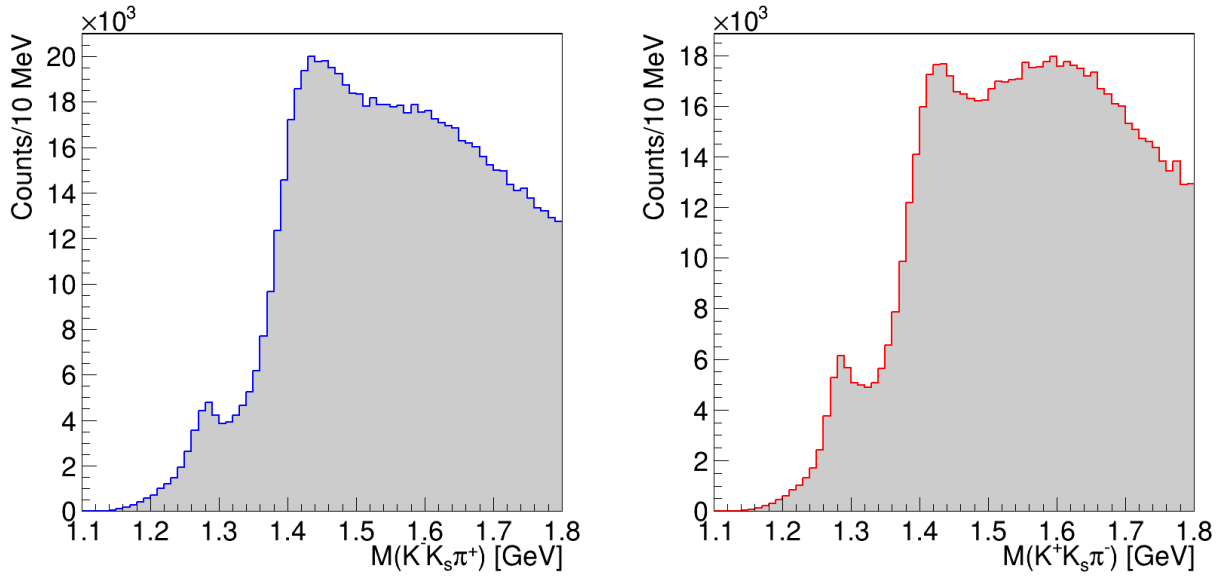

A **B**

Figure 32. $M(K^-K_s\pi^+)$ (A) and $M(K^+K_s\pi^-)$ (B) distributions after all event selection criteria has been applied except for the K^* rejections. A clear enhancement around $M(KK\pi) = 1.28$ GeV is seen in both channels. Additionally, there appears to be an additional enhancement around $M(KK\pi) = 1.4$ GeV.

3.9 K^* REJECTION

$f_1(1285)$ has not been observed to decay to KK^* as the threshold for KK^* production is well above the mass and width of $f_1(1285)$. Conversely, the potential higher mass states have been observed to decay through KK^* [20], [89], [90]. To further reduce non-$f_1(1285)$ background, we reject events with likely $K^* \to K\pi$ decays. The $M(K\pi)$ distributions for both final states are shown in Figure 33. Features corresponding to the charged and neutral K^* mesons can be seen at $M(K\pi) = 0.890$ GeV. The dalitz plots of the $KK\pi$ system in different mass regions of $KK\pi$ encompassing the mass values of the higher mass f_1 and ηs are shown in Figure 34. These dalitz plots confirm that there is very little kine-

matic phase space for the K^* to decay through in the $M(KK\pi)$ region of $f_1(1285)$.

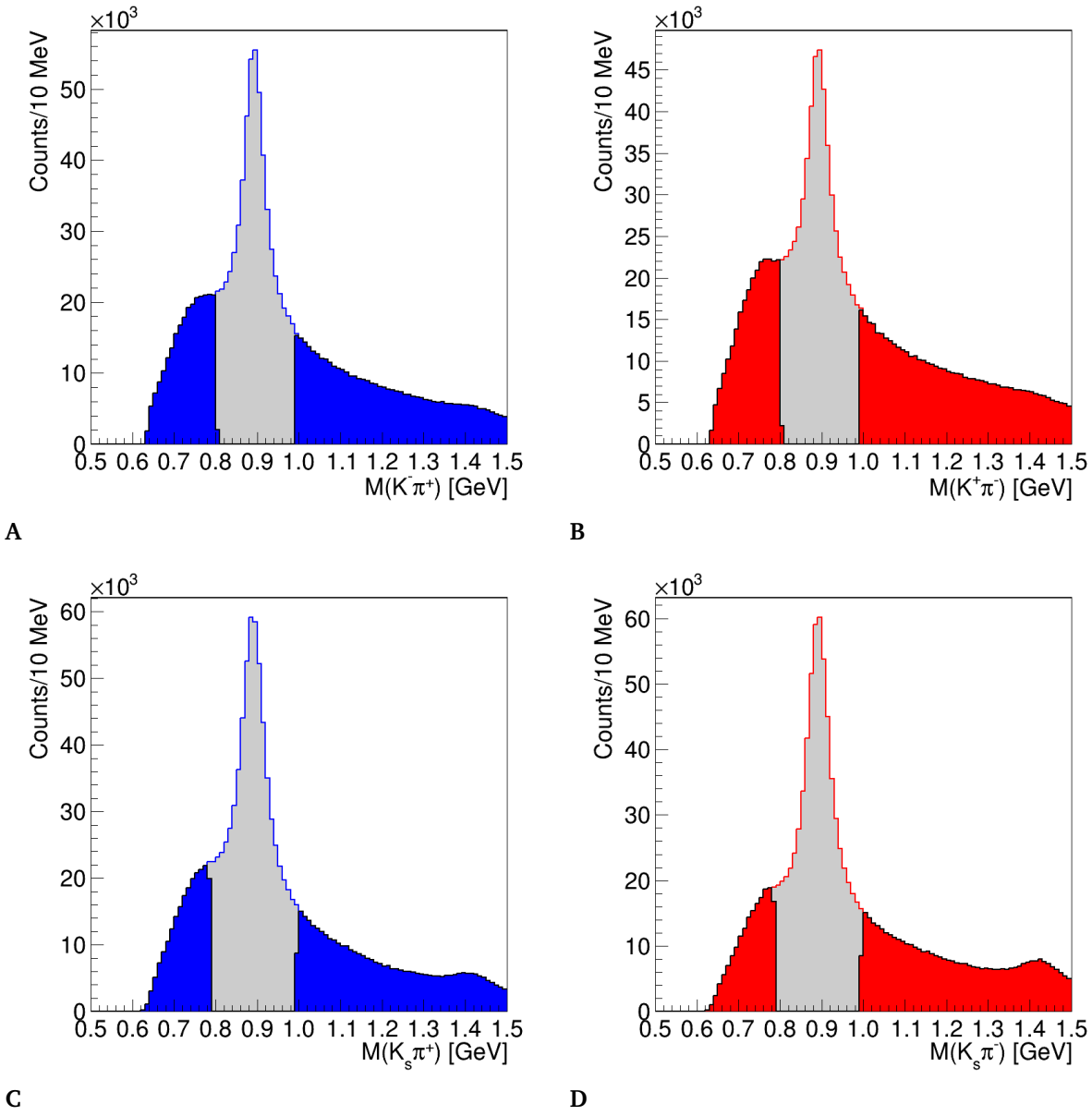

Figure 33. Distributions of $M(K^-\pi^+)$ (A), $M(K^+\pi^-)$ (B), $M(K_s\pi^+)$ (C), and $M(K_s\pi^-)$ (D). A peak corresponding to the charged and neutral K^* can be seen about 0.890 GeV. The events selected via Eqn. 49 are shaded in blue/red.

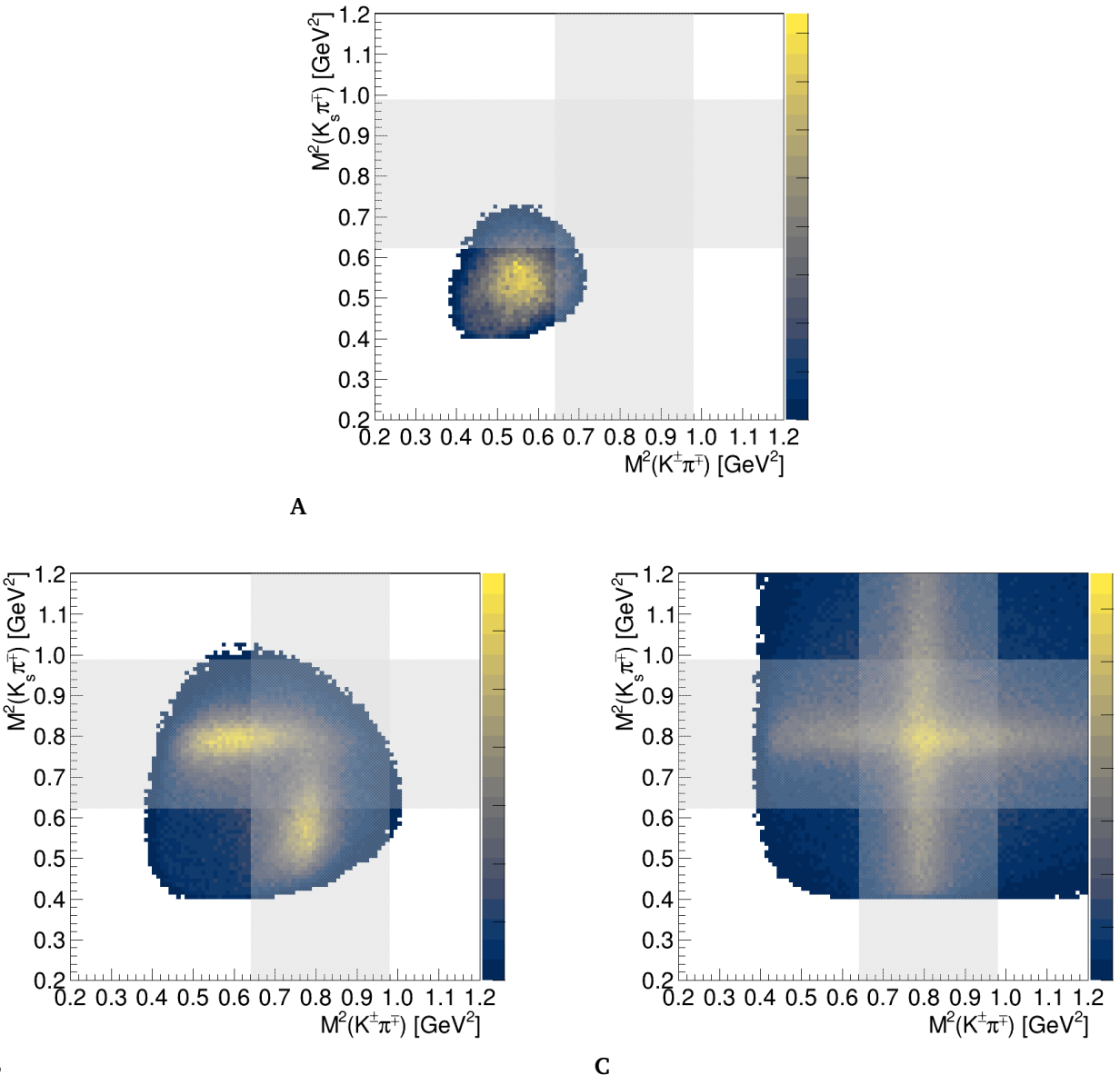

Figure 34. Dalitz plots of $K\pi$ for different regions of $M(KK\pi)$. Each figure shows $M^2(K_s\pi^+)$ vs $M^2(K^-\pi^+)$ for a different $M(KK\pi)$ mass window. The windows are $1.2 < M(K^-K_s\pi^+) < 1.34$ (A), $1.34 < M(K^+K_s\pi^-) < 1.5$ (B), and $1.5 < M(K^+K_s\pi^-)$ (C). We do not observe evidence of the K^* resonances at low $M(KK\pi)$ as there is not enough kinematic phase space for such a decay to occur. The grey boxes show the region of exclusion corresponding to Eqn. 49.

We can remove much of the resonant background by rejecting the events in the K^* mass

region of $M(K\pi)$. The nominal values for the mass and width of the K^* are $M = 891.67$ and $\Gamma = 51.4$ MeV for the charged $K^{*\pm}$ and $M = 895.55$ and $\Gamma = 47.3$ MeV for the charged K^{*0} [91]. We reject $K\pi$ events within twice the width of the K^* from the central value such that,

$$|M(K\pi) - M(K^*_{\text{pdg}})| > 2\Gamma_{K^*_{\text{pdg}}}. \tag{49}$$

The $M(K^{\mp}K_s\pi^{\pm})$ distributions before and after applying the K^* rejection criteria are shown in Figure 35. The enhancement at $M(KK\pi) = 1.28$ GeV is mostly unaffected by this cut while the higher mass enhancement and background are suppressed. These two distributions represent the final data sample of scattering events collected at GlueX that we will analyze to measure the cross-section of $f_1(1285)$. We believe we have isolated the $M(KK\pi) = 1.28$ GeV enhancement and removed most of the potential contamination from other processes with $p'K^{\mp}K_s\pi^{\pm}$ final states. A tabulated list of all the selection criteria used is given in Table 5.

Table 5. Tabulated selection criteria used to clean the GlueX dataset to measure the $f_1(1285)$ cross-section.

Cut	**Criteria**
χ^2/ndf	$\chi^2/ndf < 5$
Kinematic Fit Confidence Level	$CL_{\text{KinFit}} > 10^{-5}$
Exclusivity	$\left\|M_x^2(p'K^{\mp}K_s\pi^{\pm})\right\| < 0.01$ GeV^2
Proton Momentum	$\|\vec{p}\| > 0.4$ GeV
Pathlength Significance	Pathlength Significance > 5
K_s Mass Cut	$\|M(\pi^+\pi^-) - M(K_s)\| < 2\sigma_{K_s}$ GeV
Δ Rejection	$M(p'\pi^{\pm}) > 1.4$ GeV
Λ/Σ Rejection	$M(p'K) > 2.0$ GeV
K^* Rejection	$\left\|M(K\pi) - M(K^*_{\text{pdg}})\right\| > 2\Gamma_{K^*_{\text{pdg}}}$

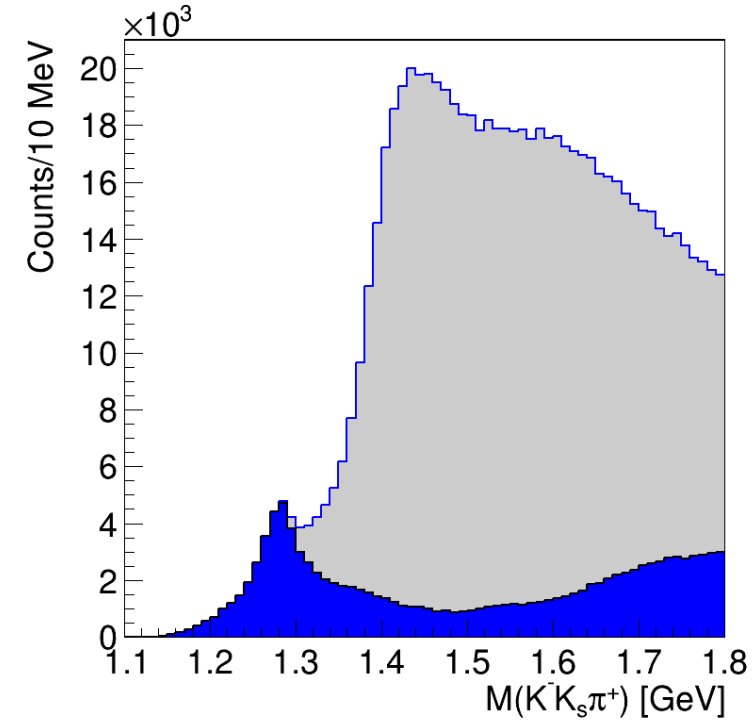

A

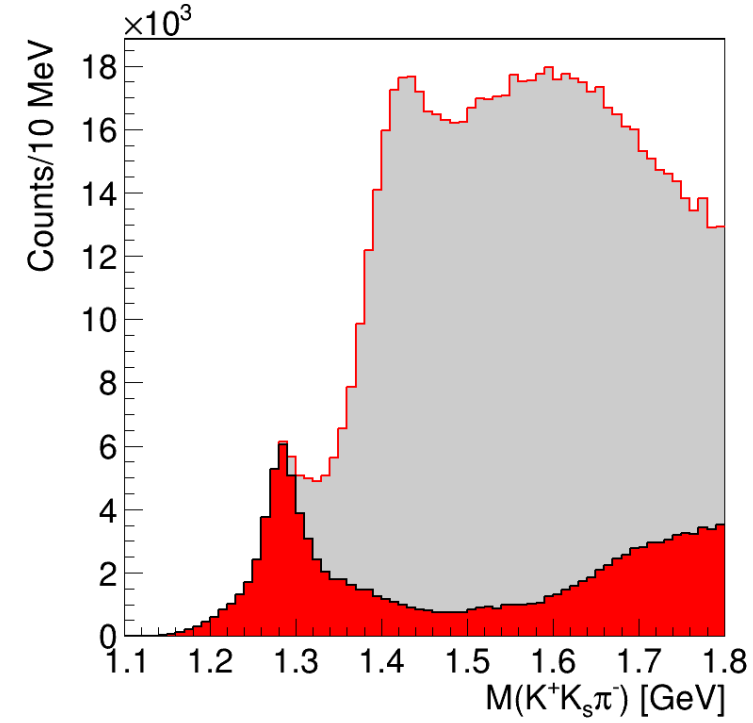

B

Figure 35. Distributions of $M(K^{-}K_{s}\pi^{+})$ (A) and $M(K^{+}K_{s}\pi^{-})$ (B) before (gray) and after (blue/red) applying the K^{*} rejection criteria. The feature at $M(KK\pi) = 1.28$ GeV is mostly unaffected while the higher mass enhancement and background are heavily suppressed.

CHAPTER 4

MONTE CARLO SIMULATION

4.1 GENERATION OF MONTE CARLO DATA

The use of simulated data is extremely important to this work. We use simulated data to evaluate detector acceptance, correct for detector efficiency, and establish reasonable selection criteria. To generate this simulated data, we use a process called Monte Carlo (MC). Monte Carlo techniques are a method of randomly sampling probability density functions (pdf). Because we know that the physics processes we are investigating are described by some pdf, we can use these Monte Carlo techniques to generate large sets of randomly sampled data that, for large enough sample sizes, model the distributions that observe in the experiment. These techniques are covered in detail in [92]. The Monte Carlo samples used in this analysis were generated with a combination of the Inverse Transform and Von Neumann methods via the gen_amp software package [93]. The back end of the generation and reconstruction process was handled via the MCWrapper GlueX software package [94].

4.1.1 $\gamma p \to p' f_1(1285)$

One of the techniques used in simulating $\gamma p \to p' f_1(1285)$ events is the inverse transform method. For a given probability density function $f(x)$ in the range of $-\infty < x < \infty$, there exists some cumulative probability function $F(a)$ that describes the probability of

$x < a$, given by,

$$F(a) = \int_{-\infty}^{a} f(x)dx. \tag{50}$$

If we choose the value of a from some random probability density $f(a)$, then $F(a)$ is also a random variable following a uniform probability density from $[0,1]$. For some randomly and uniformly generated value m, we can find a unique x chosen from the pdf $f(x)$ if,

$$m = F(x), \tag{51}$$

if we can define an inverse of F such that,

$$x = F^{-1}(m). \tag{52}$$

The advantage of this method is that it has a 100% efficiency and doesn't waste compute resources. It is useful for functions that have an easily calculable inverse, like the Breit-Wigner and exponential functions.

The first step of simulating $\gamma p \to p' f_1(1285)$ is generating or "throwing" events where the $f_1(1285)$ mass follows a Breit-Wigner distribution with the mass and width as given by the nominal PDG values [10]. We can use the inverse transform method to throw $f_1(1285)$ events that follow the prescribed Breit-Wigner. To do this, we generate a random number ρ between $-\pi$ and π and calculate s via,

$$s = M_{f_1}^2 + M_{f_1}\Gamma_{f_1}\tan(\rho), \tag{53}$$

where M_{f_1} and Γ_{f_1} are the mean and width of the Breit-Wigner given as the mass and decay width of the $f_1(1285)$. If $s > 0$, we assign the mass of the $f_1(1285)$ for the generated event to be $\sqrt{s}$.

As we are seeking to measure the differential cross-section as a function of $-t$, we must also ensure that the simulated distribution of $-t$ that we see in the region of $f_1(1285)$ in data. The $-t$ distribution can be described with an exponential function of the form,

$$f(t) = e^{-\alpha t}, \tag{54}$$

where α is the "t-slope" and t is Mandelstam-t as given by Eqn. 39. We fit a function of the form Eqn. 54 to the $-t$ distribution in our data in the mass region of $f_1(1285)$ from Eqn. 68 to determine the value of α that we will use to simulate $\gamma p \to p' f_1(1285)$ events. We again use the inverse method to throw a value of $-t$ for the event with 100% efficiency. By definition, this sets the scattering angle θ via the two-body scattering relationship,

$$t = m_a^2 + m_a^2 - 2E_a E_c + 2qq' \cos(\theta), \tag{55}$$

where a and c denote the incoming and outgoing particles in either the upper or lower vertex and m, E, and q are the mass, energy, and momentum, respectively, of the particles calculated in the Center of Mass (CM) frame [95]. As the generated value of $-t$ gives us the scattering angle θ in the CM frame, this also assigns the value of the momentum and energy to the p' and $f_1(1285)$ in the CM frame.

4.1.2 $f_1(1285) \to K^{\mp}K_s\pi^{\pm}$

The $f_1(1285) \to K^{\mp}K_s\pi^{\pm}$ 3-body decay is handled via the Von Neumann, or "accept/reject" method of Monte Carlo simulation [92]. This method is useful when the cumulative probability function $F(x)$ is unknown or too complicated to find an inverse. In short, for a given x, we can randomly generate a value for the variable of interest, lets call it P, uniformly between a minimum and maximum of the pdf $f(x)$ which describes that variable. We compare the randomly generated value to $f(x)$ for the given x. If $P > f(x)$ we reject that value. If $P < f(x)$, we accept that value.

3-body phase space decays cannot be defined in the same way as 2-body back-to-back CM decays where the system is completely determined from a randomly generated scattering angle. Instead, we must treat 2 of the 3 particles as an intermediate isobar with a randomly generated mass. The mass of the isobar is randomly generated such that,

$$(M_0 + M_1) < M_{I_{0,1}} < (M_X - M_2), \tag{56}$$

where M represents the masses of the particles in the decay $X \to 0,1,2$ and $I_{0,1}$ is the intermediate isobar comprised of the particles $0,1$. After randomly assigning a mass to the isobar between the bounds given in Eqn. 56, we proceed as if we have a 2-body decay in the rest frame of X. We assign random polar and azimuthal angles uniformly between $(-\pi,\ \pi)$ and $(0,\ 2\pi)$ respectively to the isobar. The momentum of the isobar is given by,

$$p(M, m_1, m_2) = \frac{\sqrt{N_1 N_2}}{2M}, \tag{57}$$

where,

$$N_1 = (m_1 + m_2)\left[M^2 - (m_1 + m_2)\right], \tag{58}$$

and,

$$N_2 = (m_1 - m_2)\left[M^2 - (m_1 - m_2)\right]. \tag{59}$$

The momentum of the decay particle 2 is given by $-\vec{p}(I_{0,1})$, which mean we have fully described particle 2 in the rest frame of X. For particles 0 and 1, we decay the isobar $I_{0,1}$ to particles 0 and 1 in the rest frame of $I_{0,1}$ in the exact same manner in which we treated the decay of $X \to I_{0,1} + 2$. Once we have the momentum for all 3 particles, we ensure that,

$$|\vec{p}_0||\vec{p}_{I_{0,1}}| < W, \tag{60}$$

where W is a randomly generated weight between 0 and the maximum Lorentz factor of the decay, given by,

$$M_X^2/4. \tag{61}$$

If not, we reject the event. We repeat this process of momentum generation until the event is accepted. After an event is accepted, we boost particles 0 and 1 into the rest frame of X. We then boost again into the lab frame to get the simulated event that we would see in our experiment. Functionally, this process is equivalent to defining the dalitz plot for the 3 particle system and randomly sampling it to produce the simulated data distribution. In our case, the particle X is the generated $f_1(1285)$ and particles $1,2,3$ are $K^{\mp}, K_s, \pi^{\pm}$. The generation code can be found in [96].

Figure 36 shows the generated $M(KK\pi)$ and $-t$ distributions. The $M(KK\pi)$ distribution

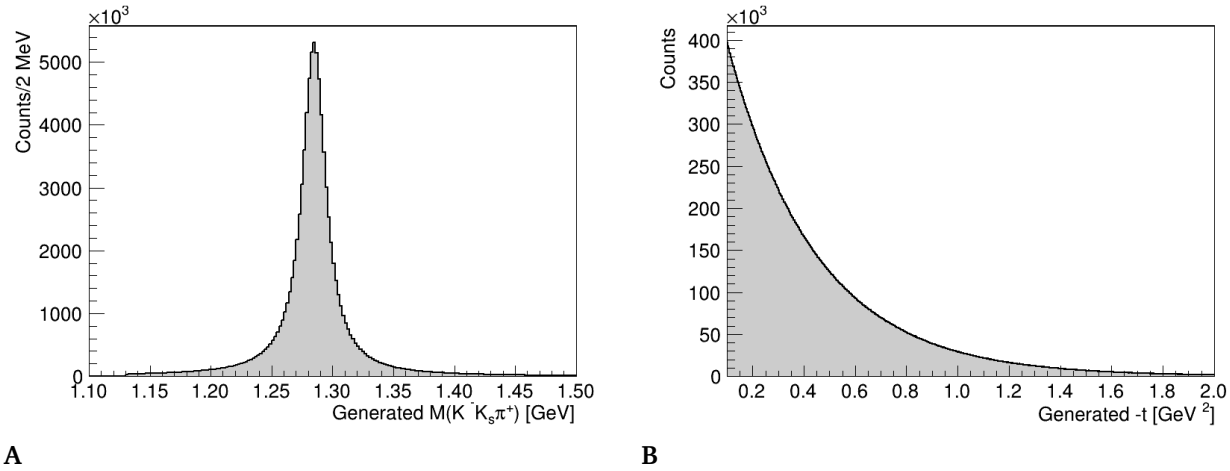

Figure 36. Thrown Monte Carlo distributions for $M(K^{-}K_s\pi^{+})$ (A) and $-t$ (B). Both distributions follow the pdf they were generated with.

follows a Breit-Wigner lineshape with the mass and width at the PDG values and the $-t$ distribution has the correct slope. Our Monte Carlo generation procedure produces distributions following the pdfs they were generated with and can be used to simulate the detector response and efficiency for $f_1(1285) \to K^{\mp}K_s\pi^{\pm}$.

4.2 RECONSTRUCTED DATA

4.2.1 Detector Simulation

Because our physics events are simulated, we must also simulate the GlueX detector to evaluate how event would interact with the detector. The detector is simulated with the `hdgeant4` software package [60], [97] using the GEANT4 library [98]–[100]. This simulation models the way the real detector subsystems interact with particles. Databases store real-time detector information, like magnetic field and detector geometry, that are passed

as inputs to the detector simulation. To ensure the outputs of the detector simulation are true-to-life, particles undergo a "smearing" that models effects such as detection efficiency and measurement resolutions. Accidental background triggers are also added to the output sample to ensure a more lifelike reconstructed sample. The smeared detector responses for each event and accidental triggers are recorded and passed along to the reconstruction process.

4.2.2 Event Reconstruction

We pass the generated events with detector responses through the reconstruction software and analysis procedure to validate that the simulated data is in good agreement with the observed data. These events are reconstructed and analyzed in the same manner as the data reconstruction and analysis process.

Figure 37 shows the $-t$, and $M(\pi^+\pi^-)$ distributions for reconstructed Monte Carlo events. We can see a broadening of the $M(\pi^+\pi^-)$ distribution, showing that there is a non-negligible momentum resolution in GlueX that must be considered. All of the selection criteria is applied except for the cut on $M(\pi^=\pi^-)$. The $-t$ distribution shows the same drop off at low values, which we expect because low-momentum protons are difficult to reconstruct in GlueX.

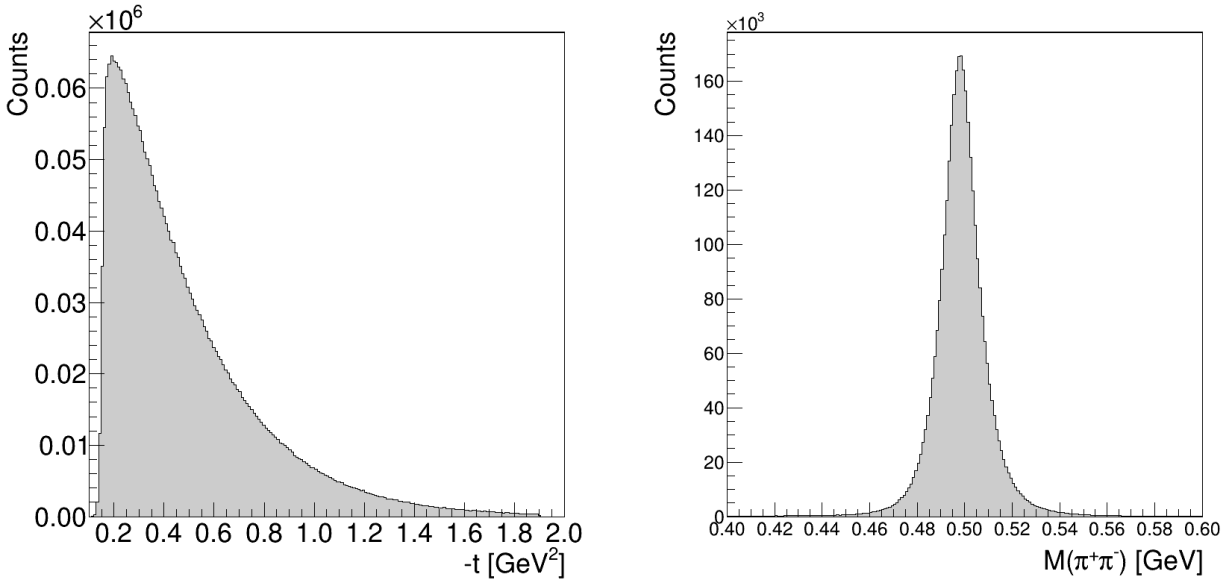

Figure 37. Reconstructed distributions of Mandelstam-t (A) and mass of the K_s via $M(\pi^+\pi^-)$ (B). All selection criteria is applied except cut on $M(\pi^+\pi^-)$. The broadening of the K_s mass points to a non-negligible detector resolution. The observed t-slope in data is well produced by the Monte Carlo.

Figures 38, 39, and 40 show kinematic distributions for the final state proton, and pion, and kaon for data and Monte Carlo. There is disagreement between the data and Monte Carlo in the momentum of the final state pion and kaon. The difference is likely due to a combination of background contamination and an isobar decay mode of the $f_1(1285) \rightarrow a_0(980)\pi$ with $a_0(980) \rightarrow KK$ (§5.6.2) that is not modeled by the Monte Carlo.

To evaluate the impact of this difference on the cross-section measurement, we investigate the reconstruction and analysis efficiency of the $f_1(1285)$ signal Monte Carlo events as a function of $\vec{p}(K^{\mp})$ and $\vec{p}(\pi^{\pm})$. Figure 41 shows that the acceptance as a function of $\vec{p}$ for the pion and kaon varies by approximately 10% over the range of good statistical precision in Monte Carlo and data. Figure 42 shows the acceptance vs $\vec{p}$ for the pion and kaon in

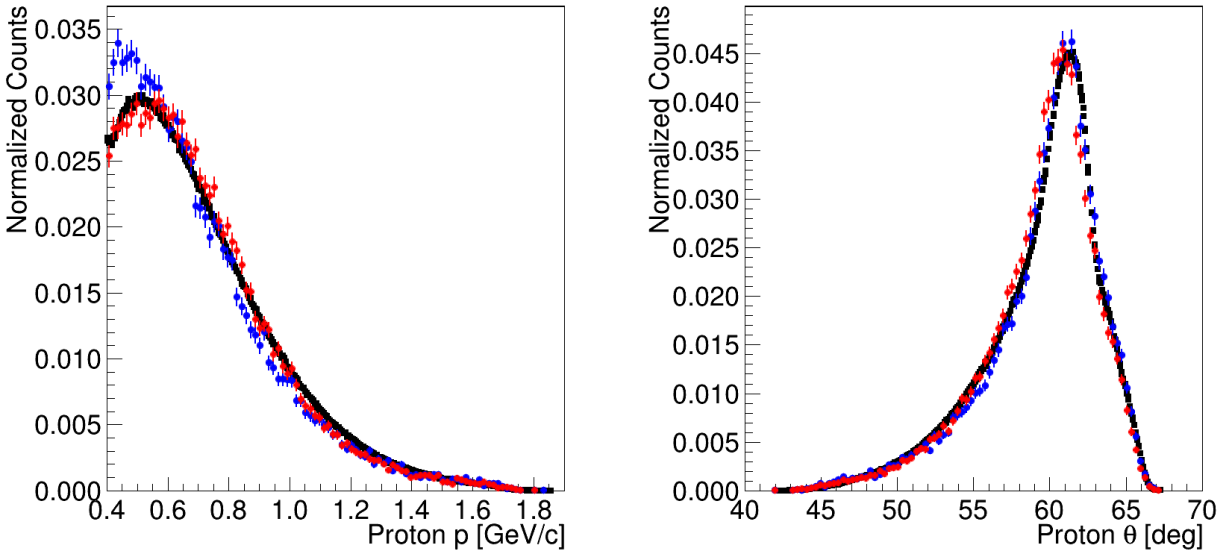

A **B**

Figure 38. Detected proton p' momentum (A) and θ (B) for $p'K^-K_s\pi^+$ (blue) and $p'K^+K_s\pi^-$ (red) in data and Monte Carlo (black). The distributions are normalized to compare the lineshapes.

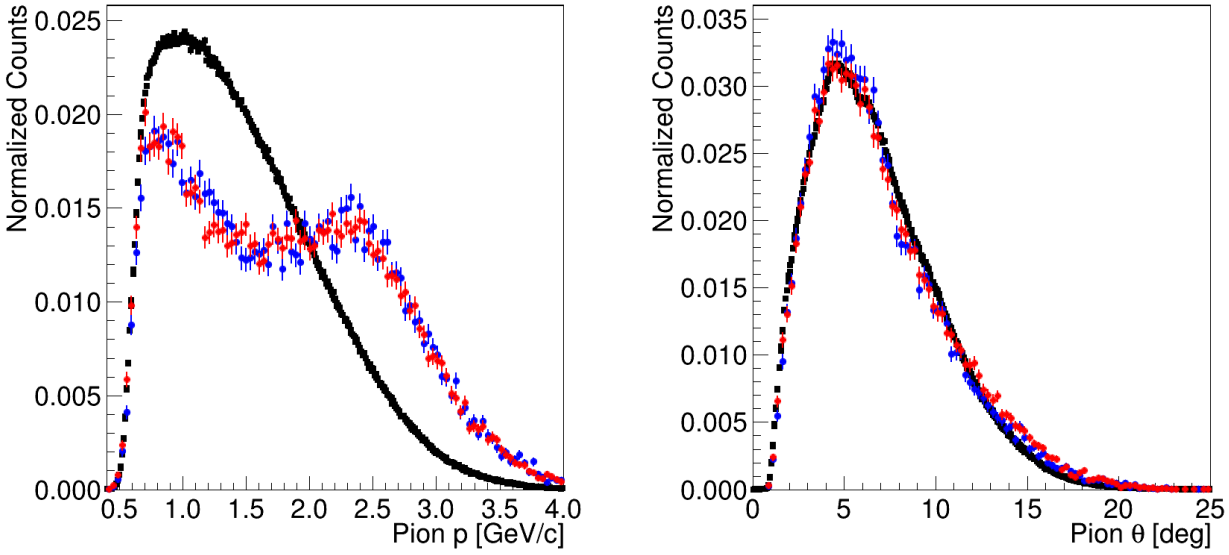

A **B**

Figure 39. Detected pion momentum (A) and θ (B) for $p'K^-K_s\pi^+$ (blue) and $p'K^+K_s\pi^-$ (red) in data and Monte Carlo (black). The distributions are normalized to compare the lineshapes. The momentum is not described well by the Monte Carlo.

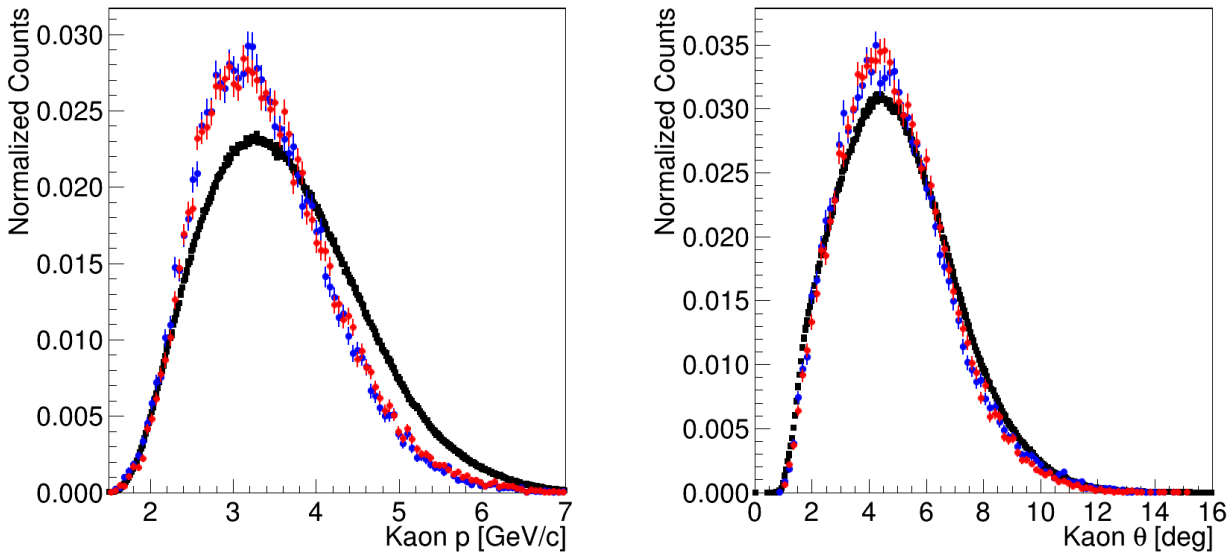

A **B**

Figure 40. Detected kaon momentum (A) and θ (B) for $p'K^-K_s\pi^+$ (blue) and $p'K^+K_s\pi^-$ (red) in data and Monte Carlo (black). The distributions are normalized to compare the lineshapes. There is slight disagreement for the momentum between data and Monte Carlo.

the $-t$ bins that the cross-section is measured in. The shape of this acceptance is stable vs $-t$, which means that the difference in the Monte Carlo and the data may lead to an overall normalization systematic error. This is discussed in further in §5.5.3. Notably, the only other measurement of the photoproduction cross-section of $f_1(1285)$ in $KK\pi$ decay also used 3-body phase space Monte Carlo [9], [45] and one of the goals of this study is to extend those results to higher beam energies. Additional discussion of the Monte Carlo model can be found in §5.6.2 and §6.7.

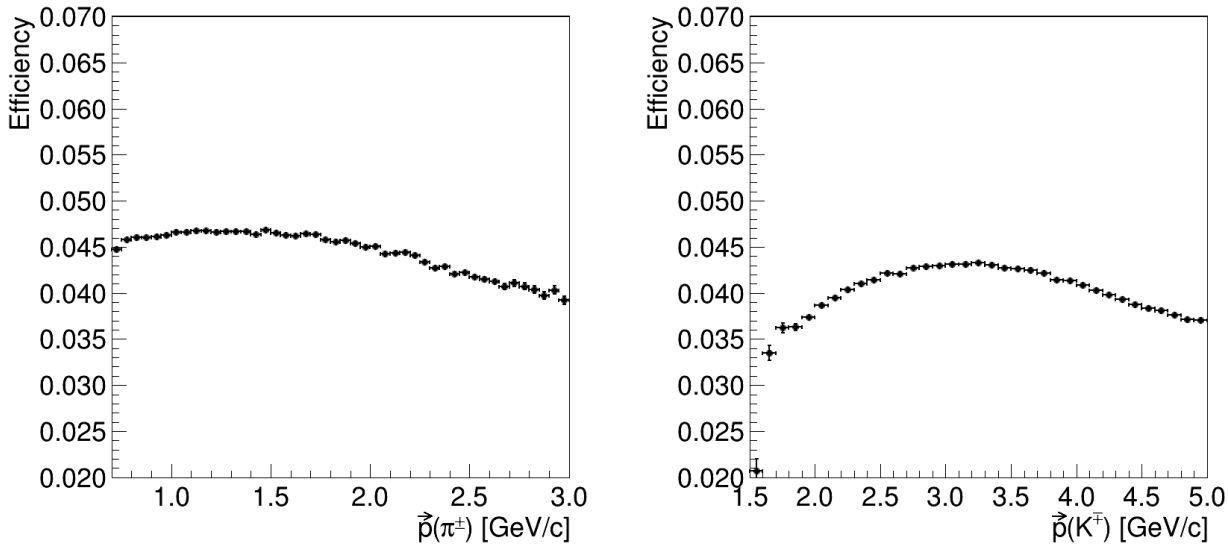

A **B**

Figure 41. Detection and analysis efficiency for $f_1(1285) \to K^{\mp}K_s\pi^{\pm}$ Monte Carlo as a function of $\vec{p}$ for the pion (A) and kaon (B). The acceptance has a moderate level of dependence on the momentum.

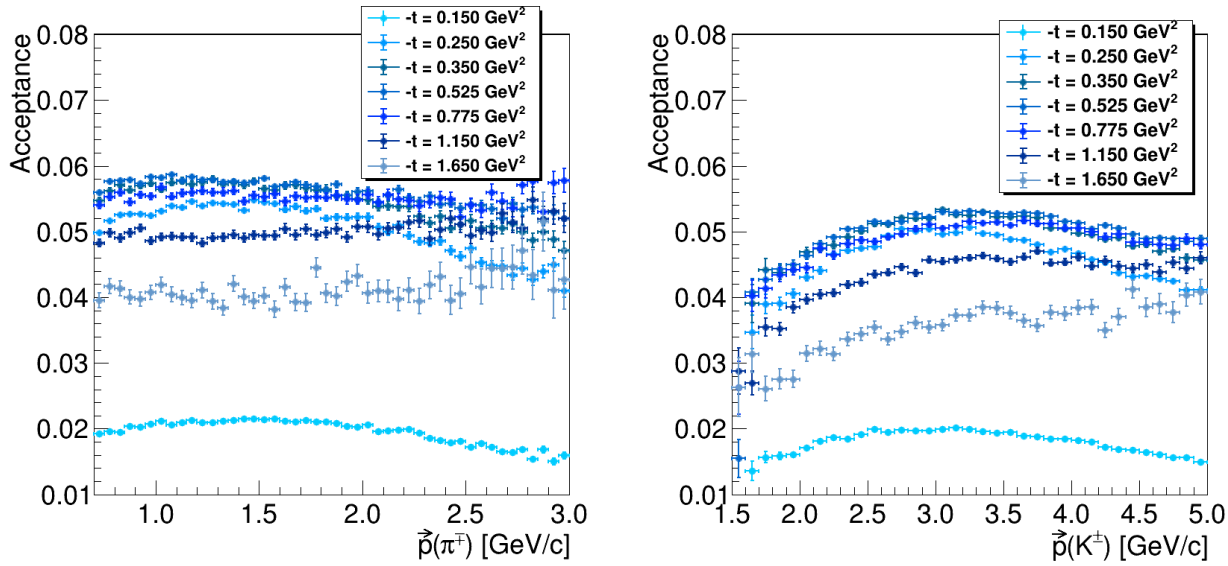

A **B**

Figure 42. Detection efficiency for bins of $-t$ as a function of $\vec{p}$ for the pion (A) and kaon (B). The shape of the acceptance is stable as a function of $-t$.

CHAPTER 5

DATA ANALYSIS

5.1 PHASE SPACE EFFICIENCY CORRECTIONS

The first thing we consider is how the K^* rejection criteria, which suppresses both the potential resonances at $M(KK\pi) = 1.4$ GeV and the phase space background, impacts the extraction of the $f_1(1285)$ yield. The rejection has a significant impact on the shape of our phase space background. This means that the standard method of describing the phase space background with a smooth polynomial when modeling the data distribution for yield extraction cannot be used. The rejection of $M(K\pi)$ events in the mass region of K^* introduces some artificial shaping to the $KK\pi$ phase space distribution. To account for this shaping, we calculate the efficiency of the K^* rejection on 3-body $KK\pi$ phase space using Monte Carlo generated data as a function of the $KK\pi$ mass and correct the $M(KK\pi)$ data distributions by this efficiency on a point-by-point basis. This allows us to account for the phase space background shaping due to the K^* rejection while still removing a majority of the resonant $M = 1.4$ GeV region events.

We select some bin size in $M(KK\pi)$ and for each mass bin between $1.0 < M(KK\pi) < 3.0$ GeV, generate 10,000 $KK\pi$ 3-body phase space events with the center-mass value being the middle of the given mass bin. The Monte Carlo sample for this correction is generated with the `ROOT.TGenPhaseSpace()` [101] method and is not run through the reconstruction and analysis procedures. We verified that the simple generated efficiency produced the same

results as the full Monte Carlo chain outlined in Chapter 4. Each generated $KK\pi$ phase space event is assigned a weight proportional to it's representation of the total phase space. We then test whether the generated event would pass or fail the K^* rejection criteria for both the neutral $K^{\pm}\pi^{\mp}$ and charged $K_s\pi^{\mp}$ combos by applying the criteria given in Eqn. 49. The efficiency is calculated by the sum of the weights of events that survived the selection criteria divided by the sum of the all the generated weights, given by,

$$\varepsilon = \frac{\sum W_{\text{passed}}}{\sum W_{\text{thrown}}}. \tag{62}$$

We correct our observed $M(KK\pi)$ distribution on a bin-by-bin basis using the calculated efficiency to produce a distribution that represents the $f_1(1285)$ and non-resonant $KK\pi$ background with a greatly suppressed contribution from the $f_1(1420)$ or $\eta(1405)$. The binned efficiency is shown in Figure 43. Figure 44 shows the $M(KK\pi)$ distributions before and after applying the charged and neutral K^* rejections and correcting the resulting distribution by the efficiency given by Eqn. 62.

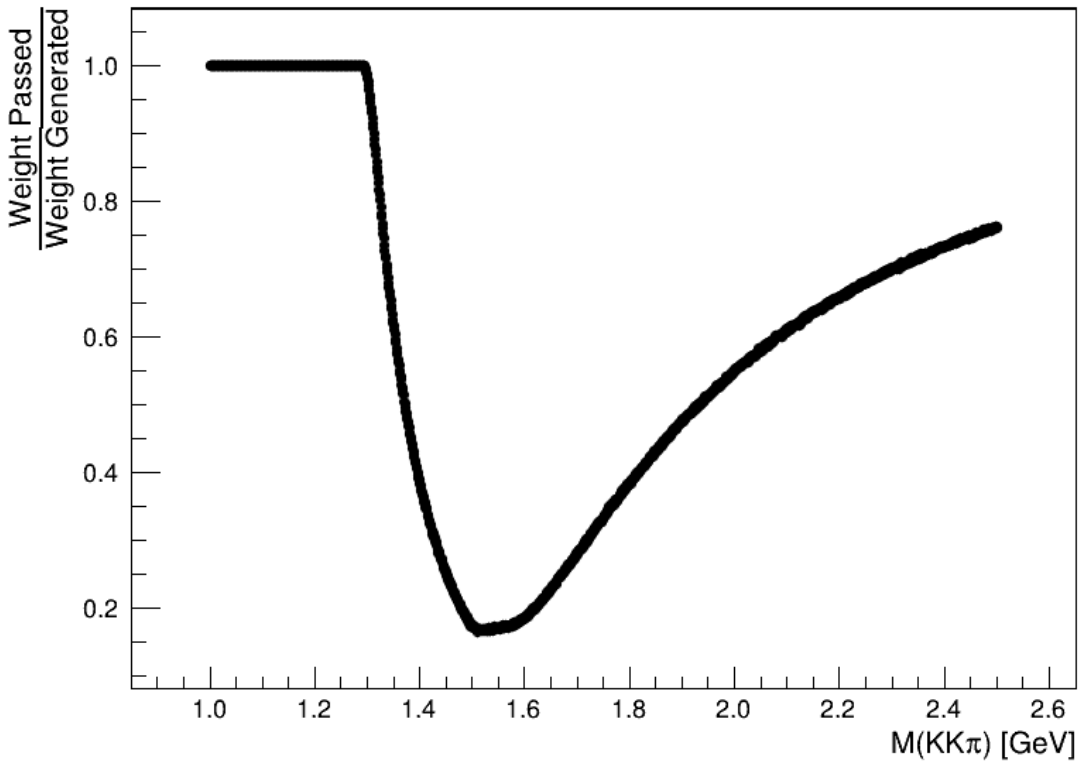

Figure 43. K^* rejection efficiency vs $M(KK\pi)$. The efficiency of the K^* rejection is given by Eqn. 62 and the Monte Carlo procedure outlined in §5.1.

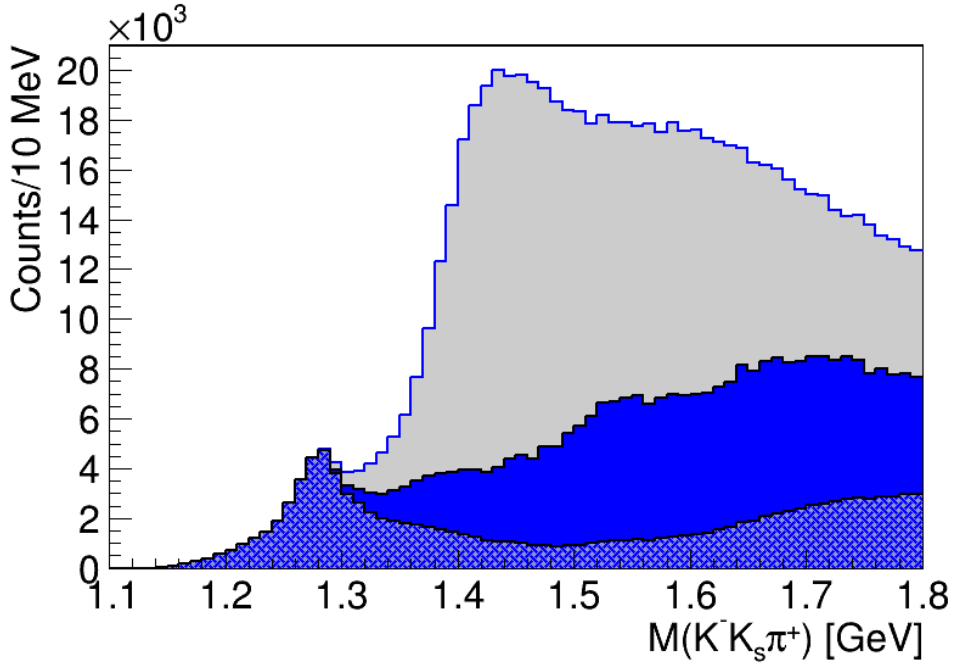

A

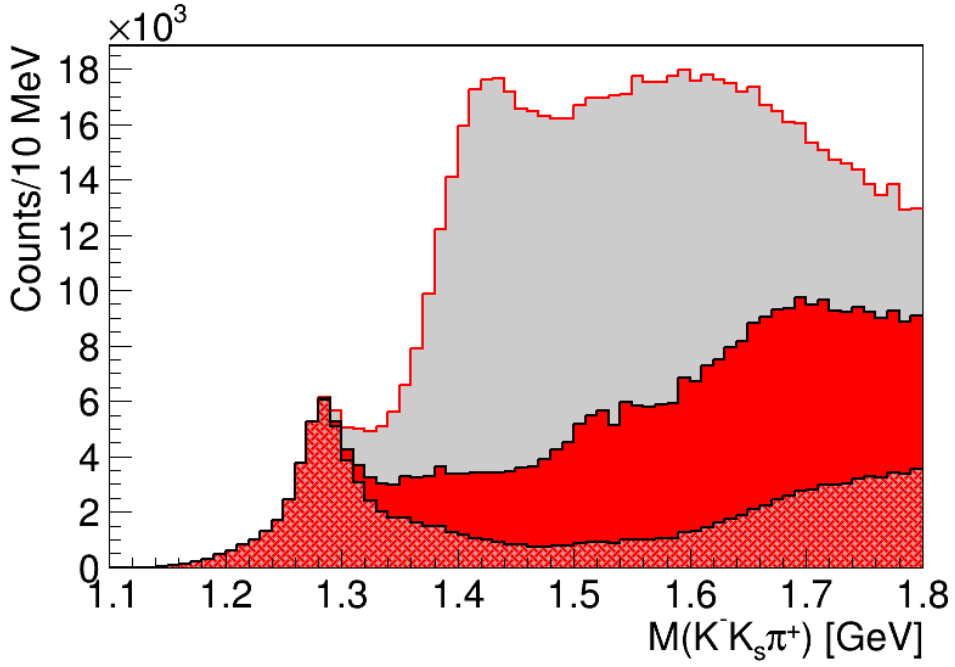

B

Figure 44. Distributions of $M(K^-K_s\pi^+)$ (A) and $M(K^+K_s\pi^-)$ (B) before the K^* rejection (gray), after applying the rejection (blue/red hatched), and correcting for the phase space efficiency (blue/red solid) shown in Figure 43. The enhancement at $M = 1.2$ GeV is mostly unaffected while the enhancement at $M = 1.4$ GeV is highly suppressed.

5.2 FITTING

5.2.1 Model Selection

The fitting procedure to extract the yield of $f_1(1285) \to KK\pi$ events is a multi-step process beginning with determination of the function to describe the enhancement corresponding to the $f_1(1285)$ at $M(K^{\mp}K_s\pi^{\pm}) = 1.28$ GeV. Short-lived, "narrow" particles like the $f_1(1285)$ can be described with a Breit-Wigner function, where the mean of the function represents the mass of the particle and the width is the inverse of the particles lifetime[102]. The Breit-Wigner distribution is given by,

$$L(E-M;\Gamma) = \frac{1}{2\pi}\frac{\Gamma}{(E-M)^2+\Gamma^2/4}, \tag{63}$$

where M is the mean of the distribution, representing the particle mass, E is the invariant mass of the $KK\pi$ system $M(K^{\mp}K_s\pi^{\pm})$, and Γ is the Breit-Wigner width, which is the particle decay width[103]. However, the GlueX detector has some non-negligible momentum resolution, which broadens the resonant particle's observed Breit-Wigner distribution. As such, we cannot use a simple Breit-Wigner to model the $f_1(1285)$ resonance feature in the $M(KK\pi)$ distribution. To account for the effect of the detector resolution, we will use a Voigt profile, which is a Breit-Wigner distribution convoluted with a Gaussian distribution [9]. The Voigt profile is given by,

$$V(M;E;\Gamma;\sigma) = \int_{\infty}^{\infty} G(M;\sigma)L(E-M;\Gamma)dE, \tag{64}$$

where G is a Gaussian as given in Eqn. 43 and L is the Breit-Wigner given by Eqn. 63. The Breit-Wigner part of the function will describe our resonance and the Gaussian will describe the detector resolution broadening effect. The mean, or mass, M and Breit-Wigner width Γ are free parameters in fits to the data.

We use our signal Monte Carlo sample, outlined in Chapter 4, to determine the $M(KK\pi)$ resolution of the GlueX detector. We have simulated 100M $\gamma p \to f_1(1285)p'$ events where $f_1 \to K^{\pm}K_s\pi^{\mp}$ for each of the three GlueX-I run periods - Spring 2017, Spring 2018, and Fall 2018. Each of these Monte Carlo samples model the $f_1(1285)$ as a Breit-Wigner with the mass and decay width set to the nominal PDG values of $M = 1.281$ GeV and $\Gamma = 22.7$ MeV. We fit a subset of these events with a Voigt function with the mass and Breit-Wigner width fixed at the generated values while allowing the Gaussian width parameter σ to float. The fit for the $f_1(1285) \to K^-K_s\pi^+$ decay Monte Carlo is shown in Figure 45. The individual Monte Carlo samples for each run period are weighted by the relative fraction of the total GlueX-I luminosity collected during that run period (Table 3) to ensure an accurate representation of the data. We then use the value of σ from the fit to the Monte Carlo data as a fixed parameter in the Voigtian component in fits to the real data. The resolution in both channels is $\sigma = 11.27$ MeV.

We must determine how to model the background events in the $M(KK\pi)$ distribution that are not due to $f_1(1285) \to K^{\mp}K_s\pi^{\pm}$ decays. This background is comprised mostly of $K^{\mp}K_s\pi^{\pm}$ phase space from arbitrary sources and higher-mass resonant $f_1/\eta \to K^{\mp}K_s\pi^{\pm}$ decays that were not removed with the K^* rejection criteria as described in §3.9. phase space backgrounds are often modeled by n-order polynomials, so we choose to model our

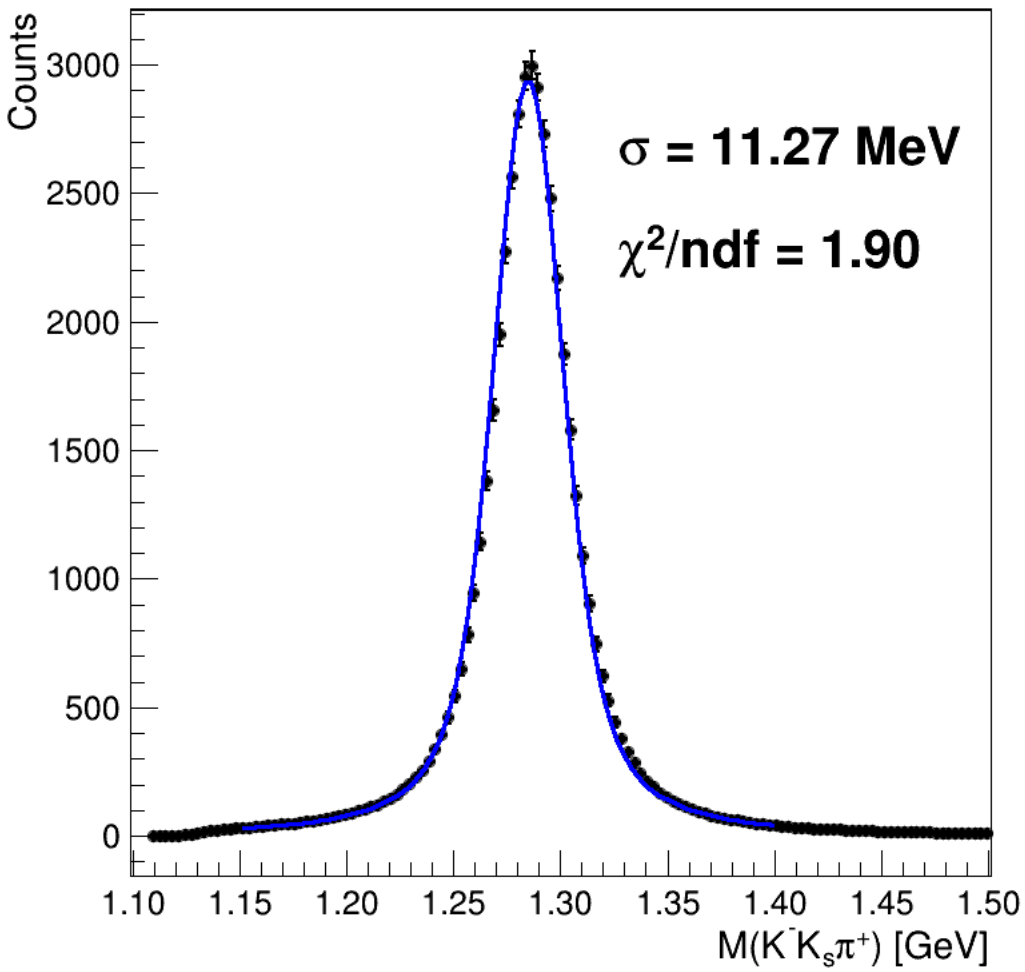

Figure 45. Resolution extraction for $f_1(1285)$ from MC. The $M(K^- K_s \pi^+)$ distribution from reconstructed $f_1(1285)$ Monte Carlo is fit with Voigt profile (blue line) where the mean and Breit-Wigner width is fixed at the generated values. The Gaussian width σ is a free parameter in the fit and is taken to be the detector resolution.

$KK\pi$ phase space with a 2nd-order polynomial of the form,

$$B(E) = c_1 E + c_2 E^2 + c_3, \tag{65}$$

where E is $M(KK\pi)$ system. We choose a 2nd-order polynomial because it is the simplest model that describes the data sufficiently well. c_1, c_2, and c_3 are all free and unconstrained parameters in the fit.

For simplicity, we use a Gaussian function to model the small enhancement we observe in the $1.35 < M(KK\pi) < 1.42$ GeV region that is likely from higher-mass f_1/η tail events that were not removed by the rejection of events in the K^* mass range as given in Eqn. 49. The mean and width of the Gaussian are both floating parameters out of necessity. In order to constrain or fix those parameters, a sufficiently accurate Monte Carlo data sample would need to be produced to model the potential f_1 and η mesons but due to the complexities of the potentially triply resonant feature and relatively sparse amount of data on said resonances, generating a suitable Monte Carlo sample goes beyond the scope of this work [20], [89], [90]. The Gaussian parameters to model this feature are constrained to broad reasonable ranges but are otherwise allowed to float in our fit.

Our final model is then,

$$f(E) = A_v V(M_{f_1}; E; \Gamma; \sigma_v) + A_g G(E - \mu_g; \sigma_g) + B(E), \tag{66}$$

where $V(M_{f_1}; E; \Gamma; \sigma_v)$ is a Voigt function given by Eqn. 64, $G(E - \mu_g; \sigma_g)$ is a Gaussian function given by Eqn. 43, $B(E)$ is a 2nd-order polynomial given by Eqn. 65, $E = M(K^{\mp} K_s \pi^{\pm})$,

M_{f_1} and Γ are the mean and Breit-Wigner width of the Voigtian representing the mass and decay width of the $f_1(1285)$, σ is the GlueX detector's $M(KK\pi)$ resolution, A_v and A_g are the amplitudes of the Voigtian and Gaussian functions, and μ_g and σ_g are the mean and width of the Gaussian modeling any leftover f_1/η resonance contamination.

5.2.2 $f_1(1285)$ Mean and Width Determination

We must determine the $f_1(1285)$ yield as a function of E_γ and $-t$ (§5.3) to calculate the cross-section. We constrain the values of the $f_1(1285)$ mass and width in order to minimize the number of free parameters in the model that we fit to our E_γ and $-t$ binned data. We measure the values of $M_{f_1(1285)}$ and Γ by fitting our model given in Eqn. 66 to the $M(KK\pi)$ distributions integrated over all E_γ and $-t$. In the fits to the binned data to extract the yield, we fix these parameters to the values obtained from the integrated fit. The fitting is done via χ^2 minimization using the MINUIT2 [104] package and the `ROOT.TH1.Fit()` method [105]. The fits to the data are shown in Figure 46. Table 6 gives the values for the mass and width extracted from the fits for both charge-conjugated final state topology, as well as the values in the PDG for the $f_1(1285)$ [10] and $\eta(1295)$[106]. The PDG values for the $f_1(1285)$ mass and width were passed as initial guesses to the model before the fit was performed. The fit range was chosen to produce reasonable χ^2/ndf values for both final state topologies. The amplitudes for the Voigtian and Gaussian components were constrained to be non-zero such that,

$$A_v, A_g > 0. \tag{67}$$

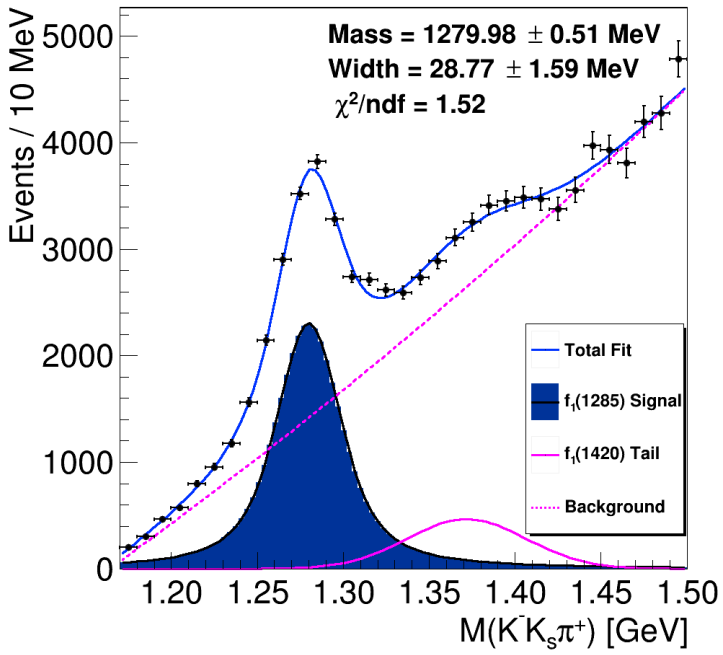

A

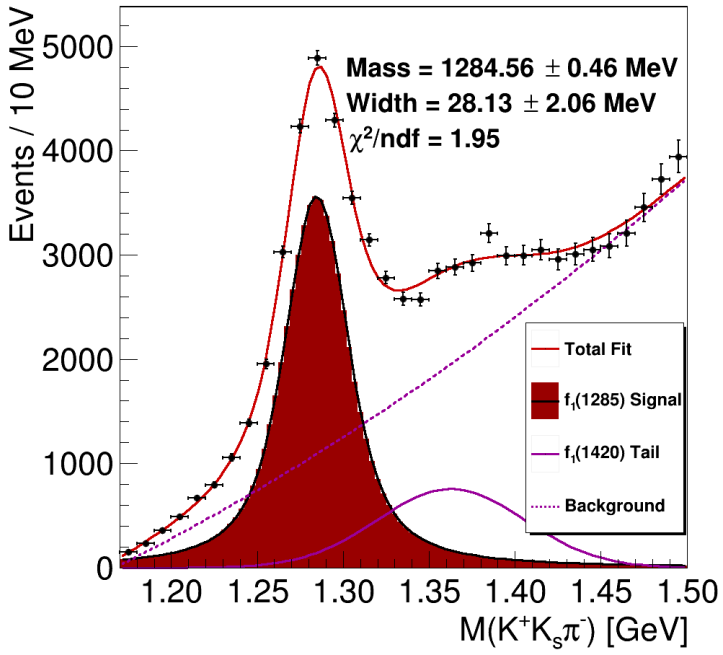

B

Figure 46. $M(K^-K_s\pi^+)$ (A) and $M(K^+K_s\pi^-)$ (B) distributions with total model (blue/red line) fit to the data. Voigt (solid blue/red fill) and background Gaussian and polynomial functions (magenta) are shown. Mass, width, and fit quality is also shown on the figure.

The mass value obtained from the fits to both the $K^-K_s\pi^+$ and $K^+K_s\pi^-$ data are in agreement with the nominal values from the PDG [10]. Additionally, they are not consistent with the PDG values for $\eta(1295)$ by several standard deviations. The measured width of $\approx 28.5 \pm 2$ MeV is $\simeq 2$ standard deviations wider than the world data, but is well within the range of measurements used for the average [10]. Our mass and width are in agreement with the values of the $f_1(1285)$ and disagree with the values of $\eta(1295)$. We can define the mass region of $f_1(1285)$ to be,

$$|M(K^{\mp}K_s\pi^{\pm}) - M_{f_1}| < 2\Gamma_{f_1}, \tag{68}$$

where M_{f_1} and Γ_{f_1} are the measured mass and width of $f_1(1285)$ from fits to the integrated $M(KK\pi)$ distribution. The values for the Gaussian and mean and width are given in Table 7. The mass and width parameters are fixed in the fits to the binned data when extracting the $f_1(1285)$ yield with the goal of reducing the degrees of freedom for the more-sparse data distributions.

Table 6. Voigt profile parameters from fits to the $M(K^-K_s\pi^+)$ and $M(K^+K_s\pi^-)$ distributions. Currently accepted mass and width values from the PDG for $f_1(1285)$ and $\eta(1295)$ and shown for comparison [10], [106]. The mass and width parameters extracted from the fit are in agreement with the $f_1(1285)$ but not $\eta(1295)$. Uncertainties are statistical only.

	Mass [MeV]	**Width [MeV]**	χ^2/ndf
$K^-K_s\pi^+$	1279.98 ± 0.50	28.77 ± 1.59	1.52
$K^+K_s\pi^-$	1284.56 ± 0.40	28.13 ± 1.25	1.95
PDG $f_1(1285)$	1282 ± 0.50	22.7 ± 1.1	-
PDG $\eta(1295)$	1294 ± 4.00	55.0 ± 5.0	-

Table 7. Gaussian parameters from fit to integrated $M(KK\pi)$ distributions for both $\pi^+K^-K_s$ and $\pi^-K^+K_s$ decay modes. Uncertainties are statistical only.

Channel	Gaussian Mean [MeV]	Gaussian Width [MeV]
$K^-K_s\pi^+$	1371.80 ± 4.05	34.56 ± 4.62
$K^+K_s\pi^-$	1362.60 ± 4.15	42.85 ± 3.93

Having determined the mean and width for the Voigtian and Gaussian components of the model, we now extract the yields of $f_1(1285)$ in bins of E_γ and $-t$ and calculate the cross-section $\frac{d\sigma}{dt}$.

5.3 CROSS SECTION

The differential cross-section of $f_1(1285)$ as measured in either final state $f_1(1285) \to K^-K_s\pi^+$ or $f_1(1285) \to K^+K_s\pi^-$ can be calculated as,

$$\frac{d\sigma}{dt}(E_\gamma;-t) = \frac{Y(E_\gamma;-t)\times I}{\Delta t \times \mathscr{A}(E;-t)\times BR\times \mathscr{L}}, \tag{69}$$

where $Y(E;-t)$ is the $f_1(1285)$ yield in a given E and $-t$ bin, I is the isospin normalization of $KK\pi$ states, Δt is the size of the bin in $-t$, $\mathscr{A}(E;-t)$ is the reconstruction efficiency or acceptance of $f_1(1285)$ for that bin, BR is the branching ratio of $f_1(1285) \to KK\pi$, and $\mathscr{L}$ is the integrated luminosity for a given E_γ bin.

5.3.1 Yield

Binned Fits

To measure the yield of $f_1(1285)$ events as a function of E_γ and $-t$, we first bin our data in beam energy, E_γ, and Mandelstam-t. The beam energy bins will be 1 GeV wide bins spanning,

$$7.5 < E_\gamma < 11.5 \text{ GeV}, \tag{70}$$

and they will be referred to by the energy of middle of the bin, corresponding to integers 7, 8, 9, and 10 GeV. The bin width in Mandelstam-t, Δt, varies over the range of measurement due to statistical constraints at higher $-t$ values. Evenly spaced bins do not allow for a sufficient number of events in higher $-t$ bins to make the measurement. The bin size was chosen such that a fit can converge to extract a yield in each bin of $-t$. The bin centers and widths can be found in Table 8. They will also be referred to by bin center value.

Table 8. $-t$ bin centers and widths. Bins were chosen to allow for measurement of cross-section to be calculated at the highest possible values of $-t$ given statistical constraints.

Bin Middle [GeV^2]	Bin Width [GeV^2]
0.150	0.10
0.250	0.10
0.350	0.10
0.525	0.25
0.775	0.25
1.150	0.50
1.650	0.50

We fit our model given in Eqn. 66 to the $M(KK\pi)$ distributions that fall into the given E_γ and $-t$ bins using the `ROOT.TH1.Fit()` method. Due to statistical constraints at higher $-t$ values, we reduce the number of free parameters by fixing the mean and width of the Voigtian and Gaussian components to the values obtained from the fits to the integrated data given in Tables 6, 7. The free parameters in the fit are the amplitudes of the Voigtian and Gaussian components A_v and A_g and background parameters c_i. The fit range is extended to higher $M(KK\pi)$ values because the statistical precision is not good enough in the binned distributions to accurately describe the shape of the phase space background over a smaller fitting range. Selected examples of these fits are shown in Figure 47 and the rest can be found in Appendix B in Figures 84-91. The yields are calculated by numerically integrating the Voigtian component of the model from $1.16 < M(KK\pi) < 1.5$ GeV. The `ROOT.TF1.Integral()` method uses the Adaptive Singular algorithm for the numerical integration, the specifics of which can be read about in Ref.[107]. The binned $f_1(1285)$ yields are given in Tables 9, 10.

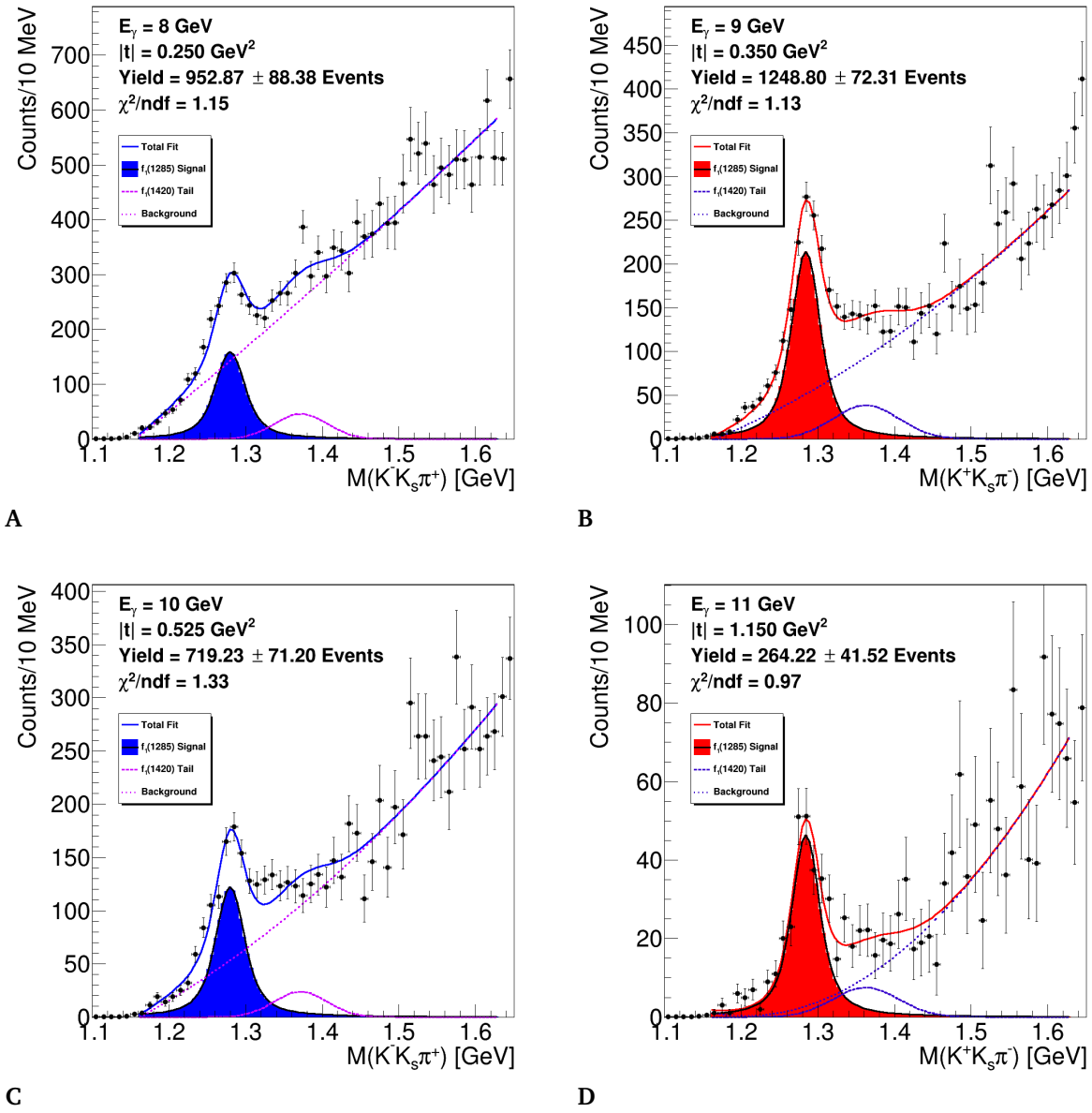

Figure 47. Fits to $M(KK\pi)$ distributions in selected bins of E_γ and $-t$. $M(K^-K_s\pi^+)$ (A, C) and $M(K^+K_s\pi^-)$ (B, D) distributions with full model (solid blue/red line), Voigt component (filled blue/red distributions), and background (dashed magenta line) shown. The bin information, $f_1(1285)$ yields, and fit quality χ^2/ndf are displayed on the figures.

Table 9. Yield, uncertainty, and fit quality for $f_1(1285) \to K^- K_s \pi^+$ decay mode for each E_γ and $-t$ bin

E_γ	-t	Yield	Yield Uncertainty	χ^2/ndf
8	0.150	503	76	1.68
8	0.250	953	88	1.15
8	0.350	869	79	1.86
8	0.525	1467	93	1.25
8	0.775	845	64	1.28
8	1.150	748	68	1.21
8	1.650	167	34	0.90
9	0.150	392	61	0.99
9	0.250	733	82	1.50
9	0.350	573	72	0.87
9	0.525	1272	84	0.96
9	0.775	764	64	1.20
9	1.150	431	57	1.03
9	1.650	138	30	0.74
10	0.150	209	58	1.01
10	0.250	505	63	0.79
10	0.350	396	68	1.48
10	0.525	719	71	1.33
10	0.775	429	56	0.93
10	1.150	260	55	1.39
10	1.650	68	28	0.72
11	0.150	166	46	1.15
11	0.250	260	55	1.38
11	0.350	248	50	1.34
11	0.525	529	61	0.76
11	0.775	302	48	1.02
11	1.150	217	43	1.62
11	1.650	56	23	0.62

Table 10. Yield, uncertainty, and fit quality for $f_1(1285) \to K^+K_s\pi^-$ decay mode for each E_γ and $-t$ bin.

E_γ	-t	Yield	Yield Uncertainty	χ^2/ndf
8	0.150	664	64	0.81
8	0.250	1483	78	1.01
8	0.350	1488	75	1.06
8	0.525	2768	96	2.09
8	0.775	1218	67	0.77
8	1.150	747	58	1.29
8	1.650	142	30	0.83
9	0.150	511	56	1.29
9	0.250	1144	76	1.30
9	0.350	1249	72	1.13
9	0.525	2186	85	1.01
9	0.775	1024	66	1.03
9	1.150	572	66	1.74
9	1.650	126	29	0.71
10	0.150	257	44	1.17
10	0.250	586	56	1.19
10	0.350	577	63	1.49
10	0.525	1219	69	1.10
10	0.775	509	54	0.68
10	1.150	310	46	0.71
10	1.650	62	27	0.88
11	0.150	175	41	1.41
11	0.250	452	55	1.76
11	0.350	511	53	1.29
11	0.525	892	60	0.74
11	0.775	451	52	1.11
11	1.150	264	42	0.97
11	1.650	37	19	0.73

Statistical Uncertainty

The fits to the binned data are quite good by both the "eye test" and χ^2/ndf values. However, as the initial statistical error from the fit is obtained simply via the the relative error on the amplitude of the Voigtian term, a correctness check is performed using a

bootstrapping process. For each bin of E_γ and $-t$, corresponding to a histogram with an $M(KK\pi)$ distribution, we generate 10,000 new pseudo-data histograms. The value for each bin of $M(KK\pi)$ in these histograms is randomly generated based on a normal distribution with a mean of the event count in the bin of the nominal histogram and a standard deviation of the uncertainty on the count in bin. We fit these pseudo-data histograms with our model and the amplitudes of the Voigtian component are recorded. The mean of the individual amplitudes of the sample μ_A is calculated as [108],

$$\mu_A = \frac{1}{n}\sum_i^n A_i, \tag{71}$$

where A_i are the individual amplitudes and n is the number of pseudo-data histograms. The unbiased estimator for the variance of the amplitudes $\bar{\sigma_A}^2$ is given by [108],

$$\bar{\sigma_A}^2 = \frac{1}{n-1}\sum_i^n (A_i - \mu_A)^2, \tag{72}$$

The standard deviation σ_A from the bootstrapping procedure for each E_γ and $-t$ bin is compared to the corresponding value obtained from MINUIT2. Figure 48 shows the ratio of the bootstrapped standard deviation to the MINUIT2 uncertainty. The bootstrapped standard deviations are between $1.2-2.4\times$ larger than the uncertainties obtained from MINUIT2, suggesting that the MINUIT2 uncertainty is likely underestimated. We denote the standard deviation obtained from the bootstrapping procedure to be our statistical uncertainty of the fit amplitude. Sample distributions of the bootstrapped amplitudes can be found in Figure 49, and the rest can be found in Appendix B in Figures 92-97. These figures show

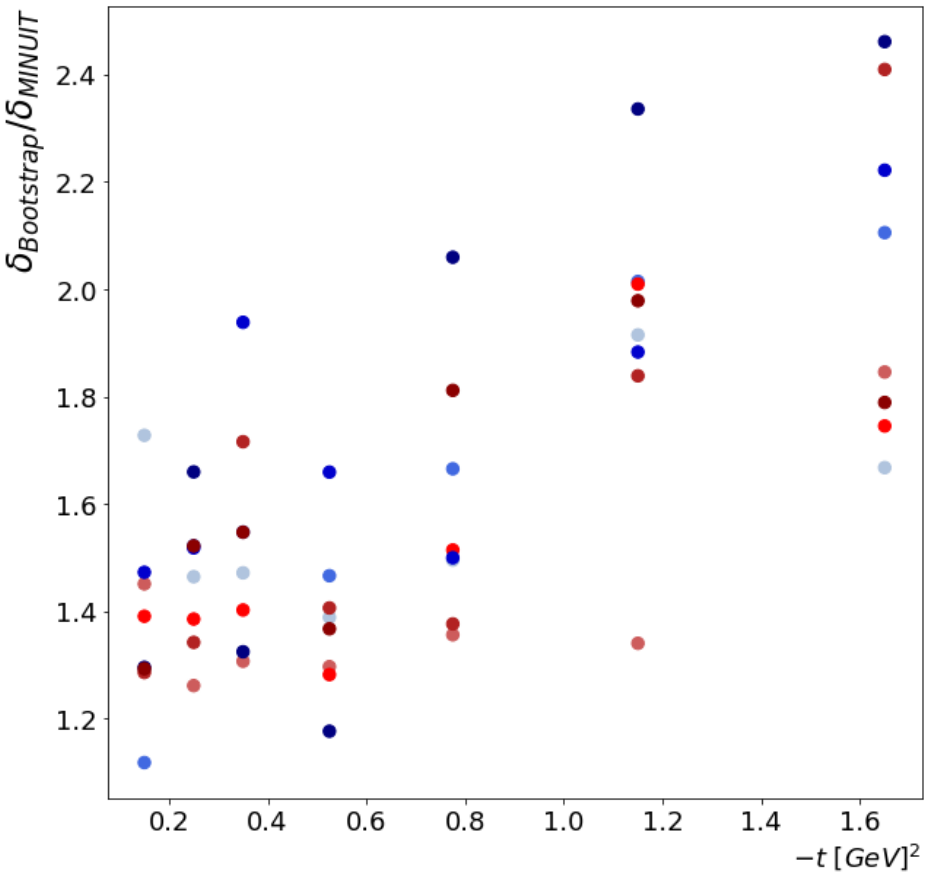

Figure 48. Ratio of the standard deviation obtained from the bootstrapping procedure to the uncertainty given by MINUIT. The different shades correspond to different beam energies. The shades of blue are for the $K^-K_s\pi^+$ final state and shades of red are for the $K^+K_s\pi^-$ final state. The bootstrapping procedure gives relative uncertainties 1.2-2.4 times larger than MINUIT.

that the amplitudes follow a normal distribution as expected, so the variance estimator provides a reasonable value for the statistical uncertainty of our obtained $f_1(1285)$ yield.

As such, the statistical uncertainty on our cross section measurement for each E_γ and t bin is the calculated cross-section value multiplied by the relative uncertainty on the bootstrapped amplitudes,

$$\delta = \left(\frac{d\sigma}{dt}\right)\frac{\bar{\sigma}_A}{\mu_A}. \tag{73}$$

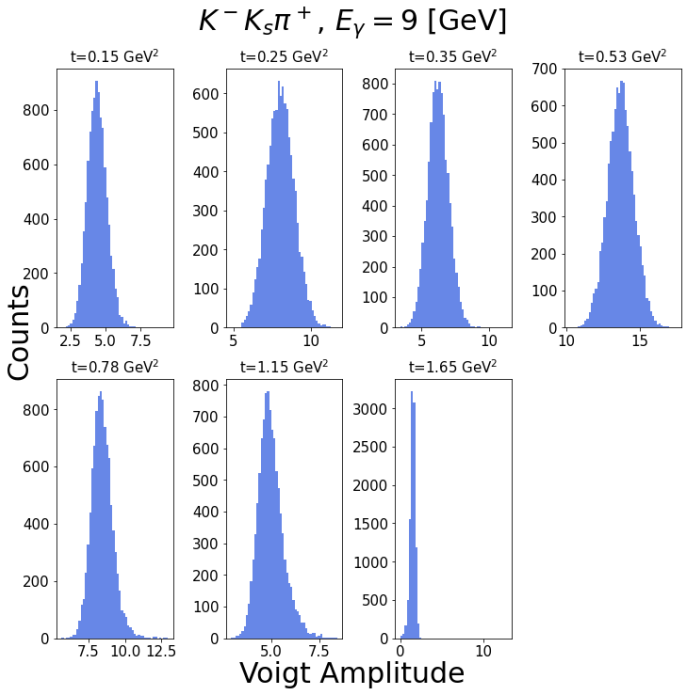

A

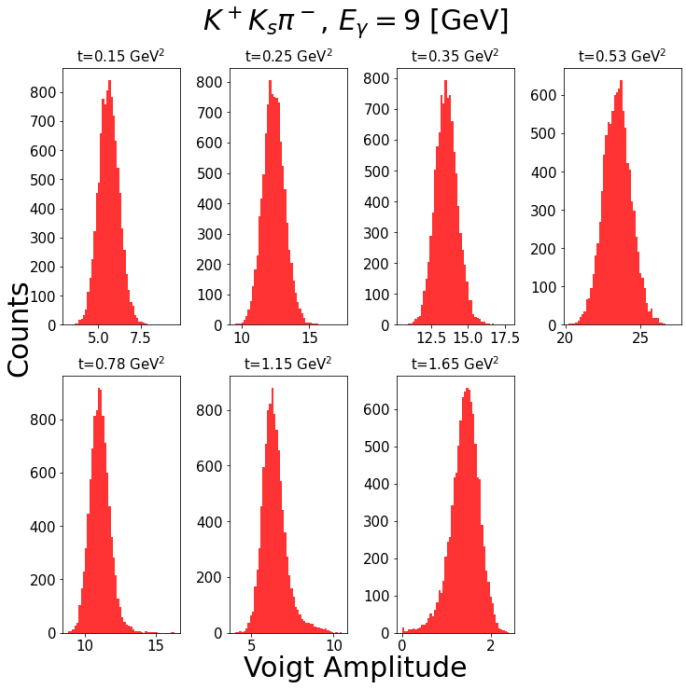

B

Figure 49. Distributions of the Voigt profile amplitudes obtained via the bootstrapping procedure as a function of $-t$ for $K^- K_s \pi^+$ (A) and $K^+ K_s \pi^-$ (B) at $E_\gamma = 9$ GeV. The amplitudes follow a normal distribution and the uncertainty is assigned to be the standard deviation as calculated via the variance estimator given by Eqn. 72.

The statistical uncertainties on the cross-section can be found in Tables 9, 10.

5.3.2 Normalization

Efficiency/Acceptance $\mathscr{A}$

Our final data sample will not include every $f_1(1285)$ event produced by the GlueX experiment. Most of our events will be undetected and more still will be removed by our selection criteria. To account for this, we calculate the fraction of $f_1(1285)$ Monte Carlo events that survive the reconstruction and analysis process relative to how many were generated (Chapter 4). For each bin of E_γ and $-t$ the number of events that are reconstructed and survive the event selection are divided by the number of events thrown and tagged such that,

$$\mathscr{A} = N(\text{Reconstructed})/N(\text{Generated}). \tag{74}$$

This number is our efficiency (or acceptance) for $f_1(1285) \to K^{\mp}K_s\pi^{\pm}$. The values of the binned acceptance are given in Table 11.

Table 11. $f_1(1285) \to K^{\mp}K_s\pi^{\pm}$ acceptance from signal Monte Carlo for the $\pi^+K^-K_s$ and $\pi^-K^+K_s$ decay modes for all bins of E_γ and $-t$.

E_γ [**GeV**]	$-t$ [**GeV**^{2}]	$\mathscr{A}$ $(K^-K_s\pi^+)$	$\mathscr{A}$ $(K^+K_s\pi^-)$
8	0.15	0.0157	0.0159
8	0.25	0.0398	0.0404
8	0.35	0.0416	0.0424
8	0.53	0.0408	0.0417
8	0.78	0.0378	0.0386
8	1.15	0.0321	0.0331
8	1.65	0.0245	0.0248
9	0.15	0.0164	0.0166
9	0.25	0.0420	0.0427
9	0.35	0.0449	0.0455
9	0.53	0.0446	0.0454
9	0.78	0.0421	0.0430
9	1.15	0.0366	0.0377
9	1.65	0.0287	0.0295
10	0.15	0.0167	0.0170
10	0.25	0.0435	0.0440
10	0.35	0.0472	0.0477
10	0.53	0.0481	0.0492
10	0.78	0.0470	0.0478
10	1.15	0.0427	0.0434
10	1.65	0.0351	0.0358
11	0.15	0.0160	0.0163
11	0.25	0.0421	0.0425
11	0.35	0.0462	0.0470
11	0.53	0.0490	0.0496
11	0.78	0.0489	0.0497
11	1.15	0.0456	0.0464
11	1.65	0.0393	0.0403

Isospin

We are evaluating the cross-section in $f_1(1285) \to KK\pi$, not just $f_1(1285) \to K^-K_s\pi^+$ or $f_1(1285) \to K^+K_s\pi^-$, so we need to account for the isospin of the $KK\pi$ decay to various

particle combos. The total $KK\pi$ isospin wave function is given by [109],

$$\frac{1}{\sqrt{6}}\left(\sqrt{2}K^{-}K^{0}\pi^{+}-\sqrt{2}K^{+}K^{0}\pi^{-}-K^{+}K^{-}\pi^{0}+K^{0}\bar{K}^{0}\pi^{0}\right). \tag{75}$$

Each of the $K^{\mp}K^{0}\pi^{\pm}$ decays represent $1/3$ of the total $I=0$ $f_1(1285)\to KK\pi$ decay. Because we require the detection of all of our final state particles, the $K^{\mp}K_L\pi^{\pm}$ final state is excluded from our analysis. Therefore, each of the final states we measure are 1/6th of the total $KK\pi$ decay and we multiply the measured differential cross-section by 6 to normalize for the $KK\pi$ decay modes.

Branching Ratio

The branching ratio *BR* (branching fraction) is the fractional probability for a particle to decay to a given final state. The PDG gives the branching ratio of $f_1(1285)\to KK\pi$ decay to be $9.1\pm0.4\%$ [10]. The $f_1(1285)$ decays to $KK\pi$ primarily through the intermediate state of $f_1(1285)\to a_0(980)\pi$ where $a_0(980)\to K\bar{K}$ but that $f_1(1285)$ branching fraction has not been measured. Indeed, the branching ratio of $a_0(980)\to K\bar{K}$ has not been well measured either [40], [110]. For these reasons, this cross-section measurement is focused on the $KK\pi$ final state, disregarding intermediate isobars.

Table 12. Tagged GlueX-I luminosity for each E_γ bin the cross-section is measured in.

Beam Energy [GeV]	**Tagged Luminosity [pb^{-1}]**
7	42.73
8	141.07
9	112.30
10	70.81
11	60.14

Integrated Luminosity

The integrated luminosity is defined to be the number of beam particles incident on the GlueX target per unit area. The luminosity can be defined as,

$$\mathscr{L}_t = \Phi \rho_{\mathrm{T}} l_{\mathrm{T}}, \tag{76}$$

where $\Phi = N_\gamma/\text{second}$, ρ_{T} is the target density, and l_{T} is the target length [111]. The integrated luminosity is then,

$$\mathscr{L} = \int \mathscr{L}_t dt = \int \frac{N_\gamma \rho_{\mathrm{T}}, l_{\mathrm{T}}}{t} dt \tag{77}$$

The full GlueX-I tagged luminosity for each of the energy ranges of this analysis is provided in Table 12. The GlueX luminosity can be calculated for any beam energy range E_γ with the use of the script in [112].

5.3.3 Measured Cross Section

The result of our cross-section measurement as obtained from the outlined methodol-

ogy is shown Figure 50. The values of the cross-section and statistical error are given in Table 13. Further discussion of the cross-section is in §6.2. There is a clear difference in the $f_1(1285)$ cross-section depending on the $K^{\mp}K_s\pi^{\pm}$ final state it was measured in. This is studied further in §5.4 and discussed in §6.5.

5.4 CROSS-SECTION ASYMMETRY

Figure 50 shows that we obtain different values for cross-section of $f_1(1285)$ depending on the final state topology we measure it in. The $f_1(1285) \to K^+K_s\pi^-$ measurement gives us a consistently larger value of $\frac{d\sigma}{dt}$ compared to the $f_1(1285) \to K^-K_s\pi^+$ measurement. Notably, the asymmetry between the two is not constant and appears to change as a function of $-t$. This was an unexpected result, as we expect there to be no physical difference between the two charge conjugated decay modes. We performed several studies to validate this behavior being a real effect rather than an analysis mistake.

The following were considered to be likely sources of systemically different values of the $f_1(1285)$ cross-section and each was investigated to determine if it could explain the asymmetry between the measurements in the change conjugated $f_1(1285) \to K^{\mp}K_s\pi^{\pm}$ decay modes.

- Reconstruction/acceptance asymmetry or bug
- Asymmetric impact of kinematic cuts
- Baryonic contamination

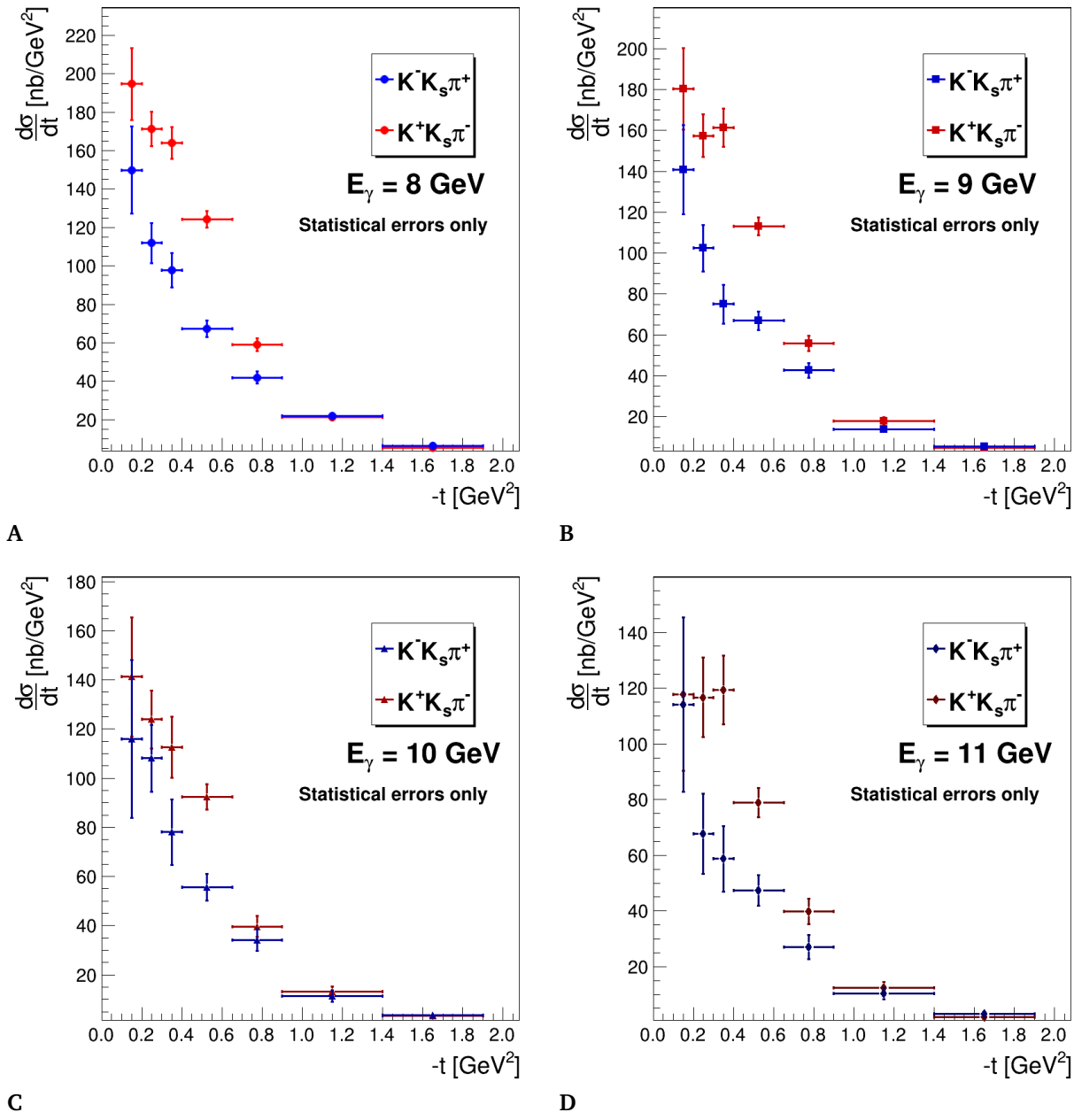

Figure 50. $f_1(1285)$ photoproduction cross-section $\frac{d\sigma}{dt}$ with statistical uncertainty only for different values of E_γ. The measurements are obtained from both the $f_1(1285) \to K^- K_s \pi^+$ (blue) and $f_1(1285) \to K^+ K_s \pi^-$ (red) decays. Error bars represent the statistical uncertainty of the measurement only. (A) shows $E_\gamma = 8$ GeV, (B) shows $E_\gamma = 9$ GeV, (C) shows $E_\gamma = 10$ GeV, and (D) shows $E_\gamma = 11$ GeV. The beam energy the cross-section was measured in is also shown on the figure.

Table 13. Differential cross-section and statistical uncertainties for each bin of E_γ and $-t$ for $f_1(1285)$ from both of the $f_1(1285) \to K^\mp K_s \pi^\pm$ decay channels.

E_γ [**GeV**]	$-t$ [$\mathbf{GeV}^2$]	$d\sigma/dt \pm \delta_{\mathbf{stat}}$ [$\mathbf{nb}/\mathbf{GeV}^2$] $(K^- K_s \pi^+)$	$d\sigma/dt \pm \delta_{\mathbf{stat}}$ [$\mathbf{nb}/\mathbf{GeV}^2$] $(K^+ K_s \pi^-)$
8.0	0.150	150 ±23	195±19
8.0	0.250	112 ±10	171±9
8.0	0.350	98 ±9	164±8
8.0	0.525	67 ±4	124±4
8.0	0.775	42 ±3	59±3
8.0	1.150	22 ±2	21±2
8.0	1.650	6 ±1	5±1
9.0	0.163	141 ±22	180±20
9.0	0.263	102 ±11	157±10
9.0	0.362	75 ±9	161±9
9.0	0.537	67 ±4	113±4
9.0	0.787	43 ±4	56±4
9.0	1.162	14 ±2	18±2
9.0	1.662	6 ±1	5±1
10.0	0.175	116 ±32	141±24
10.0	0.275	108 ±14	124±12
10.0	0.375	78 ±13	113±12
10.0	0.550	56 ±6	92±5
10.0	0.800	34 ±4	40±4
10.0	1.175	11 ±2	13±2
10.0	1.675	4 ±1	3±1
11.0	0.188	114 ±31	118±28
11.0	0.287	68 ±14	117±14
11.0	0.387	59 ±12	119±12
11.0	0.562	47 ±5	79±5
11.0	0.812	27 ±4	40±5
11.0	1.188	10 ±2	12±2
11.0	1.688	3 ±1	2±1

5.4.1 Reconstruction and Acceptance

The most obvious candidate for producing an asymmetric cross section between charge conjugated decay modes was the acceptance of the GlueX detector. To study this, a completely new Monte Carlo sample was generated for both decay channels to ensure no bugs were present in the generation of initial samples we used for our measurement. Additionally, we also tested different reconstruction software versions to see if the asymmetry changed based on software updates. We saw no change in the behavior of the cross-section for the new Monte Carlo samples, and were able to rule out a Monte Carlo software issue as the source of the difference.

We investigated the acceptance for each charge conjugated decay mode to see if there was an obvious detector reconstruction effect that could lead to the asymmetry. The ratio of the acceptance for $f_1(1285) \to K^- K_s \pi^+$ to $f_1(1285) \to K^+ K_s \pi^-$ for each of the beam energy bins is shown in Figure 51. We can see that there is a very slight asymmetry in the acceptance between the charge conjugated modes, but in the "wrong" direction. The $\pi^+ K^- K_s$ charge conjugated mode, where we observe a smaller cross-section, had the smaller acceptance. Due to the way the the cross-section is calculated, this small acceptance asymmetry will actually work in the opposite way, where all else being equal, the $\pi^+ K^- K_s$ would see an enhancement rather than the $\pi^- K^+ K_s$ enhancement we observe. Regardless, the 1-3% difference in the acceptance is far too small to explain the difference in the measured cross-section, particularly at low and medium values of $-t$.

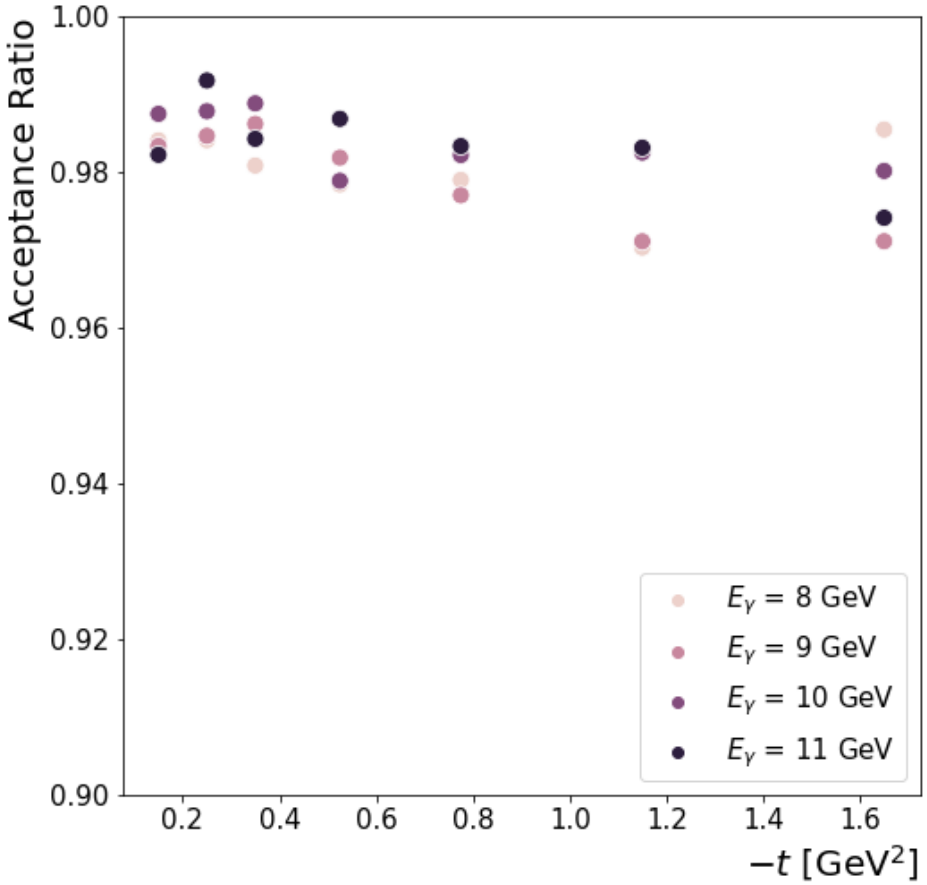

Figure 51. The ratio of the acceptances for $f_1(1285) \to K^- K_s \pi^+$ to $f_1(1285) \to K^+ K_s \pi^-$ from signal Monte Carlo for different bins of E_γ. There is a slightly better acceptance for the $K^- K_s \pi^+$ decay mode, but the ratio of efficiency for the two final states is stable and does not vary by more than 3%.

We studied the kinematic distributions of the final state particles to see if there was any obvious reconstruction differences in the two states. Figures 52, 53 show 2D distributions of $M(K^\mp K_s \pi^\pm)$ vs the momentum and polar angle θ of the final state $K^\mp$ and $\pi^\pm$ respectively. There is no clear difference between the two that would indicate reconstruction as the source of the difference in the $f_1(1285)$ cross-section measured in the two final state topologies.

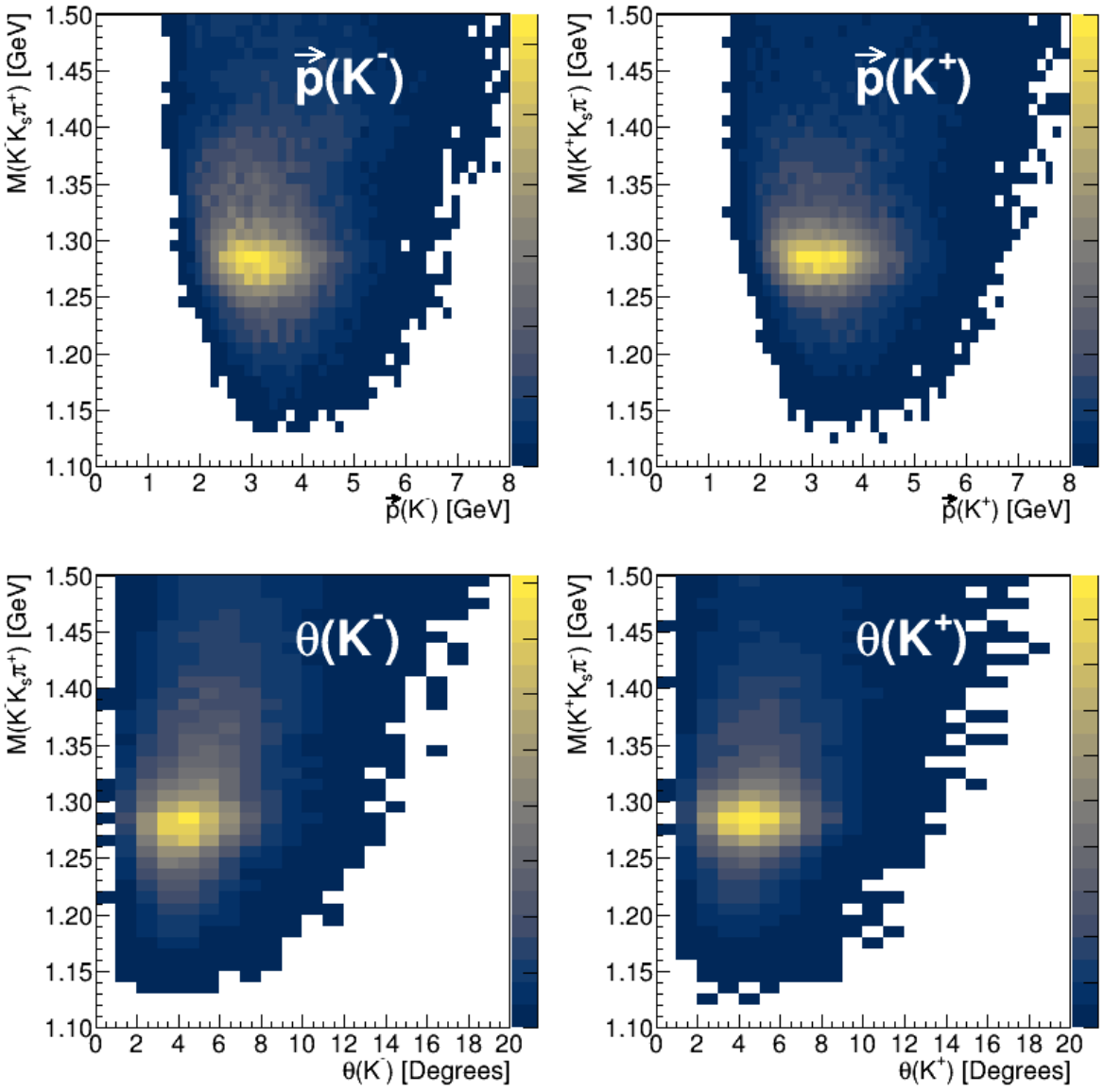

Figure 52. Kaon kinematics comparison. $M(K^{\mp}K_s\pi^{\pm})$ vs momentum (top) and polar angle (bottom) distributions for final state K^- (left) and K^+ (right) after all selection criteria is applied. There are no obvious differences between the distributions that would point to a cause of the charge conjugation cross-section difference.

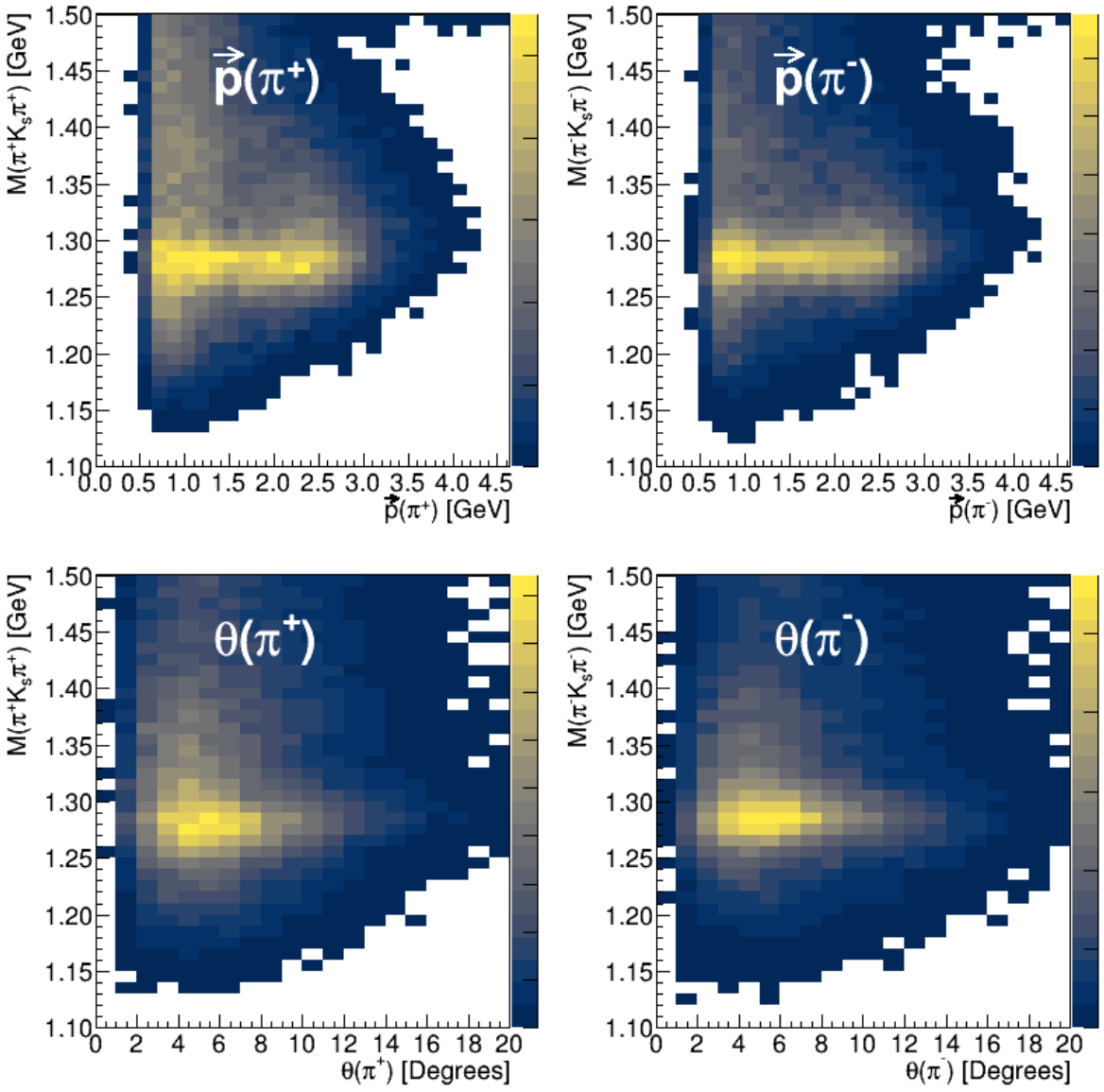

Figure 53. Pion kinematics comparison. $M(K^{\mp}K_s\pi^{\pm})$ vs momentum (top) and polar angle (bottom) distributions for final state π^+ (left) and π^- (right) after all selection criteria is applied. There are no obvious differences between the distributions that would point to a cause of the charge conjugation cross-section difference.

Figure 54 shows the real data count ratio of $N(K^-K_s\pi^+)/N(K^+K_s\pi^-)$ with all of the event selection criteria applied except for the K^* rejection. We observe a large, mass-dependent deviation from unity in this count ratio in the regions of $M(KK\pi)$ corresponding to the $f_1(1285)$ and higher mass f_1/η resonances. In the $M(KK\pi) > 1.6$ region where we do not expect to see resonant states, there is a constant, near-unity count ratio in line with the 97% acceptance ratio in Figure 51. If there were a systemic reconstruction asymmetry, we would expect it to be a global phenomena across the entire mass space as opposed to localized in regions where we expect to see resonant features. This strongly suggests a physical - not analytical or experimental - reason for the cross-section disparity as measured in the different charge conjugated final states.

5.4.2 Asymmetric Impact of Kinematic Cuts

While the two charge conjugated $K^\mp K_s\pi^\pm$ modes were studied separately and had their selection criteria applied independently, the cuts were symmetric across both channels. We studied the efficiency of each cut on real data and signal Monte Carlo data to see if one of the selection protocols was producing an outsized effect on one channel relative to the other. Table 14 shows the sequential and total impact of the cuts in data and MC. No cut had a significantly larger efficiency relative to the other charge channel. We can assume the event selection criteria is not cause of the cross-section discrepancy.

5.4.3 Baryonic Contamination

With the knowledge that the cross-section difference was likely not due to a reconstruction or Monte Carlo issue, we studied the possibility of baryonic background contamination

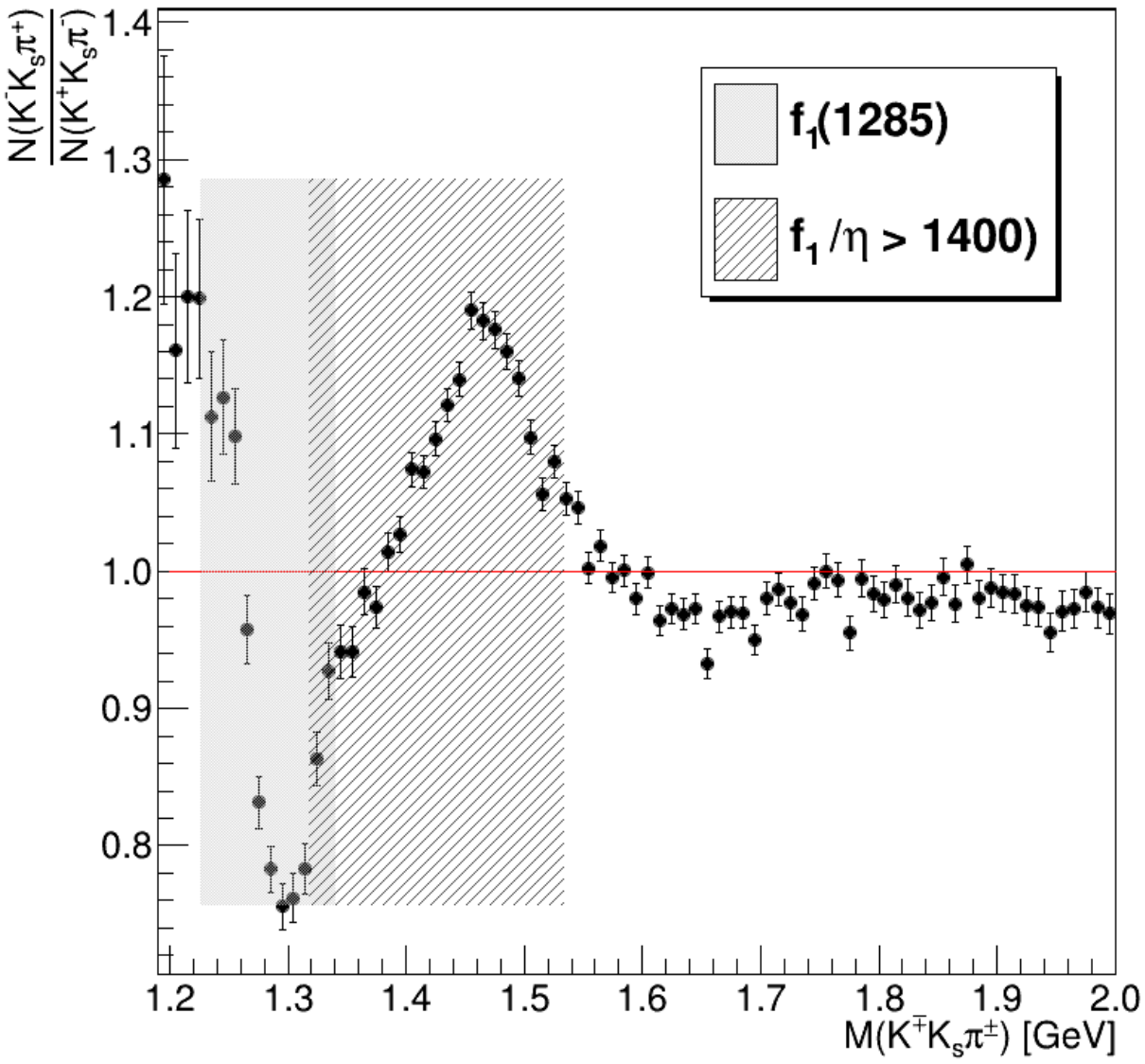

Figure 54. Count ratio of $\gamma p \to p' K^- K_s \pi^+$ to $\gamma p \to p' K^+ K_s \pi^-$ events as a function of $M(K^{\mp} K_s \pi^{\pm})$. All event selection criteria applied except the K^* rejections. The gray shaded region shows the mass range of $f_1(1285)$ as given in Eqn. 68 and the gray hatched region shows the mass range for the $\eta(1405)/f_1(1420)$ as given by $[M(\eta) - 2\Gamma(\eta)$, $M(f_1) - 2\Gamma(f_1)]$ [20], [89]. There are variable asymmetries of the binned data count ratio in the regions corresponding to resonant states at higher mass values.

Table 14. Sequential cut efficiency in data and MC for $p'K^{\mp}K_s\pi^{\pm}$. The efficiency is given by Eqn. 68). Both the $p'K^-K_s\pi^+$ and $p'K^+K_s\pi^-$ final states are shown.

Cut	**Data** ε $(K^-K_s\pi^+)$	**MC**	**Data** ε $(K^+K_s\pi^-)$	**MC**
CL_{KinFit}	0.78	0.95	0.79	0.95
$M_x^2(p\prime K^{\mp}K_s\pi^{\pm})$	0.63	0.90	0.65	0.90
$\vec{p}(p)$	0.77	0.89	0.79	0.89
Pathlength	0.37	0.75	0.39	0.75
$M(\pi^+\pi^-)$	0.76	0.93	0.78	0.93
$M(p\pi^{\pm})$	0.93	0.93	0.90	0.93
$M(pK^{\mp})$	0.99	0.99	0.99	0.99
$M(pK_s)$	0.99	0.99	0.99	0.99
$M(K\pi^{\pm})$	0.83	0.95	0.79	0.95
Total	0.082	0.47	0.087	0.47

contributing to a yield asymmetry as a function of Mandelstam-t. We looked at the following as sources of potential baryonic contamination:

- $\Lambda^0 \to p'K^-$
- $\Sigma^+ \to p'K_s$
- $\Delta/N^* \to p'\pi$

We know that the difference in the values for the cross-section varies as a function of $-t$, so we investigated the baryonic background distributions in the $M(KK\pi)$ region of the $f_1(1285)$ as a function of $-t$. Additionally, we can better isolate the source of any potential baryonic contribution by considering only the events that survive the event selection criteria.

The t-binned distributions of $M(p'K^{\mp})$ and $M(p'K_s)$ are shown in Figures 55, 56 respectively. There is an excess of events in the $K^+K_s\pi^-$ final state compared to the $K^-K_s\pi^+$ final state, but there is no enhancement structure indicating background contamination from

the Λ or Σ baryon.

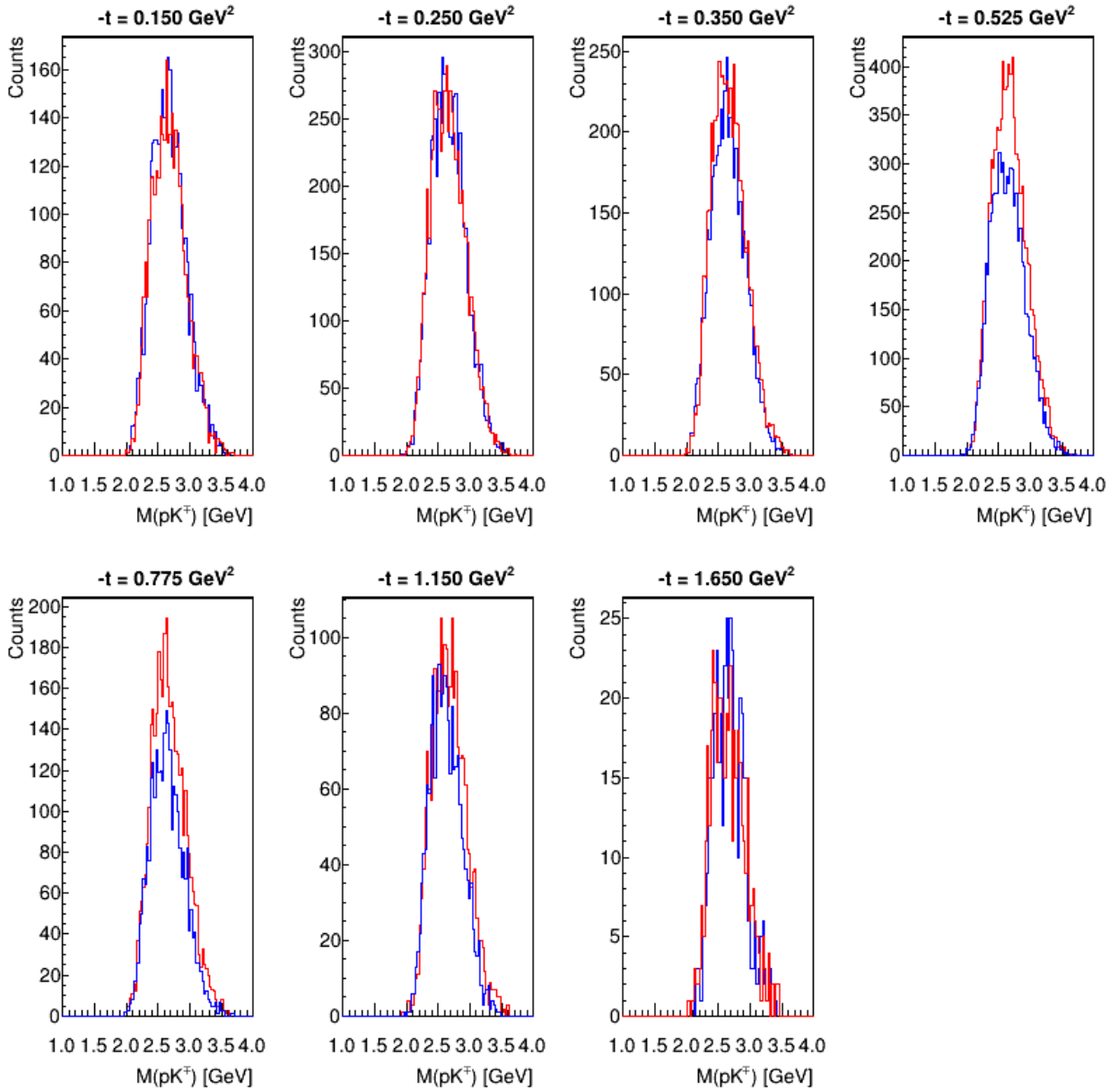

Figure 55. t-binned distributions of $M(p\prime K^{\mp})$ for the $K^{-}K_s\pi^{+}$ (blue) and $K^{+}K_s\pi^{-}$ (red) final states in the mass region of $f_1(1285)$. Bin center values of $-t$ are shown on the plot. No obvious contamination from the Λ baryon is observed.

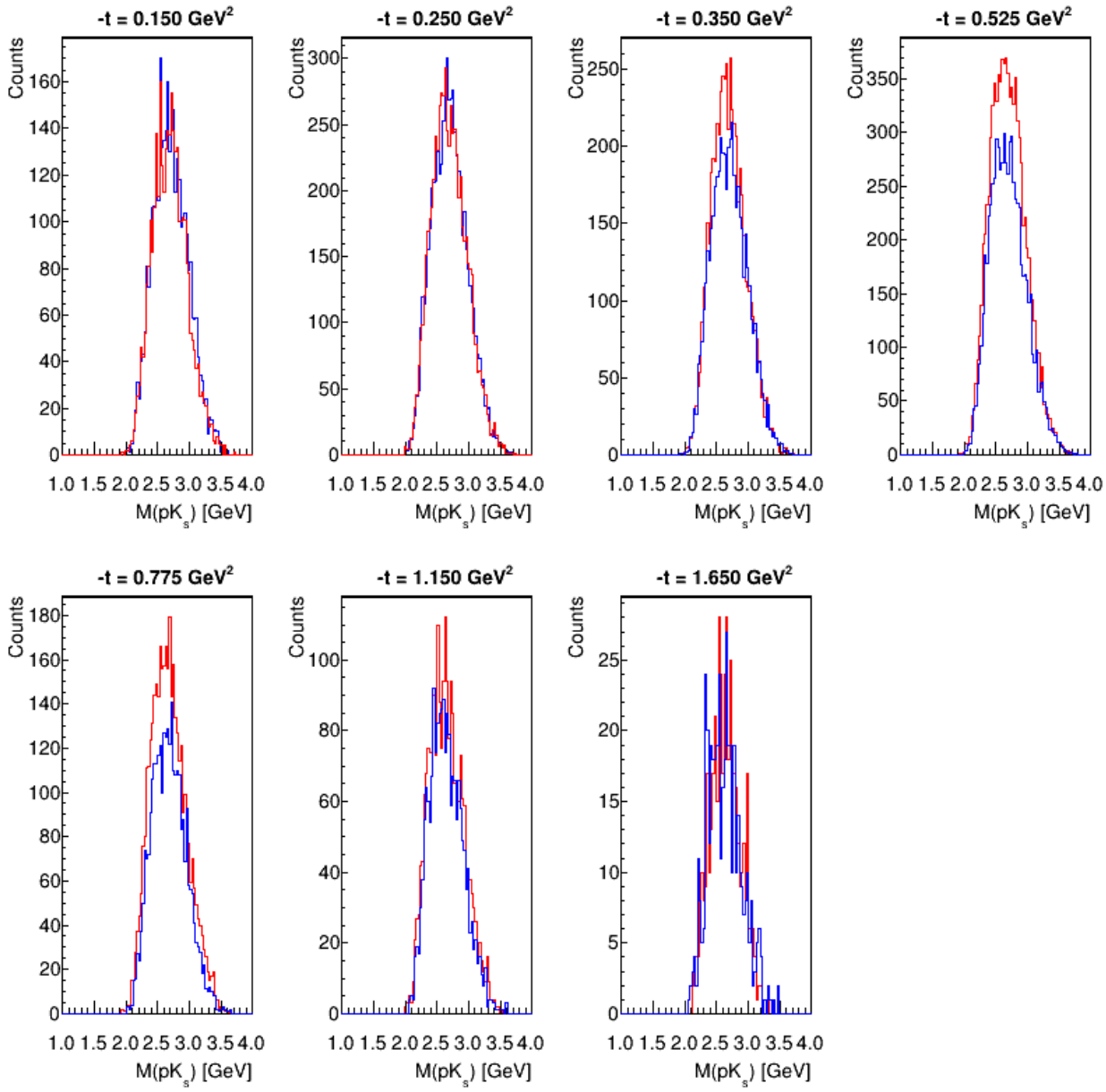

Figure 56. t-binned distributions of $M(p\prime K_s)$ for the $K^-K_s\pi^+$ (blue) and $K^+K_s\pi^-$ (red) final states in the mass region of $f_1(1285)$. Bin center values of $-t$ are shown on the plot. No obvious contamination from the Σ baryon is observed.

The $M(p'\pi)$ distributions for the $f_1(1285)$ mass rage binned in $-t$ are shown in Figure 57. There is an enhancement around the region of $M(p'\pi^-) = 1.5 - 1.9$ GeV in several of the

$K^+K_s\pi^-$ final state distributions which indicates the presence of $N^* \to p\pi^-$ decay events in these $-t$ bins. The enhancement appears to be $-t$ dependent. The measured cross-sections is not uniform as a function of $-t$ either so this points to a connection between the two. The statistical precision in the region of $f_1(1285)$ does not allow for a definitive assessment of N^* baryonic contamination, but we can make some inferences about the presence of unwanted baryons by comparing the $M(p'\pi^\pm)$ distributions in the mass region of $f_1(1285)$ to those same distributions over the full $M(KK\pi)$ range, which is shown in Figure 58. There are clear enhancement structures in this distribution at $M(p'\pi^-) = 1.5$ and $M(p'\pi^-) = 1.7$ GeV from likely $N^* \to p\pi^-$ decays. There are 8 potential N^* candidates in this mass region and all have widths between $0.11 < \Gamma(N^*) < 0.25$ GeV, so we cannot determine the contribution from any individual excitation [86]. This provides strong evidence that the excess of events observed in the $f_1(1285)$ mass region of the $M(p'\pi^-)$ t-binned distributions from $1.5 < M(p\prime\pi^-) < 1.9$ GeV are likely due to the presence of $N^* \to p\pi^-$ decay events. A further suggestion of N^* contamination can be drawn from the maximum range of observed excess $M(p'\pi^-)$ events. The disparity between the two distributions appears to have a maximum value of $M(p'\pi^\pm) = 2.2$ GeV, after which the binned counts appear to be roughly equal. This maximum mass value corresponds to the mass values of the heaviest confirmed N^* states [86].

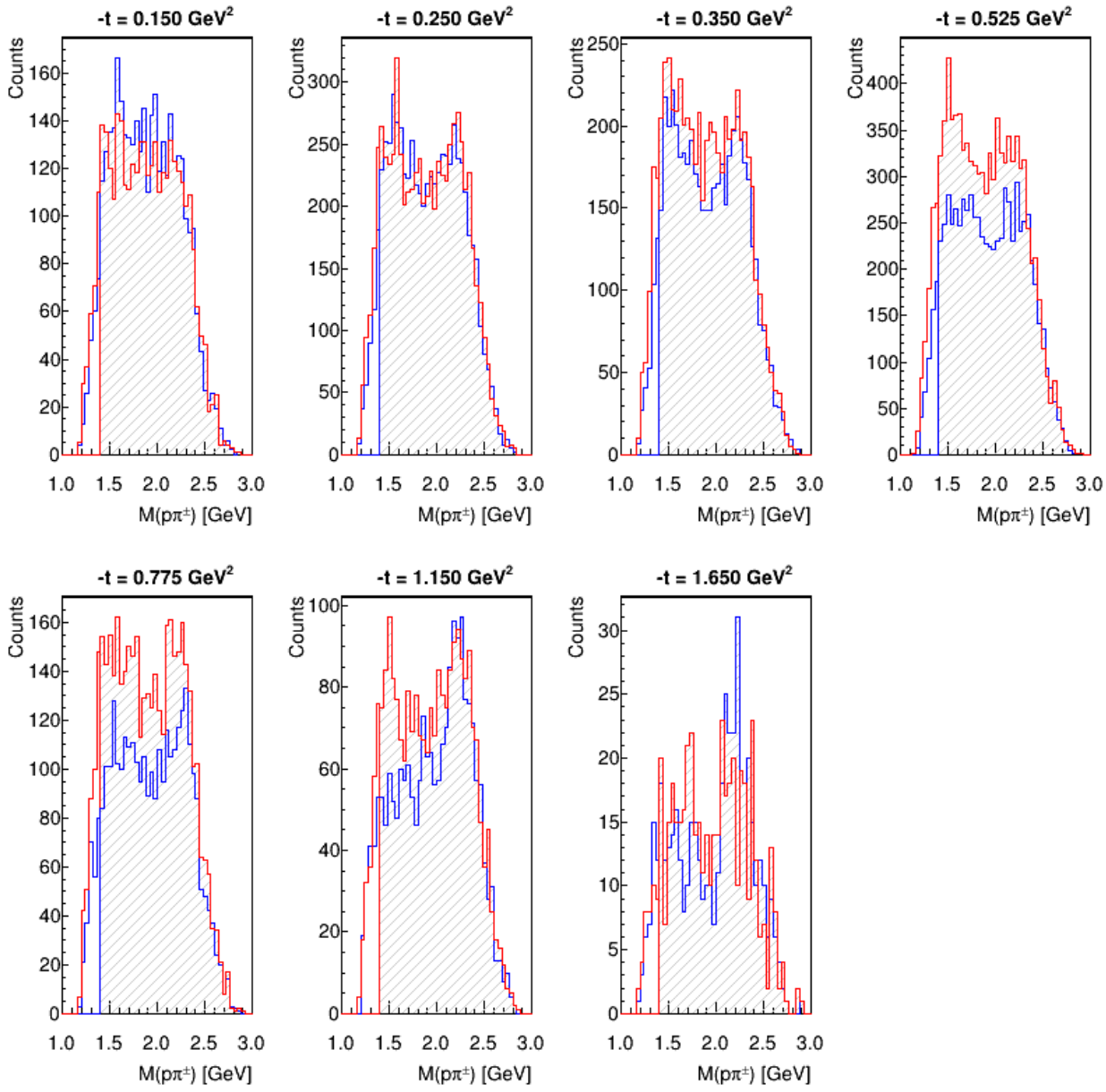

Figure 57. t-binned distributions of $M(p'\pi^{\pm})$ for the $K^{-}K_s\pi^{+}$ (blue) and $K^{+}K_s\pi^{-}$ (red) final states in the mass region of $f_1(1285)$. The shaded region indicates the events that survive the event selection criteria. There appears to be some structure at $M(p'\pi^{-}) = 1.5$ GeV that suggests the presence of 1 or more N^* resonances. These potential N^* states have a decay width $\Gamma > 0.1$ GeV.

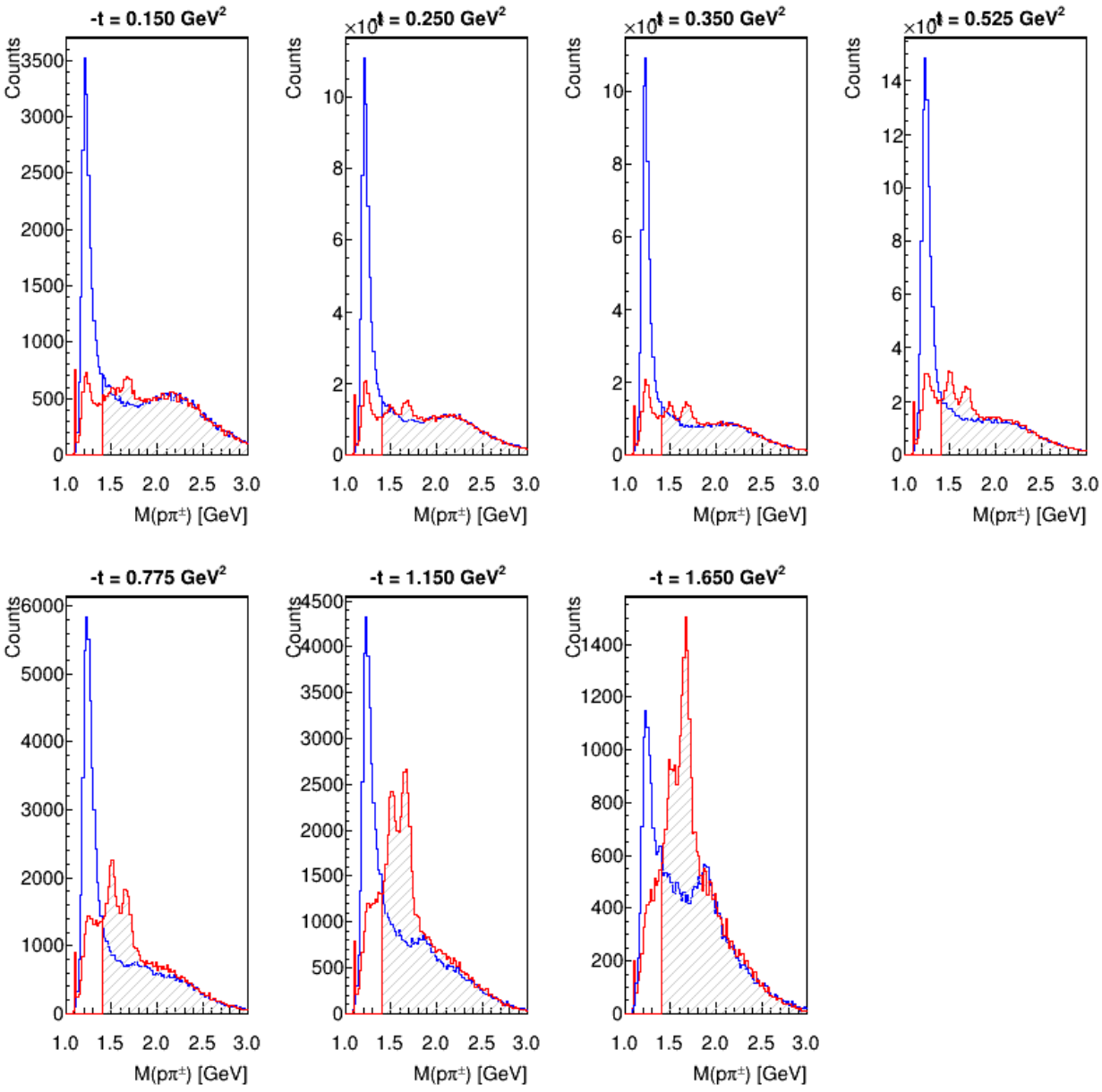

Figure 58. t-binned distributions of $M(p\prime\pi^{\pm})$ for the $K^{-}K_{s}\pi^{+}$ (blue) and $K^{+}K_{s}\pi^{-}$ (red) final states over the full $M(KK\pi)$ mass range. The shaded region indicates the events that survive the event selection criteria. There is clear structure in the surviving events at $M(p\prime\pi^{-}) = 1.5$ and $M(p\prime\pi^{-}) = 1.7$ GeV. There are 8 confirmed $N*$ states in this mass range.

5.5 SYSTEMATIC UNCERTAINTY

Every decision we make in our analysis could potentially introduce some uncertainty to the cross-section measurement. In this work, these uncertainties, called the systematic uncertainties or "systematics", come from 3 main sources:

1. Fitting procedure §5.5.1
2. Event selection criteria §5.5.2
3. Normalization §5.5.3

The systematic uncertainty from the fitting procedure and event selection are calculated on a point-by-point basis and included in the error bars for each data point. The normalization uncertainty represents uncertainty that applies equally to every data point in the same direction and are not included in the point-by-point uncertainty calculation or error bars.

5.5.1 Fitting Procedure Systematic Uncertainty

To measure the uncertainty on our fitting procedure, we study the degree to which different variations of the model change the value of the measured cross-section. The overall complexity of our chosen model means that we have many so-called "knobs to turn". We tested 15 variations of our model to evaluate the impact our fitting procedure has on our cross section measurement. A description of these variations are given in Table 15 and the change relative to nominal for each variation is given in Appendix A Tables 24-38. The variation that produces the largest change in the cross section for each bin of

E_γ and $-t$ is chosen to be the "fit systematic" δ_{fit} for that bin such that,

$$\delta_{\text{fit}} = \text{MAX}\left\{\delta_{i,\text{fit}}\right\}, \tag{78}$$

where $\delta_{i,\text{fit}}$ is the relative deviation from the nominal fit value for a given variation. The relative deviation from nominal is given by,

$$\delta_{i,\text{fit}} = \frac{|O_{\text{nominal}} - O_{\text{varied}}|}{O_{\text{nominal}}}, \tag{79}$$

where O is the differential cross-section $\frac{d\sigma}{dt}$ of the nominal and varied fitting procedure as outlined in §5.3. The values for each of the bin's systematic uncertainty from the fit can be found in Appendix A Tables 39, 40. The statistical properties of fitting procedure systematic uncertainty for each channel is given in Table 16. A large majority of bins have their fit systematic attributed to the shape of the function that we use to model the background distributions of the higher-mass resonant contamination and non-resonant phase space. The uncertainty from the fit model is approximately on the order of the statistical uncertainty.

Table 15. Fit variation descriptions. The variations on the fit model used to evaluate systemic uncertainty from the fitting procedure along with a short description of each.

Fit Variation	Description
Order 1 background	Use a polynomial of the form $y = c_1 x + c_2$ to model the background.
Order 3 background	Use a polynomial of the form $y = c_1 x^3 + c_2 x^2 + c_3 x + c_4$ to model the background.
No Gaussian component	Remove the Gaussian term that is used to describe tails of the higher-mass resonance.
Fit range	Change the range the function is fit over, making it more wide or more narrow on one or both sides.
Voigt Width Values	Fix the Voigtian width to $\pm 1\sigma$ from the integrated fit results.
Gaussian Mean/Width Values	Fix the Gaussian mean and width at $\pm 1\sigma$ from the integrated fit results.

Table 16. Statistical description of the fitting procedure component of the total systematic uncertainty.

Channel	Mean	Std. Dev.
$\pi^- K^+ K_s$	0.137	0.109
$\pi^+ K^- K_s$	0.158	0.099

5.5.2 Event Selection

Each event selection criteria we introduce to the analysis may introduce some uncertainty in the measurement of the $f_1(1285)$ cross-section. For each of our selection criteria, we change the threshold value of the quantity we are cutting on to make it more and less restrictive and re-calculate the cross-section given that varied criteria. The size of the

Table 17. Cut variations used to calculate event selection systematic uncertainty.

Cut	Nominal	Loose	Tight
$CL_{\text{KinFit}} > x$	10^{-5}	10^{-6}	10^{-4}
Pathlength Significance $> x$	5	4	6
$\lvert M(K_s) - M(\pi^+\pi^-)\rvert < n\sigma$ [GeV]	2.0	2.5	1.5
$M(p'\pi) > x$ [GeV]	1.4	1.3	1.5
$M(Kp') > x$ [GeV]	2.0	1.9	2.1
$\vec{p}(p') > x$ [GeV]	0.4	0.35	0.45
$\left\lvert M(K^{*0}) - M(K^{\mp}\pi^{\pm})\right\rvert < n\sigma$ [GeV]	2.0	1.5	2.5
$\lvert M(K^{*\pm}) - M(K_s\pi^{\pm})\rvert < n\sigma$ [GeV]	2.0	1.75	2.25
$\left\lvert M_x^2(\gamma + p - p' - K^{\mp} - K_s - \pi^{\pm})\right\rvert < x$ [GeV^2]	0.01	0.02	0.007

variations are chosen to be reasonable while not changing the underlying statistical distribution of $M(KK\pi)$ by more than $\pm 10\%$. A description of each of the variations can be found in Table 17 and plots of each distribution with cut positions marked can be found in Appendix A Figures 73-82.

We utilize the Barlow Test [113] to evaluate if a cut should be included in the calculation of the event selection systematic uncertainty. The Barlow Test is used to assess whether the deviation from nominal for a given event selection is statistically significant or potentially due to the change in the underlying statistical distribution. The barlow statistic σ_{barlow} is given by,

$$\sigma_{\text{barlow}} = \frac{O_{\text{nominal}} - O_{\text{variation}}}{\sqrt{\delta^2_{\text{stat, nominal}} - \delta^2_{\text{stat, variation}}}}, \tag{80}$$

where O is the nominal/varied cross-section values and δ_{stat} is the statistical uncertainty on that value. By convention, we use $\sigma_{\text{barlow}} = \pm 4$ as a guardrail in this evaluation. If a clear majority of deviations for a given cut lie within the ± 4 boundary, we choose to exclude that cut in the calculation of the systematic uncertainty for the event selection criteria.

The Barlow Tests for the cut variations are given in Figure 59 except for proton momentum cut $\vec{p}(p)$, which is a unique case. From these barlow statistic distributions, we conclude that only the rejections of the K^* via imposing a cut on $M(K\pi)$ warrant consideration as systematic uncertainty. The rejections of the charged and neutral K^* resonances have enough deviations from nominal that produce barlow statistic values of $|\sigma_{\text{barlow}}| > 4$ to indicate the difference in the cross-section for the varied event selection criteria from the nominal value are unlikely to be due to changes in the underlying statistical distribution and are likely due to the change of cut threshold. The Barlow Test for $\vec{p}(p)$ is shown in Appendix A Figure 83. This cut primarily impacts the lowest $-t$ bin, and all of the deviations are within the $\sigma_{\text{barlow}} = \pm 4$ threshold. We do not include this cut in the calculation of the systematic uncertainty.

For each cut, we test a more and less restrictive variation of the criteria. We conservatively take the larger absolute variation of the two to be the variation for that cut in both directions. For example, if the looser cut has a 4% change from nominal and the tighter cut has a 6% change from nominal, the tighter cut's value of 6% is be considered the uncertainty arising from that event selection criteria. If we deem that a cut has "fails" the barlow test we must assume that the deviations from nominal in any E_γ and $-t$ bin is due to the change in the event selection criteria. The relative cut systematic uncertainty is given by,

$$\delta_{\text{cuts}} = \sqrt{\delta_{K^{*0}}^2 + \delta_{K^{*\pm}}^2}, \tag{81}$$

where $\delta_{K^{*0}}$, and $\delta_{K^{*\pm}}$ are the relative uncertainties from the variations on the neutral K^* and charged K^* rejections respectively. The values for $\delta_{K^{*0}}$, and $\delta_{K^{*\pm}}$ are obtained in the

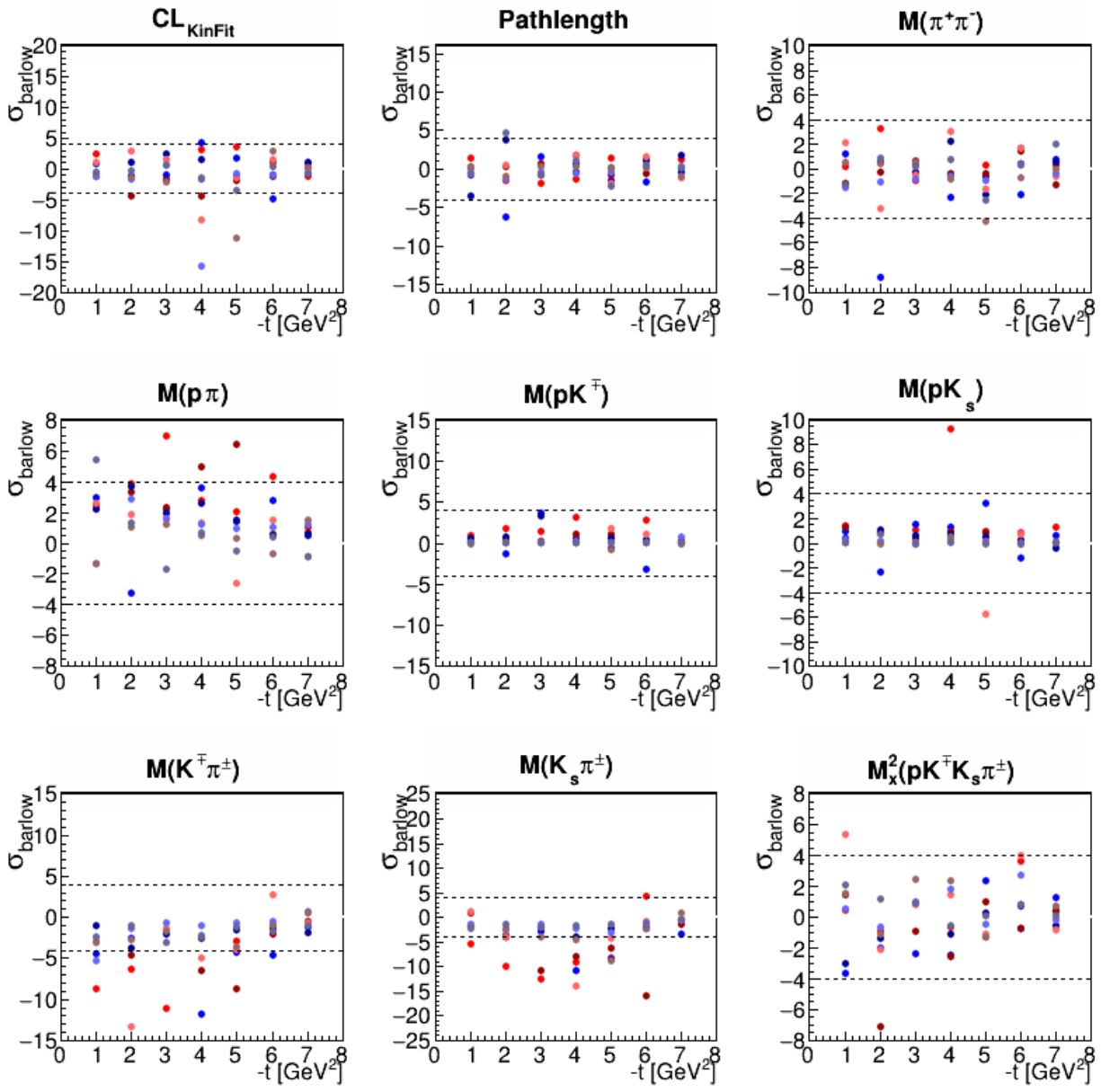

Figure 59. Barlow Test for each of the event selection criteria except the $\vec{p}(p)$ cut. The blue points are for $K^-K_s\pi^+$ and the red points are for $K^+K_s\pi^-$. The shades of the colors represent the different energy bins the cross section is measured in. The $\sigma_{\text{barlow}} = \pm 4$ threshold is indicated by the black dashed lines. $M(K^{\mp}\pi^{\pm})$ and $M(K_s\pi^{\pm})$ are chosen as the contributions to the event selection systematic.

same way we calculated $\delta_{i,\text{fit}}$ by Eqn. 79 . The values for δ_{cuts} are given in Table 18.

5.5.3 Normalization

There are overall normalization uncertainties that are not included in the error bars on the measurement itself because they impact both charge conjugated modes of the $f_1(1285) \to K^{\mp}K_s\pi^{\pm}$ decay the same amount in the same direction.

In §4.2.2 we showed that our Monte Carlo model disagrees with the data for the momentum of the pion and kaon (Figures 39, 40). This disagreement is not t-dependent (Figure 42) so any error arising from the Monte Carlo model will be an overall normalization on the scale of the differential cross-section. We calculate this Monte Carlo normalization uncertainty δ_{MC} by finding the maximum deviation from nominal on a bin-by-bin basis for the pion and kaon momentum such that,

$$\delta_{\text{MC},(K,\pi)} = MAX\left\{\frac{\mathscr{A}_{i,p,(K,\pi)} - \mathscr{A}_0}{\mathscr{A}_0}\right\}, \tag{82}$$

where $\delta_{\text{MC},(K,\pi)}$ is the uncertainty for the $K^{\mp}$ or $\pi^{\pm}$, $\mathscr{A}_{i,p,(K,\pi)}$ is the efficiency for a given bin of $\vec{p}(K)$ or $\vec{p}(\pi)$, and $\mathscr{A}_0$ is the overall acceptance over the $f_1(1285)$ mass range integrated over E_γ and $-t$ as given by Eqn. 74. The overall systematic uncertainty from the Monte Carlo model is conservatively chosen to be the linear sum of the kaon and pion momentum acceptance uncertainties such that,

$$\delta_{\text{MC}} = \delta_{\text{MC},K} + \delta_{\text{MC},\pi}. \tag{83}$$

Table 18. Cut systematic uncertainty for each bin of E_γ and $-t$. Values of the relative systematic uncertainty from event selection criteria δ_{cuts} for each E_γ and $-t$ bin for both charge conjugated decay modes of the $f_1(1285) \to K^\mp K_s \pi^\pm$ as described in Eqn. 81.

E_γ [GeV]	$-t$ [GeV^2]	$\delta_{\text{cuts}}(K^- K_s \pi^+)$	$\delta_{\text{cuts}}(K^+ K_s \pi^-)$
8	0.15	0.125	0.129
8	0.25	0.137	0.139
8	0.35	0.083	0.151
8	0.53	0.139	0.126
8	0.78	0.083	0.109
8	1.15	0.074	0.096
8	1.65	0.137	0.082
9	0.15	0.106	0.112
9	0.25	0.131	0.128
9	0.35	0.071	0.107
9	0.53	0.092	0.105
9	0.78	0.089	0.139
9	1.15	0.065	0.167
9	1.65	0.151	0.112
10	0.15	0.167	0.105
10	0.25	0.076	0.150
10	0.35	0.052	0.094
10	0.53	0.066	0.142
10	0.78	0.052	0.151
10	1.15	0.086	0.097
10	1.65	0.121	0.136
11	0.15	0.150	0.167
11	0.25	0.084	0.139
11	0.35	0.135	0.100
11	0.53	0.092	0.113
11	0.78	0.093	0.109
11	1.15	0.086	0.156
11	1.65	0.100	0.196

The GlueX detector has some overall uncertainty on the tracking of charged particles δ_{Track}. The tracking efficiency of pions $\delta_{T,\pi}$ depends on the particle's polar angle θ with respect to the beamline [114]. For pions with a polar angle between,

$$1 < \theta < 15^{\circ}, \tag{84}$$

a conservative uncertainty of 2% is suggested. An uncertainty of 5% is assigned for all pions with a larger polar angle. The overall pion tracking efficiency is a weighted average of the fraction of pions that satisfy each criteria, added linearly,

$$\delta_{T,\pi,i} = 0.02\left[\frac{n(\theta_\pi < 15)}{N}\right] + 0.05\left[\frac{n(\theta_\pi > 15)}{N}\right], \tag{85}$$

where $\delta_{T,i}$ is the tracking uncertainty for any of the 3 pions, π_i, in the final state, N is the number of events in the data sample in the $KK\pi$ mass region of $f_1(1285)$, and $n(\theta_\pi)$ is the number of π_i for $\theta_\pi < 15$ or $\theta_\pi > 15$. The total uncertainty on the pion tracking $\delta_{T,\pi}$ is a linear sum of the individual uncertainties, given by,

$$\delta_{T,\pi} = \sum_{i=1}^{3} \delta_{T,\pi,i}. \tag{86}$$

There is also an uncertainty $\delta_{T,p}$ on the tracking of the proton. For each detected proton in the final state, we assign a 5% uncertainty [115]. We have a single proton in our final state. The overall tracking efficiency is then,

$$\delta_{\text{Track}} = \delta_{T,\pi} + \delta_{T,p}. \tag{87}$$

Table 19. Source and values for various normalization uncertainties.

Source	**Relative Uncertainty δ**
Pion Tracking	0.066
Proton Tracking	0.050
Overall Tracking	0.116
Luminosity	0.050
Branching Fraction	0.044
Monte Carlo (Pion)	0.150
Monte Carlo (Kaon)	0.118
Total	**0.300**

Additionally, the tagged luminosity has a conservative preliminary estimation for the uncertainty $\delta_{\mathscr{L}}$ of 5% [116] and the branching fraction of the $f_1(1285) \to KK\pi$ has an uncertainty δ_{BR} of approximately 4% [10].

The overall normalization uncertainty is calculated by adding the Monte Carlo, tracking, luminosity, and branching fraction in quadrature,

$$\delta_{\text{norm}} = \sqrt{\delta^2_{\text{MC}} + \delta^2_{\text{Track}} + \delta^2_{\mathscr{L}} + \delta^2_{BR}}. \tag{88}$$

Values for the sources and total of the normalization uncertainty is given in Table 19

5.5.4 Total Uncertainty

The total uncertainty on the cross-section measurement of $f_1(1285) \to KK\pi$ not from a normalization factor is given by,

$$\delta_{\text{total}} = \sqrt{\delta^2_{\text{stat}} + \delta^2_{\text{sys}}}, \tag{89}$$

where,

$$\delta_{\text{sys}} = \sqrt{\delta_{\text{fit}}^2 + \delta_{\text{cut}}^2}. \tag{90}$$

The values for the individual sources and the total uncertainty on the cross-section are given in Tables 20, 21. The total uncertainty on the measurement of the $f_1(1285)$ cross-section is reasonable for the first-ever measurement in this decay channel at high E_γ.

5.6 HELICITY ANGLES

The only way to truly separate two resonances in the same mass region with different spins is a partial wave analysis, which extends beyond the scope of this work. However, there is a fairly straightforward hypothesis test that can rule out that the enhancement at $M(KK\pi) = 1.28$ GeV is dominated by a $J = 0$ particle like the $\eta(1295)$. We can consider the distribution of the decay angles of the decay particles in the parent resonance's helicity frame. The helicity frame is defined to be the rest frame of a resonance M with the z-axis defined to be along the $\vec{p}(M)$ in the reaction's center-of-mass frame [117].

5.6.1 Helicity Frame

The center-of-mass frame shares the same axes orientation as the lab frame but is defined such that the sum of momenta of the particles in the frame is 0. We can boost into this frame with a Lorentz boost along the z-axis, which is defined to be along the beamline. The boost velocity is given by,

$$\beta = \frac{E_\gamma}{E_\gamma + m_p c^2}, \tag{91}$$

where E_γ is the energy of the photon beam and m_p is the mass of the proton. The relativistic

Table 20. Individual contributions and total relative uncertainty for the bin-by-bin cross-section measurement of $f_1(1285) \to KK\pi$ from the $f_1(1285) \to K^- K_s \pi^+$ decay channel.

E_γ [GeV]	$-t$ [GeV^2]	$d\sigma/dt$ [nb/GeV^2]	δ_{stat}	δ_{fit}	δ_{cut}	δ_{sys}	δ_{total}
8	0.150	150	0.151	0.117	0.125	0.171	**0.228**
8	0.250	112	0.093	0.133	0.137	0.192	**0.213**
8	0.350	98	0.091	0.074	0.083	0.111	**0.143**
8	0.525	67	0.063	0.063	0.139	0.152	**0.165**
8	0.775	42	0.076	0.116	0.083	0.143	**0.162**
8	1.150	22	0.091	0.105	0.074	0.128	**0.157**
8	1.650	6	0.202	0.189	0.137	0.234	**0.309**
9	0.150	141	0.155	0.196	0.106	0.222	**0.271**
9	0.250	102	0.112	0.101	0.131	0.166	**0.200**
9	0.350	75	0.125	0.103	0.071	0.126	**0.177**
9	0.525	67	0.066	0.121	0.092	0.152	**0.166**
9	0.775	43	0.084	0.122	0.089	0.151	**0.173**
9	1.150	14	0.133	0.096	0.065	0.116	**0.177**
9	1.650	6	0.217	0.134	0.151	0.202	**0.296**
10	0.150	116	0.276	0.306	0.167	0.348	**0.445**
10	0.250	108	0.126	0.196	0.076	0.210	**0.245**
10	0.350	78	0.171	0.146	0.052	0.155	**0.231**
10	0.525	56	0.099	0.085	0.066	0.108	**0.146**
10	0.775	34	0.131	0.199	0.052	0.206	**0.244**
10	1.150	11	0.211	0.142	0.086	0.166	**0.269**
10	1.650	4	0.410	0.145	0.121	0.189	**0.451**
11	0.150	114	0.274	0.508	0.150	0.530	**0.597**
11	0.250	68	0.213	0.489	0.084	0.496	**0.539**
11	0.350	59	0.202	0.196	0.135	0.238	**0.312**
11	0.525	47	0.115	0.096	0.092	0.133	**0.176**
11	0.775	27	0.159	0.138	0.093	0.166	**0.230**
11	1.150	10	0.197	0.128	0.086	0.154	**0.250**
11	1.650	3	0.415	0.192	0.100	0.216	**0.469**

Table 21. Individual contributions and total relative uncertainty for the bin-by-bin cross-section measurement of $f_1(1285) \to KK\pi$ from the $f_1(1285) \to K^+K_s\pi^-$ decay channel.

E_γ [GeV]	$-t$ [GeV^2]	$d\sigma/dt$ [nb/GeV^2]	δ_{stat}	δ_{fit}	δ_{cut}	δ_{sys}	δ_{total}
8	0.150	195	0.097	0.152	0.129	0.200	**0.222**
8	0.250	171	0.053	0.060	0.139	0.152	**0.161**
8	0.350	164	0.050	0.071	0.151	0.167	**0.174**
8	0.525	124	0.035	0.039	0.126	0.132	**0.137**
8	0.775	59	0.055	0.057	0.109	0.124	**0.135**
8	1.150	21	0.078	0.097	0.096	0.136	**0.157**
8	1.650	5	0.213	0.101	0.082	0.130	**0.249**
9	0.150	180	0.110	0.201	0.112	0.230	**0.255**
9	0.250	157	0.066	0.097	0.128	0.161	**0.174**
9	0.350	161	0.058	0.055	0.107	0.120	**0.133**
9	0.525	113	0.039	0.043	0.105	0.113	**0.120**
9	0.775	56	0.065	0.070	0.139	0.156	**0.169**
9	1.150	18	0.115	0.081	0.167	0.186	**0.219**
9	1.650	5	0.231	0.117	0.112	0.162	**0.282**
10	0.150	141	0.172	0.423	0.105	0.435	**0.468**
10	0.250	124	0.095	0.178	0.150	0.233	**0.252**
10	0.350	113	0.110	0.091	0.094	0.131	**0.171**
10	0.525	92	0.057	0.073	0.142	0.160	**0.170**
10	0.775	40	0.106	0.090	0.151	0.176	**0.205**
10	1.150	13	0.149	0.134	0.097	0.166	**0.223**
10	1.650	3	0.437	0.207	0.136	0.247	**0.503**
11	0.150	118	0.234	0.518	0.167	0.544	**0.592**
11	0.250	117	0.122	0.302	0.139	0.332	**0.354**
11	0.350	119	0.103	0.132	0.100	0.166	**0.195**
11	0.525	79	0.067	0.078	0.113	0.137	**0.153**
11	0.775	40	0.116	0.090	0.109	0.142	**0.183**
11	1.150	12	0.157	0.164	0.156	0.227	**0.276**
11	1.650	2	0.513	0.328	0.196	0.382	**0.640**

γ factor is given by,

$$\gamma = \frac{E_\gamma + m_p c^2}{\sqrt{s}}, \tag{92}$$

where s is the center-of-mass energy given by,

$$s = (p_1 + p_2)^2 = m_p c^2 (2E_\gamma + m_p c^2), \tag{93}$$

where p_1 and p_2 are the four-vectors of beam photon and target proton. The boost vector $\vec{\beta}$ is then given by,

$$\vec{\beta} = [0, 0, -\beta]\,. \tag{94}$$

We can then calculate the 4-momentum in the CM frame by,

$$\begin{pmatrix} E \\ p_x c \\ p_y c \\ p_z c \end{pmatrix}_{\text{CM}} = \begin{pmatrix} \gamma & 0 & 0 & -\beta\gamma \\ 0 & 1 & 0 & 0 \\ 0 & 0 & 1 & 0 \\ -\beta\gamma & 0 & 0 & \gamma \end{pmatrix} \begin{pmatrix} E \\ p_x c \\ p_y c \\ p_z c \end{pmatrix}_{\text{lab}} . \tag{95}$$

After boosting our final state particles into the CM frame via Eqn. 95 we can boost again into the helicity frame of the $f_1(1285)$. We will refer to the $KK\pi$ system as the $f_1(1285)$. For the boost into the rest frame of $f_1(1285)$, we define,

$$p^\mu_{f_1} = p^\mu \left(K^\mp + K_s + \pi^\pm\right) = \left(E_{f_1},\ p_{x,f_1} c,\ p_{y,f_1} c,\ p_{z,f_1} c\right), \tag{96}$$

and,

$$|p_{f_1}| = \sqrt{(p_x c)^2 + (p_y c)^2 + (p_z c)^2}. \tag{97}$$

β and γ of the boost are then,

$$\beta = \frac{p_{f_1} c}{E_{f_1}}, \tag{98}$$

and,

$$\gamma = \frac{E_{f_1} c}{M_{f_1}}, \tag{99}$$

where M_{f_1} is the invariant mass of the $KK\pi$ system $M(K^{\mp}K_s\pi^{\pm})$. The 3-momenta components of β are given as,

$$\beta_i = \frac{p_{i,f_1} c}{E_{f_1}}, \tag{100}$$

where i indicate the x, y, z axes. The Lorentz boost to the f_1 rest frame for each daughter particle is given as,

$$\begin{pmatrix} E \\ p_x c \\ p_y c \\ p_z c \end{pmatrix}_{f_1,\ \text{Daughter}} = \begin{pmatrix} \gamma & -\beta_x\gamma & -\beta_y\gamma & -\beta_z\gamma \\ -\beta_x\gamma & 1+(\gamma-1)\frac{\beta_x^2}{\beta^2} & (\gamma-1)\frac{\beta_x\beta_y}{\beta^2} & (\gamma-1)\frac{\beta_x\beta_z}{\beta^2} \\ -\beta_y\gamma & (\gamma-1)\frac{\beta_x\beta_y}{\beta^2} & (\gamma-1)\frac{\beta_y^2}{\beta^2} & (\gamma-1)\frac{\beta_y\beta_z}{\beta^2} \\ -\beta_z\gamma & (\gamma-1)\frac{\beta_x\beta_z}{\beta^2} & (\gamma-1)\frac{\beta_y\beta_z}{\beta^2} & (\gamma-1)\frac{\beta_z^2}{\beta^2} \end{pmatrix} \begin{pmatrix} E \\ p_x c \\ p_y c \\ p_z c \end{pmatrix}_{\text{CM}}. \tag{101}$$

Once we have boosted into the rest frame of the $f_1(1285)$, we then define the axes of the system. The unit vector $\hat{y}_{\mathscr{H}}$ is defined to be normal to the production plane such that,

$$\hat{y}_{\mathscr{H}} = \frac{\vec{p}_{\gamma,\ \text{CM}} \times \vec{p}_{f_1,\ \text{CM}}}{|\vec{p}_{\gamma,\ \text{CM}} \times \vec{p}_{f_1,\ \text{CM}}|}, \tag{102}$$

where $\vec{p}_{\gamma,\,\mathrm{CM}}$ and $\vec{p}_{f_1,\,\mathrm{CM}}$ are the 3-momentum of the beam photon and $f_1(1285)$ respectively. The unit vector $\hat{z}_{\mathscr{H}}$ is defined to be in the opposite direction of the boost, such that,

$$\hat{z}_{\mathscr{H}} = \frac{\vec{p}_{f_1,\,\mathrm{CM}}}{|\vec{p}_{f_1,\,\mathrm{CM}}|}, \tag{103}$$

and the unit vector $\hat{x}_{\mathscr{H}}$ is then,

$$\hat{x}_{\mathscr{H}} = \hat{y}_{\mathscr{H}} \times \hat{z}_{\mathscr{H}}. \tag{104}$$

Finally, for a daughter particle i, we can define,

$$\cos\theta_{\mathscr{H}} = \frac{p_{i,\mathscr{H}z}}{|\vec{p}_{i,\mathscr{H}}|}. \tag{105}$$

5.6.2 $f_1 \to a_0(980)\pi$

A majority of the $f_1(285) \to K^{\mp}K_s\pi^{\pm}$ events likely have an intermediate isobar decay of $f_1(285) \to a_0(980)\pi$, where $a_0(980) \to K^{\mp}K_s$. Looking at distribution of $M(K^{\mp}K_s\pi^{\pm})$ vs $M(K^{\mp}K_s)$ in Figure 60, we see an enhancement near threshold that likely corresponds to the decay of $a_0(980) \to K^{\mp}K_s$. There are several reasons why we do not assume this isobar in the calculation of the cross-section. The nominal $a_0(980)$ mass is below the threshold mass of the $K^{\mp}K_s$ system, requiring a more complex Monte Carlo model to simulate the decay. Additionally, the $a_0(980)$ is not a well-understood particle [110]. The nominal mass and width values in the PDG are highly model dependent and the experimental averages for $a_0(980) \to KK$ are based on a single measurement each. There are no nominal values for the branching fraction of $a_0 \to KK$, further complicating the measurement of the

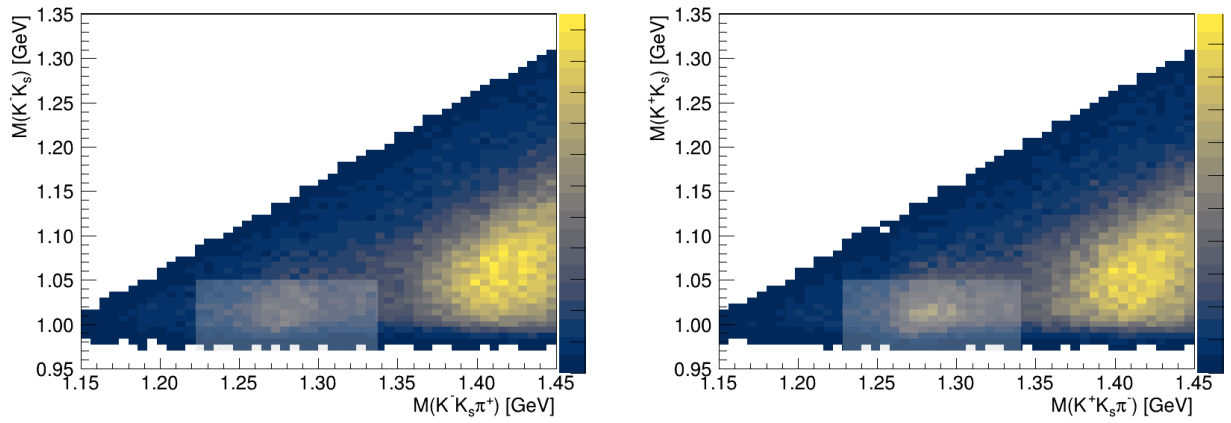

Figure 60. Distributions of $M(K^{\mp}K_s)$ vs $M(K^{\mp}K_s\pi^{\pm})$. An enhancement near threshold of $M(K^{\mp}K_s)$ is seen in the region of $1.22 < M(K^{\mp}K_s\pi^{\pm}) < 1.34$ GeV in both final states, $p'K^-K_s\pi^+$ (A) and $p'K^+K_s\pi^-$ (B), consistent with $a_0(980) \to K\bar{K}$ decay events. The gray box shows the region of interest for the helicity angle study.

$f_1(1285)$ cross-section (Eqn. 69). In experiments that the $\eta(1295)$ was observed, it was seen to decay primarily through $a_0(980)\pi$. We can model the cosine of the helicity angle distribution of the a_0 from the decay of $f_1(1285) \to a_0\pi$ in the helicity frame of the f_1 (or η) to evaluate potential strength of each J^{PC} state's contribution to the cross-section.

To select candidate events from $f_1 \to a_0(980)\pi$ decays with $a_0(980) \to K^{\mp}K_s$, we require that,

$$M(K^{\mp}K_s) < 1.05 \text{ GeV}. \tag{106}$$

The $M(KK\pi)$ distribution before and after this cut is shown in Figure 61. The enhancements corresponding to f_1/η resonant states in $M(K^{\mp}K_s\pi^{\pm})$ are still clearly present. We only consider the mass region of the $f_1(1285)$, as defined in Eqn. 68 and look at the distribution of $\cos\theta_{\mathscr{H},a_0}$ of the $K\mp K_s$ system which will refer to as the a_0 and $\cos\theta_{\mathscr{H},a_0}$.

The acceptance as a function of $\cos\theta_{\mathscr{H},a_0}$ for phase space $\gamma p \to K^{\mp}K_s\pi^{\pm}$ and acceptance

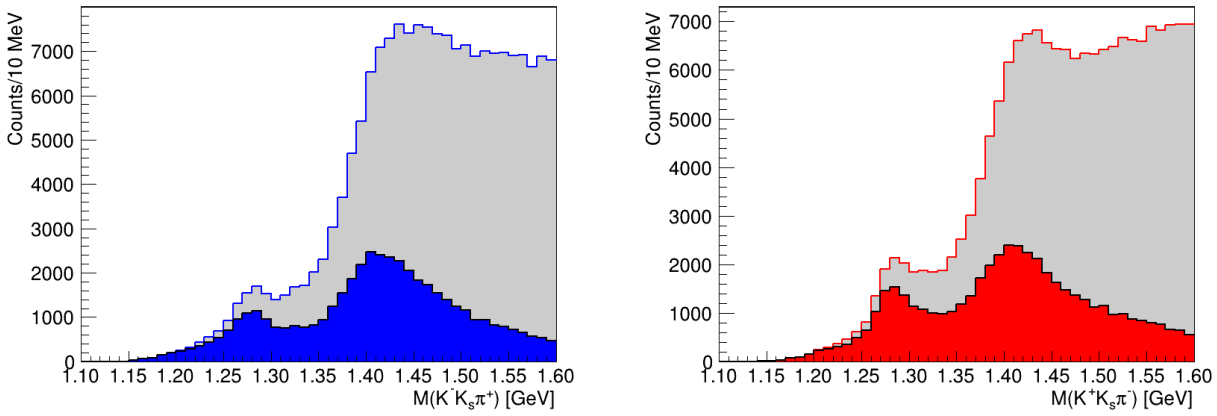

A **B**

Figure 61. Distributions of $M(K^-K_s\pi^+)$ (A) and $M(K^+K_s\pi^-)$ (B) before (gray) and after (blue/red) the cut on $M(K^\mp K_s)$ is made via Eqn. 106 to select $a_0(980)$. The enhancements in both resonant regions are still observed.

corrected distribution of $\cos\theta_{\mathscr{H},a_0}$ are shown in Figure 62. There is a very sharp falloff in both the acceptance and acceptance corrected $\cos\theta_{\mathscr{H},a_0}$ distributions towards forward angles of $\theta_{\mathscr{H}}$ that is likely non-physical. We expect a decline in the acceptance for these angles, but not to that degree. Likely, there is a detection inefficiency that is not being modeled properly by our Monte Carlo, which is why we see the corresponding non-physical falloff in the data for $\cos\theta_{\mathscr{H},a_0}$. As we suspect that this is not a well-modeled sector of the detector for our decay channel, we will confine the pseudoscalar hypothesis test to only the region in which we believe the acceptance is being modeled correctly, such that,

$$\cos\theta_{\mathscr{H},a_0} < 0.7. \tag{107}$$

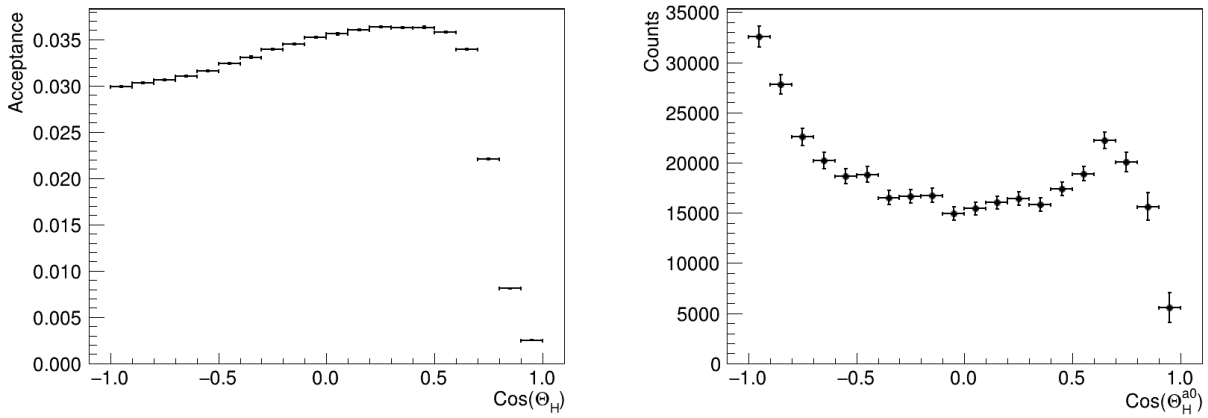

A **B**

Figure 62. Phase space acceptance of $\gamma p \to K^+ K_s \pi^-$ vs $\cos\theta_{\mathscr{H},a_0}$ (A) and the acceptance corrected distribution of $\cos\theta_{\mathscr{H},a_0}$ (B) for the $p' K^+ K_s \pi^-$ final state. There is a sharp falloff in the acceptance towards forward angles that is likely not a true representation of the detector response.

5.6.3 Pseudoscalar Helicity Angle Hypothesis

The hypothesis test for the pseudoscalar η is found in [47]. The distribution of a daughter particle in the helicity frame of it's parent particle can be described as a function of the spin-parity of the parent particle. A pseudoscalar ($J^{PC} = 0^{-+}$) parent particle will produce an angular distribution according to,

$$\frac{d\sigma}{d\cos\theta_{\mathscr{H}}} \propto |d^0_{0,0}|^2 = c, \tag{108}$$

and an axial-vector ($J^{PC} = 1^{++}$) parent particle will produce an angular distribution given by,

$$\frac{d\sigma}{d\cos\theta_{\mathscr{H}}} \propto \alpha|d^1_{0,0}|^2 + \beta(|d^1_{1,0}|^2 + |d^1_{-1,0}|^2) = \alpha\cos^2\theta_{\mathscr{H}} + \beta\cos^2\theta_{\mathscr{H}}, \tag{109}$$

where α and β are scaling factors and d are the Wigner d functions defined as,

$$d^J_{\lambda_J(\lambda_{a_0}-\lambda_\pi)} = d^J_{M_J,0}, \tag{110}$$

where J is the spin of the mother particle and λ is the helicity of the mother and daughter particles.

We fit the distribution of $\cos\theta_{\mathscr{H},a_0}$ with functions corresponding to the pseudoscalar Eqn. 108 and axial-vector Eqn. 109 hypothesis and evaluate the goodness of the fit to determine the probability of the distribution being entirely from a pseudoscalar or axial-vector. These fits don't take into account any mixing of the states. A full partial wave analysis would be needed and that extends beyond the scope of this work. This is discussed further in §6.7. The fits to the $\cos\theta_{\mathscr{H},a_0}$ distributions and the corresponding χ^2/ndf values for both $K^{\mp}K_s\pi^{\pm}$ final states are shown in Figures 63A, 63B. The pseudoscalar hypothesis does not describe the observed $\cos\theta_{\mathscr{H},a_0}$ distribution well. The axial-vector hypothesis is in much better agreement with the data, particularly for the $K^+K_s\pi^-$ final state. We cannot use this test to state that the resonance at $M(KK\pi) = 1.28$ GeV is unequivocally $f_1(1285)$, but it does let us reject the hypothesis that the resonance is entirely $\eta(1295)$. Indeed, it also suggests that the observed enhancement is primarily $f_1(1285)$, as the hypothesis for the axial vector is much stronger than that of the pseudoscalar. These fit results are in good agreement with the fits from [47] which are shown in Figures 63C, 63D. The strong suggestion of spin-1 dominance at $M(KK\pi) = 1.28$ GeV is also agreement with the results of [9] and other non-πp scattering experiments.

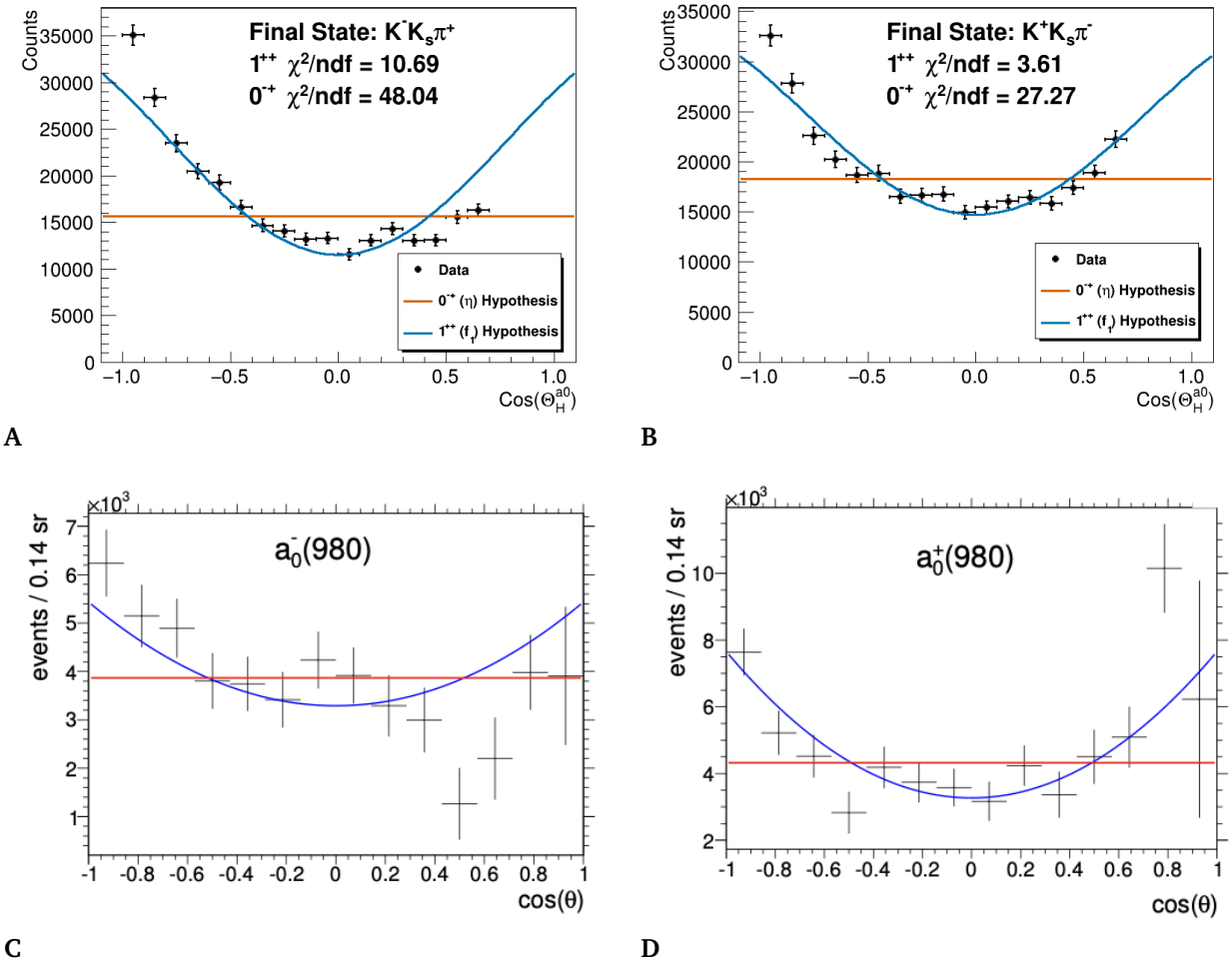

Figure 63. 0^{-+} and 1^{++} hypothesis fits to $\cos\theta_{\mathscr{H},a_0}$ for GlueX and CLAS]. GlueX distributions of $\cos\theta_{\mathscr{H},a_0}$ for $p'K^-K_s\pi^+$ (A) and $p'K^+K_s\pi^-$ (B) in the region of trusted detector efficiency modeling with fits to the data for the pseudoscalar $0^{-+}(\eta)$ (red) and axial-vector $1^{++}(f_1)$ (blue). Fit quality χ^2/ndf is shown on the plots. The axial-vector hypothesis fits are in much better agreement with the data compared to the pseudoscalar. The GlueX results are in good agreement with those from CLAS (C, D). CLAS figures from [47].

5.7 KK AND $K\pi$ MASS DISTRIBUTIONS

As discussed in §1.3.1, the $f_1(1285)$ has been proposed as a dynamically generated KK^* molecule. The authors of [17] calculated the lineshape of the $M(KK)$ and $M(K\pi)$ distributions assuming $f_1(1285)$ were a KK^* molecule but did not have data distributions to compare their predictions to. Figure 64 shows the normalized data distributions of $M(K^{\mp}K_s)$, $M(K^{\mp}\pi^{\pm})$, and $M(K_s\pi^{\pm})$ for both $K^{\mp}K_s\pi^{\pm}$ final states in the mass region of $f_1(1285)$ without the K^* rejection criteria applied. The $M(KK)$ distribution is forward peaked, as expected due to the $a_0(980)\pi$ decay mode. In turn, this shifts the $M(K\pi)$ distribution to higher masses. These distributions are not background subtracted, and the background could be on the order of 50%. These distributions are consistent with both the axial-vector nonet and KK^* molecule interpretation of the $f_1(1285)$.

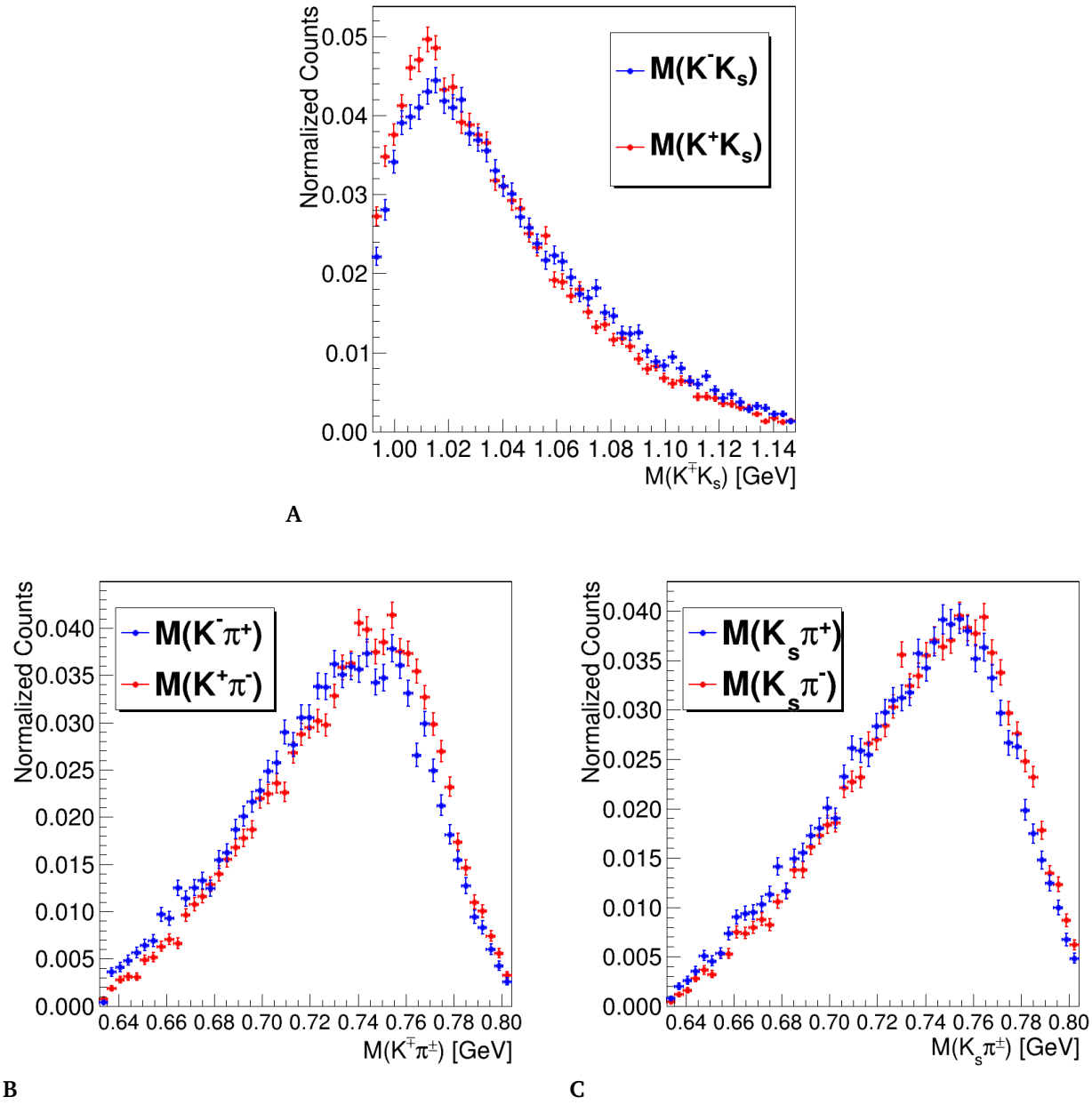

Figure 64. $M(KK)$ and $M(K\pi)$ distributions in mass region of $f_1(1285)$. The normalized distributions of $M(K^{\mp}K_s)$ (A), $M(K^{\mp}\pi^{\pm})$ (B), and $M(K_s\pi^{\pm})$ (C) for $p'K^-K_s\pi^+$ (blue) and $p'K^+K_s\pi^-$ (red) final states in the mass region of $f_1(1285)$ without K^* rejection criteria applied are shown These distributions were requested to evaluate the status of $f_1(1285)$ as a KK^* molecule.

CHAPTER 6

CONCLUSIONS

We have successfully measured the photoproduction differential cross-section as a function of Mandelstam-t of $f_1(1285)$ in the decay channels $f_1(1285) \to K^- K_s \pi^+$ and $f_1(1285) \to K^+ K_s \pi-$ at photon beam energies between $7.5 - 11.5$ GeV using the GlueX experiment, studied the helicity angle distribution of the $f_1(1285)$ daughter particles, and produced $M(KK)$ and $M(K\pi)$ distributions that could be useful in evaluating the status of $f_1(1285)$ as a KK^* molecule. These results will be discussed in greater detail in this chapter.

6.1 PARTICLE SPECIES IDENTIFICATION

While the $f_1(1285)$ is the more-oft studied particle, there is some evidence that there could be a pseudoscalar meson that decays to $KK\pi$ in the same mass region - the $\eta(1295)$. Evidence for the existence of this particle is sparse in non-πp scattering and there is speculation that the observed pseudoscalar may be a phantom state. Indeed, $\eta(1295)$ has rarely been observed in $KK\pi$ final states. Our fits to the data over all E_γ and $-t$ bins produce mass and width values that are multiple standard deviations closer to the PDG values for the f_1 compared to the η. This supports the assumption of the enhancement at $M(KK\pi) = 1.28$ GeV being dominated by the $f_1(1285)$. Additionally, the $cos(\Theta_H)$ distribution has the parabolic shape expected for a 1^{++} particle decay as opposed to the flat shape for a 0^{-+} resonance. We cannot rule out a $J = 0$ η contribution without a partial wave analysis - which has its own set of challenges - but preliminary studies of the $K^+K^-\pi^0$ channel

at GlueX have shown evidence that the $\eta(1295)$ is not present in this decay mode and may be a phantom state due to bleed-through from other waves in the PWA fits [118]. Previous photoproduction results from the CLAS collaboration also conclude that the feature at $M(KK\pi) = 1.28$ GeV is dominated by the $f_1(1285)$ and not the $\eta(1295)$. Finally, $\eta(1295)$ has only been clearly observed in $\eta \to KK\pi$ in two studies, both in $p\pi$ scattering experiments at BNL, and has been unobserved in many more [25], [33]. It is for these reasons we assume that the cross-section that we measure is dominated by the $f_1(1285)$ meson. To be clear, we cannot definitively state that the enhancement feature at $M(KK\pi) = 1.28$ GeV is entirely due to $f_1(1285)$ without a partial wave analysis to separate the different spin contributions, but due to the aforementioned reasons, we made a reasonable assumption that the measured photoproduction cross-section for $M(K^{\mp}K_s\pi^{\pm}) < 1.3$ is dominated by the $f_1(1285)$ meson.

6.2 CROSS-SECTION

The final photoproduction cross-section values of $f_1(1285)$ measured in both charge conjugated decay modes of $f_1(1285) \to K^{\mp}K_s\pi^{\pm}$, with the bin-by-bin systematic uncertainties included, is shown in Figure 65 and the values given in Tables 22, 23.

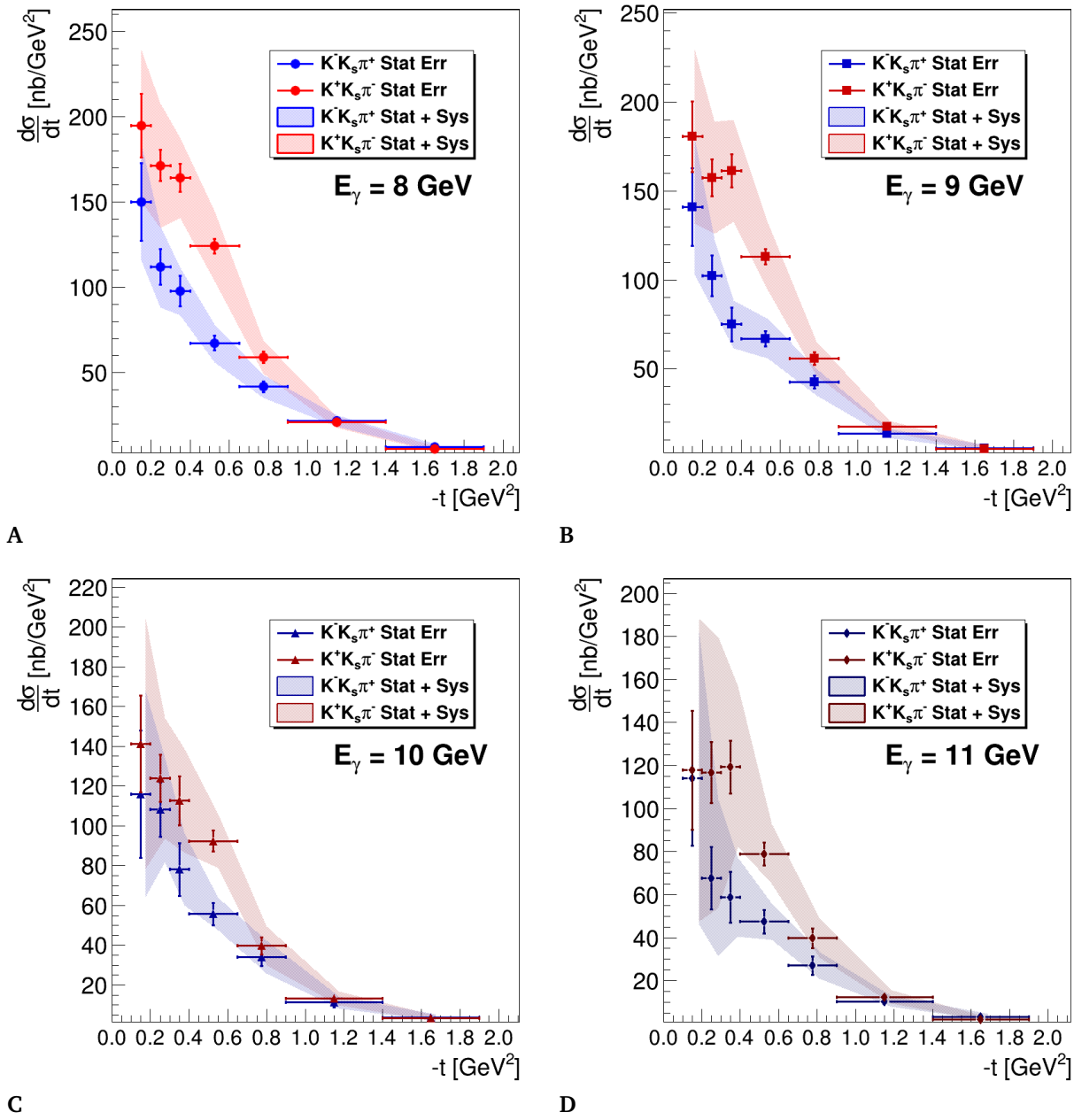

Figure 65. Photoproduction cross-section of $f_1(1285)$ with all uncertainties. Cross-section values $\frac{d\sigma}{dt}$ as a function of $-t$ for the photoproduction of $f_1(1285)$ measured in the $f_1(1285) \to K^- K_s \pi^+$ (blue points) and $f_1(1285) \to K^+ K_s \pi^-$ (red points) decay channels at different values of the photon beam energy E_γ. The error bars represent the statistical uncertainty and the shaded bands represent the systematic uncertainty from the fit and event selection criteria. Normalization uncertainties are not shown. (A) shows $E_\gamma = 8$ GeV, (B) shows $E_\gamma = 9$ GeV, (C) shows $E_\gamma = 10$ GeV, and (D) shows $E_\gamma = 11$ GeV. The beam energy the cross-section was measured in is also shown on the figure.

Table 22. Differential cross-section and uncertainties for each bin of E_γ and $-t$ for $f_1(1285)$ from the $f_1(1285) \to K^+K_s\pi^-$ decay channel.

E_γ [GeV]	$-t$ [GeV^2]	$d\sigma/dt$ [nb/GeV^2]	δ_{stat}	δ_{sys}	δ_{total}
8.0	0.150	149.9	22.7	25.7	34.2
8.0	0.250	111.9	10.4	21.4	23.8
8.0	0.350	97.7	8.9	10.8	14.0
8.0	0.525	67.3	4.3	10.2	11.1
8.0	0.775	41.8	3.2	6.0	6.8
8.0	1.150	21.8	2.0	2.8	3.4
8.0	1.650	6.4	1.3	1.5	2.0
9.0	0.163	140.8	21.8	31.3	38.1
9.0	0.263	102.4	11.5	17.0	20.5
9.0	0.362	75.0	9.4	9.4	13.3
9.0	0.537	67.0	4.4	10.2	11.1
9.0	0.787	42.7	3.6	6.4	7.4
9.0	1.162	13.8	1.8	1.6	2.4
9.0	1.662	5.6	1.2	1.1	1.7
10.0	0.175	116.0	32.0	40.4	51.6
10.0	0.275	108.1	13.6	22.7	26.5
10.0	0.375	78.1	13.3	12.1	18.0
10.0	0.550	55.7	5.5	6.0	8.1
10.0	0.800	34.0	4.4	7.0	8.3
10.0	1.175	11.3	2.4	1.9	3.0
10.0	1.675	3.6	1.5	0.7	1.6
11.0	0.188	114.1	31.3	60.4	68.1
11.0	0.287	67.7	14.4	33.6	36.5
11.0	0.387	58.7	11.9	14.0	18.3
11.0	0.562	47.4	5.4	6.3	8.3
11.0	0.812	27.1	4.3	4.5	6.2
11.0	1.188	10.4	2.1	1.6	2.6
11.0	1.688	3.1	1.3	0.7	1.5

Table 23. Differential cross-section and uncertainties for each bin of E_γ and $-t$ for $f_1(1285)$ from the $f_1(1285) \to K^- K_s \pi^+$ decay channel.

E_γ [GeV]	$-t$ [GeV^2]	$d\sigma/dt$ [nb/GeV^2]	δ_{stat}	δ_{sys}	δ_{total}
8.0	0.150	194.7	18.8	38.9	43.2
8.0	0.250	171.4	9.0	26.0	27.5
8.0	0.350	164.1	8.2	27.4	28.6
8.0	0.525	124.2	4.3	16.4	17.0
8.0	0.775	59.0	3.3	7.3	8.0
8.0	1.150	21.1	1.6	2.9	3.3
8.0	1.650	5.3	1.1	0.7	1.3
9.0	0.163	180.4	19.9	41.5	46.1
9.0	0.263	157.3	10.4	25.4	27.4
9.0	0.362	161.2	9.3	19.3	21.4
9.0	0.537	113.0	4.4	12.8	13.5
9.0	0.787	55.8	3.6	8.7	9.4
9.0	1.162	17.8	2.1	3.3	3.9
9.0	1.662	5.0	1.2	0.8	1.4
10.0	0.175	141.2	24.3	61.5	66.1
10.0	0.275	123.9	11.8	28.9	31.2
10.0	0.375	112.6	12.4	14.8	19.3
10.0	0.550	92.3	5.2	14.8	15.7
10.0	0.800	39.7	4.2	7.0	8.1
10.0	1.175	13.3	2.0	2.2	3.0
10.0	1.675	3.2	1.4	0.8	1.6
11.0	0.188	117.8	27.6	64.1	69.8
11.0	0.287	116.7	14.3	38.8	41.3
11.0	0.387	119.4	12.3	19.8	23.3
11.0	0.562	78.8	5.3	10.8	12.0
11.0	0.812	39.8	4.6	5.7	7.3
11.0	1.188	12.5	2.0	2.8	3.4
11.0	1.688	2.0	1.0	0.8	1.3

6.3 SHAPE OF THE CROSS SECTION

The shape of the differential cross section as a function of Mandelstam-t $\frac{d\sigma}{dt}$ can provide insight into the process by which a particle is produced in a scattering event. The

photoproduction of $f_1(1285)$ is expected to be t-channel dominant. Our results show an exponential fall-off in $\frac{d\sigma}{dt}$ towards higher values of $-t$ which is consistent with the production mechanism for the photoproduction of the $f_1(1285)$ meson being t-channel dominant. Previous measurements of $f_1(1285)$ photoproduction did not see a differential cross section that suggested t-channel dominant production, so this result is notable, as it is more in-line with the production mechanism used to describe this reaction in theoretical models like [48], [51], [54]. In particular, the CLAS measurement results were more consistent with an s-channel N^* decay, but there were no reasonable N^* candidates in the expected mass region per the PDG [9], [86]. The results of this work do not suggest any s-channel production and are in-line with the expected shape for a t-channel production mechanism.

Generally, the shape of the differential cross-secton as a function of $-t$ can be expressed as,

$$\frac{d\sigma}{dt} = A_\sigma e^{-bt}, \tag{111}$$

where A_σ is some scaling factor, t is Mandelstam-t, and b is the "slope". We fit this function to our measured cross-section for each E_γ bin to evaluate if there is an energy dependence to the cross-section. These fits are shown in Figure 66. The uncertainty on these slopes is on the order of 15%, so we are not sensitive to an energy dependence of the cross-section that is smaller than that. Therefore we can only conclude that if there is a dependence for the photoproduction cross-section of $f_1(1285)$ on the incoming beam photon energy E_γ, it is smaller than our measurement is sensitive to.

We also can compare the slope of the cross-sections to other types of mesons, like the vector meson ϕ. We fit the slope of the differential cross-section $\frac{d\sigma}{dt}$ for ϕ measured in

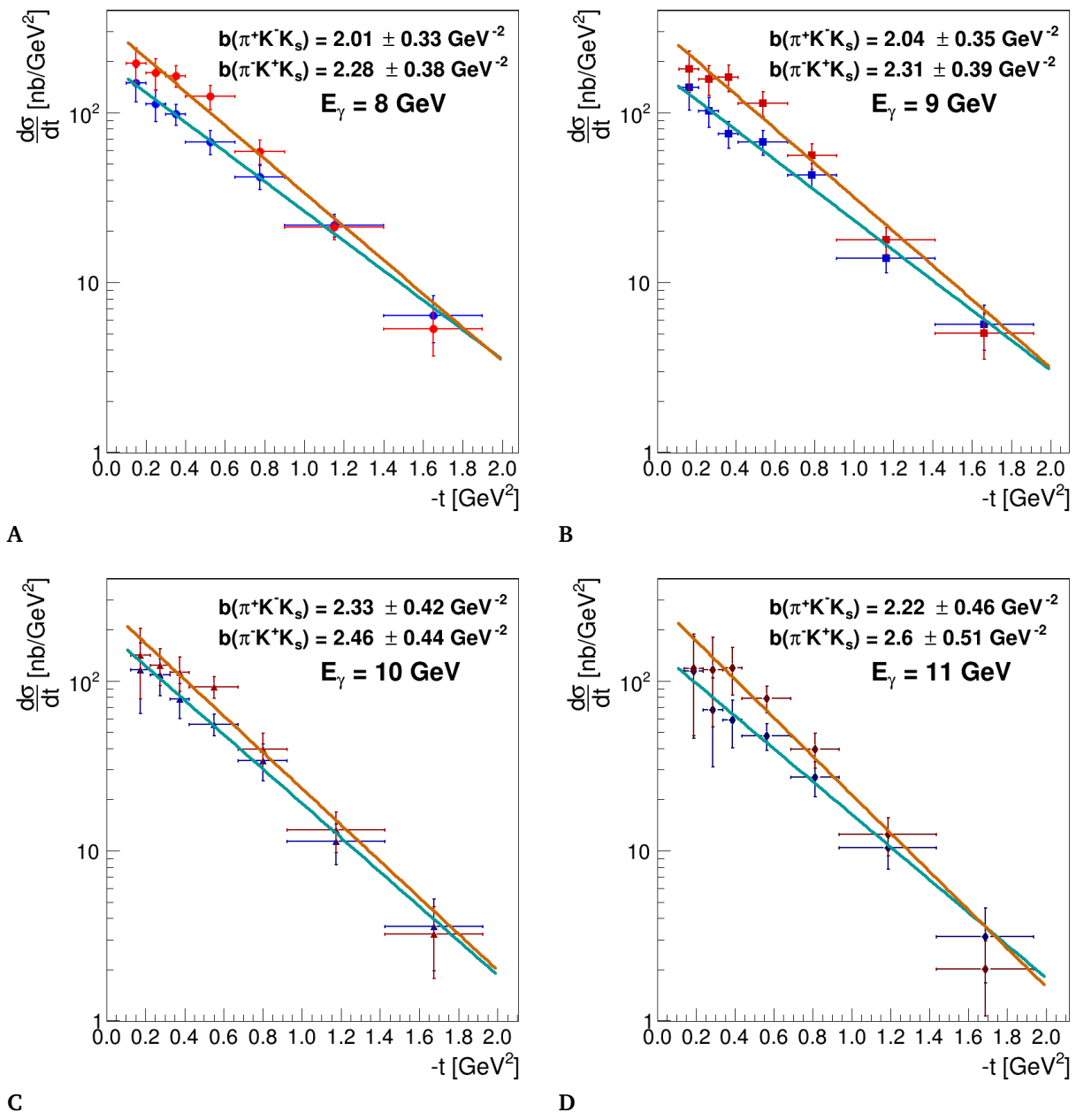

Figure 66. Cross-sections of $f_1(1285)$ with fits for t-slope. The cross-sections from Figure 65 with fits of the form $\frac{d\sigma}{dt} = Ae^{-bt}$. Cross-sections are shown on a log scale. The cyan and orange lines show the fits to the $K^-K_s\pi^+$ and $K^+K_s\pi^-$ data respectively. The values for the energy E_γ and slope parameter b are shown on the figure. Error bars represent total uncertainty. (A) shows $E_\gamma = 8$ GeV, (B) shows $E_\gamma = 9$ GeV, (C) shows $E_\gamma = 10$ GeV, and (D) shows $E_\gamma = 11$ GeV. The beam energy the cross-section was measured in is also shown on the figure.

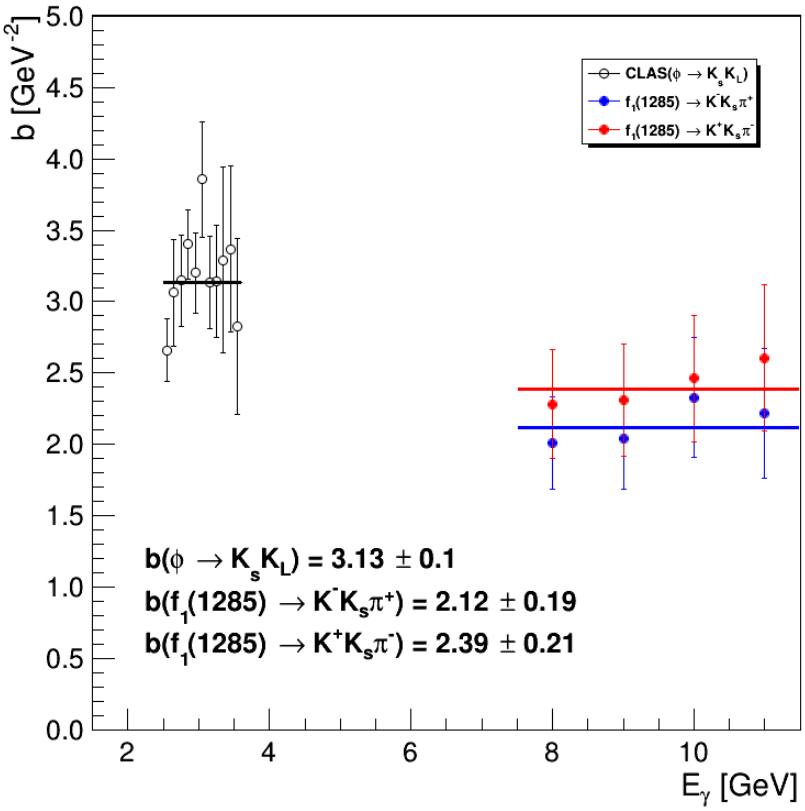

Figure 67. b vs E_γ for ϕ (CLAS) and $f_1(1285)$. Slope of the differential cross-section $\frac{d\sigma}{dt}$ of the vector meson ϕ measured in $K_s K_L$ decays at CLAS (black points) [119] compared to the cross-section of $f_1(1285)$ measured in $K^- K_s \pi^+$ (blue points) and $K^+ K_s \pi^-$ (red points) decays in this work. The fits to the respective datasets are shown in the black, blue, and red lines, and the slope values are shown. The $f_1(1285)$ slope is smaller than that of ϕ. This suggests that $f_1(1285)$ is produced with a different mechanism compared to the ϕ.

photoproduction at CLAS [119] and the $f_1(1285)$ in this work with a constant to get an idea of the relative scale of the t-slopes. Figure 67 shows the slope of the measured differential cross-section as a function of beam photon energy E_γ for ϕ and $f_1(1285)$. The slope of ϕ is steeper than that of $f_1(1285)$. The ϕ meson is produced via pomeron exchange, which the $f_1(1285)$ cannot be. The cross-section of $f_1(1285)$ is consistent with Regge exchange.

6.4 MAGNITUDE OF THE CROSS SECTION

The measurement of $f_1(1285)$ photoproduction at low E_γ with the CLAS experiment prompted the formulation of new theoretical models for the production mechanism of $f_1(1285)$ in photoproduction. These models sought to describe the production mechanism of $f_1(1285)$ with an interpolated Regge model [51], [52]. The result of both models fit the CLAS data well. The authors of [51] expanded their predictions to the higher photon beam energies of GlueX such that we could test the model [54]. The theoretical predictions at different photon beam energies are shown along with the measured values in this work in Figure 68. The magnitude of our measured cross-section disagrees with the predictions by roughly an order of magnitude. Indeed, the absolute magnitude of our measurement is in better agreement with the measurements made by CLAS, seen in Figure 69 [45]. However, the shape of the cross-section is in good agreement with the model predictions which further reinforces our conclusion that the photoproduction of $f_1(1285)$ is dominated by t-channel exchange. The magnitude of our measured cross-section is also seemingly in good agreement with the predictions made by Kochelev at $E_\gamma \simeq 3$ GeV for the CLAS experiment [48]. We requested that updated predictions for GlueX beam energies be produced by the authors, but unfortunately the lead author on the paper passed away. We believe that producing higher E_γ predictions for $f_1(1285)$ would be an interesting and worthwhile study for the theory community to undertake.

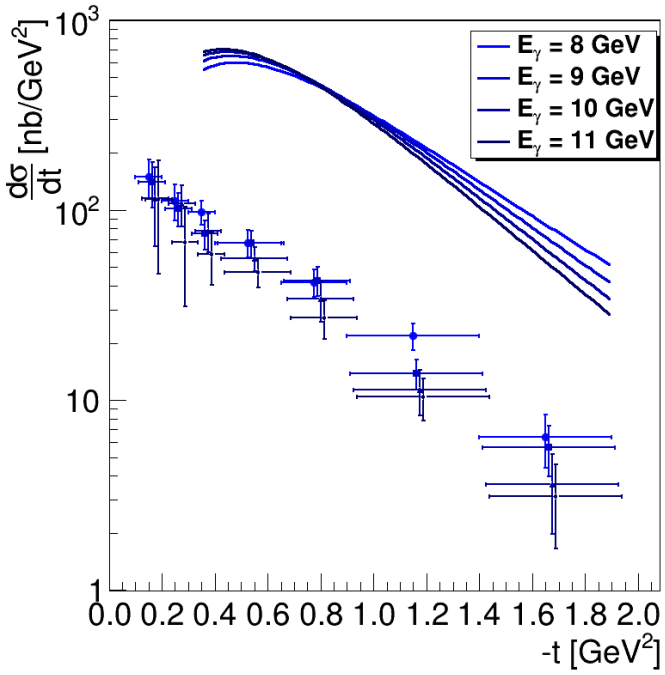

A

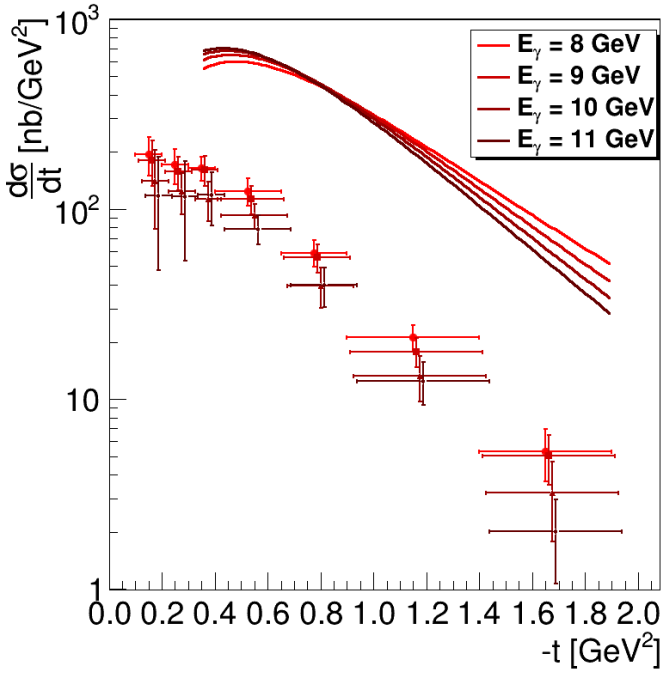

B

Figure 68. Comparison between the cross-section of $f_1(1285)$ (points with error bars) as measured in $f_1(1285) \to K^- K_s \pi^+$ (A) and $f_1(1285) \to K^+ K_s \pi^-$ (B) and theoretical predictions (solid lines) from He [51], [54] for different values of E_γ. Bin centers are shifted slightly in $-t$ for clarity. Error bars represent total uncertainty.

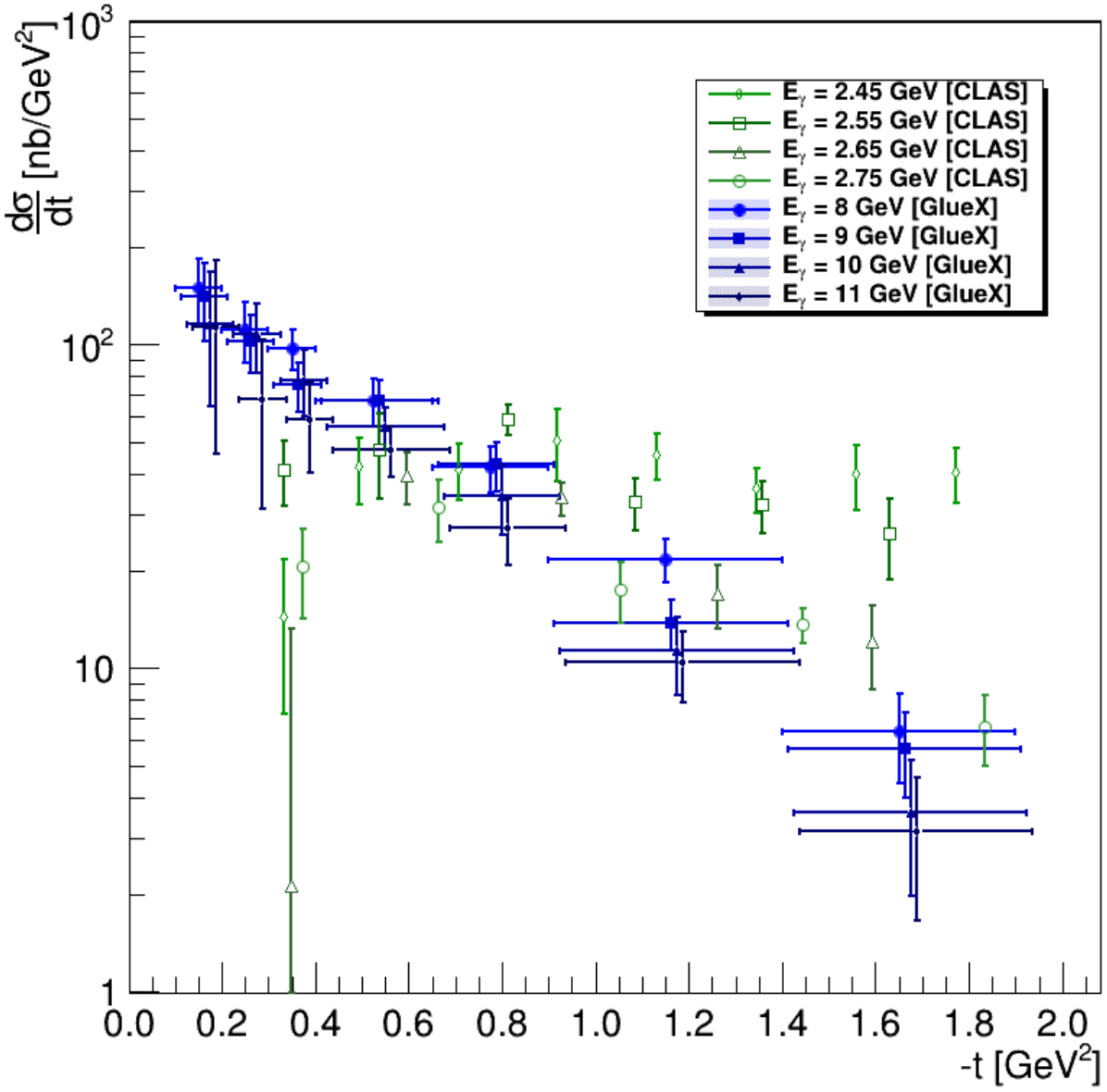

Figure 69. Differential cross-section $\frac{d\sigma}{dt}$ for $f_1(1285)$ from this work at GlueX (blue points) and at CLAS (green points) for relevant values of $-t$ [9]. The CLAS cross-section is flat at low E_γ but grows sharper as E_γ increases, consistent with s-channel production due to the lower center-of-mass energies at CLAS near the N^* mass threshold. The absolute magnitude for the cross-section across all beam energies shown is comparable. Bin centers are shifted slightly in $-t$ for clarity. Error bars represent total uncertainty.

6.5 DIFFERENCE IN CROSS-SECTION BY DECAY MODE

The difference in the cross-section measured in different charge conjugated channels of $f_1(1285) \to K^{\mp}K_s\pi^{\pm}$ appears to be due to a physical effect as opposed to an analytical one. We have ruled out that the difference is due to a difference in reconstruction or analysis efficiency. Figure 54 shows quite strikingly that the asymmetry between the data counts exists only in the $M(KK\pi)$ regions corresponding to the potential resonant states. It is particularly notable that the slope of the ratio changes right at the edge of the $f_1(1285)$ mass region. The behavior of the $K^{\mp}K_s\pi^{\pm}$ count ratio points to an underlying physical mechanism as the source of the difference.

The most likely candidate of the source of the difference appears to be N^* resonances. Figure 57 shows that there is an excess of events in the $M(p\pi^-)$ regions where we know N^* resonances exist in our data, as seen in comparisons to the full $M(KK\pi)$ range in Figure 58. We suggest some type of constructive/destructive interference between the amplitudes of these two states as a potential source of the cross-section asymmetry.

This result was unexpected and striking. However, it appears that this may not be the only analysis to have observed a yield difference in the $f_1(1285) \to K^{\mp}K_s\pi^{\pm}$ decay modes. A careful study of published $M(K^{\mp}K_s\pi^{\pm})$ distributions from CLAS and Fermilab show that the asymmetrical behavior in both resonant $M(KK\pi)$ regions at 1.28 and 1.4 GeV has been seen before. These distributions are shown in Figure 70. These distributions are not acceptance corrected and were not produced by GlueX, so it is impossible to make concrete statements on the nature of the count discrepancy, but the observed behavior of $f_1(1285) \to K^{\mp}K_s\pi^{+}$ work is also seen in these studies. This is further evidence of a real

physical phenomena driving the difference in the measured cross-section.

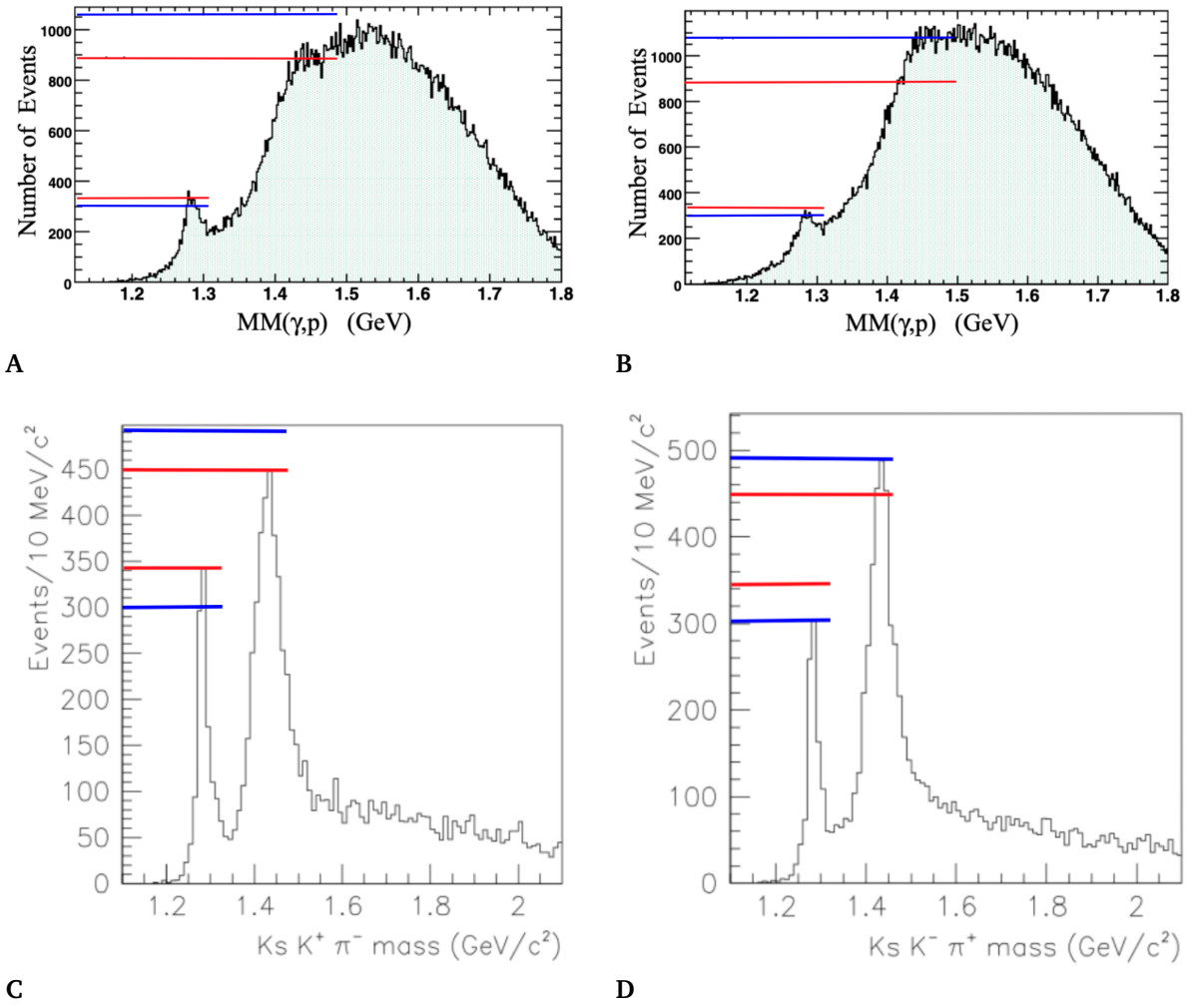

Figure 70. Raw count distributions for $K^+K_s\pi^-$ (left) and $K^-K_s\pi^+$ (right) from CLAS (A, B) [9] and FNAL E690 (C, D) [44]. The blue and red lines extending to the y-axis show the value of maximum counts of the $M(K^-K_s\pi^+)$ and $M(K^+K_s\pi^-)$ enhancements at $M = 1.28$ and $M = 1.4$ GeV, respectively. The same asymmetric behavior is seemingly observed. Figures taken from [9], [44].

6.6 $f_1(1285)$ AS A $KK^* + C.C.$ MOLECULE

The $f_1(1285)$ is generally assumed to be the low-mass $q\bar{q}$ member of the axial-vector nonet, which is experimentally supported by the results of [15] and [46]. However, it has been proposed that $f_1(1285)$ is a dynamically generated state from a KK^* molecule and the potential $M(KK)$ and $M(K\pi)$ distributions given that assumption have been calculated [17]. The authors requested that these distributions be produced so that this hypothesis could could be studied in greater detail. We have presented these distributions in Figure 64 and compare them to the theorized distributions in Figures 71, 72. Our observed distributions are consistent with both the predicted distributions of a molecular state and a $q\bar{q}$ state decaying to $a_0(980)\pi$ but there is a significant amount of background contamination. We hope this data can be used in further study of the status of $f_1(1285)$.

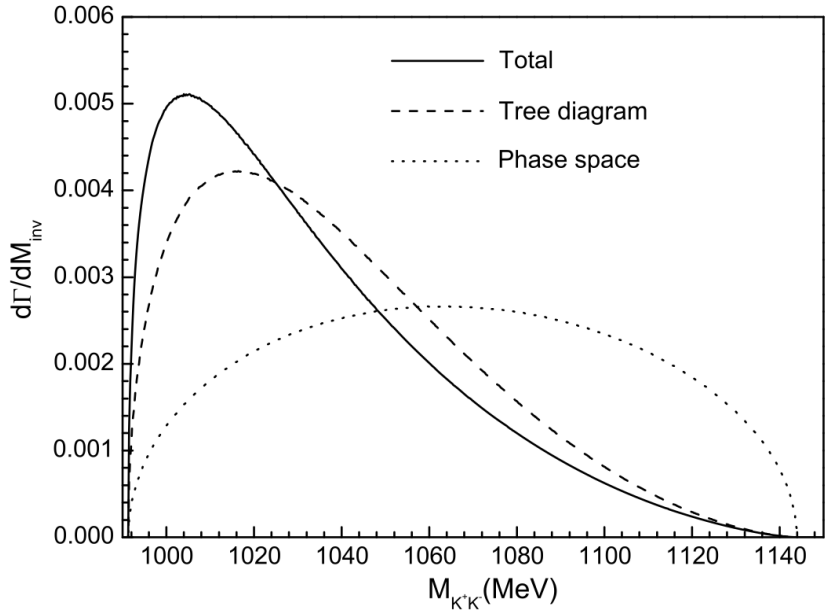

A

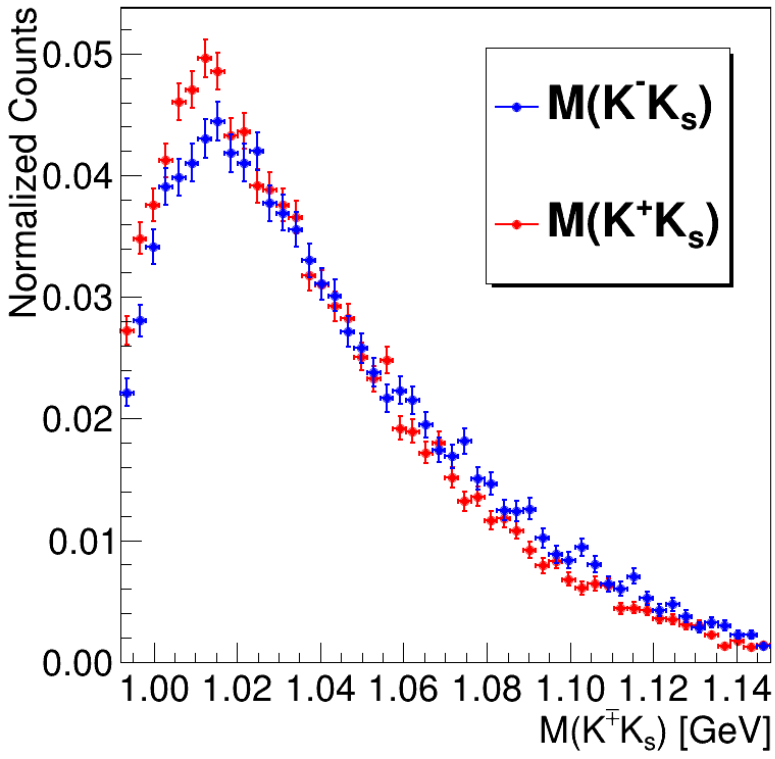

B

Figure 71. $M(KK)$ distributions in data and theory for KK^* molecule hypothesis. Comparison between theoretical predictions (A) for the distribution of $M(KK)$ assuming $f_1(1285)$ is dynamically generated as a KK^* molecule and distribution of $M(K^{\mp}K_s)$ (B) observed in the GlueX-I data. Figure (A) from [17].

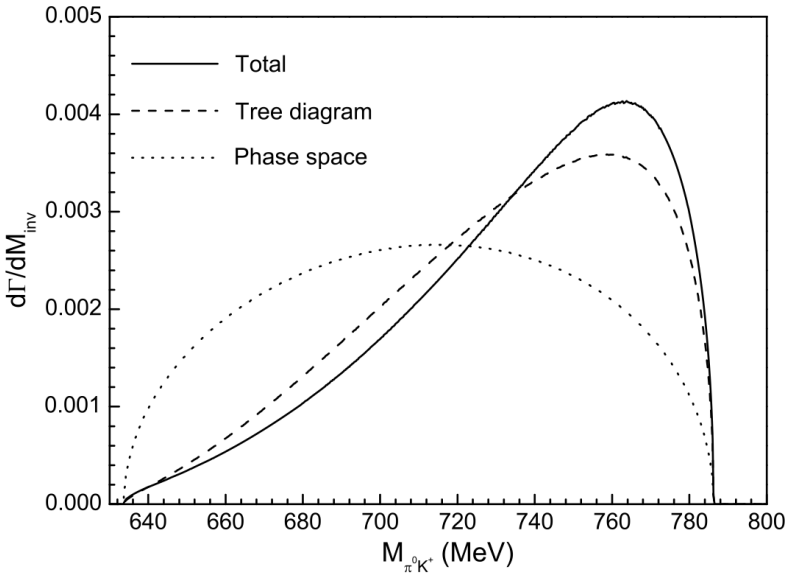

A

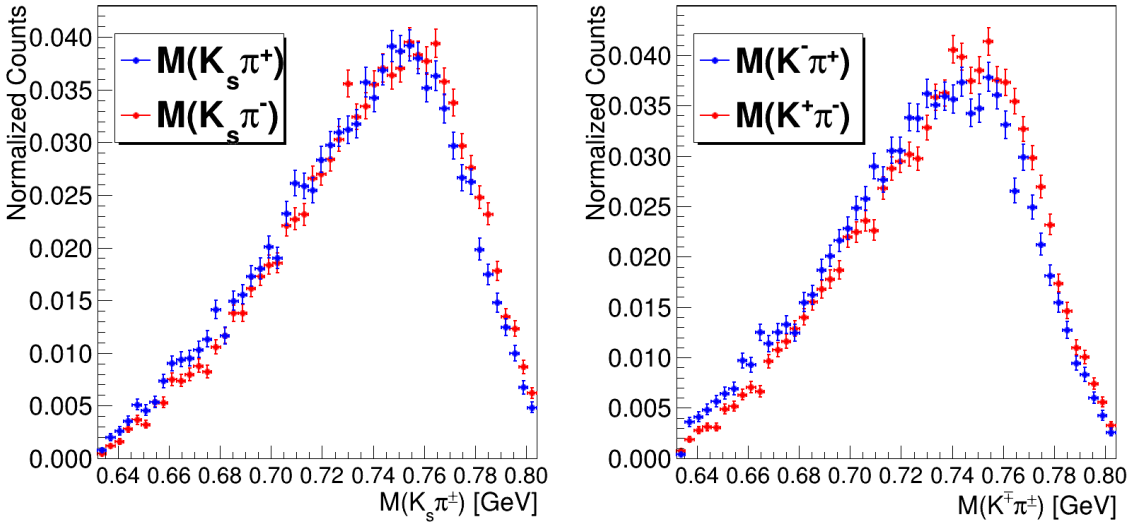

B C

Figure 72. Comparison between theoretical predictions (A) for the distribution of $M(K\pi)$ assuming $f_1(1285)$ is dynamically generated as a KK^* molecule and distribution of $M(K_s\pi)$ (B) and $M(K^{\mp}\pi)$ (C) observed in the GlueX-I data. Figure (A) from [17].

6.7 FUTURE WORK

The photoproduction of $f_1(1285)$ and the other axial-vector and pseudoscalar particles with $1.2 < M < 1.5$ requires more study. Most importantly, partial wave analyses of the $KK\pi$ and $\eta\pi\pi$ final states are needed to identify and constrain the radially excited pseudoscalar nonet and definitively determine if $\eta(1295)$ is observed in photoproduction. Additionally, the asymmetry in the cross-sections of the different $K^{\mp}K_s\pi^{\pm}$ charge conjugated modes requires a deeper study to understand the mechanism for the discrepancy. As this asymmetry appears to have been present in past $f_1 \to KK\pi$ studies at CLAS and Fermilab, determining the underlying physical process for the difference is important for the understanding the production of the $f_1(1285)$.

As a direct extension of this study, producing a more robust Monte Carlo sample that also includes the $f_1(1285) \to a_0\pi$ decay, higher mass resonances, and background phase space could play a part in reducing the uncertainty on the measured cross-section as you wouldn't need the K^* exclusion to isolate the $f_1(1285)$ from the background and would have a better constrained background in the binned fits. This could be useful for measuring branching fractions of $f_1(1285)$ and potentially $a_0(980)$.

REFERENCES

[1] Cush (2019), *Standard model of elementary particles*. [Online]. Available: https://en.wikipedia.org/wiki/File:Standard_Model_of_Elementary_Particles.svg.

[2] M. Gell-Mann, "A schematic model of baryons and mesons," *Physics Letters*, vol. 8, no. 3, pp. 214–215, 1964, ISSN: 0031-9163. DOI: 10.1016/S0031-9163(64)92001-3. [Online]. Available: https://doi.org/10.1016/S0031-9163(64)92001-3.

[3] G. Zweig, "An SU_3 model for strong interaction symmetry and its breaking," CM-P00042884, Tech. Rep., 1964.

[4] M. Gell-Mann and Y. Ne'eman, *The Eightfold Way*. W. A. Benjamin, 1964.

[5] W. Commons, *Meson nonet - spin 1.svg*, [Online; accessed 5-May-2024], 2020. [Online]. Available: https://commons.wikimedia.org/w/index.php?title=File:Meson_nonet_-_spin_1.svg&oldid=458584495.

[6] W. Heisenberg, "Über den bau der atomkerne," *Zeitschrift für Physik*, vol. 77, no. 1, pp. 1–11, 1932. DOI: 10.1007/BF01342433.

[7] R. L. Workman *et al.*, "Review of particle physics," *PTEP*, vol. 2022, p. 083C01, 2022, Section 15. Quark Model. DOI: 10.1093/ptep/ptac097. [Online]. Available: https://pdg.lbl.gov/2023/reviews/rpp2023-rev-quark-model.pdf.

[8] R. L. Workman *et al.*, "Review of particle physics," *PTEP*, vol. 2022, p. 083C01, 2022, Section 63. Spectroscopy of Light Meson Resonances. DOI: 10.1093/ptep/

ptac097. [Online]. Available: https://pdg.lbl.gov/2023/reviews/rpp2023-rev-light-mesons-spectroscopy.pdf.

[9] R. Dickson *et al.*, "Photoproduction of the $f_1(1285)$ meson," *Phys. Rev. C*, vol. 93, p. 065 202, 6 Jun. 2016. DOI: 10.1103/PhysRevC.93.065202. [Online]. Available: https://link.aps.org/doi/10.1103/PhysRevC.93.065202.

[10] R. L. Workman *et al.*, "Review of particle physics," *PTEP*, vol. 2022, p. 083C01, 2022, $f_1(1285)$. DOI: 10.1093/ptep/ptac097. [Online]. Available: https://pdg.lbl.gov/2023/listings/rpp2023-list-f1-1285.pdf.

[11] D. H. Miller *et al.*, "$K\overline{K}\pi$ resonance at 1280 MeV," *Phys. Rev. Lett.*, vol. 14, pp. 1074–1077, 26 Jun. 1965. DOI: 10.1103/PhysRevLett.14.1074. [Online]. Available: https://link.aps.org/doi/10.1103/PhysRevLett.14.1074.

[12] C. D'Andlau *et al.*, "Evidence for a non-strange meson of mass 1290 MeV," *Physics Letters*, vol. 17, no. 3, pp. 347–352, 1965, ISSN: 0031-9163. DOI: https://doi.org/10.1016/0031-9163(65)90562-7. [Online]. Available: https://www.sciencedirect.com/science/article/pii/0031916365905627.

[13] L. de Billy *et al.*, "Spin and parity of the D0(1285) meson," *Nuclear Physics B*, vol. 176, no. 1, pp. 1–12, 1980, ISSN: 0550-3213. DOI: https://doi.org/10.1016/0550-3213(80)90060-7. [Online]. Available: https://www.sciencedirect.com/science/article/pii/0550321380900607.

[14] H.-Y. Cheng, "Revisiting axial-vector meson mixing," *Physics Letters B*, vol. 707, no. 1, pp. 116–120, 2012, ISSN: 0370-2693. DOI: https://doi.org/10.1016/j.

physletb.2011.12.013. [Online]. Available: https://www.sciencedirect.com/science/article/pii/S0370269311014705.

[15] R. Aaij *et al.*, "Observation of $\overline{B}^0_{(s)} \to J/\psi\, f_1(1285)$ decays and measurement of the $f_1(1285)$ mixing angle," *Phys. Rev. Lett.*, vol. 112, p. 091 802, 9 Mar. 2014. DOI: 10.1103/PhysRevLett.112.091802. [Online]. Available: https://link.aps.org/doi/10.1103/PhysRevLett.112.091802.

[16] L. Roca, E. Oset, and J. Singh, "Low lying axial-vector mesons as dynamically generated resonances," *Phys. Rev. D*, vol. 72, p. 014 002, 1 Jul. 2005. DOI: 10.1103/PhysRevD.72.014002. [Online]. Available: https://link.aps.org/doi/10.1103/PhysRevD.72.014002.

[17] F. Aceti, J.-J. Xie, and E. Oset, "The $KK\pi$ decay of the $f_1(1285)$ and its nature as a $K^*K - cc$ molecule," *Physics Letters B*, vol. 750, pp. 609–614, 2015, ISSN: 0370-2693. DOI: https://doi.org/10.1016/j.physletb.2015.09.068. [Online]. Available: https://www.sciencedirect.com/science/article/pii/S0370269315007431.

[18] C. Dionisi *et al.*, "Observation and quantum numbers determination of the E(1420) meson in $\pi^- p$ interactions at 3.95 GeV/c," *Nuclear Physics B*, vol. 169, no. 1, pp. 1–19, 1980, ISSN: 0550-3213. DOI: https://doi.org/10.1016/0550-3213(80)90249-7. [Online]. Available: https://www.sciencedirect.com/science/article/pii/0550321380902497.

[19] G. Gidal *et al.*, "Observation of spin-1 $f_1(1285)$ in the reaction $\gamma\gamma^* \to \eta^0\pi^+\pi^-$," *Phys. Rev. Lett.*, vol. 59, pp. 2012–2015, 18 Nov. 1987. DOI: 10.1103/PhysRevLett.

59.2012. [Online]. Available: https://link.aps.org/doi/10.1103/PhysRevLett.59.2012.

[20] R. L. Workman *et al.*, "Review of particle physics," *PTEP*, vol. 2022, p. 083C01, 2022, $f_1(1420)$. DOI: 10.1093/ptep/ptac097. [Online]. Available: https://pdg.lbl.gov/2023/listings/rpp2023-list-f1-1420.pdf.

[21] R. S. Longacre, "E(1420) meson as a $KK\pi$ Molecule," *Phys. Rev. D*, vol. 42, pp. 874–883, 3 Aug. 1990. DOI: 10.1103/PhysRevD.42.874. [Online]. Available: https://link.aps.org/doi/10.1103/PhysRevD.42.874.

[22] R. L. Workman *et al.*, "Review of particle physics," *PTEP*, vol. 2022, p. 083C01, 2022, $f_1(1510)$. DOI: 10.1093/ptep/ptac097. [Online]. Available: https://pdg.lbl.gov/2023/listings/rpp2023-list-f1-1510.pdf.

[23] I. Cohen and H. Lipkin, "A phenomenological model for pseudoscalar meson mixing," *Nuclear Physics B*, vol. 151, pp. 16–28, 1979, ISSN: 0550-3213. DOI: 10.1016/0550-3213(79)90424-3. [Online]. Available: https://doi.org/10.1016/0550-3213(79)90424-3.

[24] G. Adams *et al.*, "Observation of pseudoscalar and axial vector resonances in $\pi^- p \to K^+K^-\pi^0 n$ at 18 GeV," *Physics Letters B*, vol. 516, no. 3, pp. 264–272, 2001, ISSN: 0370-2693. DOI: https://doi.org/10.1016/S0370-2693(01)00951-0. [Online]. Available: https://www.sciencedirect.com/science/article/pii/S0370269301009510.

[25] J. J. Manak *et al.*, "Partial-wave analysis of the $\eta\pi^+\pi^-$ system produced in the reaction $\pi^- \overrightarrow{p}\, \eta\pi^+\pi^- n$ at 18GeV/c," *Phys. Rev. D*, vol. 62, p. 012 003, 1 Jun. 2000.

DOI: 10.1103/PhysRevD.62.012003. [Online]. Available: https://link.aps.org/doi/10.1103/PhysRevD.62.012003.

[26] M. G. Rath *et al.*, "The $K_S^0 K_S^0 \pi^0$ system produced in $\pi^- p$ interactions at 21.4 GeV/c," *Phys. Rev. D*, vol. 40, pp. 693–705, 3 Aug. 1989. DOI: 10.1103/PhysRevD.40.693. [Online]. Available: https://link.aps.org/doi/10.1103/PhysRevD.40.693.

[27] J. .-. Augustin *et al.*, "Partial-wave analysis of DM2 Collaboration data in the $\eta(1430)$ energy range," *Phys. Rev. D*, vol. 46, pp. 1951–1958, 5 Sep. 1992. DOI: 10.1103/PhysRevD.46.1951. [Online]. Available: https://link.aps.org/doi/10.1103/PhysRevD.46.1951.

[28] Z. Bai *et al.*, "Partial-wave analysis of j/$\psi \to \gamma K_S^0 K^{\pm}\pi^{\mp}$," *Phys. Rev. Lett.*, vol. 65, pp. 2507–2510, 20 Nov. 1990. DOI: 10.1103/PhysRevLett.65.2507. [Online]. Available: https://link.aps.org/doi/10.1103/PhysRevLett.65.2507.

[29] A. Bertin *et al.*, "E decay to $KK\pi$ in pp annihilation at rest," *Physics Letters B*, vol. 361, no. 1, pp. 187–198, 1995, ISSN: 0370-2693. DOI: https://doi.org/10.1016/0370-2693(95)01136-E. [Online]. Available: https://www.sciencedirect.com/science/article/pii/037026939501136E.

[30] A. Bertin *et al.*, "A search for axial vectors in $pp \to K^{\pm}K^0\pi^{\mp}\pi^+\pi^-$ annihilations at rest in gaseous hydrogen at NTP," *Physics Letters B*, vol. 400, no. 1, pp. 226–238, 1997, ISSN: 0370-2693. DOI: https://doi.org/10.1016/S0370-2693(97)00300-6. [Online]. Available: https://www.sciencedirect.com/science/article/pii/S0370269397003006.

[31] C. Cicalo' *et al.*, "Evidence for two pseudoscalar states in the 1.4–1.5 GeV mass region," *Physics Letters B*, vol. 462, no. 3, pp. 453–461, 1999, ISSN: 0370-2693. DOI: https://doi.org/10.1016/S0370-2693(99)00898-9. [Online]. Available: https://www.sciencedirect.com/science/article/pii/S0370269399008989.

[32] F. Nichitiu *et al.*, "Study of the $K^+K^-\pi^+\pi^-\pi^0$ final state in antiproton annihilation at rest in gaseous hydrogen at NTP with the OBELIX spectrometer," *Physics Letters B*, vol. 545, no. 3, pp. 261–271, 2002, ISSN: 0370-2693. DOI: https://doi.org/10.1016/S0370-2693(02)02547-9. [Online]. Available: https://www.sciencedirect.com/science/article/pii/S0370269302025479.

[33] M. Acciarri *et al.*, "Light resonances in $K_{0S}K\pm\pi^{\pm}$ and $\eta\pi\pi$ final states in $\gamma\gamma$ collisions at LEP," *Physics Letters B*, vol. 501, no. 1, pp. 1–11, 2001, ISSN: 0370-2693. DOI: https://doi.org/10.1016/S0370-2693(01)00102-2. [Online]. Available: https://www.sciencedirect.com/science/article/pii/S0370269301001022.

[34] R. Ahohe *et al.*, "Search for $\eta(1475)\rightarrow K^0_S K^{\pm}\pi^{\mp}$ in two-photon fusion at the CLEO detector at Cornell," *Phys. Rev. D*, vol. 71, p. 072 001, 7 Apr. 2005. DOI: 10.1103/PhysRevD.71.072001. [Online]. Available: https://link.aps.org/doi/10.1103/PhysRevD.71.072001.

[35] L. Faddeev, A. Niemi, and U. Wiedner, "Glueballs, closed fluxtubes, and $\eta(1440)$," *Phys. Rev. D*, vol. 70, p. 114 033, 11 2004. DOI: 10.1103/PhysRevD.70.114033. [Online]. Available: https://link.aps.org/doi/10.1103/PhysRevD.70.114033.

[36] G. Bali *et al.*, "A comprehensive lattice study of SU(3) glueballs," *Physics Letters B*, vol. 309, no. 3, pp. 378–384, 1993, ISSN: 0370-2693. DOI: https://doi.org/10.

1016/0370-2693(93)90948-H. [Online]. Available: https://www.sciencedirect.com/science/article/pii/037026939390948H.

[37] F. Aceti *et al.*, "Isospin breaking and $f_0(980)$-$a_0(980)$ mixing in the $\eta(1405) \to \pi^0 f_0(980)$ reaction," *Phys. Rev. D*, vol. 86, p. 114 007, 11 Dec. 2012. DOI: 10.1103/PhysRevD.86.114007. [Online]. Available: https://link.aps.org/doi/10.1103/PhysRevD.86.114007.

[38] E. Klempt and A. Zaitsev, "Glueballs, hybrids, multiquarks: Experimental facts versus QCD inspired concepts," *Physics Reports*, vol. 454, no. 1, pp. 1–202, 2007, ISSN: 0370-1573. DOI: 10.1016/j.physrep.2007.07.006.

[39] E. Klempt, "Hadron spectroscopy and strong QCD," *International Journal of Modern Physics A*, vol. 21, no. 04, pp. 739–746, 2006. DOI: 10.1142/S0217751X06031971.

[40] D. Barberis *et al.*, "A measurement of the branching fractions of the $f_1(1285)$ and $f_1(1420)$ produced in central pp interactions at 450 GeV/c," *Physics Letters B*, vol. 440, no. 1, pp. 225–232, 1998, ISSN: 0370-2693. DOI: https://doi.org/10.1016/S0370-2693(98)01264-7. [Online]. Available: https://www.sciencedirect.com/science/article/pii/S0370269398012647.

[41] D. Barberis *et al.*, "A study of the centrally produced $\pi^+\pi^-\pi^+\pi^-$ channel in pp interactions at 450 GeV/c," *Physics Letters B*, vol. 413, no. 1, pp. 217–224, 1997, ISSN: 0370-2693. DOI: https://doi.org/10.1016/S0370-2693(97)01140-4. [Online]. Available: https://www.sciencedirect.com/science/article/pii/S0370269397011404.

[42] D. Barberis *et al.*, "A spin analysis of the 4π channels produced in central pp interactions at 450 gev/c," *Physics Letters B*, vol. 471, no. 4, pp. 440–448, 2000, ISSN: 0370-2693. DOI: https://doi.org/10.1016/S0370-2693(99)01413-6. [Online]. Available: https://www.sciencedirect.com/science/article/pii/S0370269399014136.

[43] D. Barberis *et al.*, "A study of the $KK\pi$ channel produced centrally in pp interactions at 450 GeV/c," *Physics Letters B*, vol. 413, no. 1, pp. 225–231, 1997, ISSN: 0370-2693. DOI: https://doi.org/10.1016/S0370-2693(97)01141-6. [Online]. Available: https://www.sciencedirect.com/science/article/pii/S0370269397011416.

[44] M. Sosa *et al.*, "Spin-parity analysis of the centrally produced $K_S^0 K^{\pm}\pi^{\mp}$ system at $800\mathrm{GeV}/c$," *Phys. Rev. Lett.*, vol. 83, pp. 913–916, 5 Aug. 1999. DOI: 10.1103/PhysRevLett.83.913. [Online]. Available: https://link.aps.org/doi/10.1103/PhysRevLett.83.913.

[45] R. Dickson *et al.*, "Photoproduction of the $f_1(1285)$ meson," *Phys. Rev. C*, vol. 93, p. 065 202, 6 Jun. 2016. DOI: 10.1103/PhysRevC.93.065202. [Online]. Available: https://link.aps.org/doi/10.1103/PhysRevC.93.065202.

[46] P. Gavillet, "Measurement of inclusive $f_1(1285)$ and $f_1(1420)$ production in Z decays with the DELPHI detector," in *Multiparticle Dynamics*, WORLD SCIENTIFIC, Mar. 2002. DOI: 10.1142/9789812778048_0009. [Online]. Available: http://dx.doi.org/10.1142/9789812778048_0009.

[47] C. Sowa, "Study of excited η mesons in photoproduction at CLAS," Apr. 2016. [Online]. Available: https://hss-opus.ub.ruhr-uni-bochum.de/opus4/frontdoor/deliver/index/docId/4936/file/diss.pdf.

[48] N. I. Kochelev, M. Battaglieri, and R. D. Vita, "Exclusive photoproduction of $f_1(1285)$ meson off the proton in kinematics available at the Jefferson Laboratory experimental facilities," *Phys. Rev. C*, vol. 80, p. 025 201, 2 Aug. 2009. DOI: 10.1103/PhysRevC.80.025201. [Online]. Available: https://link.aps.org/doi/10.1103/PhysRevC.80.025201.

[49] S. K. Domokos, H. R. Grigoryan, and J. A. Harvey, "Photoproduction through Chern-Simons term induced interactions in holographic QCD," *Phys. Rev. D*, vol. 80, p. 115 018, 11 Dec. 2009. DOI: 10.1103/PhysRevD.80.115018. [Online]. Available: https://link.aps.org/doi/10.1103/PhysRevD.80.115018.

[50] Y. Huang *et al.*, "The $\gamma p \to n a_2^+(1320) \to n\rho^0\pi^+$ reactions within an effective lagrangian approach," *International Journal of Modern Physics E*, vol. 23, no. 06, p. 1 460 002, 2014. DOI: 10.1142/S0218301314600027. eprint: https://doi.org/10.1142/S0218301314600027. [Online]. Available: https://doi.org/10.1142/S0218301314600027.

[51] J. He and X. Wang, "Analysis of recent CLAS data on $f_1(1285)$ photoproduction," *Phys. Rev. D*, vol. 95, p. 094 005, 9 May 2017. DOI: 10.1103/PhysRevD.95.094005. [Online]. Available: https://link.aps.org/doi/10.1103/PhysRevD.95.094005.

[52] Y.-Y. Wang *et al.*, "Study on the reaction of $\gamma p \to f_1(1285)p$ in regge-effective lagrangian approach," *Phys. Rev. D*, vol. 95, p. 096 015, 9 May 2017. DOI: 10.1103/

PhysRevD.95.096015. [Online]. Available: https://link.aps.org/doi/10.1103/PhysRevD.95.096015.

[53] A. Wang *et al.*, "Analysis of data for $\gamma p \to f_1(1285)p$ photoproduction," *Chinese Physics C*, vol. 48, no. 2, p. 024 105, 2024.

[54] J. He, Private Communication, 2024.

[55] Jefferson Lab, *Timeline of Jefferson Lab*, Accessed Aug 17, 2023. [Online]. Available: https://www.jlab.org/about/visitors/history.

[56] Jefferson Lab, *12 GeV approved experiments by physics topics*, Accessed Aug 17, 2023. [Online]. Available: https://misportal.jlab.org/ul/ul%5C_office/ExperimentDB/rptApprovedExperimentsByHallAndTopic.cfm.

[57] C. W. Leemann, D. R. Douglas, and G. A. Krafft, "The continuous electron beam acceleratorfacility: CEBAF at the Jefferson Laboratory," Journal Article Volume 51, 2001, 2001, pp. 413–450. DOI: https://doi.org/10.1146/annurev.nucl.51.101701.132327. [Online]. Available: https://www.annualreviews.org/content/journals/10.1146/annurev.nucl.51.101701.132327.

[58] GlueX Collaboration, *CEBAF 12GeV*. [Online]. Available: https://gluexweb.jlab.org/content/drawing/cebaf-12gev.

[59] D. Lawrence and the GlueX Collaboration, "Exotic hybrid meson spectroscopy with the GlueX detector at JLab," *EPJ Web of Conferences*, vol. 66, p. 06 011, 2014. DOI: 10.1051/epjconf/20146606011. [Online]. Available: https://doi.org/10.1051/epjconf/20146606011.

[60] S. Adhikari *et al.*, "The GlueX beamline and detector," *Nuclear Instruments and Methods in Physics Research Section A: Accelerators, Spectrometers, Detectors and Associated Equipment*, vol. 987, p. 164 807, 2021, ISSN: 0168-9002. DOI: https://doi.org/10.1016/j.nima.2020.164807. [Online]. Available: https://www.sciencedirect.com/science/article/pii/S0168900220312043.

[61] U. Timm, "Coherent bremsstrahlung of electrons in crystals," *Fortschritte der Physik*, vol. 17, no. 12, pp. 765–808, 1969. DOI: 10.1002/prop.19690171202. [Online]. Available: https://doi.org/10.1002/prop.19690171202.

[62] K. Livingston, "The stonehenge technique. a method for aligning coherent bremsstrahlung radiators," *Nuclear Instruments and Methods in Physics Research Section A: Accelerators, Spectrometers, Detectors and Associated Equipment*, vol. 603, no. 3, pp. 205–213, 2009, ISSN: 0168-9002. DOI: https://doi.org/10.1016/j.nima.2009.02.010. [Online]. Available: https://www.sciencedirect.com/science/article/pii/S0168900209003477.

[63] M. Dugger *et al.*, "Design and construction of a high-energy photon polarimeter," *Nuclear Instruments and Methods in Physics Research Section A: Accelerators, Spectrometers, Detectors and Associated Equipment*, vol. 867, pp. 115–127, 2017, ISSN: 0168-9002. DOI: https://doi.org/10.1016/j.nima.2017.05.026. [Online]. Available: https://www.sciencedirect.com/science/article/pii/S0168900217305715.

[64] F. Barbosa *et al.*, "Pair spectrometer hodoscope for Hall D at Jefferson Lab," *Nuclear Instruments and Methods in Physics Research Section A: Accelerators, Spectrometers,*

Detectors and Associated Equipment, vol. 795, pp. 376–380, 2015, ISSN: 0168-9002. DOI: https://doi.org/10.1016/j.nima.2015.06.012. [Online]. Available: https://www.sciencedirect.com/science/article/pii/S0168900215007573.

[65] E. Pooser *et al.*, "The GlueX Start Counter detector," *Nuclear Instruments and Methods in Physics Research Section A: Accelerators, Spectrometers, Detectors and Associated Equipment*, vol. 927, pp. 330–342, 2019, ISSN: 0168-9002. DOI: https://doi.org/10.1016/j.nima.2019.02.029. [Online]. Available: https://www.sciencedirect.com/science/article/pii/S0168900219302128.

[66] N. Jarvis *et al.*, "The Central Drift Chamber for GlueX," *Nuclear Instruments and Methods in Physics Research Section A: Accelerators, Spectrometers, Detectors and Associated Equipment*, vol. 962, p. 163 727, 2020, ISSN: 0168-9002. DOI: https://doi.org/10.1016/j.nima.2020.163727. [Online]. Available: https://www.sciencedirect.com/science/article/pii/S0168900220302771.

[67] T. Beattie *et al.*, "Construction and performance of the barrel electromagnetic calorimeter for the GlueX experiment," *Nuclear Instruments and Methods in Physics Research Section A: Accelerators, Spectrometers, Detectors and Associated Equipment*, vol. 896, pp. 24–42, 2018, ISSN: 0168-9002. DOI: https://doi.org/10.1016/j.nima.2018.04.006. [Online]. Available: https://www.sciencedirect.com/science/article/pii/S0168900218304807.

[68] GlueX Collaboration, *FCAL with platform*. [Online]. Available: https://gluexweb.jlab.org/content/photo/fcal-platform-0.

[69] P. Hurck, 2020, Ph.D. dissertation, Glasgow University. [Online]. Available: https://theses.gla.ac.uk/81591/7/2020pauliphd.pdf.

[70] R. E. Kalman, "A new approach to linear filtering and prediction problems," *Journal of Basic Engineering*, vol. 82, no. 1, pp. 35–45, Mar. 1960, ISSN: 0021-9223. DOI: 10.1115/1.3662552. [Online]. Available: https://doi.org/10.1115/1.3662552.

[71] GlueX Collaboration, "GlueX Phase-I dataset summary," Tech. Rep. [Online]. Available: https://halldweb.jlab.org/wiki-private/index.php/GlueX_Phase-I_Dataset_Summary.

[72] T. Viducic, May 2024. [Online]. Available: https://github.com/tylerviducic/gluex.

[73] P. Mattione, "Analysis library overhaul," GlueX Collaboration Meeting, Oct. 2017.

[74] GlueX Collaboration, *Spring 2017 analysis launch cuts*. [Online]. Available: https://halldweb.jlab.org/wiki/index.php/Spring_2017_Analysis_Launch_Cuts.

[75] M. Kunkel, *Photoproduction of π^0 on hydrogen with CLAS from 1.1 GeV - 5.45 GeV using $e^+e^-\gamma$ decay*, PhD Dissertation, 2014. DOI: 10.25777/yxgj-3c96. [Online]. Available: https://digitalcommons.odu.edu/physics_etds/54.

[76] S. Dobbs and D. Lersch, "Data analysis in hadron physics and introduction to kinematic fitting," GlueX Workshop on Kinematic Fitting, Oct. 2021. [Online]. Available: https://halldweb.jlab.org/DocDB/0053/005338/002/KinFit_Workshop_Lecture_Part1.pdf.

[77] P. Mattione, *Least squares kinematic fitting of physics reactions*, Apr. 2016. [Online]. Available: https://halldweb.jlab.org/DocDB/0021/002112/005/KinematicFitting.pdf.

[78] R. Mitchell, "Best chi squared method vs. rf sideband subtraction method," Mar. 2023. [Online]. Available: https://halldweb.jlab.org/DocDB/0059/005960/002/BestChi2Study_230330_local.pdf.

[79] R. Brun *et al.*, *root-project/root*, version v6-18-02, TMath::Prob, Jun. 2020. DOI: 10.5281/zenodo.3895860. [Online]. Available: https://root.cern.ch/root/html524/TMath.html%5C#TMath:Prob.

[80] R. Brun *et al.*, *root-project/root*, version v6-18-02, TMath::chi2_cdf_c, Jun. 2020. DOI: 10.5281/zenodo.3895860. [Online]. Available: https://root.cern.ch/doc/v608/group__ProbFunc.html#gae07ba00b57c524cfbbc9923cdff3f9b0.

[81] E. Weisstein, *Chi-squared distribution*, https://mathworld.wolfram.com/Chi-SquaredDistribution.html, From MathWorld–A Wolfram Web Resource, Apr. 27, 2023.

[82] R. L. Workman *et al.*, "Review of particle physics," *PTEP*, vol. 2022, p. 083C01, 2022, K^0. DOI: 10.1093/ptep/ptac097. [Online]. Available: https://pdg.lbl.gov/2023/listings/rpp2023-list-K-zero.pdf.

[83] R. Aaij *et al.*, "Study of charmonium decays to $K^0_S K\pi$ in the $B \to (K^0_S K\pi)K$ channels," *Phys. Rev. D*, vol. 108, p. 032 010, 3 Aug. 2023. DOI: 10.1103/PhysRevD.108.032010. [Online]. Available: https://link.aps.org/doi/10.1103/PhysRevD.108.032010.

[84] R. Pierce, *Normal distribution*, Feb. 1, 2022. [Online]. Available: http://www.mathsisfun.com/data/standard-normal-distribution.html.

[85] R. L. Workman *et al.*, "Review of particle physics," *PTEP*, vol. 2022, p. 083C01, 2022, Δ^{++}. DOI: 10.1093/ptep/ptac097. [Online]. Available: https://pdg.lbl.gov/2023/listings/rpp2023-list-Delta-1232.pdf.

[86] R. L. Workman *et al.*, "Review of particle physics," *PTEP*, vol. 2022, p. 083C01, 2022, N and Δ Resonances. DOI: 10.1093/ptep/ptac097. [Online]. Available: https://pdg.lbl.gov/2023/reviews/rpp2023-rev-n-delta-resonances.pdf.

[87] R. L. Workman *et al.*, "Review of particle physics," *PTEP*, vol. 2022, p. 083C01, 2022, $\Lambda(1520)$. DOI: 10.1093/ptep/ptac097. [Online]. Available: https://pdg.lbl.gov/2023/listings/rpp2023-list-lambda-1520.pdf.

[88] R. L. Workman *et al.*, "Review of particle physics," *PTEP*, vol. 2022, p. 083C01, 2022, $\Lambda(1820)$. DOI: 10.1093/ptep/ptac097. [Online]. Available: https://pdg.lbl.gov/2023/listings/rpp2023-list-lambda-1820.pdf.

[89] R. L. Workman *et al.*, "Review of particle physics," *PTEP*, vol. 2022, p. 083C01, 2022, $\eta(1405)$. DOI: 10.1093/ptep/ptac097. [Online]. Available: https://pdg.lbl.gov/2023/listings/rpp2023-list-eta-1405.pdf.

[90] R. L. Workman *et al.*, "Review of particle physics," *PTEP*, vol. 2022, p. 083C01, 2022, $\eta(1475)$. DOI: 10.1093/ptep/ptac097. [Online]. Available: https://pdg.lbl.gov/2023/listings/rpp2023-list-eta-1475.pdf.

[91] R. L. Workman *et al.*, "Review of particle physics," *PTEP*, vol. 2022, p. 083C01, 2022, K^*. DOI: 10.1093/ptep/ptac097. [Online]. Available: https://pdg.lbl.gov/2023/listings/rpp2023-list-K-star-892.pdf.

[92] R. L. Workman *et al.*, "Review of particle physics," *PTEP*, vol. 2022, p. 083C01, 2022, Section 42. Monte Carlo Techniques. DOI: 10.1093/ptep/ptac097. [Online]. Available: https://pdg.lbl.gov/2023/reviews/rpp2023-rev-monte-carlo-techniques.pdf.

[93] GlueX Collaboration, *gen_amp*, Dec. 2010. [Online]. Available: https://halldweb.jlab.org/wiki/index.php/HOWTO%5C_Use%5C_gen%5C_amp.

[94] T. Britton, P. Hurck, and GlueX Collaboration, *MCWrapper*, May 2019. [Online]. Available: https://github.com/JeffersonLab/gluex_MCwrapper?tab=readme-ov-file.

[95] K. Saldana, M. R. Shepherd, and J. Sikes, *Fixed target generator*, Apr. 2024. [Online]. Available: https://halldweb.jlab.org/DocDB/0064/006440/002/GlueX_Fixed_Target_Generator.pdf.

[96] M. R. Shepherd, J. Stevens, and GlueX Collaboration, *DalitzDecayFactory.cc*, Dec. 2010. [Online]. Available: https://github.com/JeffersonLab/halld_sim/blob/master/src/libraries/AMPTOOLS_MCGEN/DalitzDecayFactory.cc.

[97] R. Jones, *HDGeant4 - Geant4-based simulation of the Hall D photon beamline and the GlueX spectrometer*, version 2.30.1, Nov. 2021. DOI: 10.5281/zenodo.5725383. [Online]. Available: https://github.com/rjones30/HDGeant4.

[98] J. Allison *et al.*, "Recent developments in Geant4," *Nuclear Instruments and Methods in Physics Research Section A: Accelerators, Spectrometers, Detectors and Associated Equipment*, vol. 835, pp. 186–225, 2016, ISSN: 0168-9002. DOI: https://doi.org/10.1016/j.nima.2016.06.125. [Online]. Available: https://www.sciencedirect.com/science/article/pii/S0168900216306957.

[99] J. Allison *et al.*, "Geant4 developments and applications," *IEEE Transactions on Nuclear Science*, vol. 53, no. 1, pp. 270–278, 2006. DOI: 10.1109/TNS.2006.869826.

[100] S. Agostinelli *et al.*, "Geant4 - a simulation toolkit," *Nuclear Instruments and Methods in Physics Research Section A: Accelerators, Spectrometers, Detectors and Associated Equipment*, vol. 506, no. 3, pp. 250–303, 2003, ISSN: 0168-9002. DOI: https://doi.org/10.1016/S0168-9002(03)01368-8. [Online]. Available: https://www.sciencedirect.com/science/article/pii/S0168900203013688.

[101] R. Brun *et al.*, *root-project/root*, version v6-18-02, ROOT::TGenPhaseSpace, Jun. 2020. DOI: 10.5281/zenodo.3895860. [Online]. Available: https://root.cern.ch/doc/master/classTGenPhaseSpace.html.

[102] R. L. Workman *et al.*, "Review of particle physics," *PTEP*, vol. 2022, p. 083C01, 2022, Section 49. Kinematics. DOI: 10.1093/ptep/ptac097. [Online]. Available: https://pdg.lbl.gov/2023/reviews/rpp2023-rev-kinematics.pdf.

[103] R. L. Workman *et al.*, "Review of particle physics," *PTEP*, vol. 2022, p. 083C01, 2022, Section 50. Resonances. DOI: 10.1093/ptep/ptac097. [Online]. Available: https://pdg.lbl.gov/2023/reviews/rpp2023-rev-resonances.pdf.

[104] F. James and M. Winkler, *MINUT2*. [Online]. Available: https://root.cern/root/htmldoc/guides/minuit2/Minuit2.html.

[105] R. Brun *et al.*, *root-project/root*, version v6-18-02, ROOT::TH1, Jun. 2020. DOI: 10.5281/zenodo.3895860. [Online]. Available: https://root.cern.ch/doc/v608/classTH1.html.

[106] R. L. Workman *et al.*, "Review of particle physics," *PTEP*, vol. 2022, p. 083C01, 2022, $\eta(1295)$. DOI: 10.1093/ptep/ptac097. [Online]. Available: https://pdg.lbl.gov/2023/listings/rpp2023-list-eta-1295.pdf.

[107] M. Galassi *et al.*, *GNU Scientific Library Reference Manual*, 3rd. Network Theory Ltd., 2009, ISBN: 0954612078. [Online]. Available: http://www.gnu.org/software/gsl/.

[108] R. L. Workman *et al.*, "Review of particle physics," *PTEP*, vol. 2022, p. 083C01, 2022, Section 40. Statistics. DOI: 10.1093/ptep/ptac097. [Online]. Available: https://pdg.lbl.gov/2023/reviews/rpp2023-rev-statistics.pdf.

[109] Z. T. Draper and S. R. Sharpe, *Three-particle formalism for multiple channels: The $\eta\pi\pi + K\overline{K}\pi$ system in isosymmetric QCD*, Jul. 2024. DOI: 10.1007/jhep07(2024)083. [Online]. Available: http://dx.doi.org/10.1007/JHEP07(2024)083.

[110] R. L. Workman *et al.*, "Review of particle physics," *PTEP*, vol. 2022, p. 083C01, 2022, $a^0(980)$. DOI: 10.1093/ptep/ptac097. [Online]. Available: https://pdg.lbl.gov/2023/listings/rpp2023-list-a0-980.pdf.

[111] W. Herr and Muratori, *Concept of luminosity*, Accessed Dec 29, 2023. [Online]. Available: https://cds.cern.ch/record/941318/files/p361.pdf.

[112] J. R. Stevens and GlueX Collaboration, *plot_flux_ccdb*, Oct. 2018. [Online]. Available: https://github.com/JeffersonLab/hd%5C_utilities/blob/d2b19d00c82bff68019436d4psflux/plot%5C_flux%5C_ccdb.py.

[113] R. Barlow, *Systematic errors: Facts and fictions*, 2002. arXiv: hep-ex/0207026 [hep-ex]. [Online]. Available: https://arxiv.org/abs/hep-ex/0207026.

[114] A. M. Schertz and J. R. Stevens, "Calculation of $\pi^{\pm}$ tracking efficiencies as functions of kinematic variables from exclusive $\omega \to (\pi^{\pm})\pi^{\pm}\pi^{0}$ events," Jul. 2019. [Online]. Available: https://halldweb.jlab.org/DocDB/0041/004110/001/Pion_Tracking_Analysis_Note.pdf.

[115] B. Grube, "Study of recoil-proton reconstruction efficiency." [Online]. Available: https://halldweb.jlab.org/wiki-private/index.php/Recoil-proton_reconstruction_efficiency.

[116] S. Dobbs, Private Communication, 2024.

[117] C. A. Meyer, "Coordinate systems in GlueX," Jan. 2021. [Online]. Available: https://halldweb.jlab.org/DocDB/0048/004829/005/coordinates.pdf.

[118] M. Duggar, Private Communication, 2024.

[119] H. Seraydaryan *et al.*, "ϕ-meson photoproduction on hydrogen in the neutral decay mode," *Phys. Rev. C*, vol. 89, p. 055 206, 5 May 2014. DOI: 10.1103/PhysRevC.89.055206. [Online]. Available: https://link.aps.org/doi/10.1103/PhysRevC.89.055206.

APPENDIX A

SYSTEMATICS

Table 24. Cross-section deviations for 1st-order polynomial model variation. Relative difference from nominal for using a 1st-order polynomial for phase space background for each E_γ and $-t$ bin for $\pi^+K^-K_s$ and $\pi^-K^+K_s$ decay modes.

E_γ [GeV]	$-t$ [GeV^2]	$\lvert\delta_i(K^-K_s\pi^+)\rvert$	$\lvert\delta_i(K^-K_s\pi^+)\rvert$
8	0.15	0.023	0.152
8	0.25	0.019	0.035
8	0.35	0.065	0.036
8	0.53	0.037	0.023
8	0.78	0.063	0.040
8	1.15	0.105	0.097
8	1.65	0.189	0.101
9	0.15	0.196	0.201
9	0.25	0.009	0.097
9	0.35	0.007	0.033
9	0.53	0.065	0.030
9	0.78	0.090	0.070
9	1.15	0.096	0.081
9	1.65	0.129	0.117
10	0.15	0.306	0.423
10	0.25	0.196	0.178
10	0.35	0.054	0.091
10	0.53	0.043	0.066
10	0.78	0.199	0.002
10	1.15	0.142	0.071
10	1.65	0.145	0.207
11	0.15	0.508	0.518
11	0.25	0.489	0.302
11	0.35	0.072	0.132
11	0.53	0.094	0.078
11	0.78	0.138	0.090
11	1.15	0.128	0.164
11	1.65	0.192	0.328

Table 25. Cross-section deviations for 3rd-order polynomial model variation. Relative difference from nominal for using a 3rd-order polynomial for phase space background for each E_γ and $-t$ bin for $\pi^+K^-K_s$ and $\pi^-K^+K_s$ decay modes.

E_γ [GeV]	$-t$ [GeV^2]	$\lvert\delta_i(K^-K_s\pi^+)\rvert$	$\lvert\delta_i(K^-K_s\pi^+)\rvert$
8	0.15	0.031	0.019
8	0.25	0.029	0.020
8	0.35	0.044	0.038
8	0.53	0.028	0.037
8	0.78	0.028	0.011
8	1.15	0.016	0.012
8	1.65	0.086	0.032
9	0.15	0.017	0.014
9	0.25	0.018	0.003
9	0.35	0.012	0.018
9	0.53	0.003	0.011
9	0.78	0.005	0.035
9	1.15	0.012	0.011
9	1.65	0.034	0.036
10	0.15	0.000	0.010
10	0.25	0.041	0.002
10	0.35	0.002	0.001
10	0.53	0.002	0.033
10	0.78	0.005	0.090
10	1.15	0.002	0.134
10	1.65	0.013	0.023
11	0.15	0.020	0.005
11	0.25	0.035	0.005
11	0.35	0.196	0.001
11	0.53	0.044	0.007
11	0.78	0.088	0.002
11	1.15	0.029	0.033
11	1.65	0.014	0.102

Table 26. Cross-section deviations for removing Gaussian component model variation. Relative difference from nominal for removing Gaussian component that describes resonant tails from full model for each E_γ and $-t$ bin for $\pi^+K^-K_s$ and $\pi^-K^+K_s$ decay modes.

E_γ [GeV]	$-t$ [GeV^2]	$\lvert\delta_i(K^-K_s\pi^+)\rvert$	$\lvert\delta_i(K^-K_s\pi^+)\rvert$
8	0.15	0.115	0.065
8	0.25	0.133	0.060
8	0.35	0.074	0.071
8	0.53	0.063	0.039
8	0.78	0.116	0.057
8	1.15	0.062	0.036
8	1.65	0.059	0.048
9	0.15	0.085	0.088
9	0.25	0.089	0.073
9	0.35	0.103	0.055
9	0.53	0.121	0.043
9	0.78	0.122	0.063
9	1.15	0.078	0.043
9	1.65	0.134	0.032
10	0.15	0.186	0.058
10	0.25	0.097	0.091
10	0.35	0.071	0.062
10	0.53	0.085	0.073
10	0.78	0.180	0.050
10	1.15	0.118	0.004
10	1.65	0.006	0.028
11	0.15	0.121	0.096
11	0.25	0.337	0.100
11	0.35	0.014	0.084
11	0.53	0.096	0.073
11	0.78	0.071	0.049
11	1.15	0.074	0.062
11	1.65	0.030	0.006

Table 27. Cross-section deviations for wider fit range on low mass side variation. Relative difference from nominal for fitting the model over a wider range on low $M(KK\pi)$ side for each E_γ and $-t$ bin for $\pi^+K^-K_s$ and $\pi^-K^+K_s$ decay modes.

E_γ [GeV]	$-t$ [GeV^2]	$\lvert\delta_i(K^-K_s\pi^+)\rvert$	$\lvert\delta_i(K^-K_s\pi^+)\rvert$
8	0.15	0.117	0.029
8	0.25	0.055	0.022
8	0.35	0.022	0.004
8	0.53	0.001	0.006
8	0.78	0.018	0.004
8	1.15	0.011	0.004
8	1.65	0.062	0.018
9	0.15	0.044	0.029
9	0.25	0.101	0.032
9	0.35	0.041	0.017
9	0.53	0.013	0.006
9	0.78	0.017	0.025
9	1.15	0.027	0.002
9	1.65	0.011	0.032
10	0.15	0.096	0.010
10	0.25	0.101	0.046
10	0.35	0.146	0.048
10	0.53	0.027	0.007
10	0.78	0.071	0.030
10	1.15	0.009	0.006
10	1.65	0.025	0.036
11	0.15	0.128	0.083
11	0.25	0.103	0.009
11	0.35	0.116	0.006
11	0.53	0.015	0.014
11	0.78	0.022	0.002
11	1.15	0.023	0.047
11	1.65	0.045	0.066

Table 28. Cross-section deviations for wider fit range on high mass side variation. Relative difference from nominal for fitting the model over a wider range on the high $M(KK\pi)$ side for each E_γ and $-t$ bin for $\pi^+K^-K_s$ and $\pi^-K^+K_s$ decay modes.

E_γ [GeV]	$-t$ [GeV^2]	$\lvert\delta_i(K^-K_s\pi^+)\rvert$	$\lvert\delta_i(K^-K_s\pi^+)\rvert$
8	0.15	0.005	0.018
8	0.25	0.031	0.002
8	0.35	0.016	0.001
8	0.53	0.013	0.007
8	0.78	0.000	0.006
8	1.15	0.002	0.002
8	1.65	0.028	0.011
9	0.15	0.025	0.004
9	0.25	0.006	0.002
9	0.35	0.008	0.008
9	0.53	0.003	0.002
9	0.78	0.010	0.011
9	1.15	0.031	0.010
9	1.65	0.014	0.014
10	0.15	0.046	0.005
10	0.25	0.034	0.039
10	0.35	0.023	0.011
10	0.53	0.000	0.003
10	0.78	0.001	0.006
10	1.15	0.003	0.009
10	1.65	0.030	0.019
11	0.15	0.010	0.007
11	0.25	0.069	0.003
11	0.35	0.012	0.009
11	0.53	0.007	0.000
11	0.78	0.002	0.005
11	1.15	0.010	0.008
11	1.65	0.027	0.003

Table 29. Cross-section deviations for wider fit range variation. Relative difference from nominal for fitting the model over a wider range on both sides of $M(KK\pi)$ for each E_γ and $-t$ bin for $\pi^+K^-K_s$ and $\pi^-K^+K_s$ decay modes.

E_γ [GeV]	$-t$ [GeV^2]	$\lvert\delta_i(K^-K_s\pi^+)\rvert$	$\lvert\delta_i(K^-K_s\pi^+)\rvert$
8	0.15	0.111	0.015
8	0.25	0.027	0.022
8	0.35	0.031	0.000
8	0.53	0.002	0.005
8	0.78	0.017	0.001
8	1.15	0.009	0.003
8	1.65	0.074	0.010
9	0.15	0.028	0.031
9	0.25	0.094	0.030
9	0.35	0.034	0.022
9	0.53	0.010	0.008
9	0.78	0.009	0.026
9	1.15	0.037	0.007
9	1.65	0.024	0.021
10	0.15	0.059	0.013
10	0.25	0.093	0.040
10	0.35	0.126	0.055
10	0.53	0.028	0.008
10	0.78	0.069	0.034
10	1.15	0.012	0.013
10	1.65	0.048	0.022
11	0.15	0.132	0.086
11	0.25	0.095	0.007
11	0.35	0.123	0.001
11	0.53	0.011	0.012
11	0.78	0.023	0.002
11	1.15	0.026	0.053
11	1.65	0.058	0.061

Table 30. Cross-section deviations for narrower fit range on low mass side variation. Relative difference from nominal for fitting the model over a narrower range on the low $M(KK\pi)$ side for each E_γ and $-t$ bin for $\pi^+K^-K_s$ and $\pi^-K^+K_s$ decay modes.

E_γ [GeV]	$-t$ [GeV^2]	$\lvert\delta_i(K^-K_s\pi^+)\rvert$	$\lvert\delta_i(K^-K_s\pi^+)\rvert$
8	0.15	0.067	0.030
8	0.25	0.070	0.020
8	0.35	0.019	0.016
8	0.53	0.013	0.001
8	0.78	0.025	0.008
8	1.15	0.009	0.005
8	1.65	0.055	0.025
9	0.15	0.054	0.056
9	0.25	0.062	0.020
9	0.35	0.043	0.014
9	0.53	0.020	0.008
9	0.78	0.015	0.000
9	1.15	0.025	0.000
9	1.65	0.010	0.041
10	0.15	0.026	0.029
10	0.25	0.004	0.016
10	0.35	0.118	0.034
10	0.53	0.004	0.003
10	0.78	0.021	0.023
10	1.15	0.031	0.008
10	1.65	0.009	0.076
11	0.15	0.124	0.086
11	0.25	0.155	0.021
11	0.35	0.018	0.021
11	0.53	0.044	0.008
11	0.78	0.021	0.010
11	1.15	0.100	0.001
11	1.65	0.068	0.041

Table 31. Cross-section deviations for narrower fit range on high mass side variation. Relative difference from nominal for fitting the model over a narrower range on the high $M(KK\pi)$ side for each E_γ and $-t$ bin for $\pi^+K^-K_s$ and $\pi^-K^+K_s$ decay modes.

E_γ [GeV]	$-t$ [GeV^2]	$\lvert\delta_i(K^-K_s\pi^+)\rvert$	$\lvert\delta_i(K^-K_s\pi^+)\rvert$
8	0.15	0.054	0.001
8	0.25	0.027	0.008
8	0.35	0.010	0.018
8	0.53	0.010	0.009
8	0.78	0.021	0.008
8	1.15	0.009	0.013
8	1.65	0.001	0.006
9	0.15	0.004	0.007
9	0.25	0.009	0.003
9	0.35	0.030	0.003
9	0.53	0.005	0.000
9	0.78	0.010	0.001
9	1.15	0.010	0.000
9	1.65	0.002	0.001
10	0.15	0.014	0.007
10	0.25	0.018	0.019
10	0.35	0.003	0.011
10	0.53	0.006	0.001
10	0.78	0.013	0.004
10	1.15	0.007	0.007
10	1.65	0.002	0.023
11	0.15	0.003	0.002
11	0.25	0.017	0.006
11	0.35	0.020	0.004
11	0.53	0.001	0.005
11	0.78	0.003	0.003
11	1.15	0.045	0.008
11	1.65	0.010	0.018

Table 32. Cross-section deviations for narrower fit range variation. Relative difference from nominal for fitting the model over a narrower range on both sides of $M(KK\pi)$ for each E_γ and $-t$ bin for $\pi^+K^-K_s$ and $\pi^-K^+K_s$ decay modes.

E_γ [GeV]	$-t$ [GeV^2]	$\lvert\delta_i(K^-K_s\pi^+)\rvert$	$\lvert\delta_i(K^-K_s\pi^+)\rvert$
8	0.15	0.030	0.034
8	0.25	0.053	0.012
8	0.35	0.033	0.013
8	0.53	0.002	0.004
8	0.78	0.002	0.014
8	1.15	0.002	0.011
8	1.65	0.055	0.017
9	0.15	0.051	0.050
9	0.25	0.077	0.050
9	0.35	0.018	0.019
9	0.53	0.028	0.009
9	0.78	0.004	0.000
9	1.15	0.014	0.000
9	1.65	0.013	0.046
10	0.15	0.001	0.019
10	0.25	0.025	0.041
10	0.35	0.119	0.050
10	0.53	0.005	0.005
10	0.78	0.039	0.020
10	1.15	0.024	0.014
10	1.65	0.008	0.032
11	0.15	0.131	0.091
11	0.25	0.176	0.030
11	0.35	0.044	0.028
11	0.53	0.048	0.006
11	0.78	0.027	0.006
11	1.15	0.118	0.001
11	1.65	0.054	0.025

Table 33. Cross-section deviations for narrower Voigtian variation. Relative difference from nominal for fixing the Voigtian width to be 1σ smaller than the nominal value, as given in Table 6, for each E_γ and $-t$ bin for $\pi^+K^-K_s$ and $\pi^-K^+K_s$ decay modes.

E_γ [GeV]	$-t$ [GeV^2]	$\lvert\delta_i(K^-K_s\pi^+)\rvert$	$\lvert\delta_i(K^-K_s\pi^+)\rvert$
8	0.15	0.028	0.002
8	0.25	0.026	0.002
8	0.35	0.033	0.002
8	0.53	0.031	0.002
8	0.78	0.024	0.002
8	1.15	0.027	0.002
8	1.65	0.026	0.003
9	0.15	0.030	0.002
9	0.25	0.035	0.002
9	0.35	0.038	0.002
9	0.53	0.030	0.002
9	0.78	0.029	0.003
9	1.15	0.032	0.002
9	1.65	0.027	0.002
10	0.15	0.036	0.002
10	0.25	0.013	0.002
10	0.35	0.034	0.002
10	0.53	0.033	0.002
10	0.78	0.026	0.002
10	1.15	0.021	0.002
10	1.65	0.016	0.001
11	0.15	0.031	0.002
11	0.25	0.033	0.002
11	0.35	0.033	0.002
11	0.53	0.035	0.002
11	0.78	0.029	0.002
11	1.15	0.008	0.002
11	1.65	0.026	0.002

Table 34. Cross-section deviations for wider Voigtian variation. Relative difference from nominal for fixing the Voigtian width to be 1σ larger than the nominal value, as given in Table 6, for each E_γ and $-t$ bin for $\pi^+K^-K_s$ and $\pi^-K^+K_s$ decay modes.

E_γ [GeV]	$-t$ [GeV^2]	$\lvert\delta_i(K^-K_s\pi^+)\rvert$	$\lvert\delta_i(K^-K_s\pi^+)\rvert$
8	0.15	0.028	0.002
8	0.25	0.026	0.002
8	0.35	0.033	0.002
8	0.53	0.027	0.002
8	0.78	0.024	0.002
8	1.15	0.027	0.002
8	1.65	0.026	0.003
9	0.15	0.030	0.002
9	0.25	0.035	0.002
9	0.35	0.039	0.002
9	0.53	0.030	0.002
9	0.78	0.028	0.003
9	1.15	0.032	0.002
9	1.65	0.027	0.002
10	0.15	0.036	0.002
10	0.25	0.077	0.002
10	0.35	0.035	0.002
10	0.53	0.033	0.002
10	0.78	0.026	0.002
10	1.15	0.021	0.002
10	1.65	0.016	0.001
11	0.15	0.031	0.002
11	0.25	0.033	0.002
11	0.35	0.033	0.002
11	0.53	0.035	0.002
11	0.78	0.029	0.002
11	1.15	0.066	0.002
11	1.65	0.025	0.002

Table 35. Cross-section deviations for Gaussian mean lighter variation. Relative difference from nominal for fixing the Gaussian mean to be 1σ smaller than the nominal value, as given in Table 7, for each E_γ and $-t$ bin for $\pi^+K^-K_s$ and $\pi^-K^+K_s$ decay modes.

E_γ [GeV]	$-t$ [GeV^2]	$\lvert\delta_i(K^-K_s\pi^+)\rvert$	$\lvert\delta_i(K^-K_s\pi^+)\rvert$
8	0.15	0.013	0.014
8	0.25	0.010	0.013
8	0.35	0.000	0.014
8	0.53	0.001	0.009
8	0.78	0.009	0.015
8	1.15	0.004	0.009
8	1.65	0.003	0.015
9	0.15	0.011	0.024
9	0.25	0.001	0.016
9	0.35	0.002	0.009
9	0.53	0.011	0.011
9	0.78	0.010	0.016
9	1.15	0.001	0.008
9	1.65	0.010	0.007
10	0.15	0.015	0.019
10	0.25	0.031	0.023
10	0.35	0.001	0.014
10	0.53	0.007	0.016
10	0.78	0.003	0.011
10	1.15	0.001	0.002
10	1.65	0.000	0.007
11	0.15	0.015	0.038
11	0.25	0.023	0.027
11	0.35	0.009	0.020
11	0.53	0.000	0.014
11	0.78	0.006	0.011
11	1.15	0.006	0.009
11	1.65	0.011	0.001

Table 36. Cross-section deviations for Gaussian mean heavier variation. Relative difference from nominal for fixing the Gaussian mean to be 1σ larger than the nominal value, as given in Table 7, for each E_γ and $-t$ bin for $\pi^+K^-K_s$ and $\pi^-K^+K_s$ decay modes.

E_γ [GeV]	$-t$ [GeV^2]	$\lvert\delta_i(K^-K_s\pi^+)\rvert$	$\lvert\delta_i(K^-K_s\pi^+)\rvert$
8	0.15	0.010	0.012
8	0.25	0.009	0.012
8	0.35	0.004	0.003
8	0.53	0.007	0.000
8	0.78	0.006	0.013
8	1.15	0.002	0.008
8	1.65	0.002	0.013
9	0.15	0.013	0.025
9	0.25	0.002	0.014
9	0.35	0.001	0.007
9	0.53	0.008	0.010
9	0.78	0.007	0.014
9	1.15	0.003	0.006
9	1.65	0.007	0.006
10	0.15	0.010	0.020
10	0.25	0.055	0.022
10	0.35	0.005	0.011
10	0.53	0.010	0.013
10	0.78	0.003	0.009
10	1.15	0.003	0.002
10	1.65	0.000	0.008
11	0.15	0.013	0.035
11	0.25	0.016	0.026
11	0.35	0.010	0.018
11	0.53	0.004	0.015
11	0.78	0.010	0.009
11	1.15	0.032	0.013
11	1.65	0.010	0.001

Table 37. Cross-section deviations for Gaussian width narrower variation. Relative difference from nominal for fixing the gaussian width to be 1σ smaller than the nominal value, as given in Table 7, for each E_γ and $-t$ bin for $\pi^+K^-K_s$ and $\pi^-K^+K_s$ decay modes.

E_γ [GeV]	$-t$ [GeV^2]	$\lvert\delta_i(K^-K_s\pi^+)\rvert$	$\lvert\delta_i(K^-K_s\pi^+)\rvert$
8	0.15	0.000	0.011
8	0.25	0.006	0.011
8	0.35	0.006	0.010
8	0.53	0.000	0.009
8	0.78	0.004	0.012
8	1.15	0.007	0.006
8	1.65	0.005	0.015
9	0.15	0.023	0.017
9	0.25	0.004	0.015
9	0.35	0.009	0.009
9	0.53	0.000	0.009
9	0.78	0.006	0.010
9	1.15	0.009	0.007
9	1.65	0.001	0.008
10	0.15	0.010	0.017
10	0.25	0.007	0.020
10	0.35	0.014	0.014
10	0.53	0.012	0.014
10	0.78	0.011	0.009
10	1.15	0.021	0.001
10	1.65	0.000	0.002
11	0.15	0.006	0.041
11	0.25	0.016	0.024
11	0.35	0.006	0.019
11	0.53	0.002	0.015
11	0.78	0.006	0.009
11	1.15	0.038	0.006
11	1.65	0.011	0.001

Table 38. Cross-section deviations for Gaussian width wider variation. Relative difference from nominal for fixing the gaussian width to be 1σ larger than the nominal value, as given in Table 7, for each E_γ and $-t$ bin for $\pi^+K^-K_s$ and $\pi^-K^+K_s$ decay modes.

E_γ [GeV]	$-t$ [GeV^2]	$\lvert\delta_i(K^-K_s\pi^+)\rvert$	$\lvert\delta_i(K^-K_s\pi^+)\rvert$
8	0.15	0.007	0.012
8	0.25	0.030	0.011
8	0.35	0.013	0.024
8	0.53	0.009	0.013
8	0.78	0.003	0.011
8	1.15	0.002	0.006
8	1.65	0.001	0.015
9	0.15	0.015	0.017
9	0.25	0.009	0.015
9	0.35	0.010	0.009
9	0.53	0.008	0.008
9	0.78	0.002	0.010
9	1.15	0.003	0.007
9	1.65	0.008	0.007
10	0.15	0.022	0.017
10	0.25	0.037	0.021
10	0.35	0.018	0.014
10	0.53	0.003	0.014
10	0.78	0.002	0.009
10	1.15	0.010	0.001
10	1.65	0.000	0.000
11	0.15	0.002	0.040
11	0.25	0.016	0.025
11	0.35	0.003	0.019
11	0.53	0.009	0.015
11	0.78	0.001	0.010
11	1.15	0.028	0.007
11	1.65	0.010	0.001

Table 39. Value and source for fit systematic for each E_γ and $-t$ bin for $f_1(1285) \to \pi^+ K^- K_s$ decay mode

E_γ [GeV]	$-t$ [GeV^2]	Variation	|Varied - Nominal|/Nominal
8	0.150	1st-Order Polynomial	0.152
8	0.250	No Gaussian Component	0.060
8	0.350	No Gaussian Component	0.071
8	0.525	No Gaussian Component	0.039
8	0.775	No Gaussian Component	0.057
8	1.150	1st-Order Polynomial	0.097
8	1.650	1st-Order Polynomial	0.101
9	0.150	1st-Order Polynomial	0.201
9	0.250	1st-Order Polynomial	0.097
9	0.350	No Gaussian Component	0.055
9	0.525	No Gaussian Component	0.043
9	0.775	1st-Order Polynomial	0.070
9	1.150	1st-Order Polynomial	0.081
9	1.650	1st-Order Polynomial	0.117
10	0.150	1st-Order Polynomial	0.423
10	0.250	1st-Order Polynomial	0.178
10	0.350	1st-Order Polynomial	0.091
10	0.525	No Gaussian Component	0.073
10	0.775	3rd-Order Polynomial	0.090
10	1.150	3rd-Order Polynomial	0.134
10	1.650	1st-Order Polynomial	0.207
11	0.150	1st-Order Polynomial	0.518
11	0.250	1st-Order Polynomial	0.302
11	0.350	1st-Order Polynomial	0.132
11	0.525	1st-Order Polynomial	0.078
11	0.775	1st-Order Polynomial	0.090
11	1.150	1st-Order Polynomial	0.164
11	1.650	1st-Order Polynomial	0.328

Table 40. Value and source for fit systematic for each E_γ and $-t$ bin for $f_1(1285) \to \pi^- K^+ K_s$ decay mode.

E_γ [GeV]	$-t$ [GeV^2]	Variation	|Varied - Nominal|/Nominal
8	0.150	Wider Fit Range (Low Side)	0.117
8	0.250	No Gaussian Component	0.133
8	0.350	No Gaussian Component	0.074
8	0.525	No Gaussian Component	0.063
8	0.775	No Gaussian Component	0.116
8	1.150	1st-Order Polynomial	0.105
8	1.650	1st-Order Polynomial	0.189
9	0.150	1st-Order Polynomial	0.196
9	0.250	Wider Fit Range (Low Side)	0.101
9	0.350	No Gaussian Component	0.103
9	0.525	No Gaussian Component	0.121
9	0.775	No Gaussian Component	0.122
9	1.150	1st-Order Polynomial	0.096
9	1.650	No Gaussian Component	0.134
10	0.150	1st-Order Polynomial	0.306
10	0.250	1st-Order Polynomial	0.196
10	0.350	Wider Fit Range (Low Side)	0.146
10	0.525	No Gaussian Component	0.085
10	0.775	1st-Order Polynomial	0.199
10	1.150	1st-Order Polynomial	0.142
10	1.650	1st-Order Polynomial	0.145
11	0.150	1st-Order Polynomial	0.508
11	0.250	1st-Order Polynomial	0.489
11	0.350	3rd-Order Polynomial	0.196
11	0.525	No Gaussian Component	0.096
11	0.775	1st-Order Polynomial	0.138
11	1.150	1st-Order Polynomial	0.128
11	1.650	1st-Order Polynomial	0.192

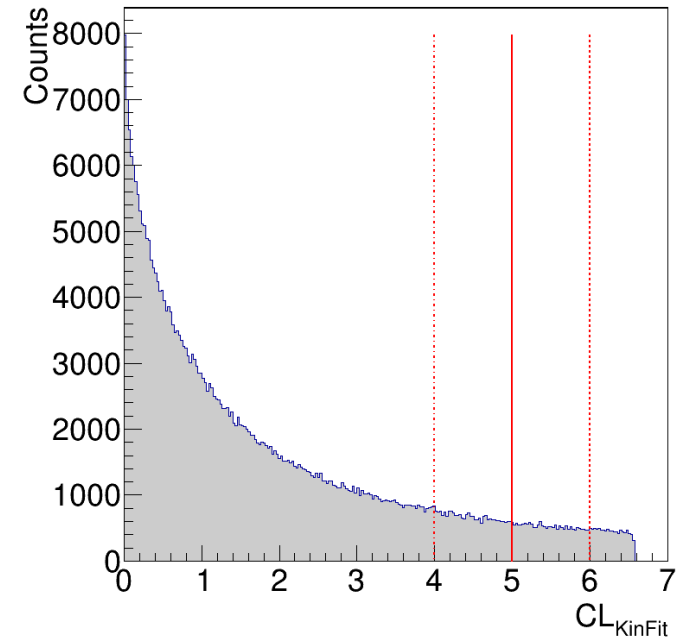

A

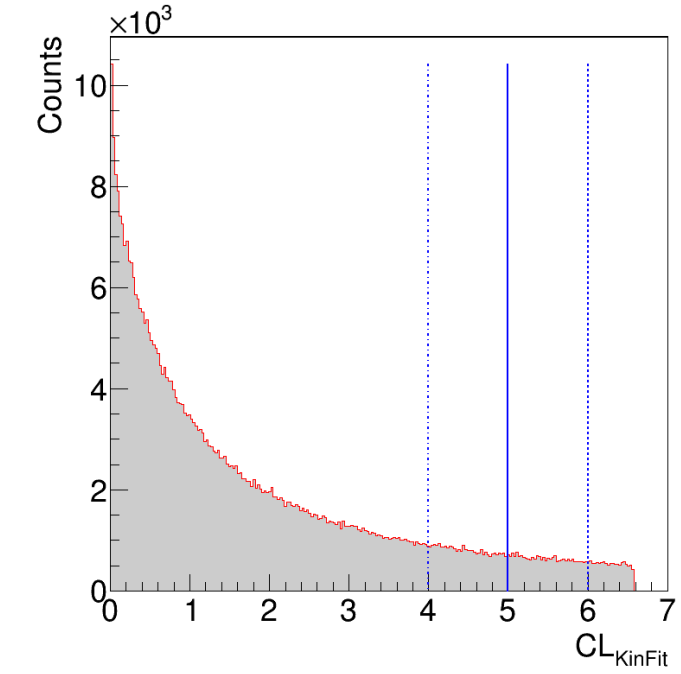

B

Figure 73. CL_{KinFit} variations. Distributions of CL_{KinFit} for final states $p'K^-K_s\pi^+$ (A) and $p'K^+K_s\pi^-$ (B). All other selection criteria is applied. Nominal (solid/middle line), loose (dashed/right line), and tight (dot-dash/left line) cut positions are marked

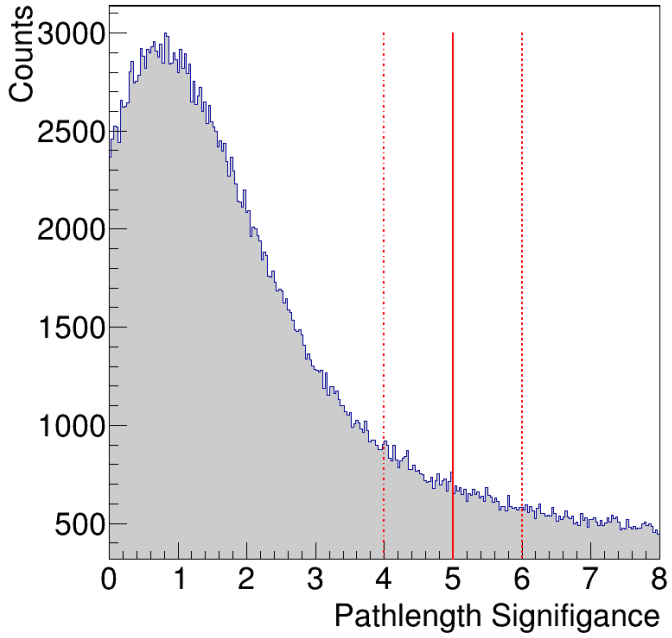

A

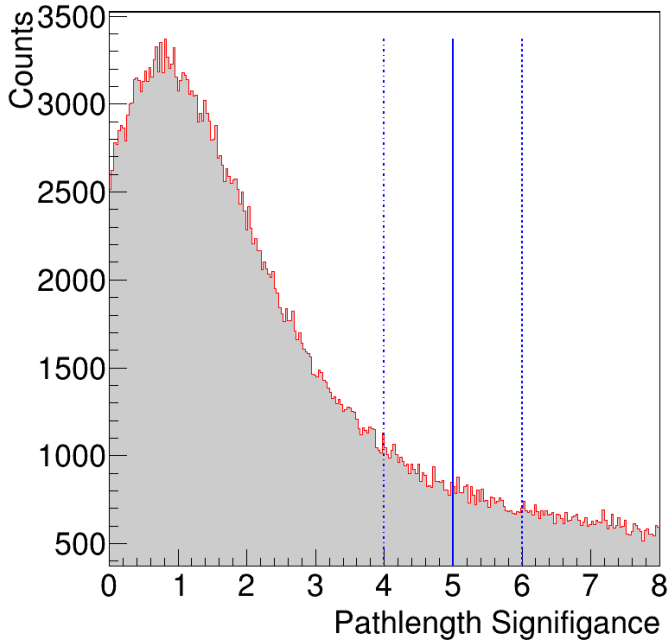

B

Figure 74. Pathlength Significance variations. Distributions of Pathlength Significance for final states $p'K^-K_s\pi^+$ (A) and $p'K^+K_s\pi^-$ (B). All other selection criteria is applied.. Nominal (solid/middle line), loose (dashed/left line), and tight (dot-dash/right line) cut positions are marked

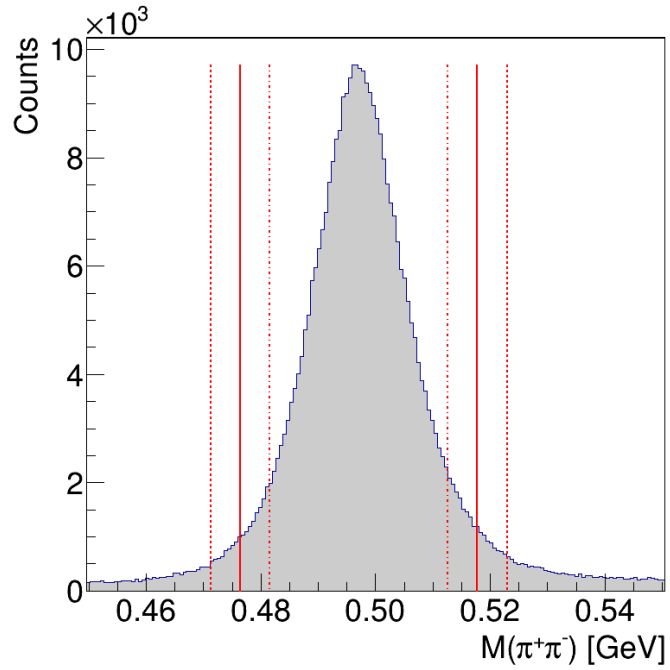

A

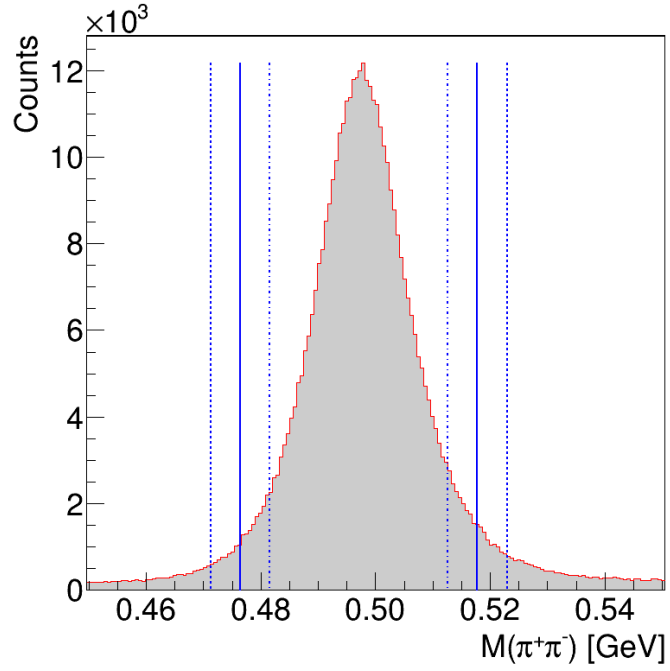

B

Figure 75. $M(\pi^+\pi^-)$ variations. Distributions of $M(\pi^+\pi^-)$ for final states $p'K^-K_s\pi^+$ (A) and $p'K^+K_s\pi^-$ (B). All other selection criteria is applied. Nominal (solid/middle line), loose (dashed/outer line), and tight (dot-dash/inner line) cut positions are marked

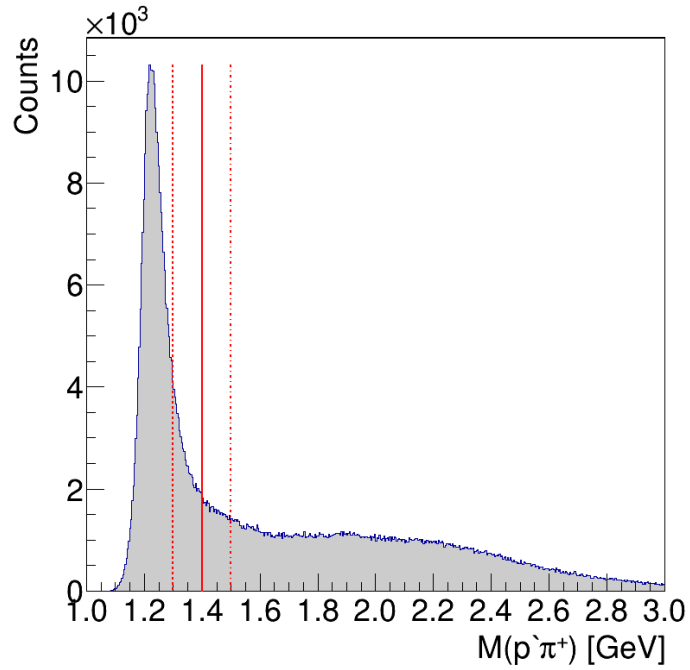

A

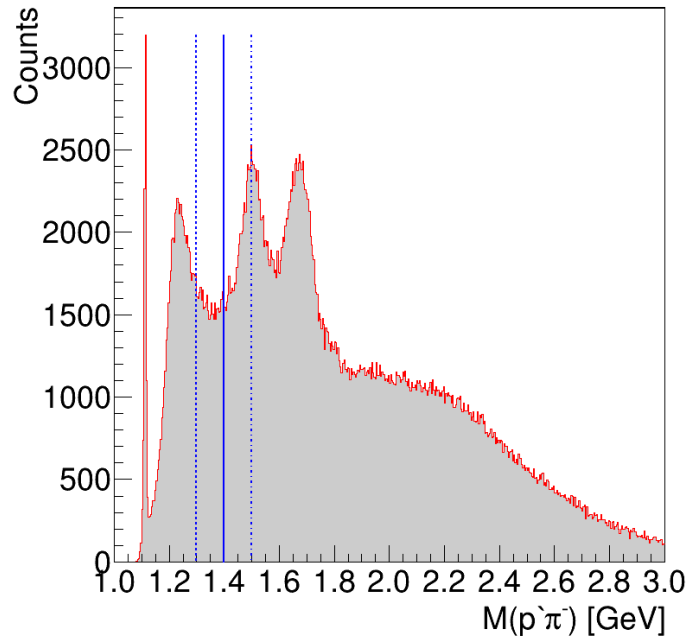

B

Figure 76. $M(p\pi)$ variations. Distributions of $M(p\pi)$ for final states $p'K^-K_s\pi^+$ (A) and $p'K^+K_s\pi^-$ (B). All other selection criteria is applied. Nominal (solid/middle line), loose (dashed/left line), and tight (dot-dash/right line) cut positions are marked

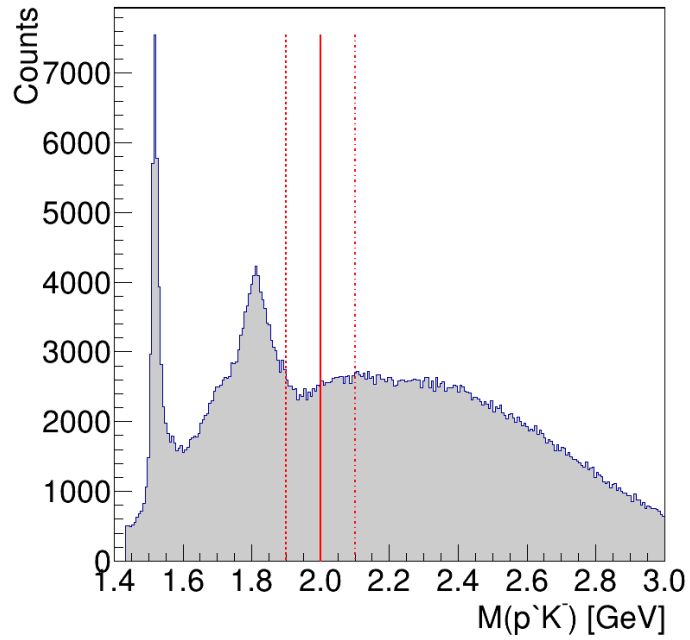

A

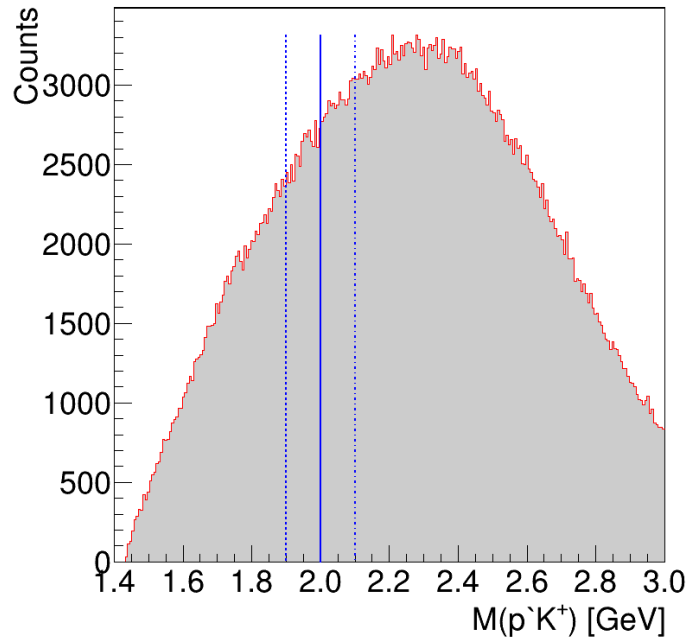

B

Figure 77. $M(pK^{\mp})$ variations. Distributions of $M(pK^{\mp})$ for final states $p'K^{-}K_s\pi^{+}$ (A) and $p'K^{+}K_s\pi^{-}$ (B). All other selection criteria is applied. Nominal (solid/middle line), loose (dashed/left line), and tight (dot-dash/right line) cut positions are marked

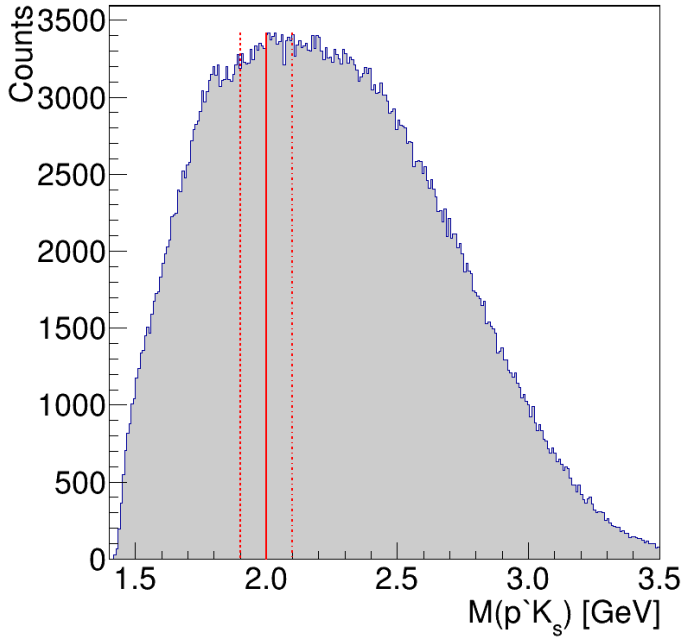

A $K^-K_s\pi^+$

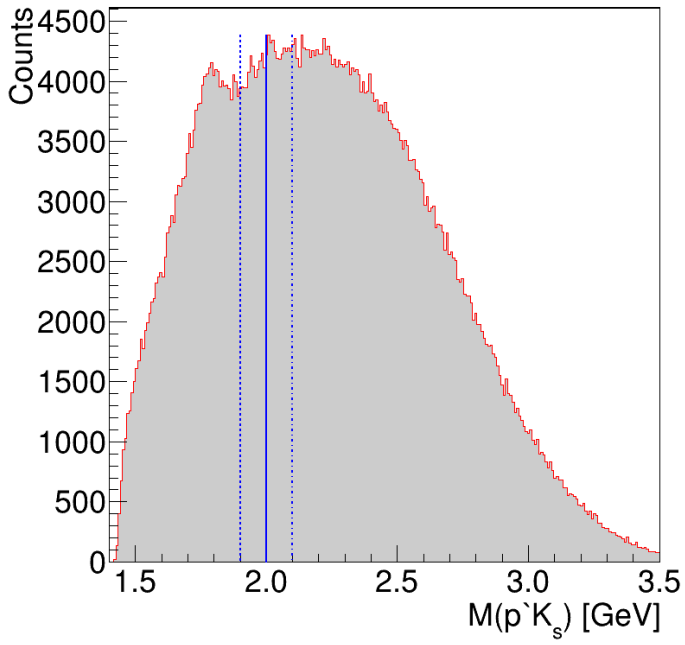

B $K^+K_s\pi^-$

Figure 78. $M(pK_s)$ variations. Distributions of $M(pK_s)$ for final states $p'K^-K_s\pi^+$ (A) and $p'K^+K_s\pi^-$ (B). All other selection criteria is applied. Nominal (solid/middle line), loose (dashed/left line), and tight (dot-dash/right line) cut positions are marked

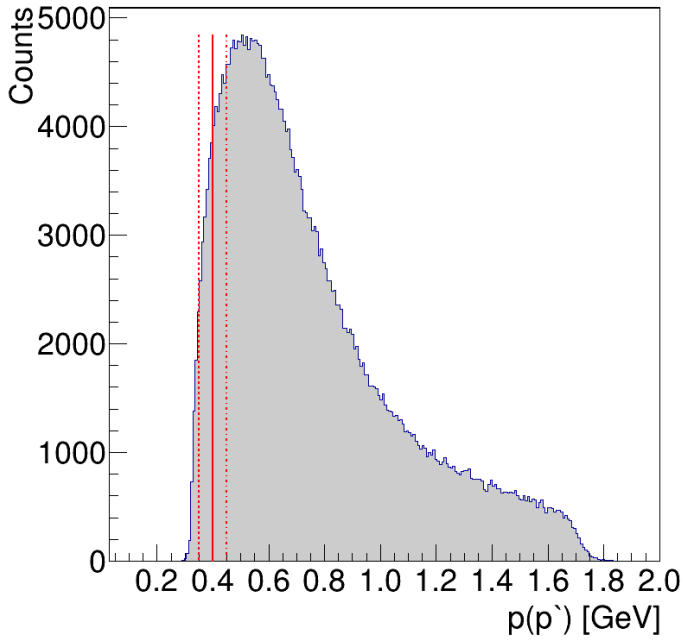

A

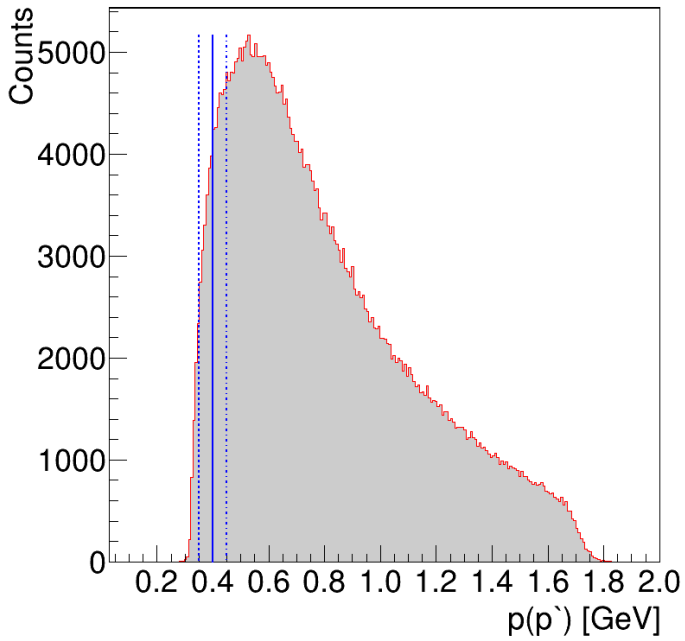

B

Figure 79. $\vec{p}(p)$ variations. Distributions of $\vec{p}(p)$ for final states $p'K^-K_s\pi^+$ (A) and $p'K^+K_s\pi^-$ (B). All other selection criteria is applied. Nominal (solid/middle line), loose (dashed/left line), and tight (dot-dash/right line) cut positions are marked

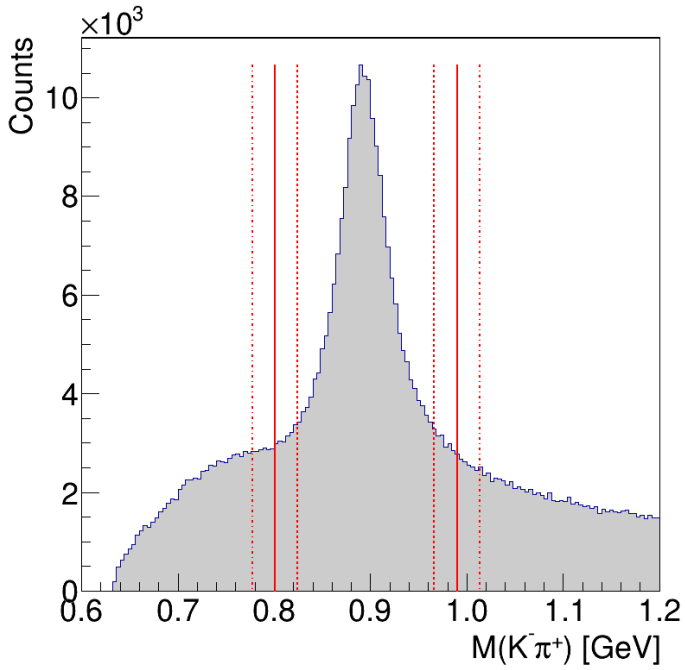

A

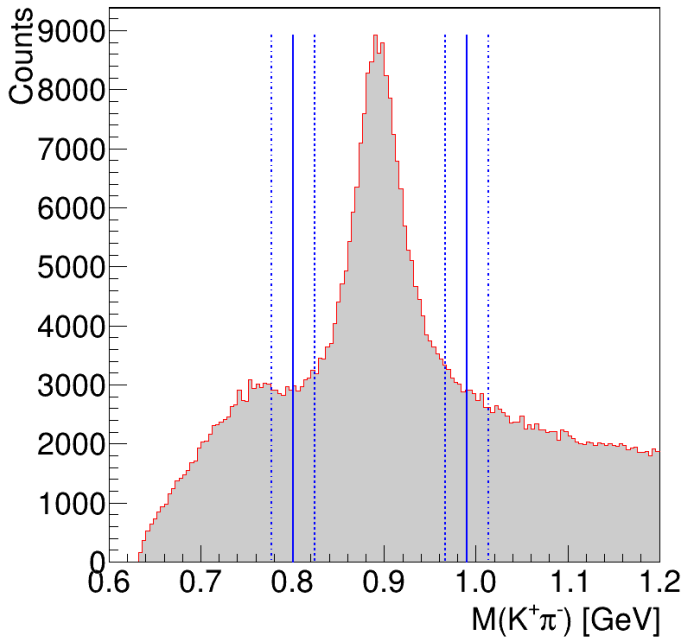

B

Figure 80. $M(K^{\mp}\pi^{\pm})$ variations. Distributions of $M(K^{\mp}\pi^{\pm})$ for final states $p'K^{-}K_s\pi^{+}$ (A) and $p'K^{+}K_s\pi^{-}$ (B). All other selection criteria is applied. Nominal (solid/middle line), loose (dashed/inner line), and tight (dot-dash/outer line) cut positions are marked

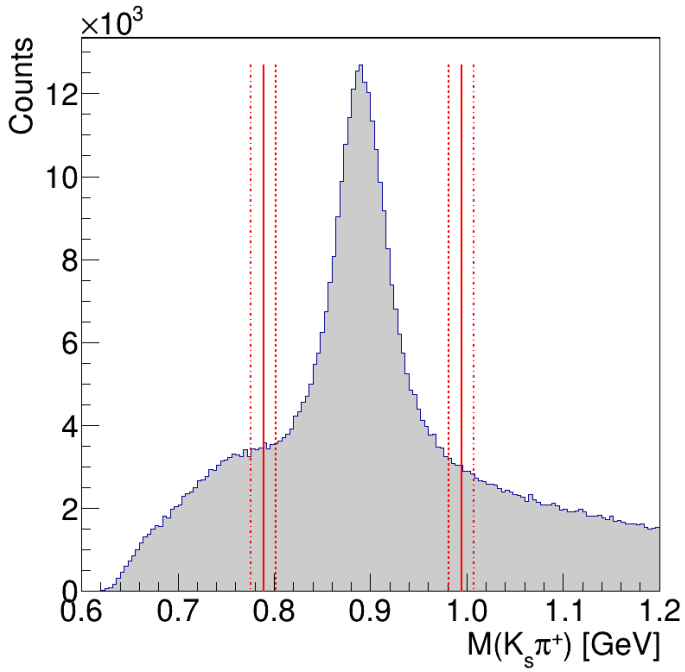

A

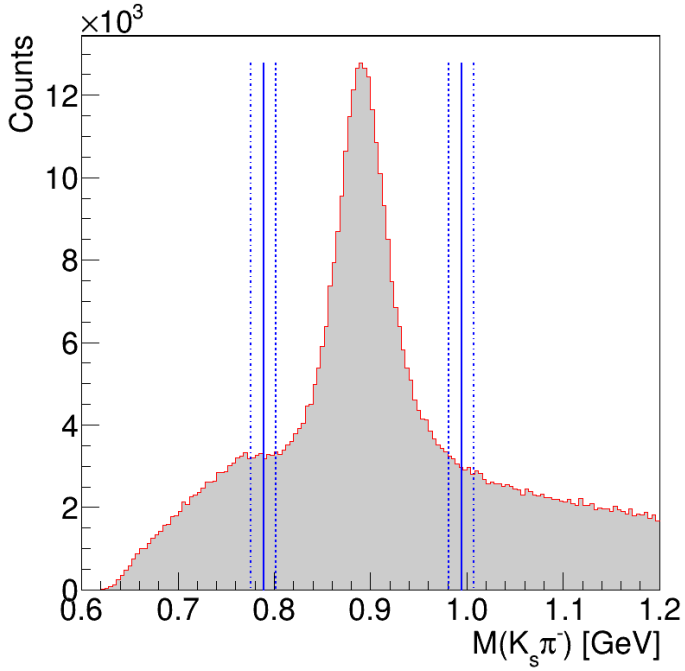

B

Figure 81. $M(K_s\pi^{\pm})$ variations. Distributions of $M(K_s\pi^{\pm})$ for final states $p'K^-K_s\pi^+$ (A) and $p'K^+K_s\pi^-$ (B). All other selection criteria is applied. Nominal (solid/middle line), loose (dashed/inner line), and tight (dot-dash/outer line) cut positions are marked

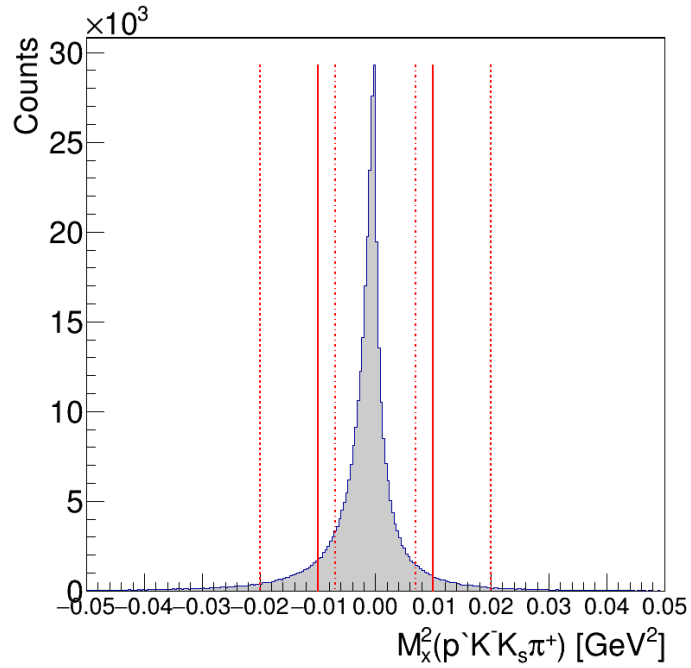

A

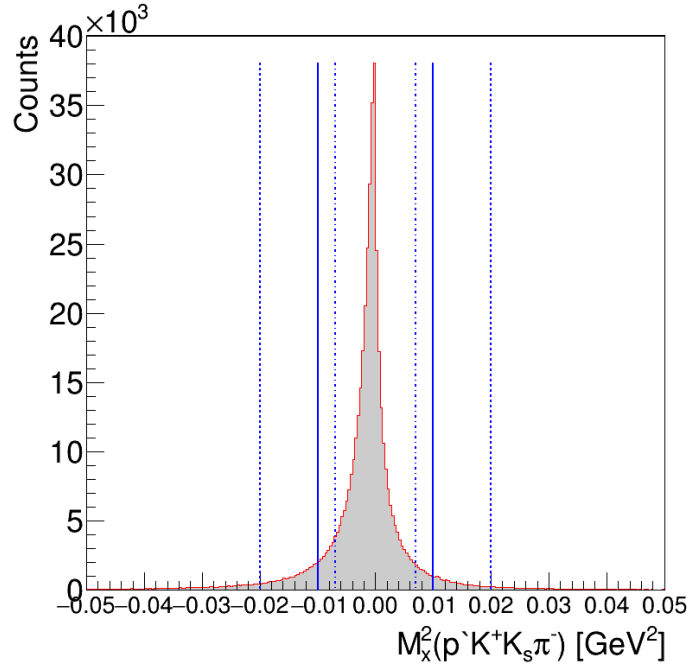

B

Figure 82. $M_x^2(p'K^{\mp}K_s\pi^{\pm})$ variations. Distributions of $M_x^2(p'K^{\mp}K_s\pi^{\pm})$ for final states $p'K^-K_s\pi^+$ (A) and $p'K^+K_s\pi^-$ (B). All other selection criteria is applied. Nominal (solid/middle line), loose (dashed/inner line), and tight (dot-dash/outer line) cut positions are marked

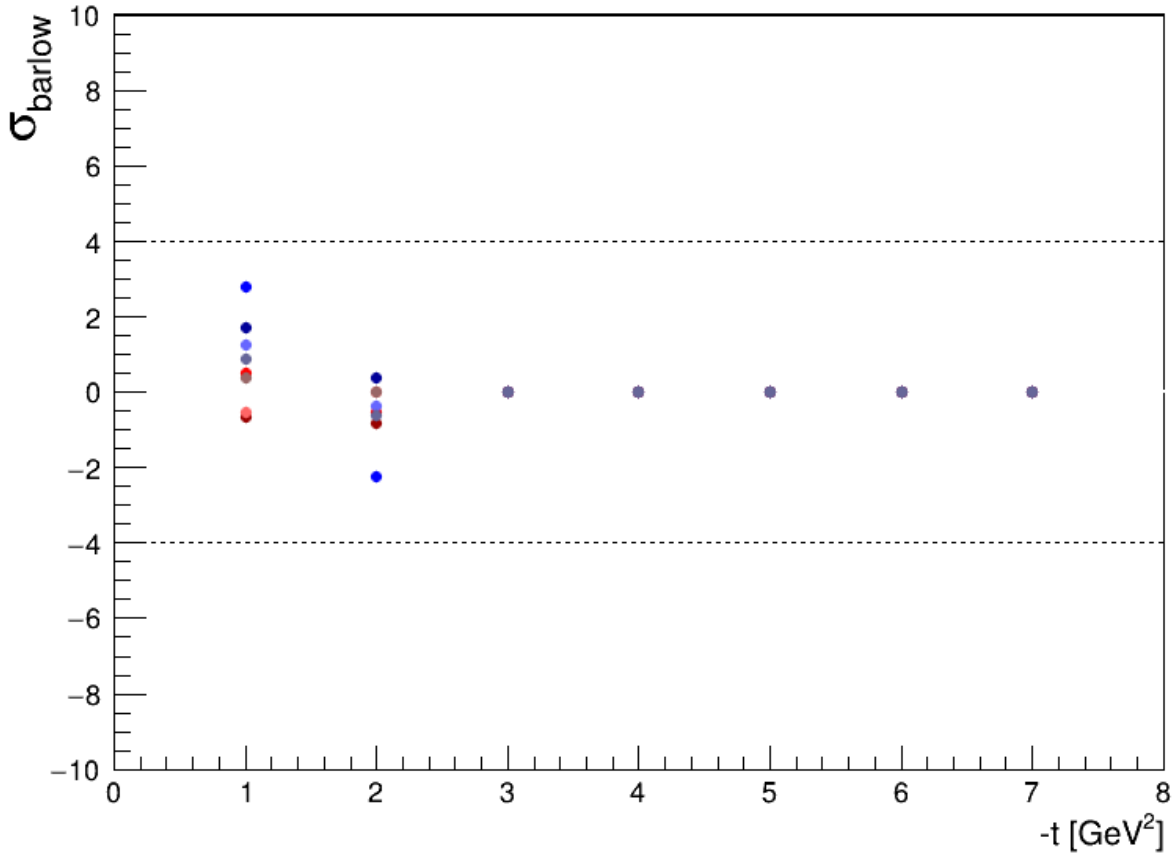

Figure 83. Barlow Test for the $\vec{p}(p)$ cut. The blue points are for the $p'K^-K_s\pi^+$ final state and the red points are for the $p'K^+K_s\pi^-$ final state. The shades of the colors represent the different energy bins the cross section is measured in. The dashed black lines are drawn at the $\sigma_{\text{barlow}} = \pm 4$ threshold. This cut only impacts the lowest $-t$ bin and does not exceed the barlow test threshold. It is not included in the systematic uncertainty calculations

APPENDIX B

ANALYSIS PROCEDURE

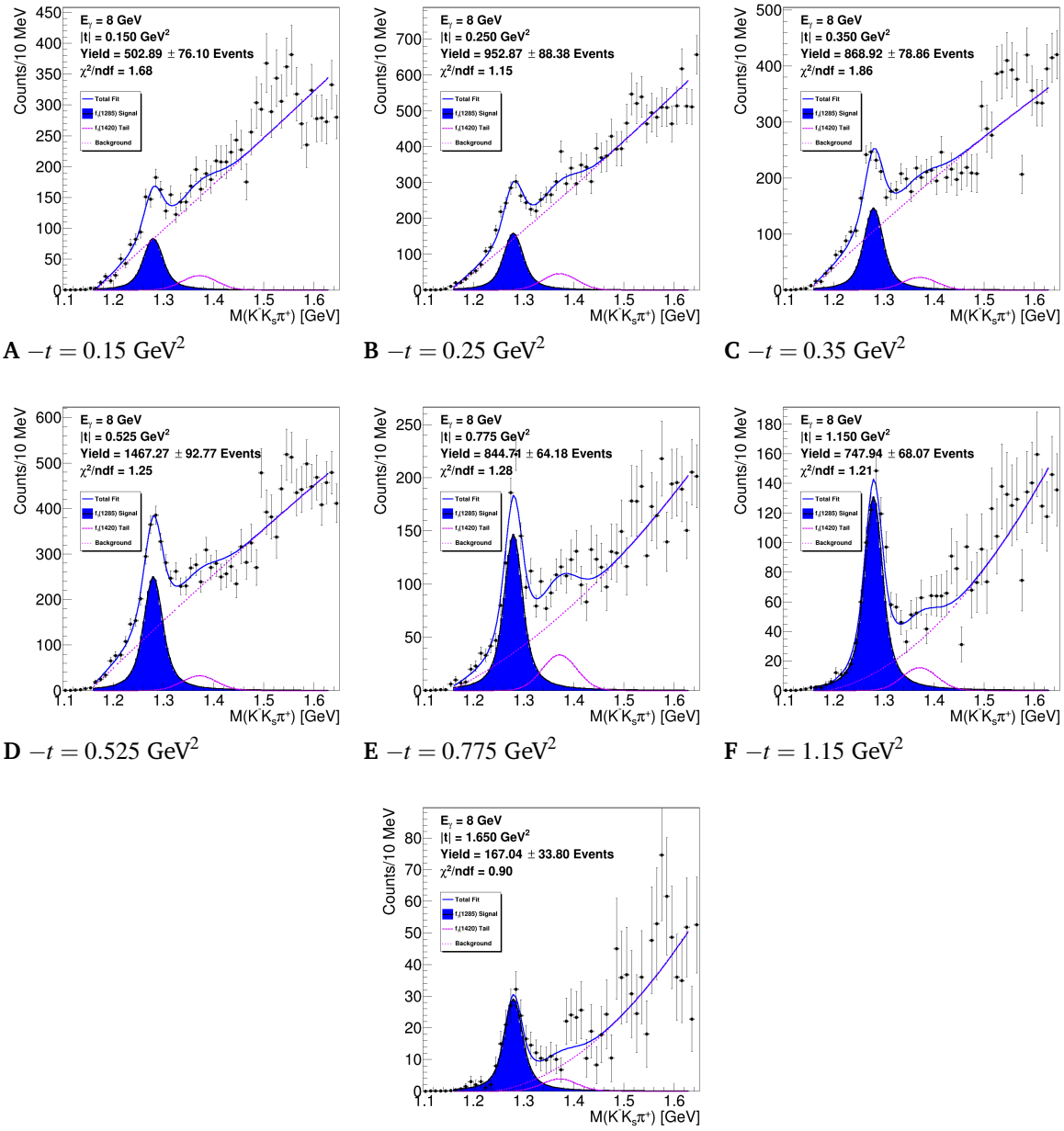

A $-t = 0.15$ GeV^2 **B** $-t = 0.25$ GeV^2 **C** $-t = 0.35$ GeV^2

D $-t = 0.525$ GeV^2 **E** $-t = 0.775$ GeV^2 **F** $-t = 1.15$ GeV^2

G $-t = 1.65$ GeV^2

Figure 84. Fits to t-binned distributions of $M(K^-K_s\pi^+)$ for photon beam energy $7.5 < E_\gamma < 8.5$ GeV.

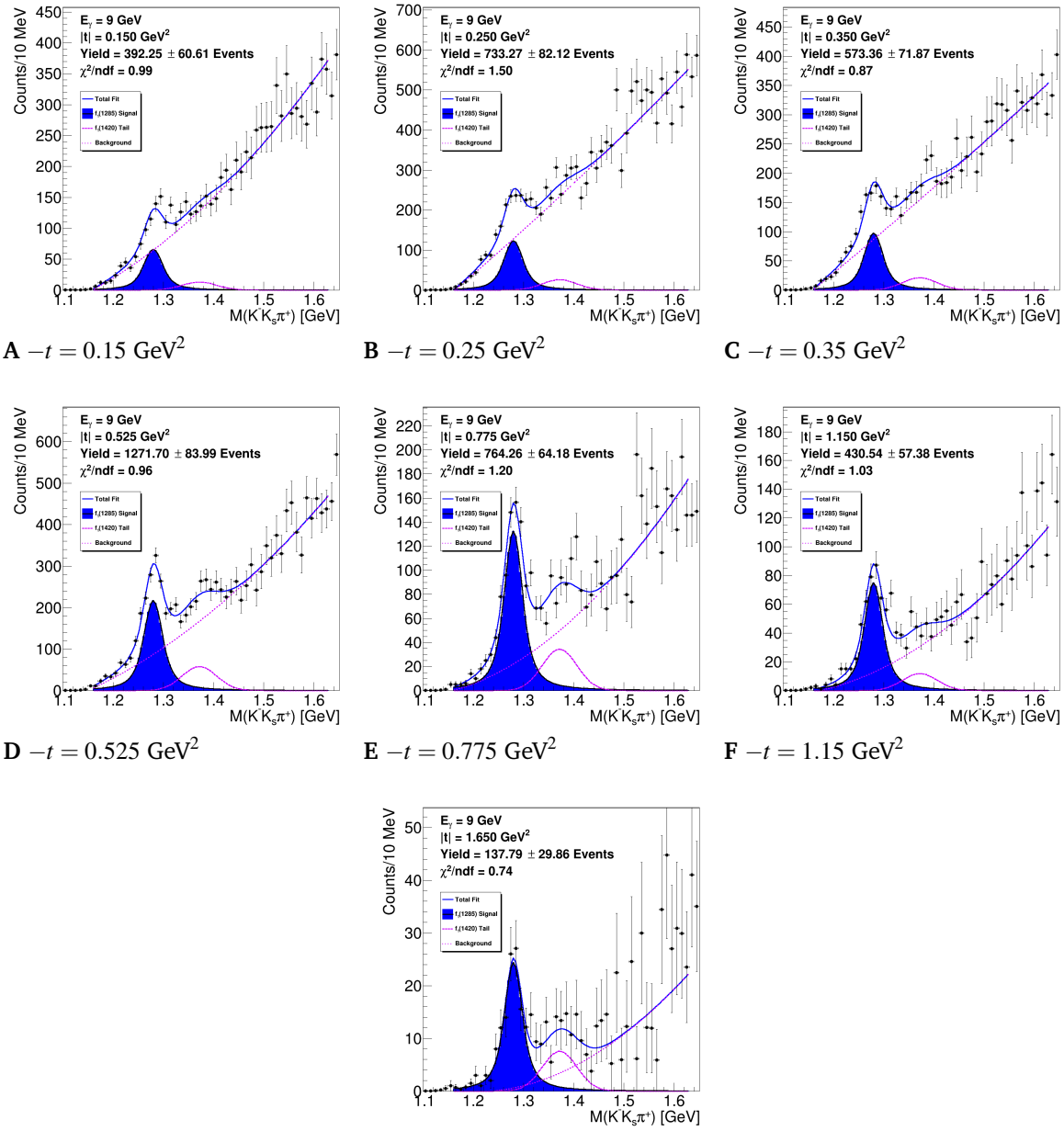

A $-t = 0.15$ GeV^2 **B** $-t = 0.25$ GeV^2 **C** $-t = 0.35$ GeV^2

D $-t = 0.525$ GeV^2 **E** $-t = 0.775$ GeV^2 **F** $-t = 1.15$ GeV^2

G $-t = 1.65$ GeV^2

Figure 85. Fits to t-binned distributions of $M(K^-K_s\pi^+)$ for photon beam energy $8.5 < E_\gamma < 9.5$ GeV.

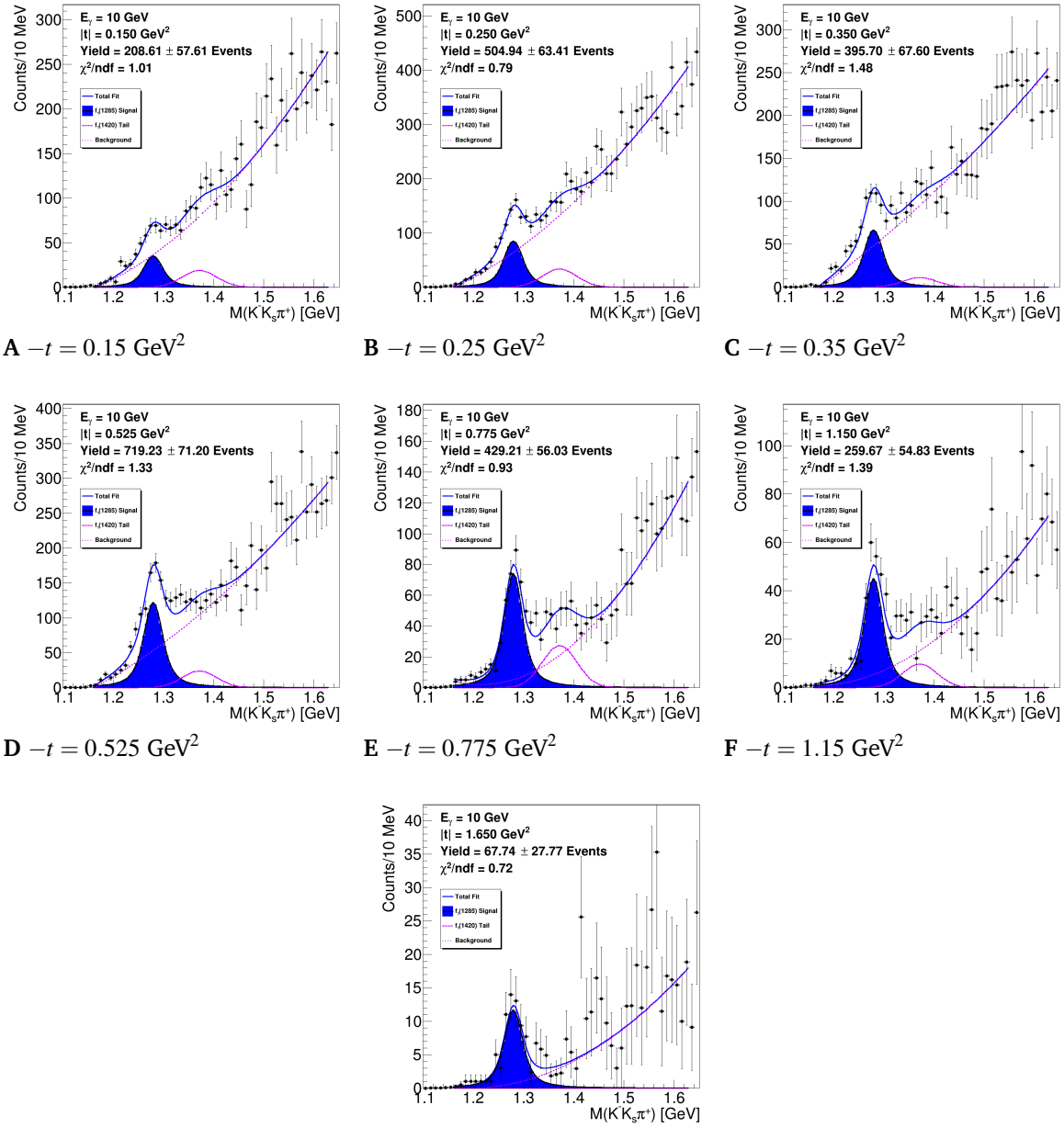

A $-t = 0.15$ GeV^2 **B** $-t = 0.25$ GeV^2 **C** $-t = 0.35$ GeV^2

D $-t = 0.525$ GeV^2 **E** $-t = 0.775$ GeV^2 **F** $-t = 1.15$ GeV^2

G $-t = 1.65$ GeV^2

Figure 86. Fits to t-binned distributions of $M(K^-K_s\pi^+)$ for photon beam energy $9.5 < E_\gamma < 10.5$ GeV.

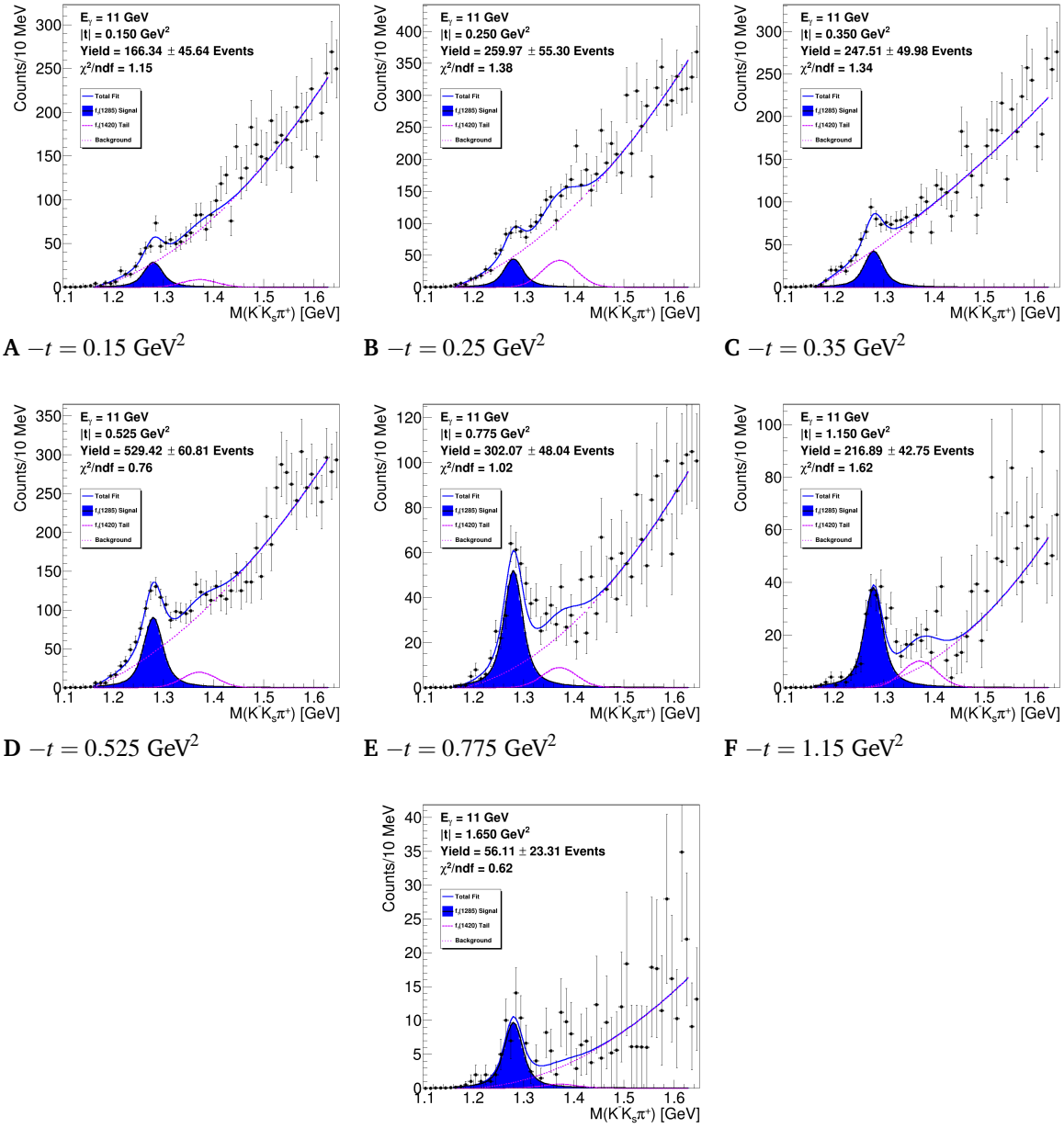

A $-t = 0.15$ GeV^2 **B** $-t = 0.25$ GeV^2 **C** $-t = 0.35$ GeV^2

D $-t = 0.525$ GeV^2 **E** $-t = 0.775$ GeV^2 **F** $-t = 1.15$ GeV^2

G $-t = 1.65$ GeV^2

Figure 87. Fits to t-binned distributions of $M(K^-K_s\pi^+)$ for photon beam energy $10.5 < E_\gamma < 11.5$ GeV.

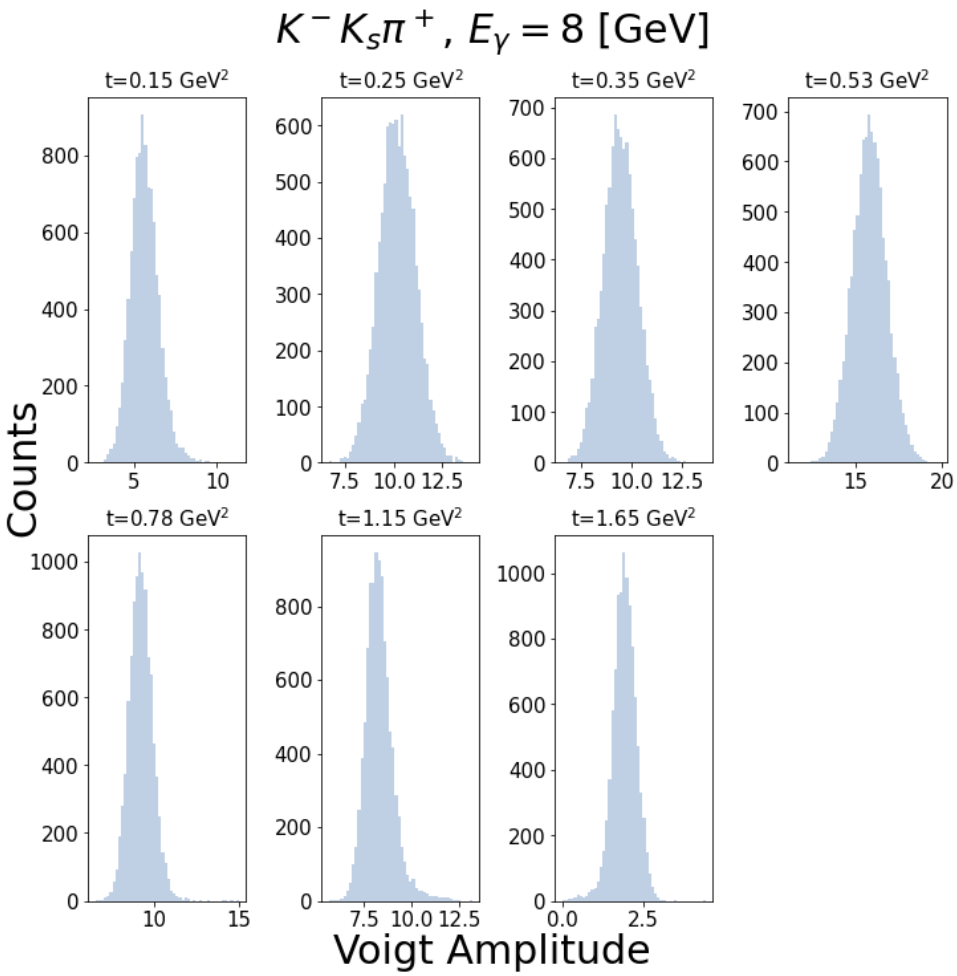

Figure 92. Bootstrapped amplitude distribution for $K^-K_s\pi^+$ at $E_\gamma = 9$ GeV. Distributions of the amplitudes obtained via the bootstrapping procedure outlined in §73 as a function of $-t$ for $K^-K_s\pi^+$ at $E_\gamma = 8$ GeV. Value of $-t$ for each bin is shown above the figure. The amplitudes follow a normal distribution and the uncertainty is calculated using the variance estimator given by Eqn. 72.

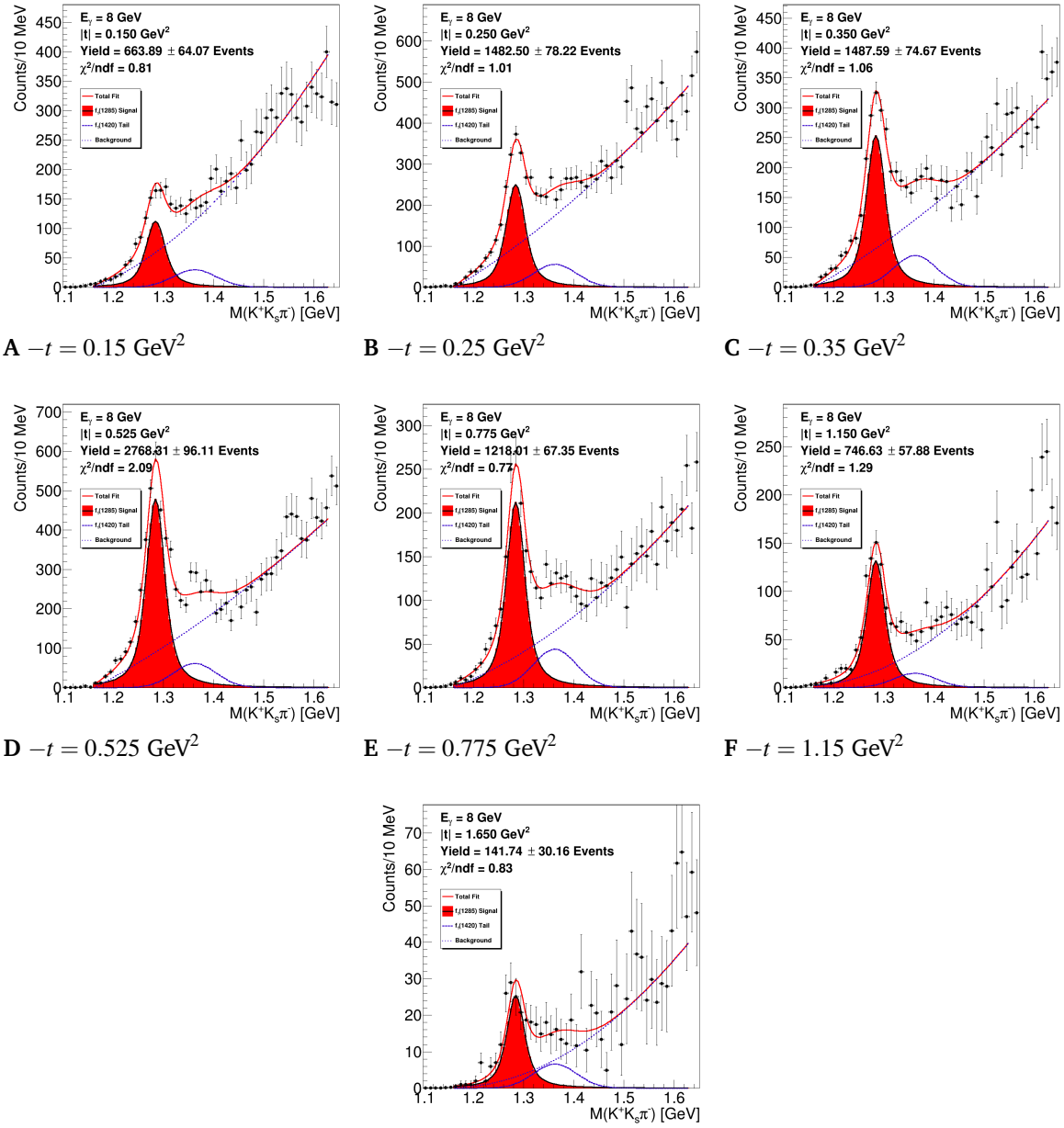

A $-t = 0.15$ GeV^2 **B** $-t = 0.25$ GeV^2 **C** $-t = 0.35$ GeV^2

D $-t = 0.525$ GeV^2 **E** $-t = 0.775$ GeV^2 **F** $-t = 1.15$ GeV^2

G $-t = 1.65$ GeV^2

Figure 88. Fits to t-binned distributions of $M(K^+K_S\pi^-)$ for photon beam energy $7.5 < E_\gamma < 8.5$ GeV.

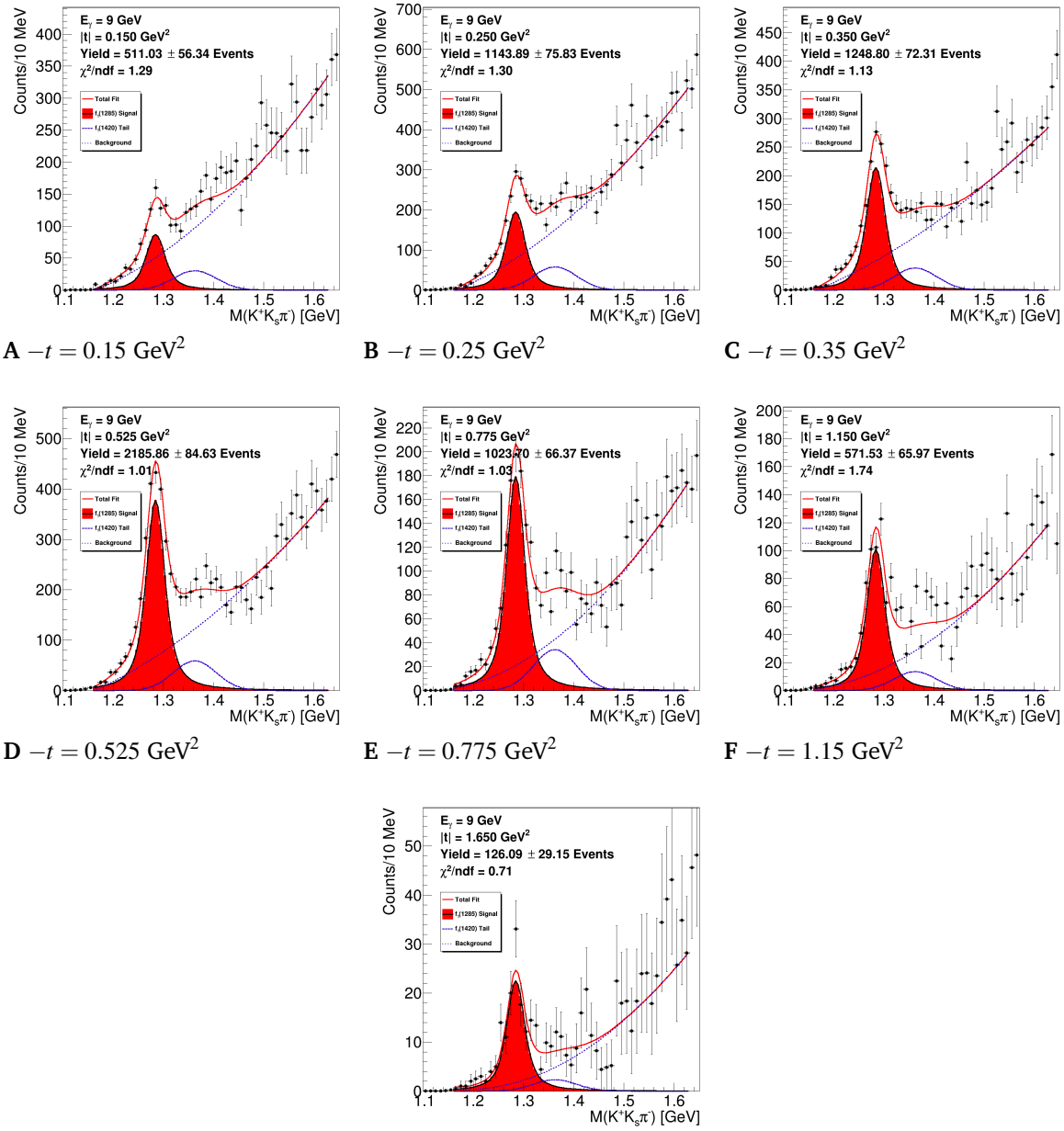

A $-t = 0.15$ GeV^2 **B** $-t = 0.25$ GeV^2 **C** $-t = 0.35$ GeV^2

D $-t = 0.525$ GeV^2 **E** $-t = 0.775$ GeV^2 **F** $-t = 1.15$ GeV^2

G $-t = 1.65$ GeV^2

Figure 89. Fits to t-binned distributions of $M(K^+K_s\pi^-)$ for photon beam energy $8.5 < E_\gamma < 9.5$ GeV.

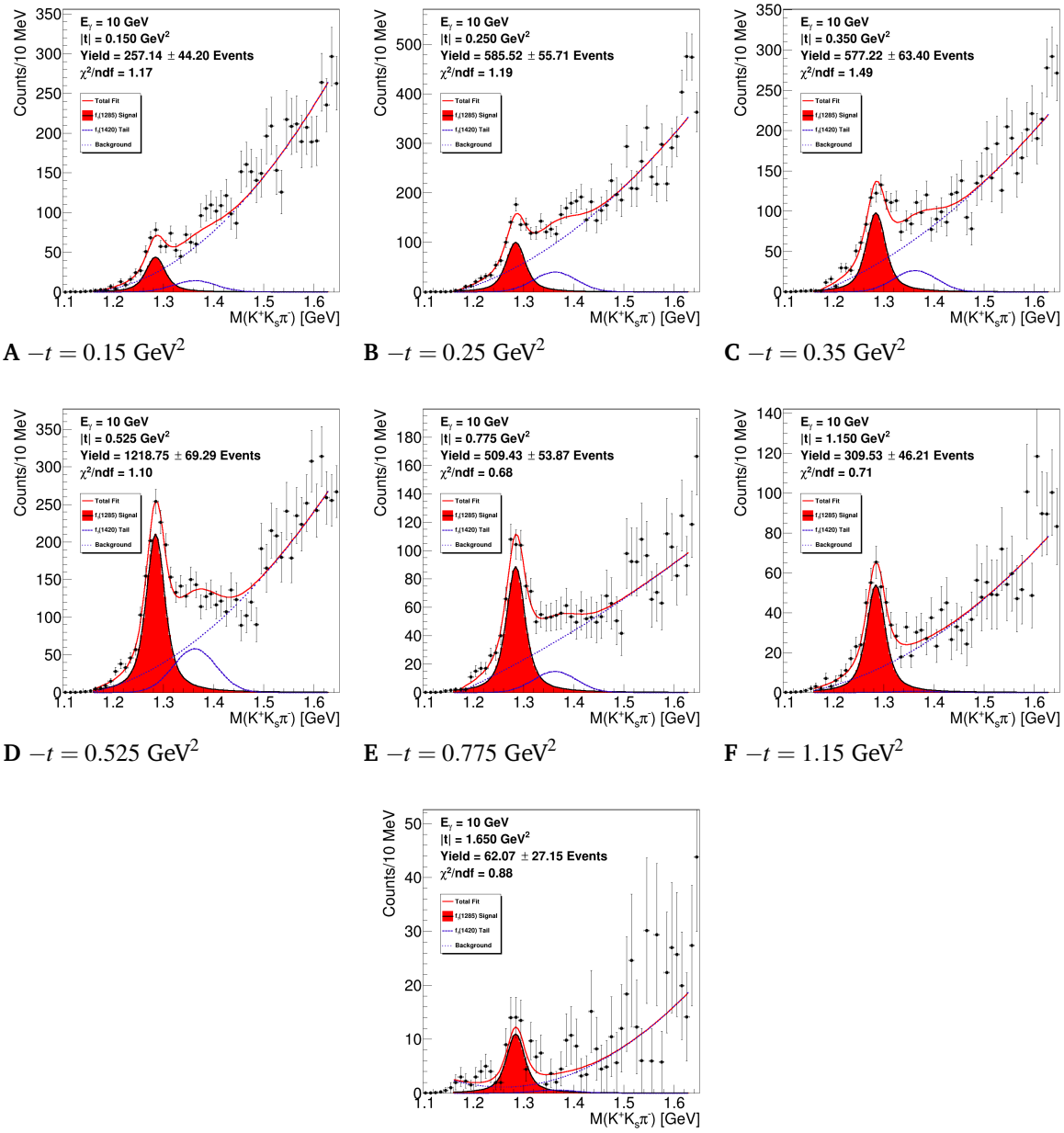

A $-t = 0.15$ GeV^2 **B** $-t = 0.25$ GeV^2 **C** $-t = 0.35$ GeV^2

D $-t = 0.525$ GeV^2 **E** $-t = 0.775$ GeV^2 **F** $-t = 1.15$ GeV^2

G $-t = 1.65$ GeV^2

Figure 90. Fits to t-binned distributions of $M(K^+K_s\pi^-)$ for photon beam energy $9.5 < E_\gamma < 10.5$ GeV.

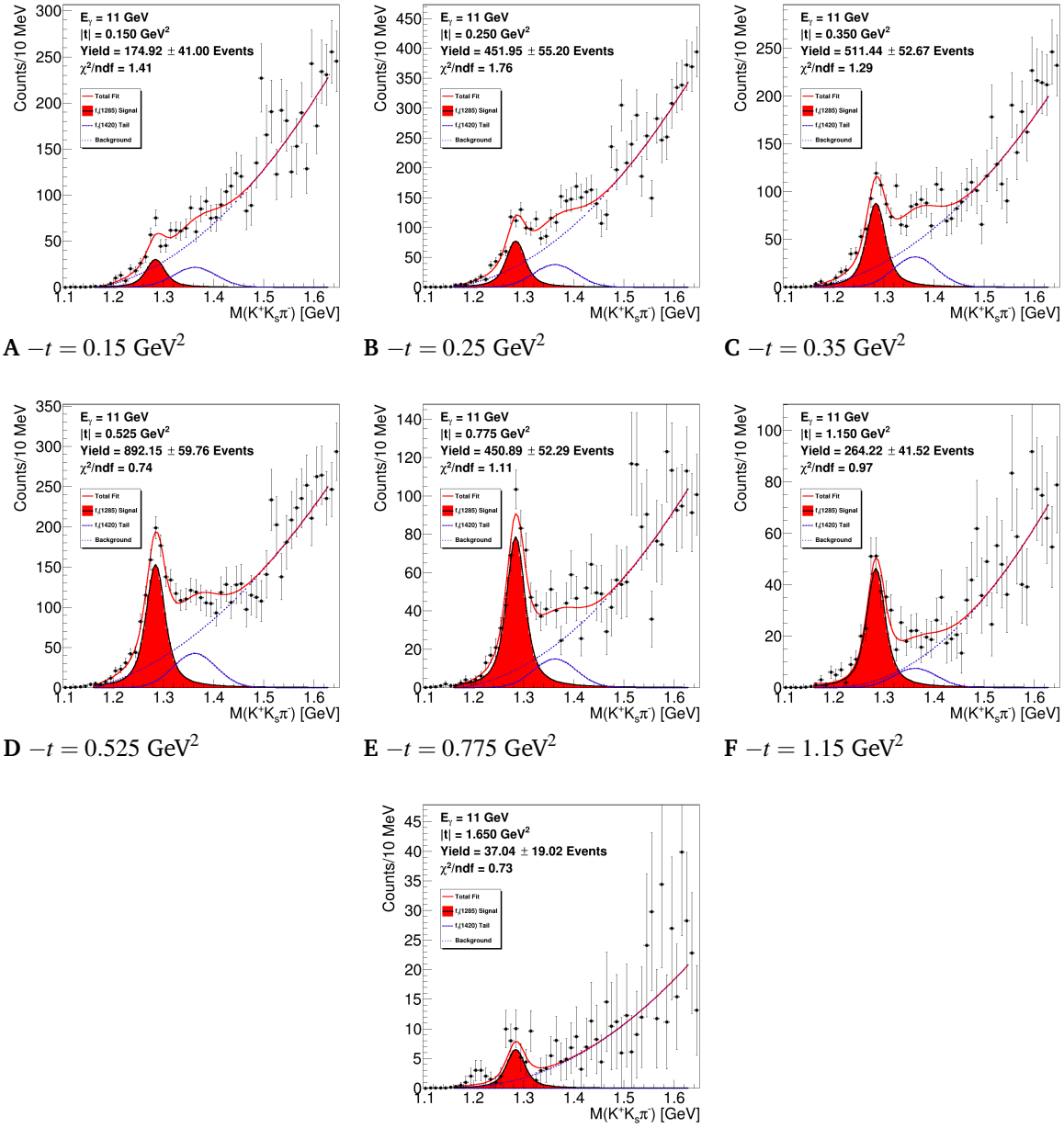

Figure 91. Fits to t-binned distributions of $M(K^+K_s\pi^-)$ for photon beam energy $10.5 < E_\gamma < 11.5$ GeV.

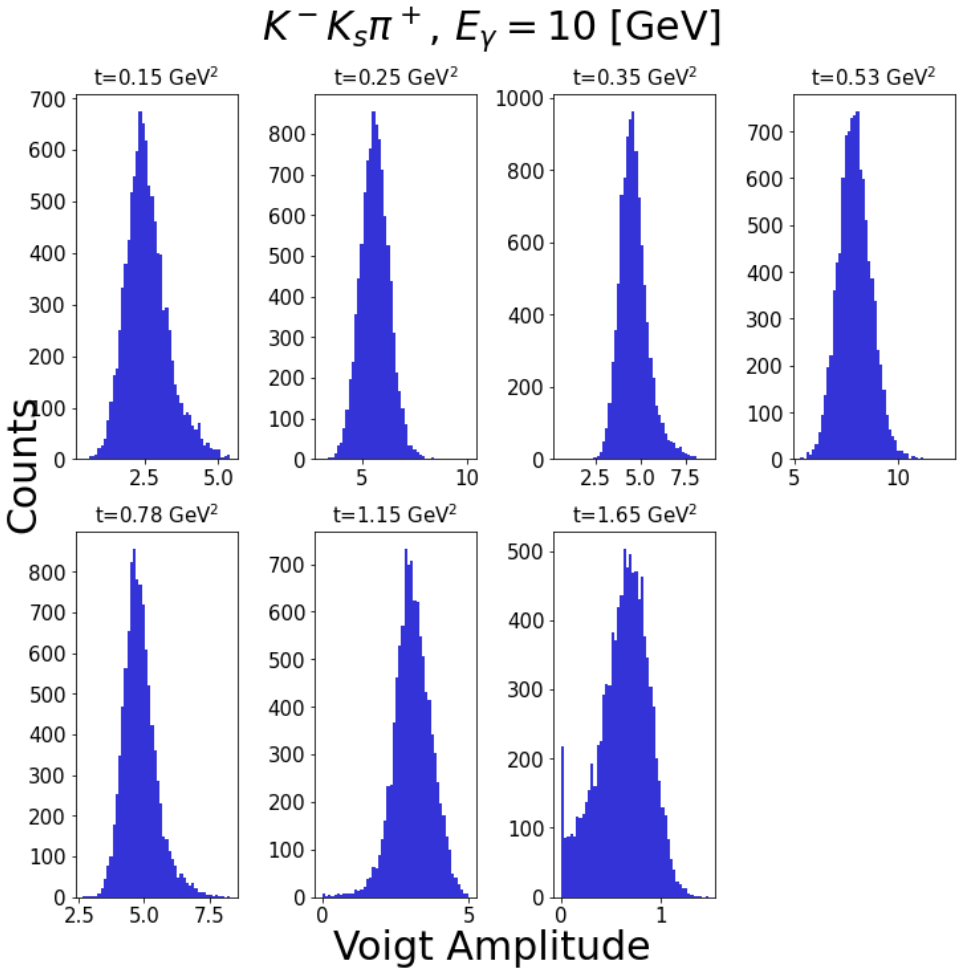

Figure 93. Bootstrapped amplitude distribution for $K^-K_s\pi^+$ at $E_\gamma = 10$ GeV. Distributions of the amplitudes obtained via the bootstrapping procedure outlined in §73 as a function of $-t$ for $K^-K_s\pi^+$ at $E_\gamma = 10$ GeV. Value of $-t$ for each bin is shown above the figure. The amplitudes follow a normal distribution and the uncertainty is calculated using the variance estimator given by Eqn. 72.

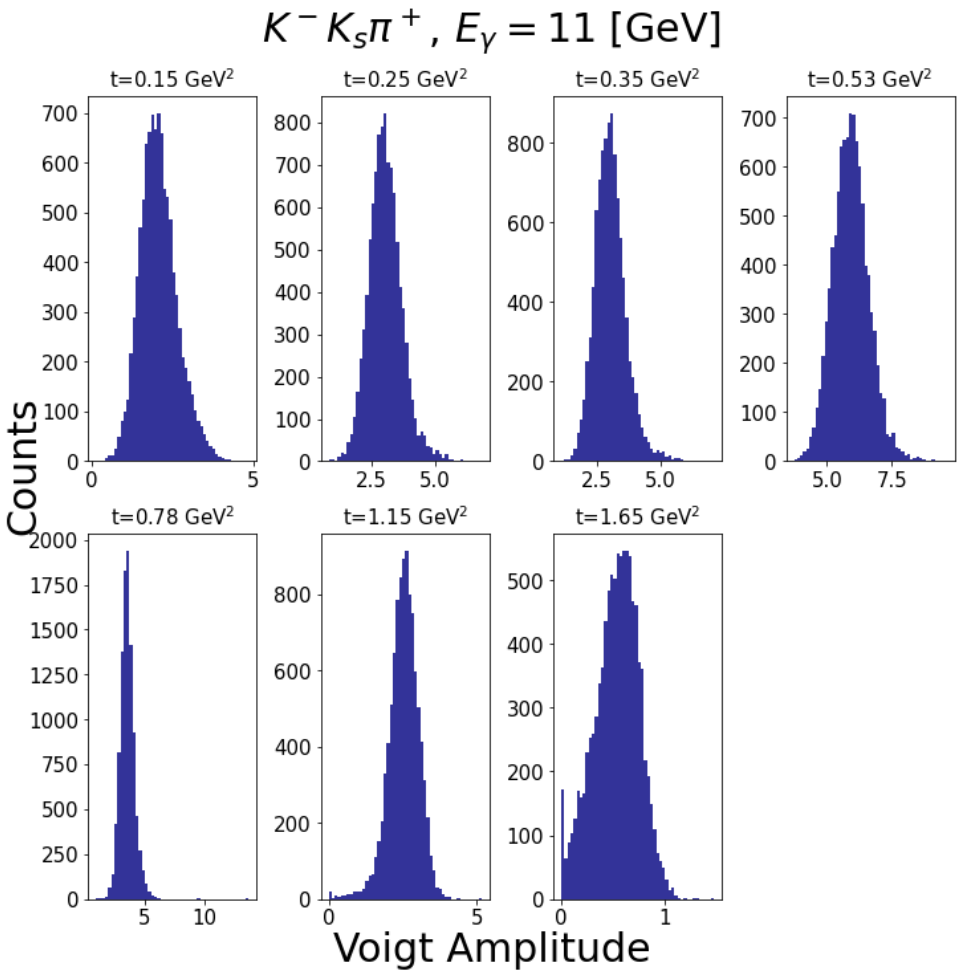

Figure 94. Bootstrapped amplitude distribution for $K^-K_s\pi^+$ at $E_\gamma = 11$ GeV. Distributions of the amplitudes obtained via the bootstrapping procedure outlined in §73 as a function of $-t$ for $K^-K_s\pi^+$ at $E_\gamma = 11$ GeV. Value of $-t$ for each bin is shown above the figure. The amplitudes follow a normal distribution and the uncertainty is calculated using the variance estimator given by Eqn. 72.

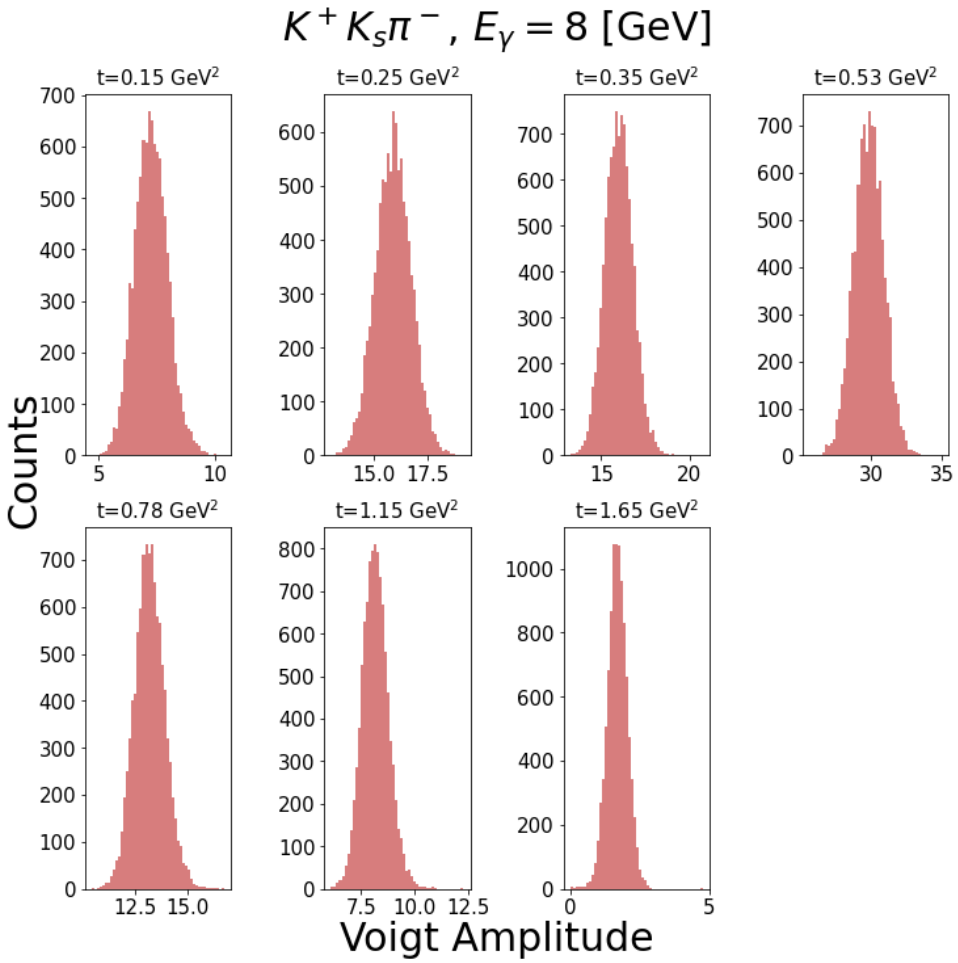

Figure 95. Bootstrapped amplitude distribution for $K^+K_s\pi^-$ at $E_\gamma = 8$ GeV. Distributions of the amplitudes obtained via the bootstrapping procedure outlined in §73 as a function of $-t$ for $K^+K_s\pi^-$ at $E_\gamma = 8$ GeV. Value of $-t$ for each bin is shown above the figure. The amplitudes follow a normal distribution and the uncertainty is calculated using the variance estimator given by Eqn. 72.

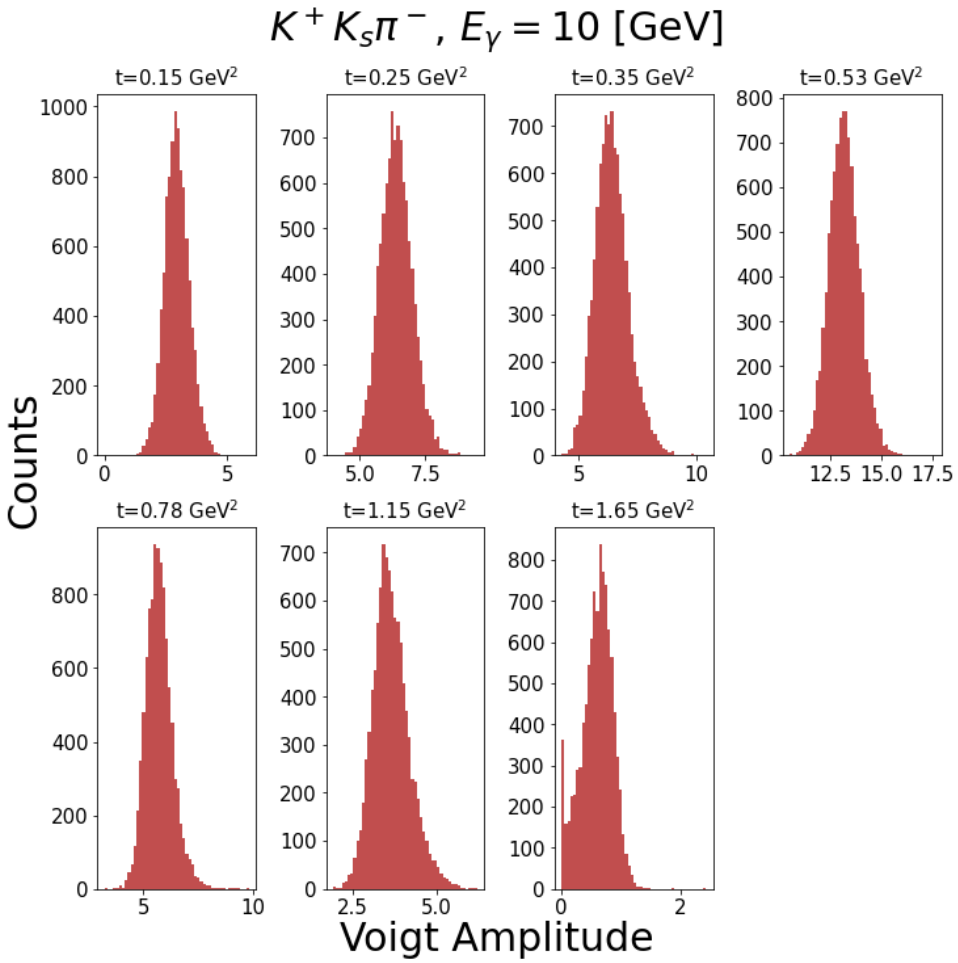

Figure 96. Bootstrapped amplitude distribution for $K^+K_s\pi^-$ at $E_\gamma = 10$ GeV. Distributions of the amplitudes obtained via the bootstrapping procedure outlined in §73 as a function of $-t$ for $K^+K_s\pi^-$ at $E_\gamma = 10$ GeV. Value of $-t$ for each bin is shown above the figure. The amplitudes follow a normal distribution and the uncertainty is calculated using the variance estimator given by Eqn. 72.

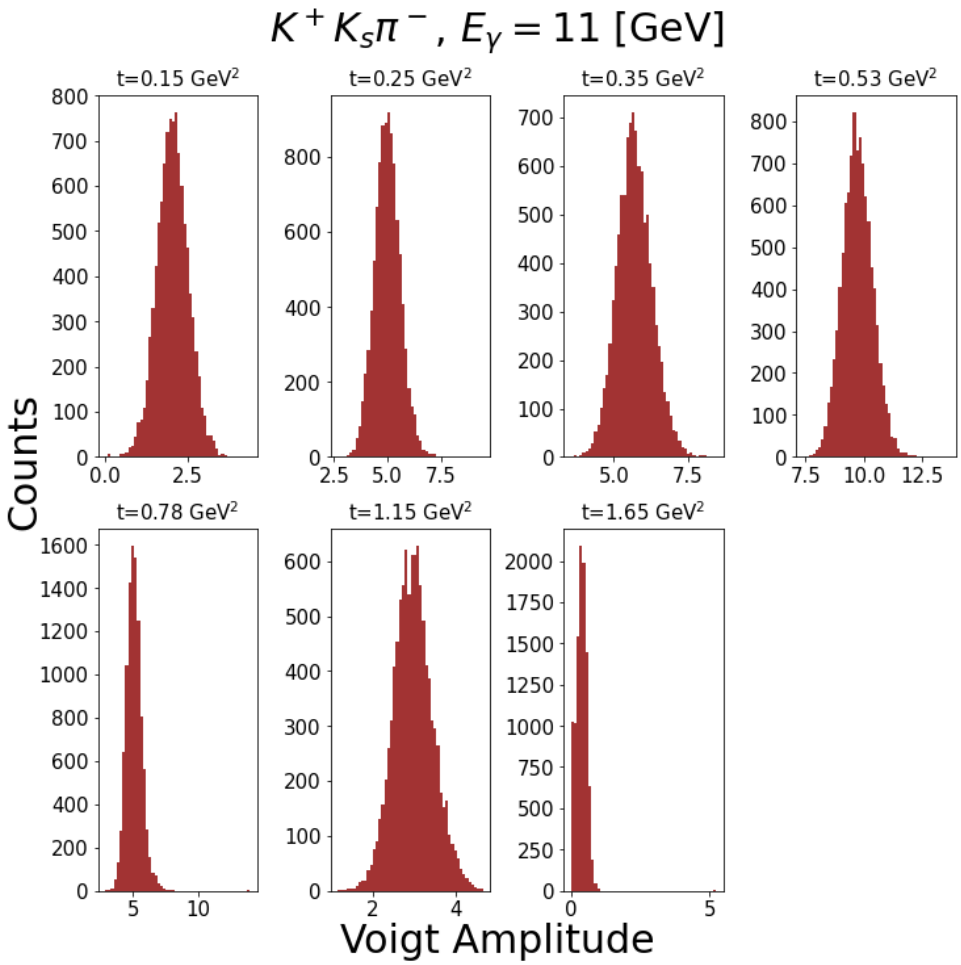

Figure 97. Bootstrapped amplitude distribution for $K^+K_s\pi^-$ at $E_\gamma = 11$ GeV. Distributions of the amplitudes obtained via the bootstrapping procedure outlined in §73 as a function of $-t$ for $K^+K_s\pi^-$ at $E_\gamma = 11$ GeV. Value of $-t$ for each bin is shown above the figure. The amplitudes follow a normal distribution and the uncertainty is calculated using the variance estimator given by Eqn. 72.

VITA

Tyler Viducic
Department of Physics
Old Dominion University
Norfolk, VA 23529

EDUCATION

2018-2024 (expected), Ph.D., Physics, Old Dominion University
2016-2018, M.S., Physics, Old Dominion University
2012-2016, B.S., Physics, The College of New Jersey.

PROFESSIONAL EXPERIENCE

2024, Quantitative Researcher, Proprietary Trading Firm
2018-2024, Graduate Research Assistant, ODU Research Foundation
2016-2018, Graduate Teaching Assistant, Old Dominion University

CONFERENCE PRESENTATIONS

1. Joint Meeting of the APS Division of Nuclear Physics and the Physical Society of Japan - Hawaii, First Measurement of the Photoproduction Cross-Section of $f_1(1285)$ at High Energies with GlueX, 11/2023
2. DNP April Meeting - New York City, First Measurement of the Photoproduction Cross-Section of $f_1(1285)$ at High Energies with GlueX, 4/2022
3. DNP Fall Meeting - Boston, First Measurement of the Photoproduction Cross-Section of $f_1(1285)$ at High Energies with GlueX, 10/2021
4. Texas Symposium for Relativistic Astrophysics, Attenuation of Gravitational Waves, 12/2015

Typeset using LaTeX.